Hydrodynamics of Nematic Liquid Crystals for Diffractive Optical Elements

Rowan Edward Morris

University of Leeds

Department of Physics and Astronomy

Submitted in accordance with the requirements for the degree of

Doctor of Philosophy

August 2021

The candidate confirms that the work submitted is their own, except where work which has formed part of jointly authored publications has been included. The contribution of the candidate and the other authors to this work has been explicitly indicated below. The candidate confirms that appropriate credit has been given within the thesis where reference has been made to the work of others.

Chapters 2 and 4 contain small elements of “Liquid Crystal Devices for Beam Steering Applications”. The candidate, Cliff Jones and Mamatha Nagaraj published this in Micromachines in 2021. As a review article, no experimental work was undertaken and the majority of writing was done by the candidate, with advice and help from co-authors.

Chapters 5 and 6 contain work from “Continuously variable diffraction gratings using electroconvection in liquid crystals for beam steering applications” and “Variable pitch hydrodynamic electro-optic gratings utilising bent liquid crystal dimers”. The candidate, Cliff Jones and Mamatha Nagaraj published these in the Journal of Applied Physics in 2019 and Soft Matter in 2020, respectively. The candidate did the majority of experimental work and writing, with advice and help from co-authors.

Acknowledgements

As with mesogenic materials, a clear direction within a PhD relies on many contributing components. Firstly, I would like to thank my supervisors Dr Mamatha Nagaraj and Professor Cliff Jones who were phenomenal as a team to run this project. Mamatha is a brilliant scientist, who has a great aptitude to allow her students to pursue their own interests and give guidance, while ensuring the objectives of research are completed. She has always been highly supportive and encouraged me in many endeavours, which have aided both my research and personal development more generally. Cliff has an incredible ability to come up with, and understand other's ideas, a talent which although unnerving at times, is an absolute asset when undertaking research. During my studies, I had the pleasure to attend many conferences with him, which were some of the high points of my PhD. So thank you for both being such good mentors, all the great advice and always being keen to just have a chat.

I give thanks to my industrial sponsor Merck Chemicals UK who part funded my research through a CASE award. Particularly, I would like to thank Dr Benjamin Snow and Dr Owain Parri for always being keen to hear about my research, and providing both scientific and commercial insights.

I would also like to thank several people from other research groups who have aided my scientific understanding of the messy topic of acoustics. These are Professor Megan Povey of the Food Science Department of the University of Leeds, Dr Rachel Edwards and Dr Oksana Trushkevych of the University of Warwick and Dr Chris Wood of the Electronic Engineering Department of the University of Leeds. I would also like to thank Dr Mannan Ali and Dr Ben Johnson for providing both training and advice on lithography.

I was thankful within my PhD to also be surrounded by a fantastic group of postgrads, postdocs and academics, so thanks to the Soft Matter Physics Group at Leeds for all the conversations about how to get stuff to work. A special thanks to James Bailey, Peter Wyatt, Harry Litt, Stuart Weston and Dan Baker, who all helped significantly in various parts of the work. Also thanks to everyone who was keen to come to the pub on a Friday and aid me in my complaints about science!

I have also been fortunate to have a great network of people outside of work. Thanks to Rob, Paul, Nick, and everyone else who did their bit to keep me sane during the process! Of course, thankyou to all my family, especially my parents who have unwaveringly supported me through this endeavour. Finally, thanks to Eleanor. From the Manchester-Leeds commutes to visit me, to allowing me to frenziedly write up in the same flat as you, you have been amazing throughout this entire process and I could not have done it without you.

"If I had thought about it, I wouldn't have done the experiment. The literature was full of examples that said you can't do this." - Spencer Silver

"What, sir, would you make a ship sail against the wind and currents by lighting a bonfire under her deck? I pray you, excuse me, I have not the time to listen to such nonsense." - Napoleon Bonapart

"Amplifying acoustic instruments more than a little is really cheating, and everything becomes a compromise" - Richard Thompson

Abstract

Nematic Liquid Crystals (NLCs) are used widely as adaptive optical materials in devices such as lenses, beam steerers and displays. Usually in NLC Diffractive Optical Elements (DOEs), limitations exist in one or more essential parameters, such as diffraction angle, diffraction intensity, aperture size or adaptive behaviour.

This thesis will investigate an unusual method to create NLC DOEs, through inducing hydrodynamic flow within the materials. Here, several techniques are used to induce periodic flow patterns within the materials, which result in periodic changes to the device's optical properties. These periodic structures are evaluated for potential as adaptive optical components.

Fraunhofer diffraction theory is introduced as a means to evaluate the potential of various DOEs theoretically. Details of a computer programme developed during the project is presented, which allows calculation of Fraunhofer diffraction patterns. This programme is used to provide quantified analysis of losses in diffraction efficiency caused by imperfect or non-optimized DOEs. The application of these results may be used in aiding DOE device design, which will be discussed.

The first method used to create hydrodynamic domains uses a low frequency electric field applied across the NLC. This induces periodic ion flow within the material, leading to the NLCs adopting a state of electrohydrodynamic instability (EHDI). Of several EHDI modes identified, the 1D Normal Roll (NR) mode was most promising as a DOE. The periods of these gratings are strongly dependent upon device spacing (d). In all calamitic materials, the grating period continuously varied from d to $\frac{d}{2}$ as electric field frequency was increased. This lead to a simultaneous decrease in diffraction efficiency. Elastic constant dependency on EHDI is also investigated, where a material of low k_{33} is created using a bent dimeric mixture. This displays a desirable property of lower grating period by a factor of around 1.5.

The second method of creating hydrodynamic patterns in NLCs uses bulk and surface acoustic waves. Acoustic wave transmission in bulk NLCs is discussed. Techniques of measuring the speed of sound (v_s) in fluids are given, which are used to obtain a value for v_s in the NLC mixture E7 of $1720 \pm 70 \mathrm{ms}^{-1}$ at ambient temperatures. NLC structural changes under acoustic fields are examined. These investigations are used to create a novel device where the surface acoustic wavelength was varied using a chirped electrode structure. This created a hydrodynamic grating of continuously variable pitch from 100 µm to 450 µm using frequency modulation

The findings and performance of the hydrodynamic gratings investigated are evaluated in the context of currently available DOE technologies. Possible further device improvements and theoretical limits using the results from Fraunhofer diffraction modelling are discussed.

Publications

Morris, R.; Perivolari, E. Report on the 18th Optics of Liquid Crystals Conference, 8th-13th September 2019, Quebec City. *Liq. Cryst. Today* **2019**, *28*, 76–81, doi:10.1080/1358314X.2019.1693604.

Morris, R.; Jones, J.C.; Nagaraj, M. Continuously variable diffraction gratings using electroconvection in liquid crystals for beam steering applications. *J. Appl. Phys.* **2019**, *126*, 224505, doi:10.1063/1.5128205.

Morris, R.; Jones, J.C.; Nagaraj, M. Variable pitch hydrodynamic electro-optic gratings utilising bent liquid crystal dimers. *Soft Matter* **2020**, *16*, 10439–10453, doi:10.1039/d0sm01425g.

Morris, R.; Jones, C.; Nagaraj, M. Liquid Crystal Devices for Beam Steering Applications. *Micromachines* **2021**, *12*, 247, doi:10.3390/mi12030247.

Morris, R.; Jones, C.; Nagaraj, M. Inducing Variable Pitch Gratings in Nematic Liquid Crystals Using Chirped Surface Acoustic Wave Transducers. In Submission Process.

Presentations

"Phase Amplitude Gratings in Liquid Crystal Devices through Electroconvection", *British Liquid Crystal Society Conference*, Manchester (UK), April 2018 (Oral).

"Phase Amplitude Gratings in Liquid Crystal Devices through Electroconvection", *Merck Case Conference*, Southampton (UK), April 2018 (Oral).

"Electroconvection in Nematic Liquid Crystals for Continuously Variable Diffraction Gratings", *British Liquid Crystal Society Conference*, Leeds (UK), April 2019 (Poster).

"Electroconvection in Nematic Liquid Crystals for Continuously Variable Diffraction Gratings", *Optics of Liquid Crystal Conference*, Quebec (Canada), September 2020 (Poster).

"Liquid Crystal Acoustics for Beamsteering Applications", *University of Leeds Food Science Symposium*, Leeds (UK), May 2020 (Oral).

"Nematic Liquid Crystals Interacting with Surface Acoustic Waves for Beam Steering Applications", *University of Leeds Food Science Symposium*, Leeds (UK), April 2021 (Oral).

Techniques Developed

Several of the techniques used in this project were not available within the Soft Matter Physics Group of the University of Leeds at the beginning of the project. This meant a considerable amount of time during the project was spent developing these techniques. The most prominent of these are outlined below, with details of the candidates involvement:

- **Bulk Cell Fabrication.** Much of the equipment required to complete this task was available at the start of the project, however correct parameterisation of what is a complex process took a significant amount of time. This was not done by the candidate alone, with contributions from several MPhys students, PhD students and postdocs.
- **Diffraction Modelling.** These techniques were solely developed by the candidate using standardly available Python libraries.
- **Speed of sound measurement with the Pitch & Catch Method.** These techniques were solely developed by the candidate, under supervisorial guidance and advice from Professor Megan Povey.
- **Fabrication of SAW Transducers.** These techniques were solely developed by the candidate, under supervisorial guidance and advice from Dr's Peter Wyatt, Mannan Ali and Ben Johnson.

COVID-19 Impact Statement

As was the case with the majority of research degrees, the worldwide COVID 19 pandemic significantly affected the course of this research, leading to additional challenges. Below these impacts are summarised:

- Being unable to attend university laboratories from March-August 2020.
- Having significantly more restricted access to laboratories from August 2020-April 2021 (when experimental work was concluded).
- Increased challenges in developing collaborations with other research groups and accessing external laboratories.

These issues were significantly mitigated by receiving a six month funded extension to complete the studies. Additionally the results in Chapter 4 are the result of modelling work completed during the work from home period.

Contents

List of Figures

Chapter 1 Motivation and Road Map

Historically, liquid crystal materials have been successfully used in a plethora of optoelectronic devices [1–8]. More recently, there has been an increased interest in using LCs to create new materials [9–13] and applications in medicine [14,15], as well as better understanding of the formation of biological structures [16,17] and a playground for testing theories of fundamental physics [18,19].

This thesis focusses on investigating hydrodynamics in Nematic Liquid Crystals (NLCs) as Diffractive Optical Elements (DOEs). The methods used to induce hydrodynamic flow were electronic and acoustic fields. The majority of key studies on these phenomena were conducted in the 60s and 70s [20–27]. This leads to few systematic investigations of the effects having been completed, where the dependencies of the phenomena on both geometry and material parameters are not established. The aim of this thesis is firstly to address this gap, by investigating the key device parameters that determine the observed behaviours of electrohydrodynamic and acoustohydrodynamic effects. Once identified, tuning these key parameters will allow optimization of the DOEs, and an evaluation of their potential as a competitive technology.

To guide the reader through the order of the thesis, Figure 1.1 shows a roadmap of the thesis. Chapters 2 and 3 aim to introduce the fundamental physics of NLCs required to understand their function as hydrodynamic DOEs. This includes their ordering, viscoelastic properties, dielectric properties and their application as adaptive optical components. They summarise the experimental techniques used throughout the project, including liquid crystal device fabrication and analysis.

Chapter 4 then introduces the equations of diffractive optics required to examine the performance of DOEs theoretically. Here, a computer programme is introduced which is capable of predicting diffraction efficiencies. Quantified analysis of losses in diffraction efficiency caused by imperfect DOEs is made using this programme. The potential use of the results from this analysis in device design is discussed.

Chapters 5 and 6 present results investigating hydrodynamic phenomena due to ions in NLCs. This ionic flow causes the materials to adopt a state of electrohydrodynamic instability (EHDI), which can operate as a DOE. The dependencies of the patterns formed on device spacing, elastic constants, sample temperature and material conductivity are investigated, with an aim to optimize performance.

Chapters 7 and 8 investigate acoustic phenomena in NLCs. Chapter 7 discusses the properties of acoustic wave transmission in fluids, and presents the results of measuring the speed of sound in a NLC. Chapter 8 then looks at the formation of periodic hydrodynamic structures in NLCs, formed by applying either bulk or surface acoustic waves. Methods to control these domains for DOEs are investigated.

Chapter 9 then brings together the findings from Chapters 4 to 8, to conclude the work and give an assessment of the prospects of hydrodynamics in NLCs for DOEs. This includes comparison with more established technologies[28,29] and discusses the possible future directions of the research.

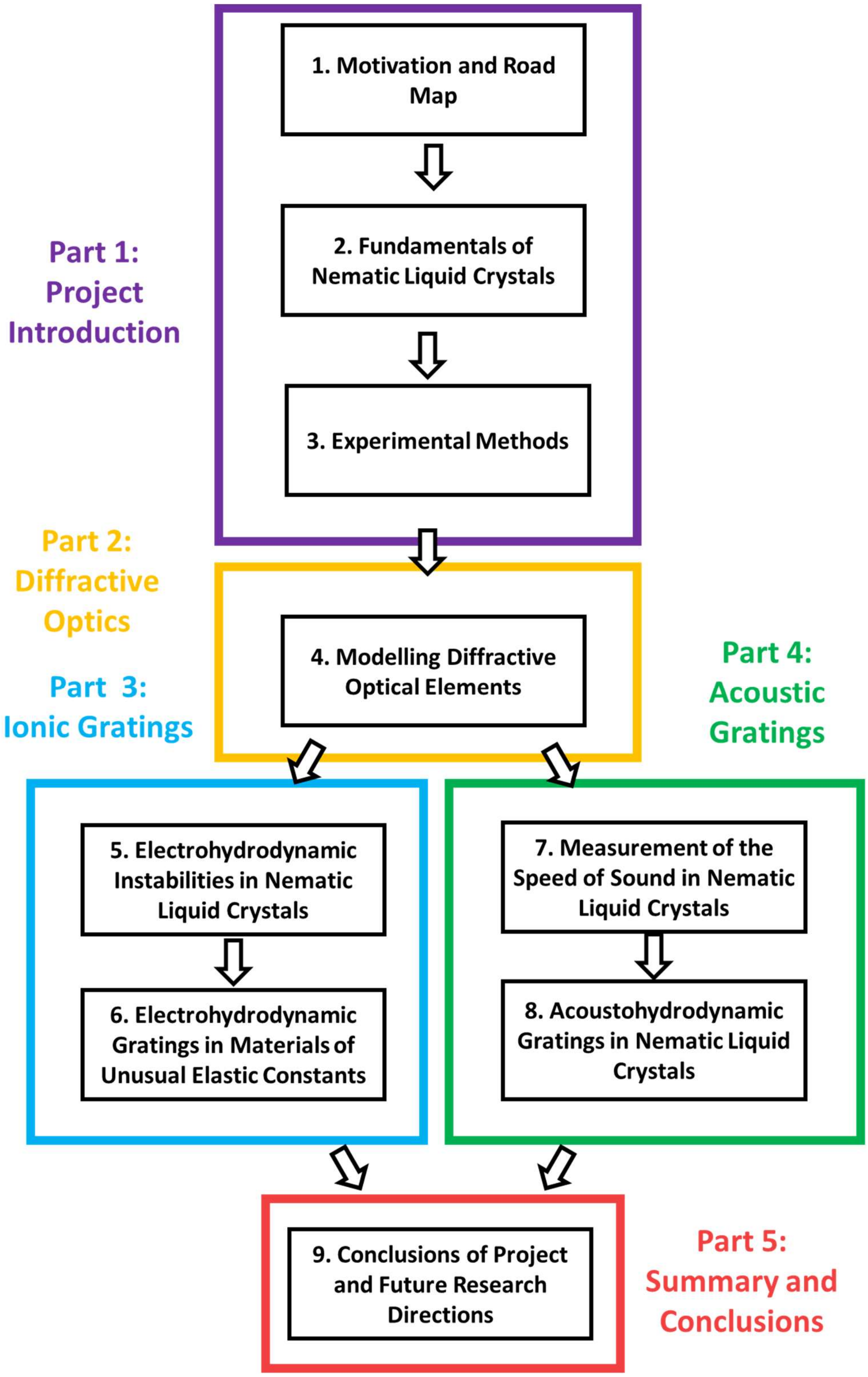

Figure 1.1. Roadmap of the thesis broken into five main parts, each containing chapters.

Chapter 2 Fundamentals of Nematic Liquid Crystals

The central theme of this thesis is to induce and understand hydrodynamic phenomena in Nematic Liquid Crystals (NLCs) and investigate their potential applications to optical devices. This chapter introduces several important aspects of the required underlying physics of NLCs. The chapter starts by defining NLCs and discuss the origins and manifestations of their important viscoelastic and electronic properties. The final section provides a brief overview of the use of NLCs in optical devices.

2.1 Order in Nematic Liquid Crystals

2.1.1 Nematic Mesogens

Thermotropic Liquid Crystals (LCs) are a state of matter that is spontaneously formed by mesogenic molecules under certain thermodynamic conditions. These liquid crystal phases exist at temperatures between the solid (crystalline or glassy) and isotropic liquid states of the material [30]. Generally, these phases are fluidic, with individual molecules being allowed to freely move and rotate, however they can also possess orientational and positional order.

The materials used most in this work form NLC phases only. The nematic phase is arguably the simplest of the LC phases, displaying orientational order only. NLCs are of great importance technologically as they exhibit many anisotropic properties due to their directional ordering, and can be manipulated with relatively small fields due to large response functions[31]. Of particular note is their dielectric and optical anisotropy, which leads to the phases being uniaxially anisotropic and switchable with an electrical field[1,2,32–35].

The reason specific mesogens form LC phases can be understood from their molecular chemistry. For example, Figure 2.1 shows two molecules that form NLC phases. Here (a) shows a calamitic (rod-like) mesogen while (b) shows a discotic (disc-like) material. In this work, the majority of materials will be comprised of calamitic molecules. Both calamitic and discotic mesogens possess properties which promote the likelihood of them forming LC phases, such as approximate cylindrical symmetry, large aspect ratio, strong anisotropic intramolecular bonds and fluid enhancing fatty tails[31]. More quantitative procedures of determining whether specific molecules (or a mixture of them) form a LC phase are also available. Here, a simulation of a box of molecules are performed to predict their molecular ordering [36,37]. These simulations allow more accurate prediction of the LC phases (nematic, smectic, cholesteric etc.) a material will form; however, experimental examination is the only certain way to assessing a sample’s phase behaviour.

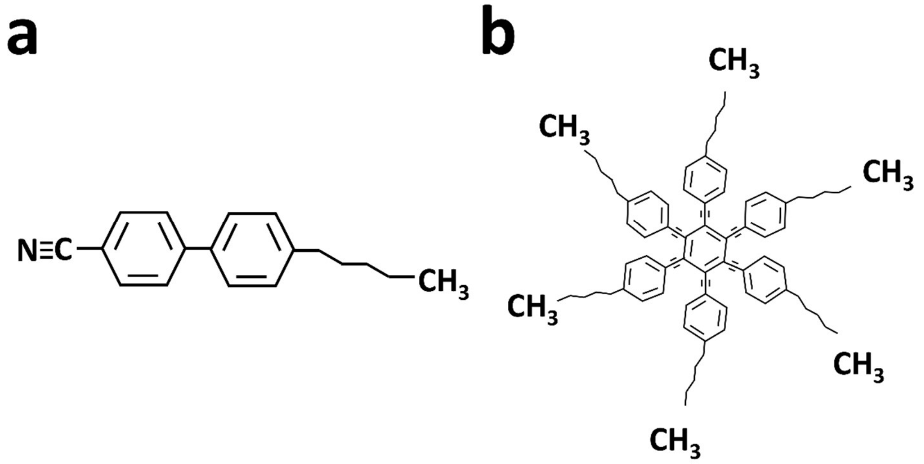

Figure 2.1.Examples of molecular structures that form nematic phases. a) One of the most common calamitic mesogens, 4-Cyano-4'-pentylbiphenyl or 5CB[38]. b) An example of a discotic mesogen hexakis(phenylethynyl)benzenes[39].

2.1.2 The Order Parameter

To simplify the molecular picture of NLCs, a pseudo-vector, ***n***, known as the director is considered. Here, ***n**,* is the average orientation of molecules at a point in space (***r***) at time (*t*),

$$\boldsymbol{n} = n(\boldsymbol{r}, t). \tag{2-1}$$

As most calamitic mesogens possess approximate cylindrical symmetry,

$$\boldsymbol{n} = -\boldsymbol{n}. \tag{2-2}$$

The orientational order parameter for the nematic phase (*S)* can be defined relative to ***n***, where the distribution of angles (ρ) is written as a sum of Legendre polynomials of order *l* (P_l)[40],

$$\rho \ = \sum_{l=0}^{l=\infty}\left[\frac{2l+1}{2}\langle P_l(cos\theta\rangle P_l(cos\theta)\right], \tag{2-3}$$

where θ is the difference in the angle of a molecule to ***n***.

For standard calamitic NLCs, a reasonable approximation that describes the distribution is to consider the shape of the P_2 term only [40], giving the expression for *S* as [30]

$$S \ \approx \ P_2 = < \frac{3cos^2\theta}{2} - \frac{1}{2} > = \frac{3 < cos^2\theta >}{2} - \frac{1}{2}. \tag{2-4}$$

This equation has the properties of,

$$S_{NLC}(< cos^2\theta >= 0) = 1$$

and

$$S_{NLC}\left(< cos^2\theta >= \frac{1}{3}\right) = 0.$$

In a liquid crystal material that only forms the nematic LC phase, on cooling from the isotropic phase two phase transitions will occur (Isotropic→ NLC and NLC→Crystal, Figure 2.2a). The temperatures where these phase transitions occur are named T_{NI} and T_{XN}, respectively.

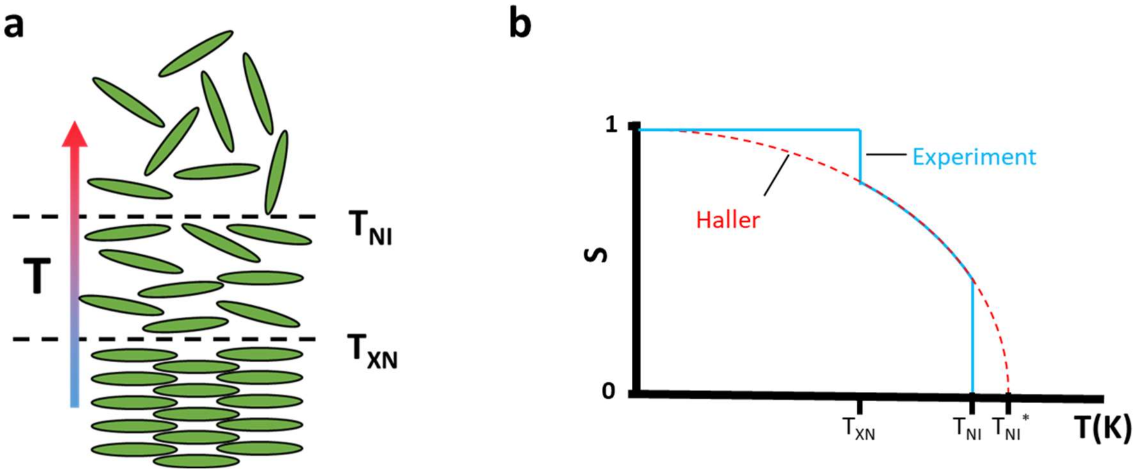

Figure 2.2. The behaviour of the nematic orientational order parameter (S) as the temperature is varied. a) A cartoon of mesogens, which on heating go from a crystal to NLC to isotropic. b) The behaviour of S as a function of temperature (T). Below T_{XN} S=1, above T_{NI} S=0. At $T_{XN}<T<T_{NI}$, 0<S<1 and can be described approximately by Haller's equation.

Typical behaviour of S as a function of temperature (T) is shown in Figure 2.2b. The transitions at T_{NI} and T_{XN} are first-order in S, where values very close to zero or unity are not observed (the range for typical NLC 5CB is ≈0.35-0.65[41]). Within the nematic range, S can be modelled using Haller's equation (see Figure 2.2b) [42],

$$S = \left(1 - \frac{T}{{T_{NI}}^*}\right)^{n_{hal}}. \tag{2-5}$$

Here T is taken in Kelvin, T_{NI}* is the temperature typically a couple of degrees above the measured T_{NI}[42] and n_{hal} is a material-dependent exponent.

2.2 Elastic Properties of Nematic Liquid Crystals

2.2.1 Elasticity in NLCs

This section will consider the elastic properties of NLCs. This elasticity is caused by an energetic cost associated with the deformation of the nematic field by $\boldsymbol{n}$ changing orientation in space. This is known as the elasticity of the nematic field. A theoretical treatment of the elasticity of the nematic field was provided in 1958 by Sir Charles Frank, who developed the previous work of Carl Wilhelm Oseen [43,44]. This treatment quantified the elastic free energy of the nematic director field with three elastic constants (k_{ii}). The constants are associated with the splay (k_{11}), twist (k_{22}) and bend (k_{33}) deformations of the nematic phase (Figure 2.3a). This elastic free energy is written as,

$$F_{El} = \frac{1}{2}\int [k_{11}\,(\nabla.\boldsymbol{n})^2 + k_{22}(\boldsymbol{n}.\nabla\times\boldsymbol{n}) + k_{33}(\boldsymbol{n}\times\nabla\times\boldsymbol{n})]dV. \tag{2-6}$$

The influence of defects can be added to this expression with an additional surface integral,

$$F_{Defects} = -\int k_{24}\bar{\boldsymbol{s}}[(\bar{\boldsymbol{n}}\nabla.\bar{\boldsymbol{n}}) + \bar{\boldsymbol{n}}\times\nabla\times\bar{\boldsymbol{n}}]dS. \tag{2-7}$$

Here k_{24} is the saddle-splay elastic constant. As this work does not include defect formation, (2-6) is sufficient for understanding all further discussion.

For a typical (calamitic) NLC forming mesogen, the elastic constants tend to obey,

$$k_{33} > k_{11} > k_{22}. \tag{2-8}$$

Elastic constants for a typical NLC are shown in Figure 2.3b as a function of temperature (from reference [45]). In recent years, many novel materials have been synthesised, including dimers and bent-core liquid crystals, which do not follow the (2-8) [12,46–53]. More discussion on using such to tune the diffractive properties of hydrodynamic gratings is given in Chapter 6.

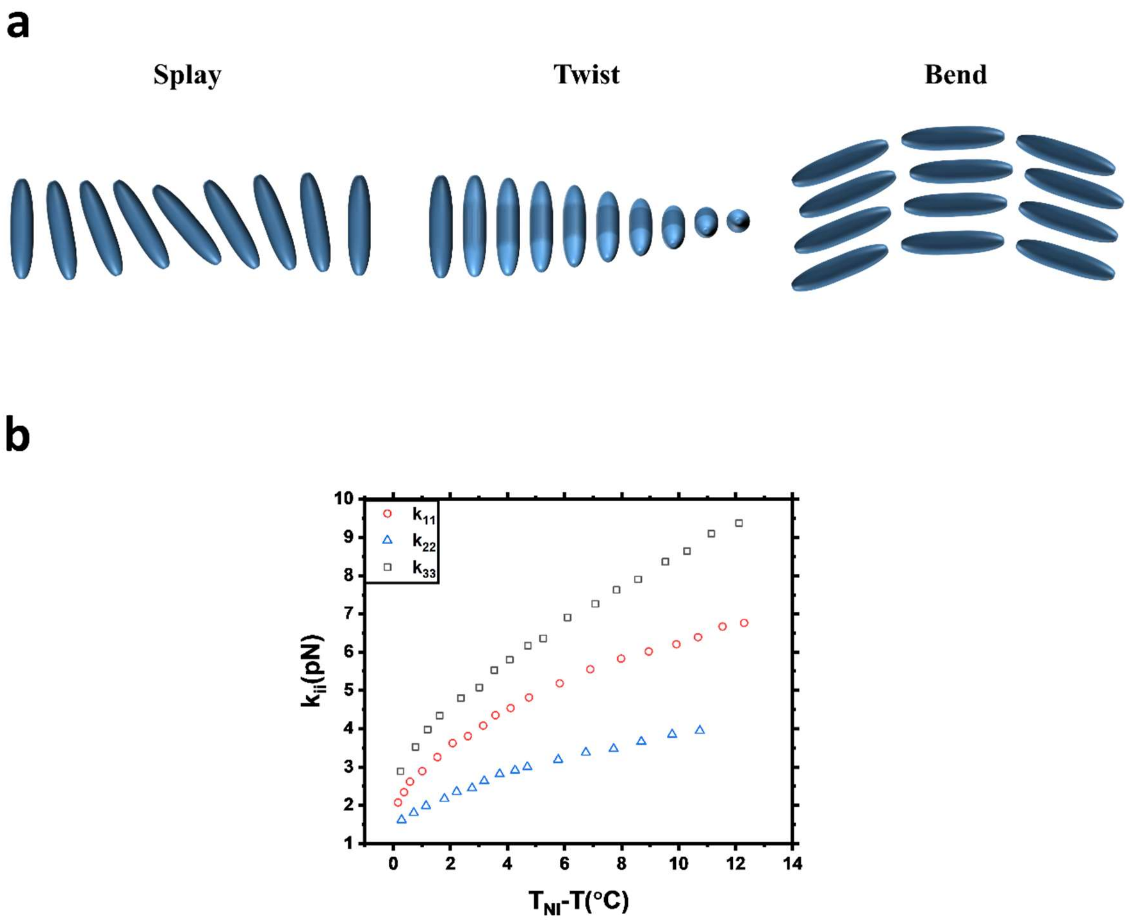

Figure 2.3. (a) Cartoons illustrating splay, twist and bend deformation of a nematic field.(b) Quantitative measurements of k_{ii} in typical nematic liquid crystal (5CB), taken from reference[45].

2.2.2 Alignment of NLCs

Usually, in order to use NLCs in devices, a well-controlled initial state is required. This device alignment, dictates the homogenousness of the director field in the absence of external stimuli. Specific alignments can be achieved by manipulating the surfaces enclosing the NLC. As the elastic forces within a NLC will seek to align the director homogenously to minimize elastic distortion (equation (2-6)), such alignment allows ***n*** to be dictated in the bulk of the device.

The study of LC alignment is important for device fabrication. Many techniques have been developed to induce alignment including mechanically rubbed thin films[54–57], directed evaporation of thin films[58], topographical structures[59–62], Slippery films[63], optically patterned films [64–70] and stacked alignment layers[71,72]. Figure 2.4a shows schematics of planar (PL), homeotropic (HT), planar homogenous (PH) and rubbed homeotropic (RHT) devices. Here, planar and homeotropic alignments are closer to being within the x,y plane and parallel to z, respectively. Both planar and homeotropic alignments usually deviate from these perfect behaviours by a small amount, known as the alignment pretilt (θ_p).

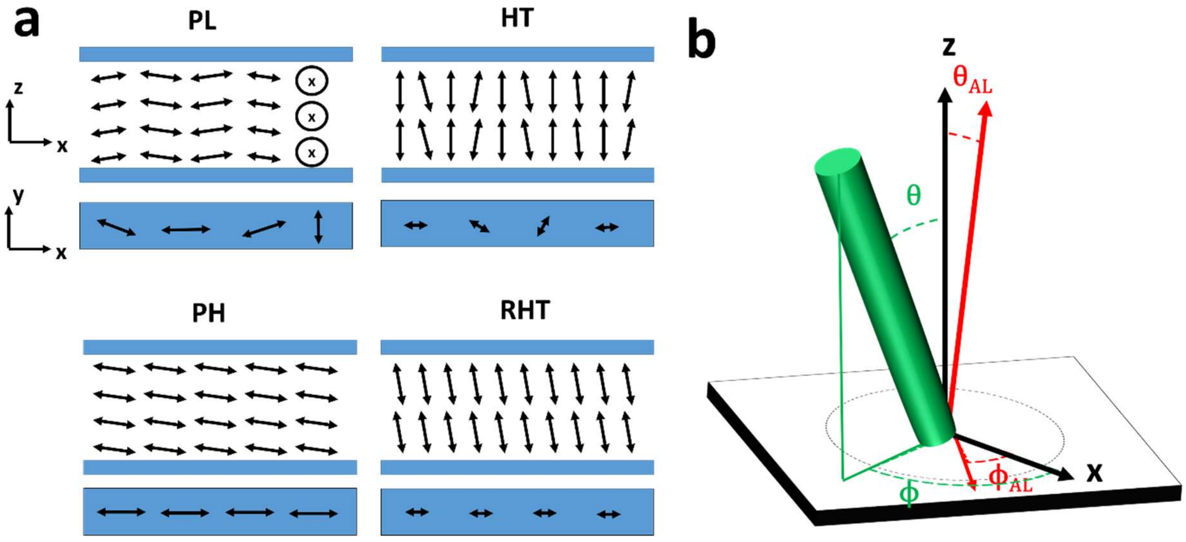

Figure 2.4. a) Schematics of director configurations in devices with PL, HT, PH and RHT alignments. All alignments have been given some pretilt (usually being less than 10°[73]). b) A cartoon explaining the roles of θ_{AL} and ϕ_{AL} in alignment layers. The director (green) with angular position (ϕ, θ) experiences an elastic force towards the position (ϕ_{AL}, θ_{AL}).

Similar to the elasticity in NLCs, the effects of alignment layers can be quantified by a contribution to the system free energy. The director at a point on a surface is defined by two angles; θ and ϕ, which describe the azimuthal and radial angles respectively, to the *x,y* plane (Figure 2.4b). The preferred alignment of the director at the surface is written as,

$$\boldsymbol{n}_{\boldsymbol{AL}} = \boldsymbol{n}(\theta_{AL}, \phi_{AL}) \tag{2-9}$$

where θ_{AL} and ϕ_{AL} are the values of θ and ϕ induced on the director by the alignment. At these surfaces, any deviation of θ and ϕ from θ_{AL} and ϕ_{AL} increases system's free energy. To first approximation, the free energy term of alignment (F_{AL}) can be written as a linear combination of θ and ϕ[74,75],

$$F_{AL}(\theta, \phi) = F_{AL,\theta}(\theta) + F_{AL,\phi}(\phi) \tag{2-10}$$

where,

$$F_{AL,\theta}(\theta) = \frac{1}{2}\int_{\Sigma} W_{\theta} sin^2(\theta - \theta_{AL}) d\Sigma \tag{2-11}$$

and

$$F_{AL,\phi}(\phi) = \frac{1}{2}\int_{\Sigma} W_{\phi} sin^2(\phi - \phi_{AL}) d\Sigma. \tag{2-12}$$

Here, W_θ and W_ϕ are anchoring energies, which are usually very large compared to material's elasticity or the effect of external fields, meaning $\boldsymbol{n}$ is pinned in place at the surfaces. This means even when an external force acts to reorient $\boldsymbol{n}$ in the majority of the bulk NLC, very close to the surfaces, $\boldsymbol{n}$ will still be dictated by alignment (See section 2.4.4). In the absence of external fields, the director field shape can be calculated by minimizing F_{static}, where,

$$F_{static} = F_{NLC} + F_{AL}. \tag{2-13}$$

2.3 Viscosity in Nematic Liquid Crystals

2.3.1 Viscoelasticity in Isotropic Soft Matter Systems

NLCs display viscoelastic behaviour similar to many soft matter systems. In NLCs, this behaviour is complex mainly due to the anisotropy of the liquid crystalline phase. This section will therefore introduce viscoelasticity in isotropic systems, which are simpler to describe.

If an isotropic material is viscoelastic, this means that a material does not always act as a perfectly elastic solid, described by[76],

$$\sigma_{el} = \kappa_{el} \cdot \varepsilon_{el}, \tag{2-14}$$

or a Newtonian fluid, where,

$$\sigma_{vis} = \eta \cdot \frac{\partial \varepsilon_{vis}}{\partial \mathrm{t}}. \tag{2-15}$$

Here σ_{el} is the elastic stress, σ_{vis} is the viscous stress, ε_{el} the elastic strain tensor, ε_{vis} the viscous strain tensor, κ_{el} the system elasticity and η is the viscosity. A simple model for viscoelastic materials is to assume they act as a spring and piston in series (Maxwell material) with an additional spring in parallel (discussed further in Chapter 7). Here, the stress (σ_T) in both the viscous and elastic response is the same,

$$\sigma_T = \sigma_{el} = \sigma_{vis} \tag{2-16}$$

and the total strain (ε_T) is the combination from elastic and viscous responses,

$$\varepsilon_T = \varepsilon_{el} + \varepsilon_{vis}. \tag{2-17}$$

This gives,

$$\varepsilon_T = \frac{\sigma_T}{\kappa} + \int_0^t \frac{\sigma_T}{\eta} dt \tag{2-18}$$

Intuitively (2-18) simply states that the strain a material undergoes is a sum of the instantaneous elastic response and a viscous response which takes some time. Often, the differential form of (2-18) is instead used[76],

$$\frac{\delta\varepsilon_T}{\delta t} = \frac{1}{\kappa}\frac{\delta\sigma_T}{\delta t} + \frac{\sigma_T}{\eta} \qquad \text{or} \qquad \dot{\varepsilon_T} = \frac{\dot{\sigma_T}}{\kappa} + \frac{\sigma_T}{\eta}. \tag{2-19}$$

Where the "·" indicates the time derivative.

The time dependency of the viscoelastic response is of great importance, as different material properties are observed as mechanical impulses are applied on different timescales. Usually, a critical time scale (τ_0) is used to describe these responses, where short impulses ($\tau \ll \tau_0$) experience an elastic medium, while long ($\tau \gg \tau_0$) a viscous one. This will be particularly important in Chapter 7 where propagation of acoustic waves in NLCs is discussed.

2.3.2 Viscosity in Nematic Liquid Crystals

A common method to measure the viscoelasticity of a material is shear rheology[76]. Here, a layer of material is sandwiched between two plates, which are put into relative motion. Here, if one of the plates is accelerated with a force moving in the x direction (F_x, see Figure 2.5a), the shear stress which will be placed upon a plate (σ_{xy}) which is at rest can be written,

$$\sigma_{xy} = \frac{F_x}{A}, \tag{2-20}$$

where A is the plate area. This stress causes a shear strain (ε_x),

$$\varepsilon_x = \frac{\Delta x}{d}. \tag{2-21}$$

Here the viscosity of the material links the shear stress and strain by

$$\eta = \frac{\sigma_{xz}}{\dot{\varepsilon}_x}. \tag{2-22}$$

In the case of NLCs, due to the anisotropic properties of the phase, the effective viscosity depends on the relative orientation between $\boldsymbol{n}$ and the plate surfaces. Figure 2.5b illustrates this, where the NLC anisotropy leads to 4 principle viscosities (η_n). Figure 2.5c shows work competed by Orr and Pethrick measuring η_n on a typical NLC (5CB) [77]. It was found across the temperature range studied,

$$\eta_1 > \eta_{45} > \eta_3 > \eta_2 \tag{2-23}$$

and all η_n were within approximately 20% of their mean value.

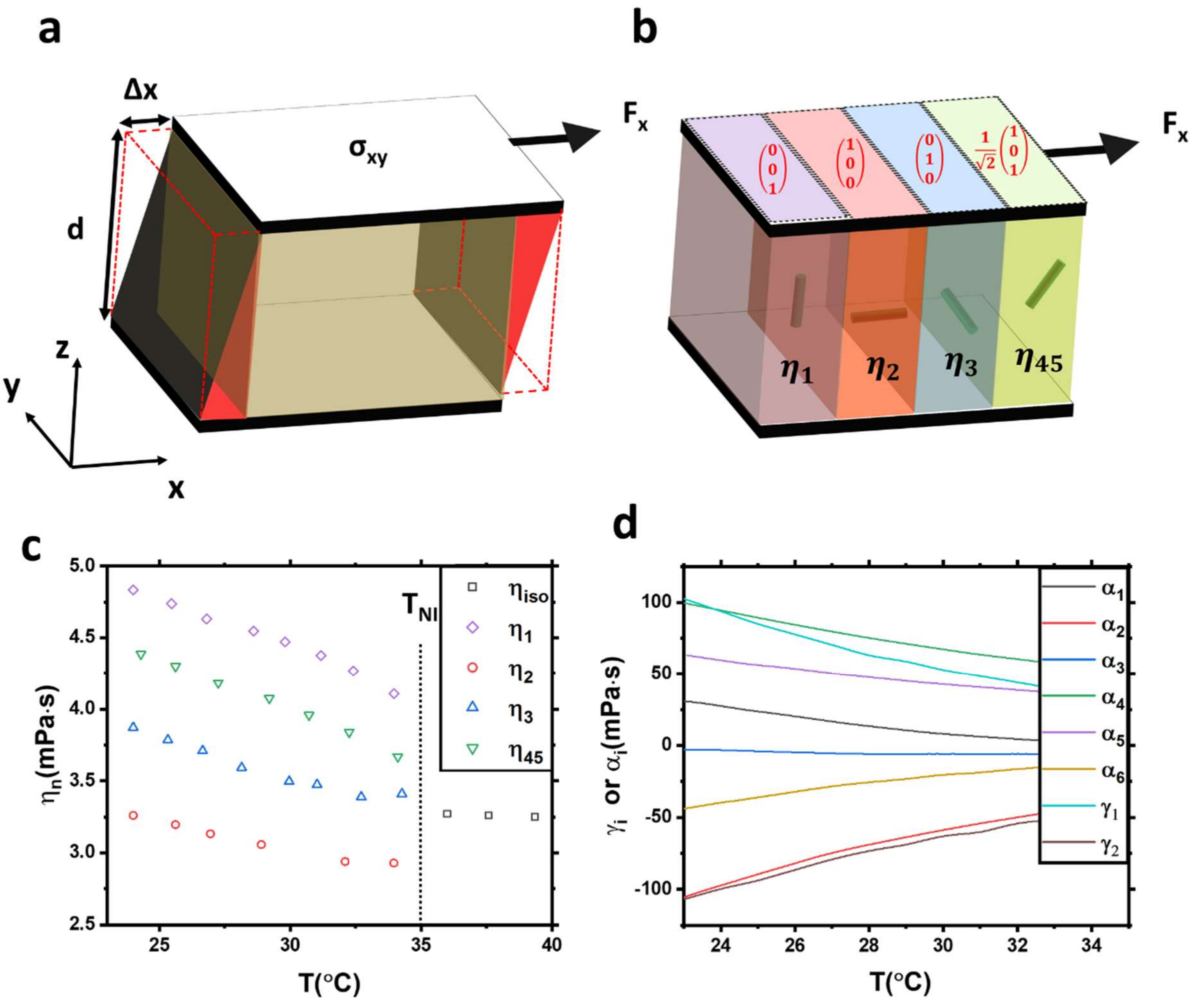

Figure 2.5. (a) An illustration of shear stress and strain due to a force being applied in the x direction. (b) The four principle viscosities of nematic liquid crystal. The four slabs of different colour represent different director orientations (shown by internal green cylinders). The unit vectors of the directors are also given in red for clarity. (c) Values of η_n measured by Orr and Penthrick in 5CB and (d) The corresponding Leslie coefficients (α_n) and rotational and torsional viscosities (γ_n)[77]. These are explained in section 2.3.3.

2.3.3 Ericksen Leslie Theory

One of the complexities in describing the viscoelasticity of NLCs is that, when stressed ***n*** will reorient. This results in non-linear interactions, where flow is determined by viscosity, which is determined by flow direction and flow rate. To account for this, equations (2-20), (2-21) and (2-22) need to be solved in small elements, so are altered to their differential forms,

$$\sigma_{xz} = \frac{\delta F_x}{\delta A} = \eta \dot{\varepsilon}_x = \eta \frac{\delta^2 x}{\delta z \delta t} = \eta \frac{\delta v_x}{\delta z}. \qquad (2\text{-}24)$$

Or for more general geometries,

$$\sigma_{\alpha\beta} = \eta\nabla_\beta v_\alpha. \tag{2-25}$$

Ericksen-Leslie theory solves this equation[78–80], to give an expression for $\sigma_{\alpha\beta}$ [81] as,

$$\sigma_{\alpha\beta} = \alpha_1(n_\alpha n_\beta n_\mu n_Q A_{\mu Q}) + \alpha_2(n_\alpha N_\beta) + \alpha_3(n_\beta N_\alpha) + \alpha_4(A_{\alpha\beta}) + \alpha_5(n_\alpha n_\mu A_{\mu\beta}) + \alpha_6(n_\beta n_\mu A_{\mu\alpha}). \tag{2-26}$$

Here

$$A_{\alpha\beta} = \frac{1}{2}\left(\frac{\partial v_\beta}{\partial\alpha} + \frac{\partial v_\alpha}{\partial\beta}\right), \tag{2-27}$$

$$N_\alpha = \frac{\partial n_\alpha}{\partial t} - \left[\frac{\nabla \times v_\alpha}{2} \times n_\alpha\right], \tag{2-28}$$

and α_n are the Leslie viscosity coefficients. Equation (2-26) is complex, and considering the nature of this project full understanding of it is not required. Instead we relate the α_n terms to their corresponding η_n values[45,77,79],

$$\eta_1 = \frac{-\alpha_2 + \alpha_4 + \alpha_5}{2}, \tag{2-29}$$

$$\eta_2 = \frac{\alpha_3 + \alpha_4 + \alpha_6}{2}, \tag{2-30}$$

$$\eta_3 = \frac{\alpha_4}{2} \tag{2-31}$$

and

$$\eta_{45} = \frac{\eta_1 + \eta_2}{2} + \frac{\alpha_1}{2}. \tag{2-32}$$

Although there are six α_n terms work by Parodi mathematically proved that there is in fact five independent ones, due to [82],

$$\alpha_2 + \alpha_3 = \alpha_6 + \alpha_5. \tag{2-33}$$

Two other coefficients which are often used are the rotational viscosity (γ_1) and torsion coefficient(γ_2), defined as[79,83],

$$\gamma_1 = \alpha_3 - \alpha_2. \tag{2-34}$$

and

$$\gamma_2 = \alpha_6 - \alpha_5, \tag{2-35}$$

respectively. These can be understood qualitatively as the viscosities when moving in a circle with the director in the plane or out of the plane [84].

In the work by Orr and Pethrick[77] the values α_n and γ_n were found from η_n as shown in Figure 2.5d. These viscosities are of high importance in describing how hydrodynamic vortices within NLCs can cause director reorientation, which will be used to create DOEs in Chapters 5, 6 and 8.

2.4 Dielectric Properties of Static Nematic Liquid Crystals

The dielectric properties of NLCs are a key part of their widespread application to optoelectronic devices[1,5,6,33]. In this thesis, a thorough introduction to electric field interactions with a wide variety of materials (liquid crystals, ions, piezoelectrics) is useful to understanding measurements obtained and device function. This will be the focus of this section.

2.4.1 Dielectric Materials in Electric Field

By definition, a dielectric material is one that can become polarized, when an electric field is applied across it. This can be written in terms of applied electric field (E_{app}), material polarization (P_{mat}) and electric field inside the material (E_{mat}) as,

$$E_{app} = \varepsilon_0 E_{mat} + P_{mat}. \tag{2-36}$$

Here ε_0 is the permittivity of free space. P_{mat} can be rewritten in terms of electric susceptibility (how polarised a material will become when E_{mat} is applied to it, χ),

$$P_{mat} = \varepsilon_0 \chi E_{mat}, \tag{2-37}$$

and a relative permittivity (ε), can be defined from χ,

$$\varepsilon = \varepsilon_0(1+\chi). \tag{2-38}$$

Combining (2-36), (2-37) and (2-38) gives,

$$E_{app} = \varepsilon_0 E_{mat} + P_{mat} = \varepsilon_0 E_{mat}(1+\chi) = \varepsilon_0 \varepsilon E_{mat}. \tag{2-39}$$

In general, the total amount a material becomes polarized is the summation of several (N) contributing mechanisms (P_n) which are frequency (ω) dependent[85,86],

$$P_{mat}(\omega) = \sum_{n=1}^{n=N} P_n(\omega). \tag{2-40}$$

Where the functions $P_n(\omega)$ tend to have properties

$$P_n(\omega \ll \omega_{0,n}) = P_{n,DC}. \tag{2-41}$$

and

$$P_n(\omega \gg \omega_{0,n}) = 0. \tag{2-42}$$

Here, $\omega_{0,n}$ is a characteristic frequency of process P_n and $P_{n,DC}$ is the maximum polarisation a process can contribute. As ω is increased (2-41) and (2-42) describe the reduction in polarisation a specific P_n will contribute from $P_{n,DC}$ to zero, this is known as a relaxation process. These relations naturally lead to relations for $P_{mat}(\omega)$,

$$P_{mat}\left(\omega \ll all\ \omega_{0,n}\right) = P_{mat,DC} = \sum_{n=1}^{n=N} P_{n,DC}. \tag{2-43}$$

and

$$P_{mat}\left(\omega \gg all\ \omega_{0,n}\right) = 0. \tag{2-44}$$

When studying dielectrics it is usual to measure the dimensionless ε instead of P_{mat}. Due to its frequency dependent nature, it is useful to treat ε as a complex quantity, (ε^*),

$$\varepsilon^* = \varepsilon' + i\varepsilon'', \tag{2-45}$$

where ε' is the so far discussed real part ($\varepsilon' = \varepsilon$) and ε'' is the imaginary component, which captures out of phase behaviour.

Rearranging equations (2-37) and (2-38), the following expression can be obtained,

$$P_{mat} = \varepsilon_0(\varepsilon - 1)\, E_{mat} \tag{2-46}$$

This means when P_{mat} undergoes a single relaxation process the value of ε will reduce by an amount $\delta\varepsilon_n$ where,

$$\delta\varepsilon_n = \varepsilon\left(\omega \ll \omega_{0,n}\right) - \varepsilon\left(\omega \gg \omega_{0,n}\right) = \frac{P_{mat}\left(\omega \ll \omega_{0,n}\right) - P_{mat}\left(\omega \gg \omega_{0,n}\right)}{\varepsilon_0 E_{mat}} = \frac{P_{n,DC}}{\varepsilon_0 E_{mat}}. \tag{2-47}$$

A simple model of the behaviour ε^* during a relaxation process is the Debye Model [86],

$$\varepsilon^*(\omega) = \varepsilon_\infty + \frac{\varepsilon_S - \varepsilon_\infty}{1 + i\left(\frac{\omega}{\omega_0}\right)}. \tag{2-48}$$

Where ε_S and ε_∞ are the values ε at ω much above and below the relaxation frequency, respectively. This is often further generalized with the Havriliak-Negami expressions, where additional exponents α and β are added[86–88],

$$\varepsilon^*(\omega) = \varepsilon_\infty + \frac{\varepsilon_S - \varepsilon_\infty}{\left(1 + i\left(\frac{\omega}{\omega_0}\right)^{1-\alpha}\right)^{\beta}}. \tag{2-49}$$

Here, the terms α and β manipulate the function to account for the loss peaks asymmetric and symmetric broadening respectively.

An alternative form relaxation processes can take is of a resonance-type, where close to ω_0 the value of ε will increase before dramatically decreasing. Here polarisation may be modelled as a simple harmonic oscillator allowing ε^* to be written[89],

$$\varepsilon^*(\omega) = \varepsilon_\infty + \frac{\varepsilon_S - \varepsilon_\infty}{1 - \left(\frac{\omega}{\omega_{res}}\right)^2 + i\left(\frac{\omega}{\omega_0}\right)}, \tag{2-50}$$

where ω_{res} is the natural frequency of the oscillator.

2.4.2 Dielectric Response of Molecular Isotropic Liquids

Before moving to the more complex case of NLCs, this section will discuss dielectrics of a molecular isotropic liquid. Within these materials, the major components contributing to the polarisation are the molecule electron clouds (P_e), atomic nuclei reorientations (P_a), permanent molecular dipoles (P_{dip}) and free ions (P_{ions}) [85,86]. This means (2-40) becomes,

$$P_{mat}(\omega) = P_e(\omega) + P_a(\omega) + P_{dip}(\omega) + P_{ions}(\omega). \tag{2-51}$$

The corresponding ε^* is,

$$\varepsilon^*(\omega) = 1 + \delta\varepsilon_e^*(\omega) + \delta\varepsilon_a^*(\omega) + \delta\varepsilon_{dip}^*(\omega) + \delta\varepsilon_{ions}^*(\omega), \tag{2-52}$$

where $\delta\varepsilon_n^*$ represents the change in permittivity when a process n undergoes a relaxation process. Figure 2.6 shows cartoons illustrating the different processes n and typical behaviour of ε as ω is varied. Here P_{dip} and P_{ions} appear to undergo standard Debye-like relaxation processes, while P_e and P_a display resonance behaviour.

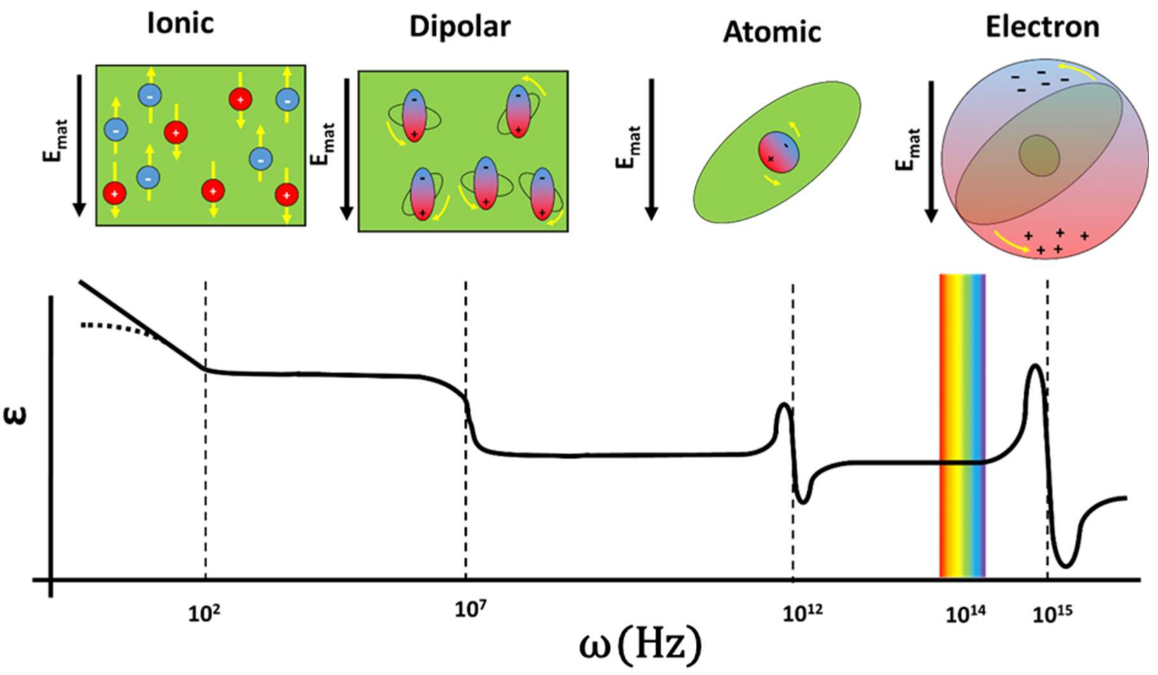

Figure 2.6. The typical behaviour of permittivity as a function of frequency in liquid consisting of dipolar molecules. Typical relaxation frequencies of each process are shown with a cartoon illustrating them. The approximate location of the frequency range of visible light is shown as the rainbow pattern.

Both P_e and P_a are caused by inducing dipolar character within the material using an electric field (from the electron cloud and atomic nucleus respectively). The polarisation of these processes can be quantified by the number of molecules (N) and the polarizability of the electrons ($\bar{\alpha}_e$),

$$P_{e,DC} = \frac{N\bar{\alpha}_e E_{mat}}{V}. \tag{2-53}$$

and atoms ($\bar{\alpha}_a$)

$$P_{a,DC} = \frac{N\bar{\alpha}_a E_{mat}}{V} \tag{2-54}$$

respectively[89,90].

The polarization from permanent dipoles meanwhile can be written as[86],

$$P_{dip,DC} = \frac{N}{V}\langle\mu\rangle E_{mat} = \frac{N}{V}\frac{\mu^2}{3k_B T}E_{mat}. \tag{2-55}$$

Here N is the number of dipoles, V the volume of material, μ the dipole moment, $<\mu>$ the mean dipole moment and k_B is Boltzmann's constant. Values P_n given in (2-53), (2-54), and (2-55) can then be put into equation (2-47) to find corresponding $\delta\varepsilon_n$ values.

The behaviour of $P_{ions}(\omega)$ is complex to describe, and highly relevant to Chapters 5 and 6 which utilize ions to create hydrodynamic flow. Within isotropic dielectric liquids, ions (usually caused by slight material contamination or degradation) move to electrodes of opposite polarity due to a coulomb interaction. Typically low frequencies (<100Hz) are required for these interactions to contribute to ε, as the ions require time to transit the material. This is similar to other processes of P_n in the fact that it increases ε. However it is more complex as: *(i)* ions can aggregate in such quantities at electrodes that they firstly depolarise the electrodes, then start to form Debye double layer structures. These layered dielectric structures have very high permitivities, which can cause a dramatic reduction in E_{mat} [91]. (*ii*) Applying voltage at such low frequencies can cause further injection of ions into the material at electrode surfaces (Schottky charge injection)[92] and *(iii)* applying these close to DC voltages can cause material degradation, which in turn can increase ion numbers[93,94]. Due to these complexities, studying very low frequency (<1Hz) ionic processes is a highly specialised field.

An important frequency regime for optical materials is the visible light range (480-750THz). The permittivity is related to the refractive index (n_{ref}), through relation[90],

$$n_{ref} = \sqrt{\mu_{mag}\varepsilon} \approx \sqrt{\varepsilon}, \tag{2-56}$$

Where μ_{mag} is the relative magnetic susceptibility of the material. At such frequencies all contributions to ε, but P_e relax, and the corresponding ε and n_{ref} are[90],

$$\varepsilon = 1 + \frac{P_{e,DC}}{\varepsilon_0 E_{mat}} = 1 + \frac{N\bar{\alpha}_e}{V\varepsilon_0}. \tag{2-57}$$

and

$$n_{ref} = \sqrt{1 + \frac{N\bar{\alpha}_e}{V\varepsilon_0}} \tag{2-58}$$

respectively.

2.4.3 Dielectric Response of NLCs

For NLCs the expressions discussed in section 2.4.2 need to be adjusted for the anisotropy of the materials. Two permitivities $\varepsilon_{\perp}$ and $\varepsilon_{||}$ (measured perpendicular or parallel to ***n*** respectively) are used. These can be written in the same form as ε as in equation (2-52), with all the components P_n having a dependency on the orientation of ***n*** and the order parameter *(S)*.

To describe this anisotropy, Onsager developed a mean field theory[95], for the interaction between a single molecule and a dielectric spherical cavity (radius a) which it was placed within. He derived expressions for the effective reduction of a dipole within the cavity (h),

$$h = \frac{3\varepsilon}{2\varepsilon + 1} \tag{2-59}$$

and an expression for the increased localised field due to the dipole[95],

$$F = \frac{1}{1 - \alpha\left(\frac{2(\varepsilon - 1)}{\varepsilon_0(2\varepsilon + 1)}\frac{1}{4\pi a^3}\right)} \,. \tag{2-60}$$

Maier and Meier then applied this theory to NLCs[96]. The resulting expressions for the electron and atomic components are[95],

$$\delta\varepsilon_{\perp,\mathrm{n}} = \frac{NhF}{V\varepsilon_0}\left\{\bar{\alpha}_n - \frac{\Delta\alpha_n S}{3}\right\} \tag{2-61}$$

and [95]

$$\delta\varepsilon_{||,\mathrm{n}} = \frac{NhF}{V\varepsilon_0}\left\{\bar{\alpha}_n + \frac{2\Delta\alpha_n S}{3}\right\} \tag{2-62}$$

where $\bar{\alpha}_n$ is the average electron or atomic polarizability for *n=e* or *a* respectively. Here,

$$\bar{\alpha}_n = \frac{\alpha_{||,n} + 2\alpha_{\perp,\mathrm{n}}}{3} \tag{2-63}$$

and $\Delta\alpha_n$ is the polarizability anisotropy,

$$\Delta\alpha_n = \alpha_{||,\mathrm{n}} - \alpha_{\perp,n}. \tag{2-64}$$

The dipole components are[95],

$$\delta\varepsilon_{\perp,\mathrm{dip}} = \frac{NhF^2}{3Vk_BT\varepsilon_0}\left(\mu_{||}^2(1 - S) + \mu_{\perp}^2\left(1 + \frac{S}{2}\right)\right) \tag{2-65}$$

and [95]

$$\delta\varepsilon_{||,\mathrm{dip}} = \frac{NhF^2}{3Vk_BT\varepsilon_0}\left(\mu_{||}^2(1 + 2S) + \mu_{\perp}^2(1 - S)\right). \tag{2-66}$$

Often of more importance than the absolute value of *ε* to the function of NLCs is the permittivity anisotropy (*Δε*),

$$\Delta\varepsilon = \varepsilon_{||} - \varepsilon_{\perp}. \tag{2-67}$$

In the kHz range (where ions are relaxed) this may be written as,

$$\Delta\varepsilon = \delta\varepsilon_{||,\mathrm{e}} + \delta\varepsilon_{||,\mathrm{a}} + \delta\varepsilon_{||,\mathrm{dip}} - \delta\varepsilon_{\perp,\mathrm{e}} - \delta\varepsilon_{\perp,\mathrm{dip}} - \delta\varepsilon_{\perp,\mathrm{a}}. \tag{2-68}$$

Whereas in the optical range (where dipoles and atomic processes are relaxed),

$$\Delta\varepsilon = \delta\varepsilon_{||,\mathrm{e}} - \delta\varepsilon_{\perp,\mathrm{e}}. \tag{2-69}$$

This allows expression for sample birefringence (*Δn)* to be written,

$$\Delta n = \sqrt{\varepsilon_{||}} - \sqrt{\varepsilon_{\perp}} = \sqrt{1 + \delta\varepsilon_{||,\mathrm{e}}} + \sqrt{1 + \delta\varepsilon_{\perp,\mathrm{e}}}. \tag{2-70}$$

Combining these relations gives Vuks' equation, which links the molecular polarizability anisotropy to the birefringence by order parameter[97],

$$\frac{n_{||}{}^2 + n_e{}^2}{\overline{n}^2 - 1} = \frac{\Delta\alpha}{\overline{\alpha}} S. \tag{2-71}$$

2.4.4 The Fréedericksz Transition

In section 2.4.3, the origin of both $\Delta\varepsilon$ and Δn in NLCs are discussed. These two parameters are critical to all NLC optical devices, as Δn allows switchable optical properties depending on the orientation of the plane of polarisation of light relative orientation $\boldsymbol{n}$, while $\Delta\varepsilon$ allows a mechanism to control $\boldsymbol{n}$.

The way $\Delta\varepsilon$ allows $\boldsymbol{n}$ to be reoriented is through a process known as a Fréedericksz transition[32]. Here, when a large electric field ($\boldsymbol{E_{app}}$) is applied across a NLC, the system seeks to reduce the internal field within the material ($\boldsymbol{E_{mat}}$) maximally. To do this, $\boldsymbol{n}$ reorients so that the maximum value ε is oriented in the direction of the electric field lines.

This interaction is written in terms of the total free energy of the system, where (see equation (2-13)),

$$F_T = F_{Static} + F_{Fred}. \tag{2-72}$$

F_{Fred} is the free energy component associated with the Fréedericksz transition[98],

$$F_{Fred} = \int \Delta\varepsilon\varepsilon_0 (\boldsymbol{E_{app}} \cdot \boldsymbol{n})^2 \, dV. \tag{2-73}$$

It can be seen that F_{Fred} adopts a minimum value when $\boldsymbol{E_{app}}$ is parallel or perpendicular to $\boldsymbol{n}$ if $\Delta\varepsilon$ is positive or negative, respectively (Figure 2.7a).

Figure 2.7b shows a device with PH alignment filled with a positive $\Delta\varepsilon$ material. Here, as $\boldsymbol{E_{app}}$ is increased (via a voltage, V) the reorientation of $\boldsymbol{n}$ starts to occur above a threshold voltage (V_{th}). This reorientation does not occur uniformly throughout the material as the anchoring at surfaces is strong. $\boldsymbol{n}$ first reorients in the middle of the device and spreads out as V is increased[98]. Interestingly, this voltage is not a function of device spacing (d). This is due to the fact that although voltage reduces proportional to $1/d$ so does the anchoring strength [99], meaning the two effects cancel one another.

The value of V_{th} depends on the elastic deformation the nematic field, and the value of $\Delta\varepsilon$ driving the transition. This can be written as[99],

$$V_{th} = \pi \sqrt{\frac{k_{eff}}{\varepsilon_0 \Delta\varepsilon}} \tag{2-74}$$

where k_{eff} is a combination of the elastic constants of the material corresponding to the deformations occurring. In certain configurations, k_{eff} equals to one of the principal elastic constants (k_{11}, k_{22}or k_{33}). In the example shown in Figure 2.7b, the primary deformation is splay; therefore k_{eff} would equal k_{11}. If it is for a negative $\Delta\varepsilon$ nematic in a HT aligned sample, then the first deformation will be bend, therefore, $k_{eff} = k_{33}$.

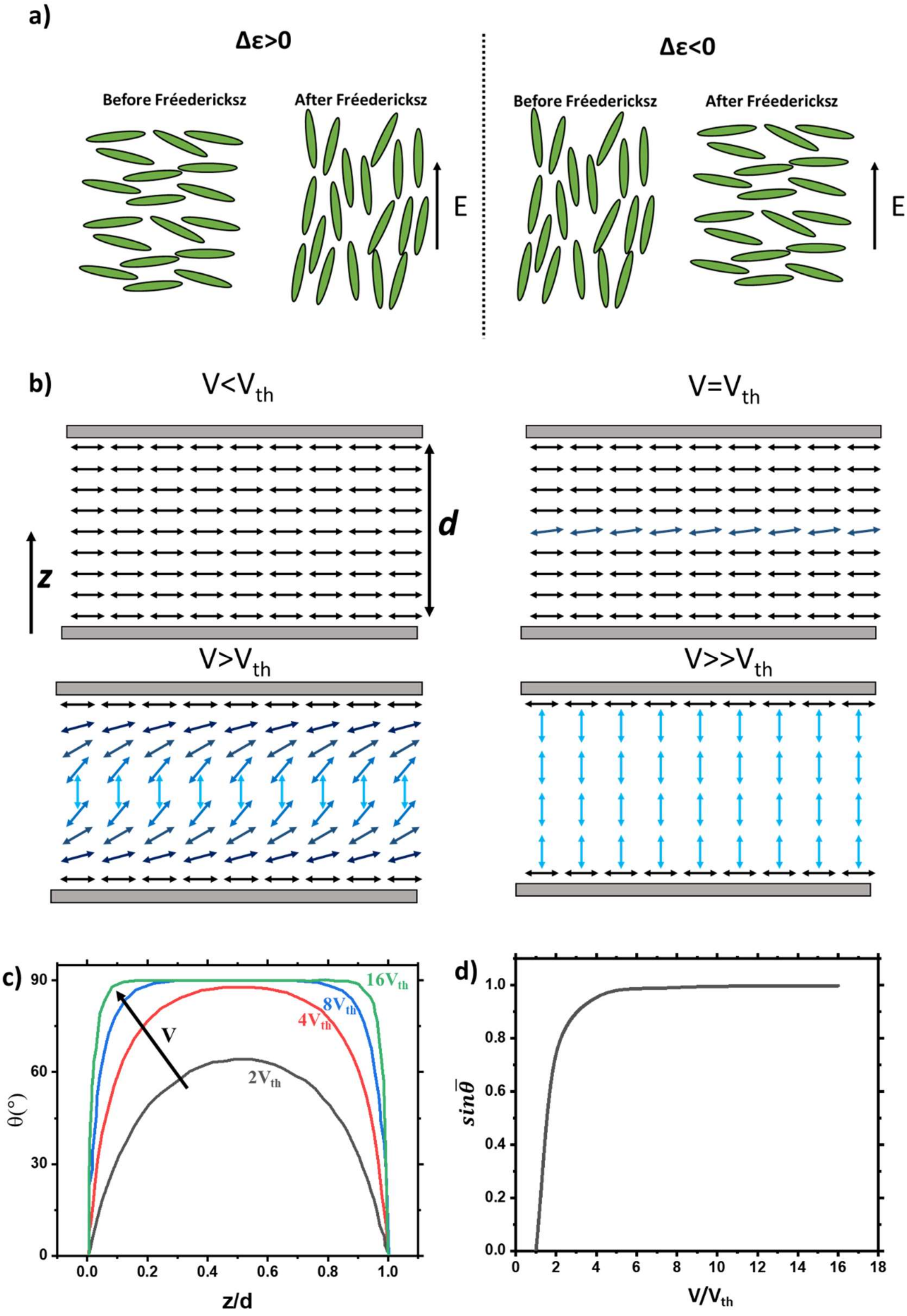

Figure 2.7. a) A Fréedericksz transition in a material with postive and negative dielectric anisotropy. In both cases the material reorients with the larger permtivity oriented along the electric field. (b) a schematic of a Fréedericksz transition, where the material is planar homogenously aligned and has a positive $\Delta\varepsilon$. (c) Shows the plots of θ as a function of z, where more and more of the LC is reoriented to $\theta=90°$ as voltage is increased[100]. *(d) The average θ value ($\bar{\theta}$) as V is increased.*

When V increases above V_{th}, other deformations begin to occur. Figure 2.7b shows that in a PH device splay and bend both exist at V equal to several V_{th}. This combined with the effects of pretilt makes a full description of ***n*** for arbitrary voltage and alignment reasonably complex. Assuming the case shown in Figure 2.7b where there is zero pretilt, the deviation angle θ_m can be found through solving[99,100],

$$\frac{V}{V_{th}} = \frac{2}{\pi}\sqrt{\frac{\Delta\varepsilon}{\varepsilon_\perp}sin^2\theta_m + 1}\int_0^{\theta_m}\sqrt{\frac{1+\kappa sin^2\theta}{\left(\frac{\Delta\varepsilon}{\varepsilon_\perp}sin^2\theta_m + 1\right)(sin^2\theta_m - sin^2\theta)}}d\theta \tag{2-75}$$

where

$$\kappa = \frac{k_{33} - k_{11}}{k_{11}}$$

and [99,100]

$$sin\theta_m = \sqrt{\left(\frac{4}{\kappa+1}\right)\left(\frac{V}{V_{th}} - 1\right)}.$$

Given the complexity of even this most straightforward case, solutions to these equations are usually found computationally. The Fréedericksz transition will be used in this work to measure material elastic constants. Here, the values k_{11} and k_{33} are obtained by fitting $\varepsilon(V)$ curves using techniques described in references [100,101]. Conversely to the case shown in Figure 2.7, a Fréedericksz transition will also occur in a HT device filled with a $\Delta\varepsilon<0$ material. Similar fitting methods can be utilized however; the primary deformation is k_{33} instead of k_{11}.

2.5 Nematic Liquid Crystals for Beamsteering Applications

2.5.1 NLCs in Optical Devices

NLC materials are used widely in switchable optical devices, where electric fields are used to vary director orientation, allowing shutters[4,102], filters[103,104], lenses[105–108], beam steerers [103,109–112] and diffractive optical elements (DOEs)[21,113,114] to be created. In this section, a brief overview of diffractive beam steering devices and DOEs relevant to the work carried out in this project is provided. A more comprehensive review on the topic was also published in the course of the project in reference [115]. LC optical devices may operate utilizing both refractive and diffractive properties of light, which will be discussed in 2.5.2 and 2.5.3, respectively.

2.5.2 Refractive Optical Devices

Refractive NLC devices are widely used in technology. Here, we split refractive devices into geometric switchable index (GSI) and Gradient Index (GRIN) devices.

GSI devices are shaped in a wedged or lensing shape, where focussing or beam deflection is dictated by the contrasting refractive indices between container and LC. Here, by reorienting $\boldsymbol{n}$ the value n_{eff} can be switched from $n_{\perp}$ to $n_{||}$ or vice-versa. This allows switching of the angle of emergent ray (Figure 2.8a). This method has been used to create switchable lenses and beam steering components[107,110,116–118]. At the interfaces the angles are described by Snell's Law (Figure 2.8b),

$$\frac{n_1}{n_2} = \frac{sin\theta_2}{sin\theta_1}, \tag{2-76}$$

where n_1 and n_2 are the refractive indices of the first and second medium, while θ_1 and θ_2 are the input and emergent angles.

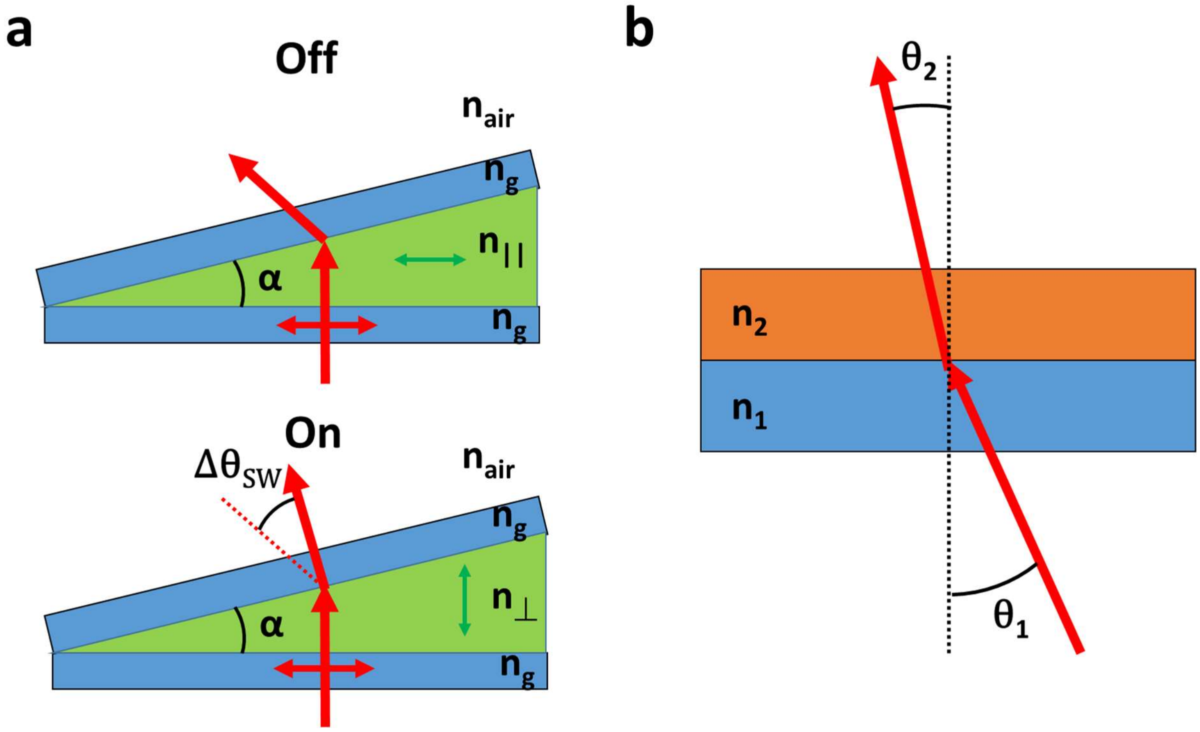

Figure 2.8. GSI device operation. (a) A geometric wedge filled with liquid crystal. When the director is reoriented the effective refractive index changes, leading to a change in angle ($\Delta\theta_{SW}$). Here, n_g and n_{air} are the refractive index of glass and air respectively. The green arrow indicates director orientation. (b) Snell's law diagram.

GRIN devices smoothly vary n_{eff} within a device, where the difference in light's transmission speed causes its direction to deviate (Figure 2.9a) [119–122]. This deviation is described by the differential form of Snell's law [119,120,123],

$$\frac{\partial^2 x}{\partial z^2} = \frac{1}{n} \cdot \frac{\partial n_{eff}}{\partial x}. \tag{2-77}$$

Equivalent structures can be achieved for polarized light using liquid crystals, where the director smoothly reorients so that n_{eff} varies from $n_\perp$ to $n_{//}$ (Figure 2.9b). Practically, this structure can be achieved using a number of methods including pixelated electrode addressing[4,28,130–139,29,140–143,103,124–129], fringing electric fields[108,144,153–158,145–152], optical addressing[159–161] or alignment coatings[65,70,169,71,162–168] (for reviews see [28,29,33,115]).

Usually for both GSI and GRIN type devices, the angle which an emerging beam can be switched ($\Delta\theta_{SW}$) is modest (<1°). This is usually due to the beneficial properties of NLCs being reliant on relatively thin layers of material, which limits large steering angles. One method of increasing these angles is using a Fresnel structure, which allows a thicker lens to be approximates by a flattened thinner structure[170–172]. However, using Fresnel structures usually increases fabrication complexity and often reduces optical quality.

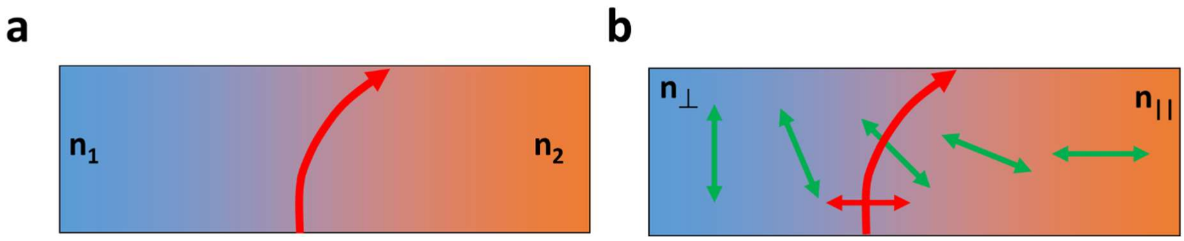

Figure 2.9. (a) A GRIN beam deflector. The optical beam moves towards the greater refractive index (n_2) due to relatively lower speed. (b) The structure made of a NLC. The director's reorientation in space causes deflection of the beam. This can be overridden by a large electric field, allowing switching.

2.5.3 Diffractive Optical Devices

Diffractive effects are also used to create switchable optical components using NLCs. The most relevant type to this project are Raman-Nath (RN) gratings, which are optically thin obeying[173],

$$\frac{\pi^2 d^2}{\Lambda_{gr}^2}\frac{\Delta n_{eff}}{\bar{n}_{eff} cos^2\theta} < 1, \tag{2-78}$$

where Δn_{eff} is the effective birefringence, $\bar{n}_{eff}$ the average birefringence, d the device spacing, θ is the refraction angle and Λ_{gr} the grating period. For typical NLC parameters this reduces to,

$$d < \Lambda_{gr} cos^2\theta. \tag{2-79}$$

When light passes through a RN diffraction grating, it will be divided into m orders the position of which obey the grating equation,

$$m\lambda = \Lambda_{gr} sin\theta_m, \tag{2-80}$$

where λ is the wavelength of light. The intensities of the various orders (I_m) are usually described by absolute efficiencies (η_m), where[174,175],

$$\eta_m = \frac{I_m}{\sum_m I_m}. \tag{2-81}$$

Prediction of the values η_m are possible using scalar diffraction theory[174,175], and will be discussed in more detail in Chapter 4. Blazed-phase grating structures (Figure 2.10a) where the maximum optical phase difference (ϕ_{max}) equals 2π can create 100% efficient beamsteering to $\theta_{m=1}$. The optical phase difference *(ϕ)* may be calculated using,

$$\phi = \frac{2\pi}{\lambda}\int_0^d (n_{\mathrm{eff}}(z) - n_\perp)dz, \tag{2-82}$$

and can be achieved either by rotating the director azimuthally or radially (Figure 2.10b-c).

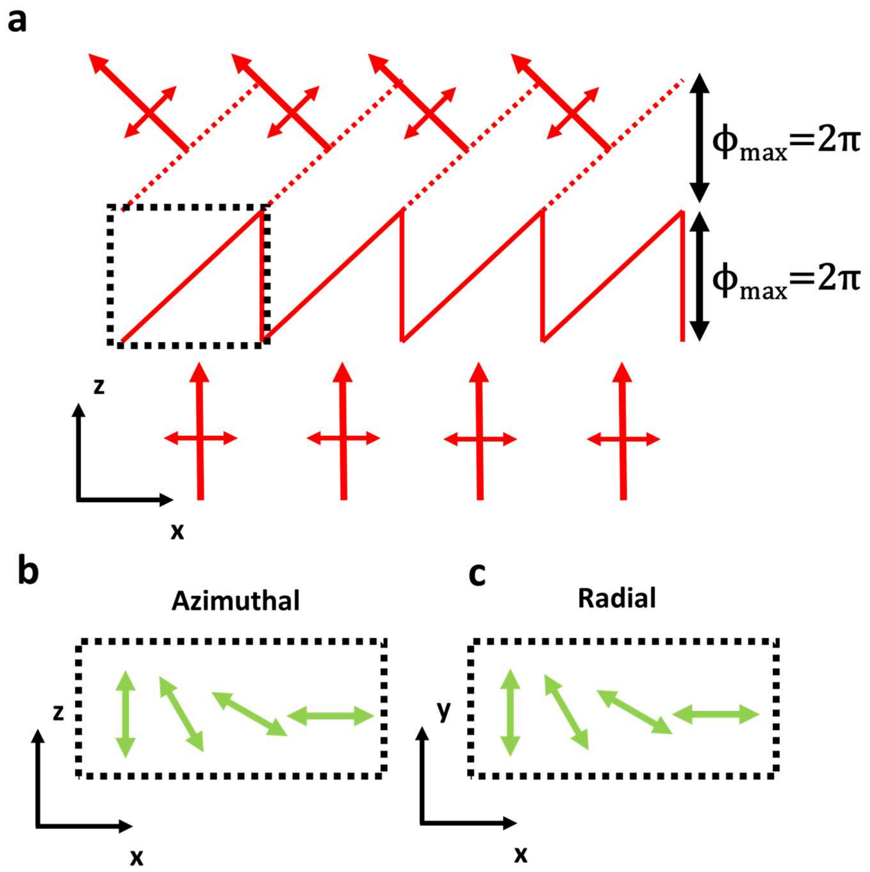

Figure 2.10. Diffraction from blazed grating structures. (a) Illustration of why blazed gratings can achieve high efficiency. If $\phi_{max}=2\pi$ each wave front connects perfectly with the next and previous in the x-direction. This leads to all wavefronts deviating by an angle described by the grating equation. This ϕ structure can be achieved using NLCs by varying azimuthal (b) angle or radial (c) angles (note different axis in (b) and (c).

The high efficiency, potentially wide-angle steering characteristics of blazed gratings, makes their fabrication of with NLCs a large field of research. They can be created using a number of methods:

Dielectric Inclusions. Here, a physical blazed grating is placed within the NLC device [112,176], where usually, the refractive index of the grating will match either $n_{\perp}$ to $n_{//}$. When a large electric field is applied to these devices, the diffraction will switch from a high η_0 to η_1 or vice versa. This allows efficient beam steering but is digital, as the diffraction angle is set by fixed Λ_{gr}. Also, the thick grating between electrodes and the LC usually increases the required applied voltage for the Fréedericksz transition dramatically.

Pixelated Electrode Addressing. Some of the most successful LC optical devices are liquid crystal on silicon (LCOS) diffractive gratings[4,130,131,136,177]. Here, pixelated electrodes are individually addressed to reorient the director allowing programmable phase profiles to be induced on light with sub 10μm precision. The main drawback of such devices are that to create a blazed profile, many pixels are necessary to approximate a linear phase ramp, meaning an inverse relation between efficiency and steering angle[28,178].

Specialised Alignment Layers. Some alignment layers present opportunities to engineer alignment to the microscale. This creates a director pattern, with an outgoing phase profile which resembles a blazed phase grating. This can be achieved a number of ways. Stacked alignment layers (SALs) change the azimuthal angle of the director alignment through layering a homeotropic and planar alignment layer and selectively removing the upper layer[65,71,162,179]. Alternatively photoalignment can be used to create an alignment layer which smoothly reorients the director[64,69,70], usually radially. Relatively recently, such methods have been used to create Pancharatnum-Berry devices which display close to 100% efficiency through inducing a near perfect blazed grating structure on circular polarized light[180–182]. Similarly to devices based on dielectric inclusions, these device are limited in the fact their response is digital.

From reviewing various methods of creating diffractive optical devices[115], it is found that trade-offs exist in creating an ideal device having: high efficiency, wide steering angle, wide range of steering angles and continuously variable behaviour. Improving these factors holistically is a technological challenge with applications in a variety of industries[183–186], making it a wide and active area of research.

2.6 Summary

This project seeks to assess the viability of NLC hydrodynamics as a method of creating diffractive optical elements (DOEs). These hydrodynamic DOEs have been known to exist for many decades, however testing their application and limits in devices has been fairly limited. The two main kinds of hydrodynamic DOE investigated in this work are based on ion[22,23,187,188] and acoustic[24–27,189] induced flow within the materials. The background literature for these specific interactions will be described in their appropriate chapters. This chapter has introduced the important NLC characteristics, which are necessary to describe these processes, namely their order, viscoelastic, dielectric and optical properties. The following chapter will discuss the general methods throughout this work, where more specific methods will be given in the relevant chapters.

Chapter 3 Experimental Methods

The experimental techniques used throughout this project will be introduced in this chapter. This predominantly consists of fabrication (section 3.1) and characterization (section 3.2) methods for LC devices. A practical guide to these methods is included in addition to scientific background. Several techniques, including lift-off photolithography and bulk cell fabrication, were not established within the Soft Matter Group at start of the project, and I contributed significantly to establish these processes during this thesis. The bulk cell fabrication was developed along with major contributions from other members of the group mainly from Dr P Wyatt, Dr J Bailey and Mr H Litt.

3.1 Fabrication of Liquid Crystal Sandwich Devices

3.1.1 Standard Liquid Crystal Sandwich Devices

The main geometry of the liquid crystal devices investigated in this project were LC sandwich devices (Figure 3.1). This geometry is transparent to the majority of light, while allowing voltages to be applied across the LC material, making it ideal for studying electro-optic effects. The devices were sealed such that the LC could not flow out, and had alignment layers allowing the unperturbed director orientation to be set.

In this project, LC sandwich devices were either purchased from the Military University of Technology Warsaw (AWAT), or made in the facilities available to the Soft Matter Physics Group of the University of Leeds (SMP). This section will describe the fabrication of the latter, which allowed more customised designs.

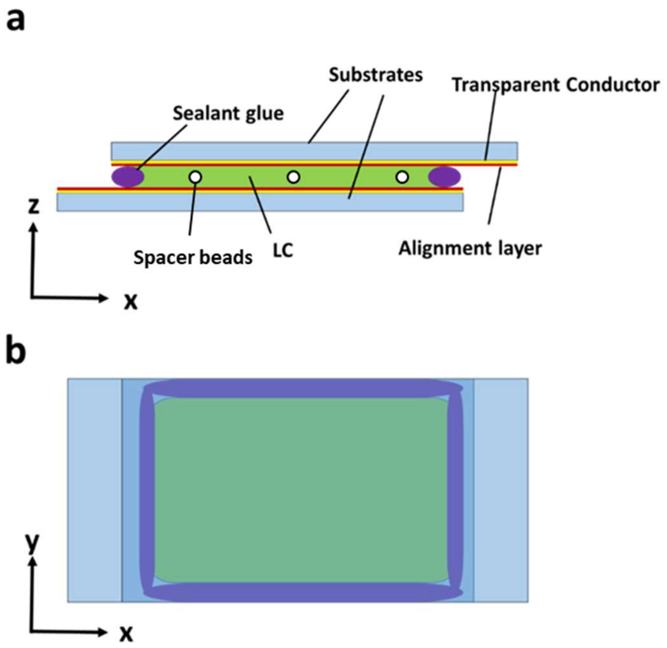

Figure 3.1. A liquid crystal sandwich device. (a) Side view and (b) top view. .

3.1.2 Custom Electrode Fabrication

3.1.2.a *Overview of the Process*

Electrodes in LC devices can be patterned in different designs including unpatterned, square/rectangular (SR), interdigitated (IDE) and guard ring (GR) (Figure 3.2). Generally, only unpatterned and SR type electrodes are commercially available, therefore establishing techniques to create arbitrary electrode patterns with sub 10μm feature sizes is highly useful.

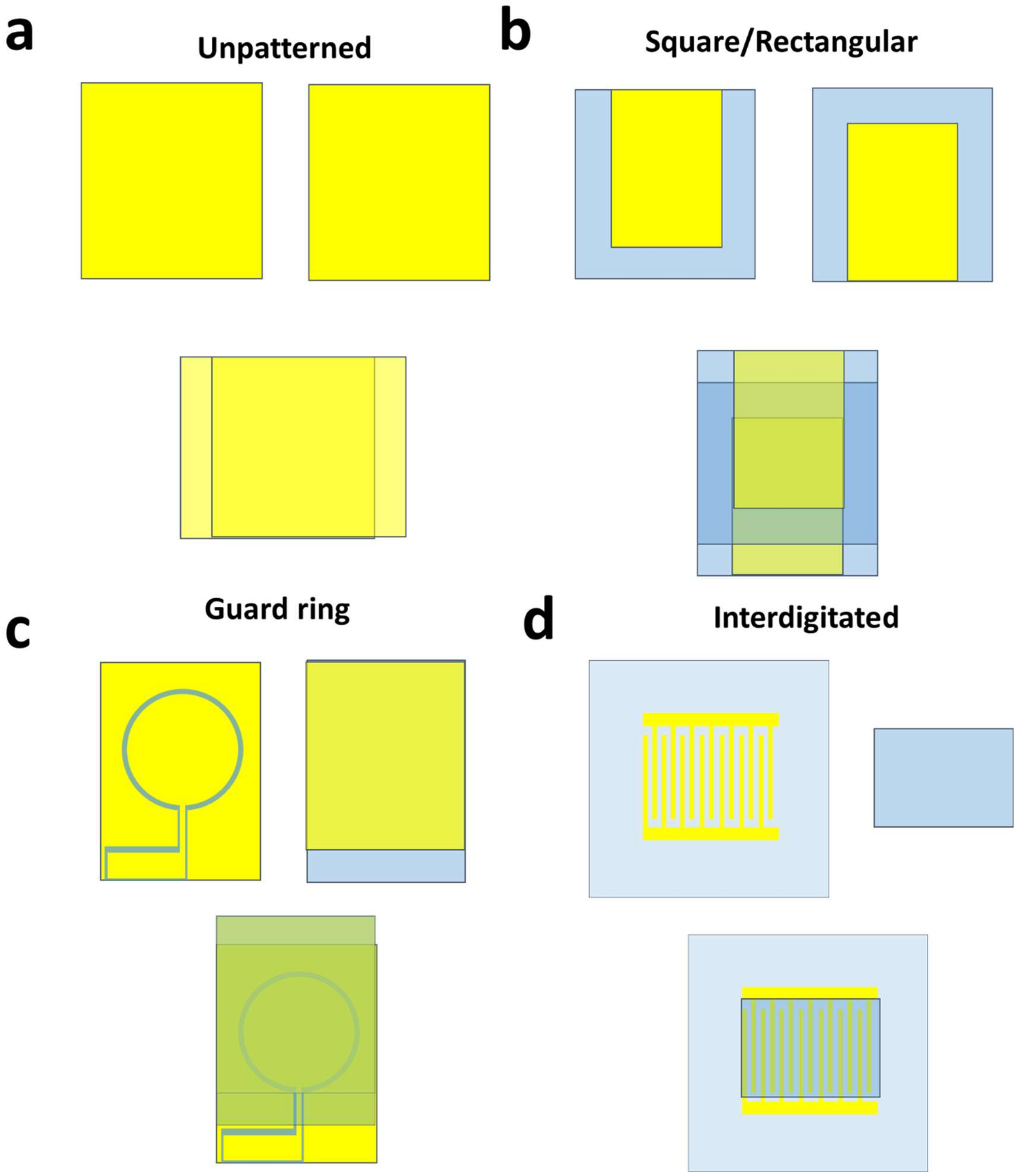

Figure 3.2. The four kinds of electrode configuration used in this thesis. a-d) Show: Unpatterned, square, guard ring and interdigitated respectively.

In this project, the electrode fabrication was done using photolithography with an acid etch (using techniques previously developed within SMP by Dr P Wyatt and Dr J Bailey [190]). The substrates used for this project were unpatterned 0.7-1.1mm thick pieces of glass coated with a thin layer of conductive Indium Tin Oxide (ITO, purchased Folium or Display Data). The process is illustrated in Figure 3.3, where the key steps involved are: cleaning, photoresist deposition, exposure, development, etching and cleaning. Further details of these will be discussed in the following sections.

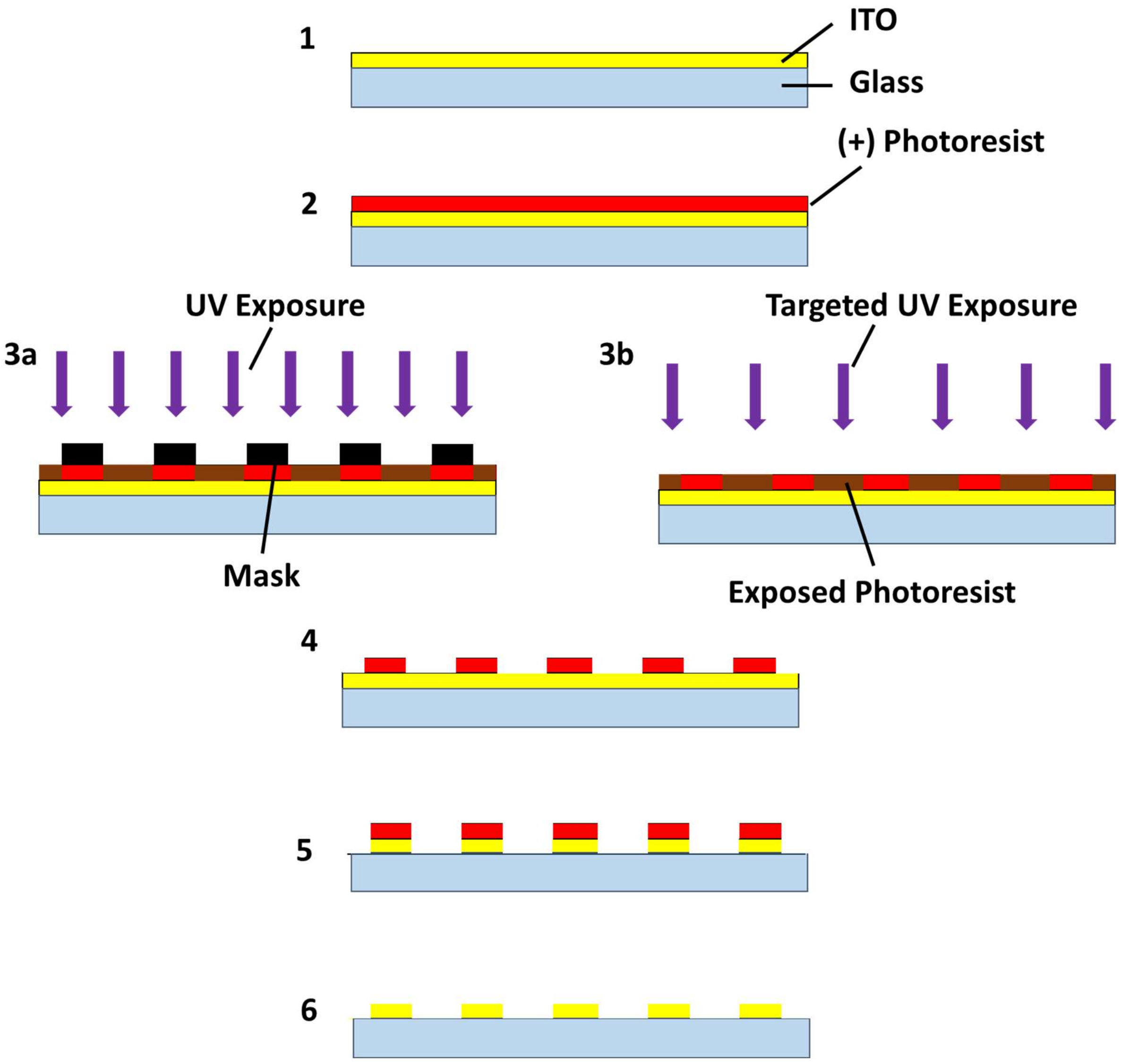

Figure 3.3. The key steps involved in positive tone photolithography with acid etch. 1) A substrate with ITO placed upon it. 2) The deposition of positive tone photoresist (red). 3a and b) Exposure methods using masked and unmasked photolithography, respectively. 4-6) The removal of exposed photoresist (development), acid etch and removal of residual photoresist, respectively.

3.1.2.b *Cleaning*

Cleanliness was of great importance throughout the cell fabrication process particularly when sub 10µm resolution electrode patterns were desired. To achieve this the ITO coated glass substrates were cleaned thoroughly before the photolithography steps. To clean, the substrates went through a series of subsequent sonication steps each lasting 30 minutes (deionised water with 10% Decon 90, deionised water, methanol, propon-2-ol). The substrates were then exposed to UV light in an ozone environment, which has been shown to remove further contaminants[191].

3.1.2.c *Photoresist Deposition*

The photoresist used for photolithography was S1813 (Shipley). This is a positive tone photoresist, meaning it has enhanced solubility with some solvents (the developer) when exposed to light of a certain wavelength[192] (for details of reaction see references [193–195]).

S1813 was deposited onto the substrates using a filtered syringe. After this, the substrates were spun to a high speed (typically 4000rpm) using a WS-650-MZ spin coater from Laurell Corp (Figure 3.4a), in a method illustrated in Figure 3.4b. Spin coating is a well-established method to achieve uniform thin films[196]. The final film thickness depends on the viscosity(η) and solids concentration (C) of the materials and the spin speed (ω)[197]

$$h_{film}\alpha\frac{C^{\beta}\eta^{\gamma}}{\omega^{\alpha}}, \tag{3-1}$$

where α, β and γ are fluid and substrate determined constants. Thus, controlling spin speed while temperature and material composition remains constant, presents a simple way of controlling film thickness.

During the spin-coating process, the majority of solvent evaporates, leaving an approximately solid film of resin. However, this is confirmed through a of 1 minute 'soft bake' at a temperature of 110°C, which has the added benefit of reducing any stresses within the film[192].

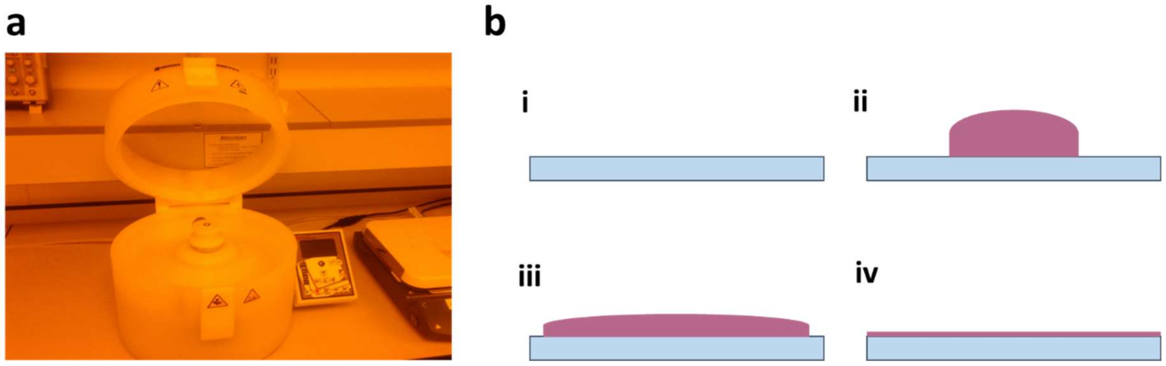

Figure 3.4 a) The spin coater used .b) A diagram of spin coating process: (i) the cleaned substrate, (ii) The droplet initially put onto the substrate. (iii) The droplet mechanically spread over substrate, (iv) The uniform layer after spin coating.

3.1.2.d *Exposure*

Once the photoresist was deposited onto the substrate, it was selectively exposed to UV light. This was done using either Direct Write Lithography (DWL) or Aligned Masked Lithography (AML).

DWL works through the relative movement between a laser focus and a substrate, allowing exposure of the photoresist to light with micron-scale precision. The machine used for this was a MicroWriter

ML2 DWL (Durham Magneto Optics Ltd. Figure 3.5a), which has several inbuilt lasers which can be used to expose substrates to a variety of wavelengths with different spot sizes. During the exposure, these lasers raster across the substrate, exposing the material selectively to draw the desired pattern (Figure 3.5b). The wavelength used throughout this work is 405nm, which can be produced with laser spots of 0.6, 1 and 5µm diameter. The choice of which spot size to use was determined by the desired feature size and the time allowed for the experiment, as smaller spots allow greater precision, while larger sizes reduce writing time. Here the quantity of light shone onto the material was controlled by setting the dosage, and typically was within region 100-400mJcm^{-2}. Table 3-1 shows the approximate laser diameters, and exposure modes found best fulfil these criteria throughout this project. These also apply to the steps used in Lift-off photolithography, which will be discussed in section 8.3.1.

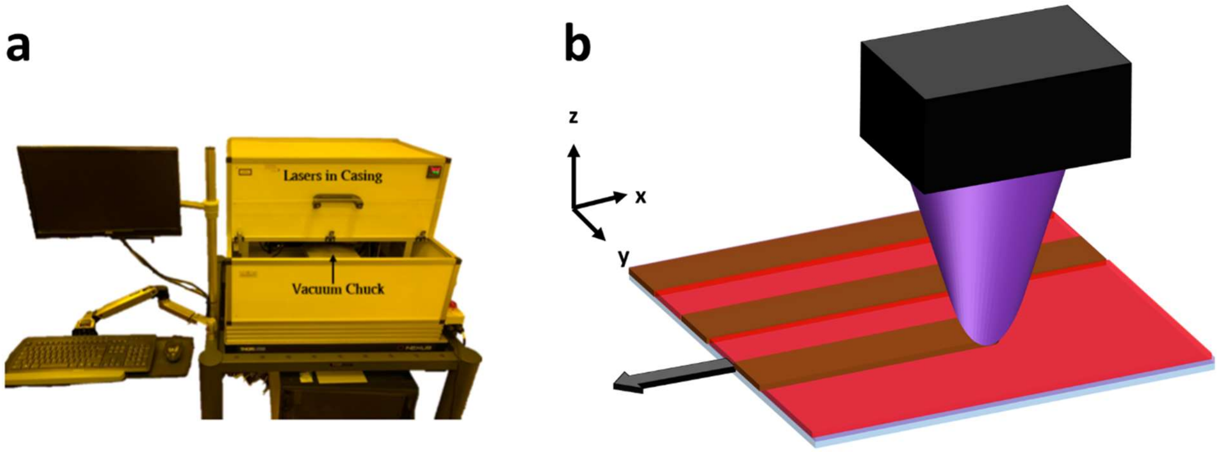

Figure 3.5 a) Picture of the DWL[190]. *b) Diagram of exposure method.*

Table 3-1. The list of spot diameters (L) used to write features of different sizes (w).

Feature range (*w*)	**Spot diameter (*L*)**	**Exposure mode**
***w*< 20µm**	0.6µm	x-raster
***20* µm <*w*<*50* µm**	1µm	x-raster
***100µm*>*w*>50 µm**	5µm	x-raster
100µm*>*w	5µm	Turbo

For AML an “OAI Model 200: Mask Aligner and UV Exposure System” was used. This technique works by exposing the entire substrate area, with a physical mask placed between the light source (A high power Mercury bulb, of wavelength 365nm) and the substrate shielding the desired areas (Figure 3.6). Typically these masks consist of glass covered with a reflective metal (here chrome). These masks were commercially purchased (JD Photonics). Typically, the exposure takes less than 10s, demonstrating the advantage of this technique over DWL for repeated structures.

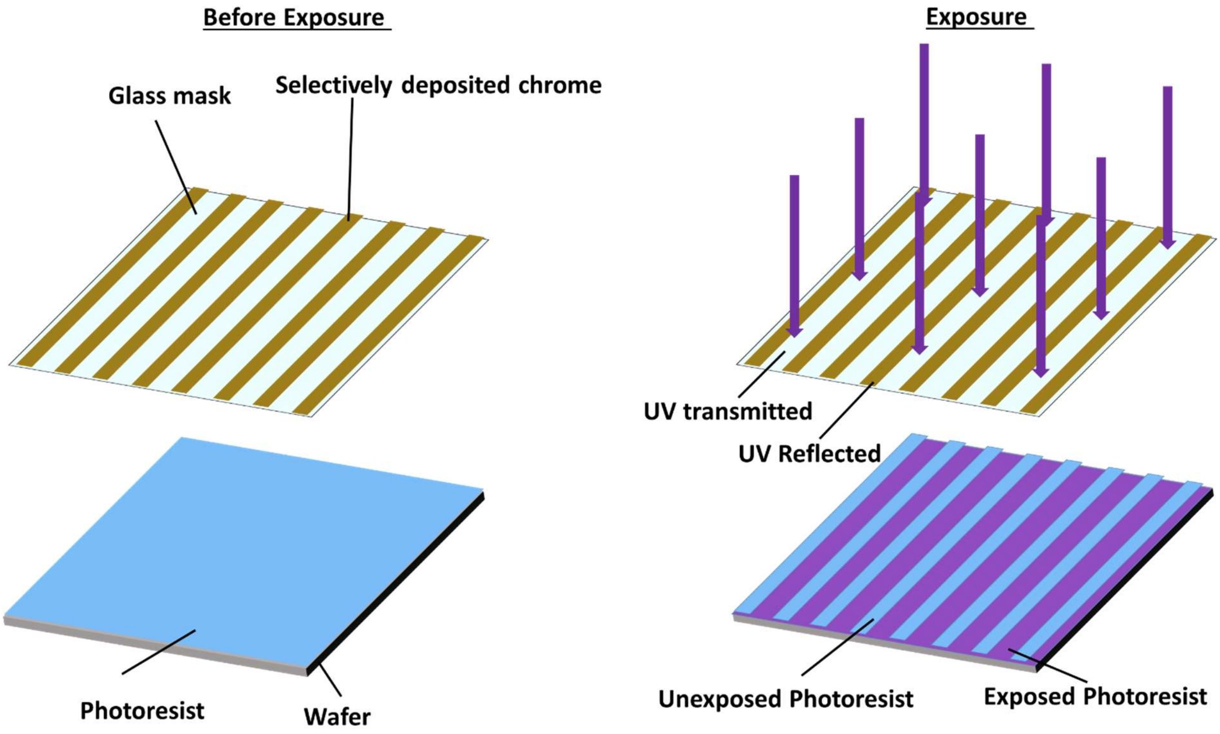

Figure 3.6. Diagram of the aligned masked lithography exposure method. The UV light is reflected by chrome and transmitted by the glass. Note, in actual exposure the mask is in direct contact with the wafer, rather than being spaced apart. This is not shown here for clarity.

3.1.2.e *Development and Hard Baking*

After exposure, the structures are developed using Shipley developer MF319 (water with 2% Tetramethylammonium hydroxide and other trace elements). This was found to be most effectively done by: placing the substrate on a spin coater, doming MF319 on top, waiting 20s, spinning at 500rpm for 30s to remove developer and developed S1813, repeating this process, then rinsing with copious deionized water and blown dry.

Once dried, samples were etched; however, when there was a significant delay between development and acid etching, it was advised to hard bake the samples[190]. To hard bake, they were placed on a hot plate at 110°C for 30 minutes, which removed any residual solvent.

3.1.2.f *Etching*

After the substrates were developed, they were etched using a combination of nitric and hydrochloric acids which remove the ITO in exposed areas (see Wyatt's thesis for further details[190]). Once etched, the substrates were rinsed with acetone, which removed residual S1813 leaving only the desired electrode pattern. These substrates were cleaned before cell fabrication, to remove contaminants.

3.1.3 Alignment Layers

To achieve the desired alignment in liquid crystal devices, thin (50-150nm) films of polyimide (PI, Figure 3.7a) were used. Here, PI was filtered and deposited in solvent onto cleaned substrates using spin coating (3000rpm for 60s, WS-650-MZ, Laurell Corp). These materials are capable of aligning LCs due to the Van der Waals and steric forces between the polymer chains and the liquid crystal's elongated stiff cores[43,44,55,96]. Various polyimides and solvent concentrations were used throughout the project (Table 3-2). These were designed to achieve different alignments (homeotropic, HT or planar, PL) and pretilt (θ_p) [73]. After spin coating, residual solvent was evaporated and the PI was bonded to the glass by placing on a hotplate at 180°C for 120 minutes.

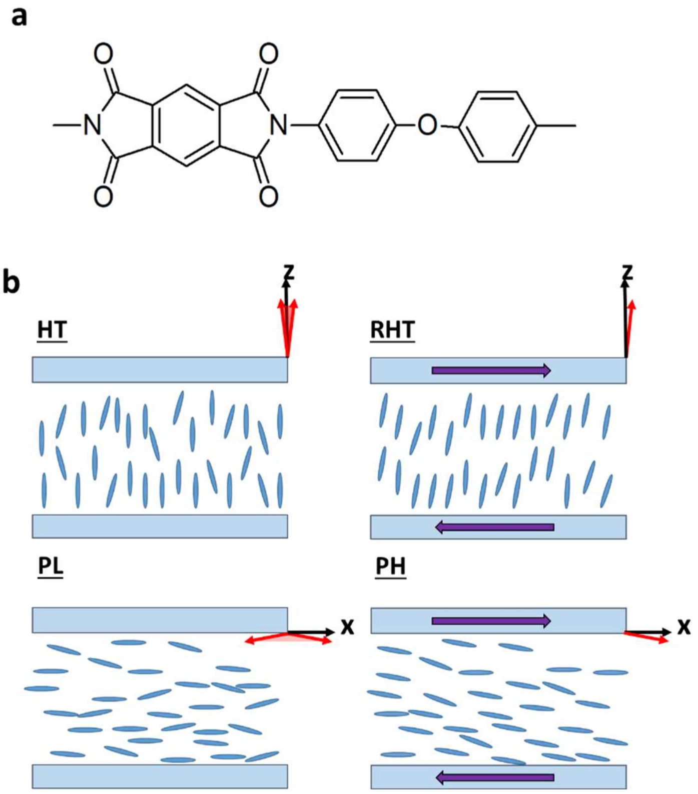

Figure 3.7a) Chemical structure of a polyimide b) Effects of rubbing homeotropic and planar cells. Purple and red arrows, respectively show the rubbing direction and director orientation. By rubbing therefore the director can be forced to have a single direction throughout the device which is approximately parallel to z or x (for HT or PL), but with a small difference due to pretilt.

Table 3-2. The various solutions of PI used in this project with details regarding their alignment and pretilt according to Nissan Chemicals[73].

Alignment layer	**Alignment type**	**Solvent used**	**Φ_{PI}**	**θ_p**	**Final solids (C)**
SE2170	PL	DMF	66%	~2°	5.3%
SE3510	PL	DMF	66%	~7-8°	4.0%
SE1211	HT	DMF	20%	~0°	1.2%

After baking, the PI layers could be given directionality by subjecting them to mechanical rubbing[54,55,60,198]. This change in direction is generally thought to be caused by a combination of either polymer chain reorientation[54,57] or scratching microgrooves in the material[56,199]. References[60,200] which compare effects conclude the reorientation of chains is likely dominant. This rubbing changes PL alignment to PH and HT to HTR. The pressure at which the polyimide is rubbed is a crucial parameter in the resulting rubbing strength (L), which can be quantified as [99,201],

$$L = Nl\left(1 + \frac{2\pi r\omega}{60\nu}\right), \tag{3-2}$$

where N is the number of passes, l a length scale associated with the brushes and distance between roller and substrate, ω is the revolutions per minute, r is the radius of the roller, and ν is the substrate speed.

Practically rubbing was achieved using a rubbing machine (Figure 3.8, designed by Dr J Bailey). This allowed repeatable fixed values of N, r, ω and ν; allowing l to be varied by raising and lowering the roller with two grub screws. This allowed planar homogenous (PH) and rubbed homeotropic (RHT) alignments (Figure 3.7b).

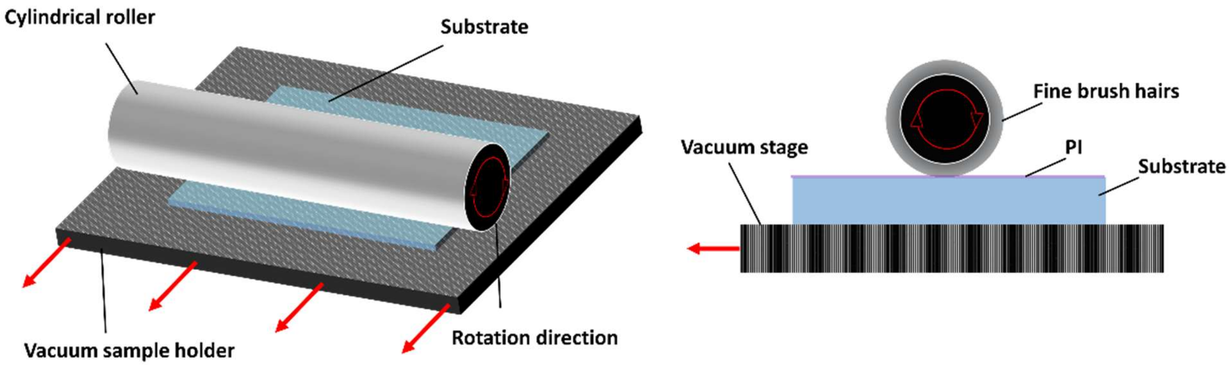

Figure 3.8. The method of rubbing samples using a cylindrical roller. A sample is held rigidly by applying a vacuum through small holes in the vacuum sample holder. This holder is placed at a height so that the roller just touches the substrate. The roller is actively rotated while the sample holder is linearly translated at relatively low speed compared to that of the roller's rotation.

3.1.4 Spacing and Gluing

Once the alignment layers were deposited sandwich cells were constructed, where the two substrates were glued together with a uniform spacing (*d*) between them. Bonding was achieved using either UV (UVS93, Norland) or thermal glue (Struct bond XN-21-F). These could be deposited mechanically using a cocktail stick or using a glue deposition robot (Figure 3.9, designed by Dr J Bailey).

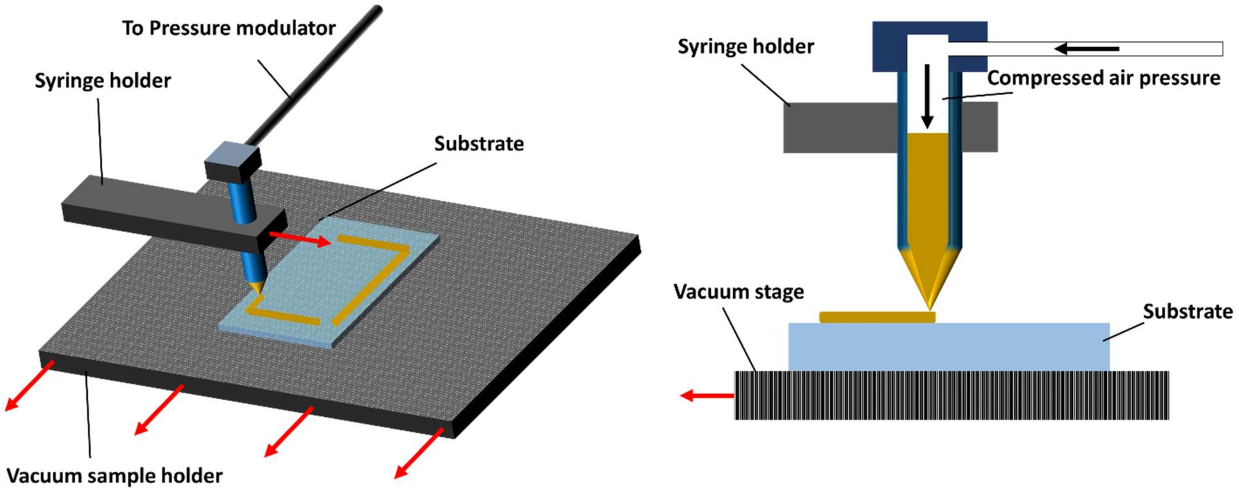

Figure 3.9. A diagram of the glue deposition technique. The vacuum holder moves similarly to when a sample is being rubbed, however now as 2-dimensional relative movement is required, the syringe holder also moves in an orthogonal direction. The glue was deposited by applying air pressure, pushing the material through the needle. The speed of relative movement and pressure applied were both tuned to deposit glue seals of desired thickness.

The value of *d* was controlled by placing either spacer film or beads of known size between the two substrates. These space the device to the same thickness when pressure is applied. For spacer films, they were cut to the desired device size and placed on the edges of the device (Figure 3.10a). Meanwhile, spacer beads were deposited using a spacer bead deposition chamber (Figure 3.10b). This involved placing a calibrated amount of spacer beads into a small reservoir, which was then blown through with air to disperse the beads into the chamber. The number of beads was calibrated to achieve uniform *d* (Jones[99] recommends roughly 50-100mm^{-2}).

If the mass of some number of spherical beads (m_{beads}) is written as,

$$m_{beads} = N\rho V = \frac{4\pi}{3}N\rho r^3 \tag{3-3}$$

and the desired number of beads per unit area at the bottom of the chamber (n_{beads}) as,

$$n = \frac{N}{A} \tag{3-4}$$

Where N, ρ, V, r are the total number, density, volume and radius of beads respectively. A is the area of the bottom of the chamber. Combining (3-3)and(3-4), we can write the total mass required to be placed into the chamber assuming 100% efficiency as,

$$m_{beads} = \frac{4\pi}{3} An\rho r^3. \tag{3-5}$$

If the values for 10μm glass beads and the area of the spacer deposition chamber are put into equation (3-5), we find the theoretical m_{beads} amount for n =50-100mm^{-2} is 6-12mg. This calculation was used as a starting point for finding the mass of beads which should be placed in the reservoir, where the best results for uniform well-spaced cells was found to be 10-15mg.

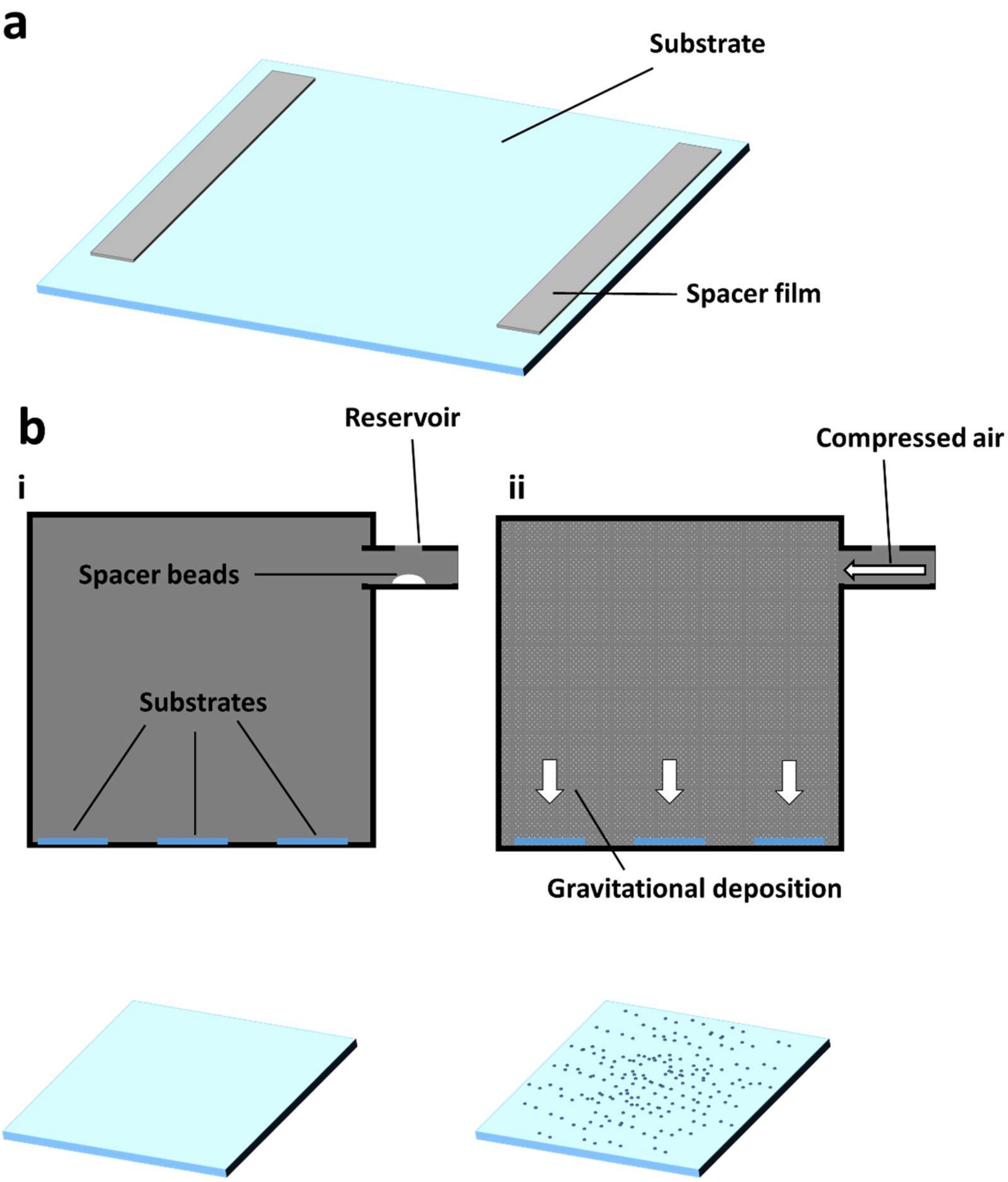

Figure 3.10a) Placement of spacer films on a substrate. b) The method of spacer bead deposition where beads are placed in a reservoir then blown through and slowly land on substrates due to gravity.

Once spaced, the devices had pressure applied to them while the glue was cured. The method of applying pressure depended on glue type (UV glue was exposed to UV light for 30 minutes, and thermal glue was heated to 160°C for 120 minutes) and size of the substrate (more homogenous pressure is required for larger substrates). The different methods of applying pressure (clips, weights, magnets and vacuum) are detailed in Figure 3.11. In general, clips or magnets were used for single-cell fabrication with UV glue, while weights and vacuum bags were used for thermal glue.

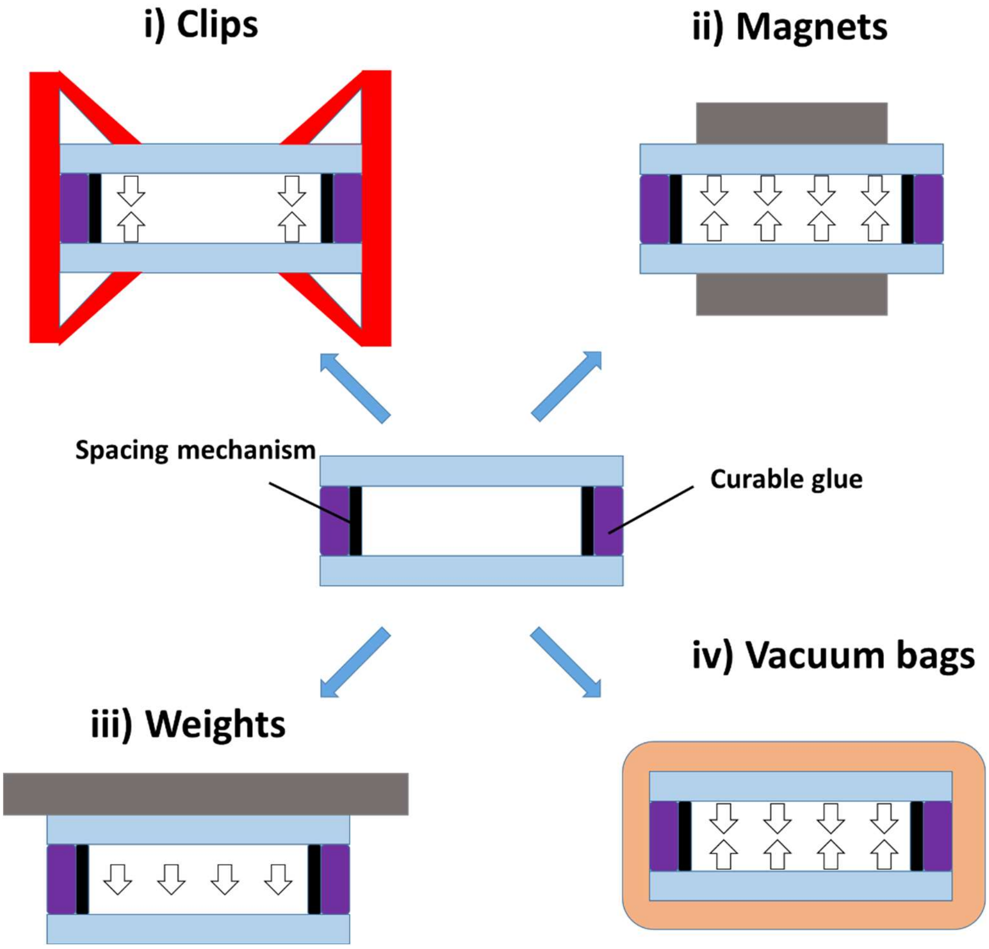

Figure 3.11. Illustrations of different methods of applying pressure to a cell while glue cures. Different methods are compatible with different glue types based on the environment requirements for curing.

3.1.5 Adjustments for Bulk Fabrication of Guard Rings

In this project, a significant amount of time was spent adjusting existing techniques for single cells, such that sandwich devices could be fabricated in bulk. Here, 8x8cm patterned electrodes were processed simultaneously, which were then singulated into 12 individual devices, usually, guard rings. The advantage of such processing is manifold compared to single-cell fabrication, with some advantages offered being: decreased time per unit, decreased materials required, increased cross device uniformity and increased cleanliness. In performing bulk cell fabrication, the method varies from single cells in several ways (illustrated in Figure 3.12). Here, the main differences were the point at which glass is cut and the fact spacer beads and the glue robot needed to be used.

3.1.6 Filling, Sealing and Electrodes

AWAT or fabricated cells were then filled with liquid crystal material. Here, a small quantity of material was placed on the edge of the device near an opening, which would be drawn in by the capillary forces. Once filled the LC devices were sealed by placing a small quantity of Norland UVS93 on to plug gaps used to fill it. The entire device was then exposed to UV to cure the glue, here foil was used to minimize LC exposure to UV. Wires were also attached to the electrodes using indium solder, where a iron temperature of 190°C was used.

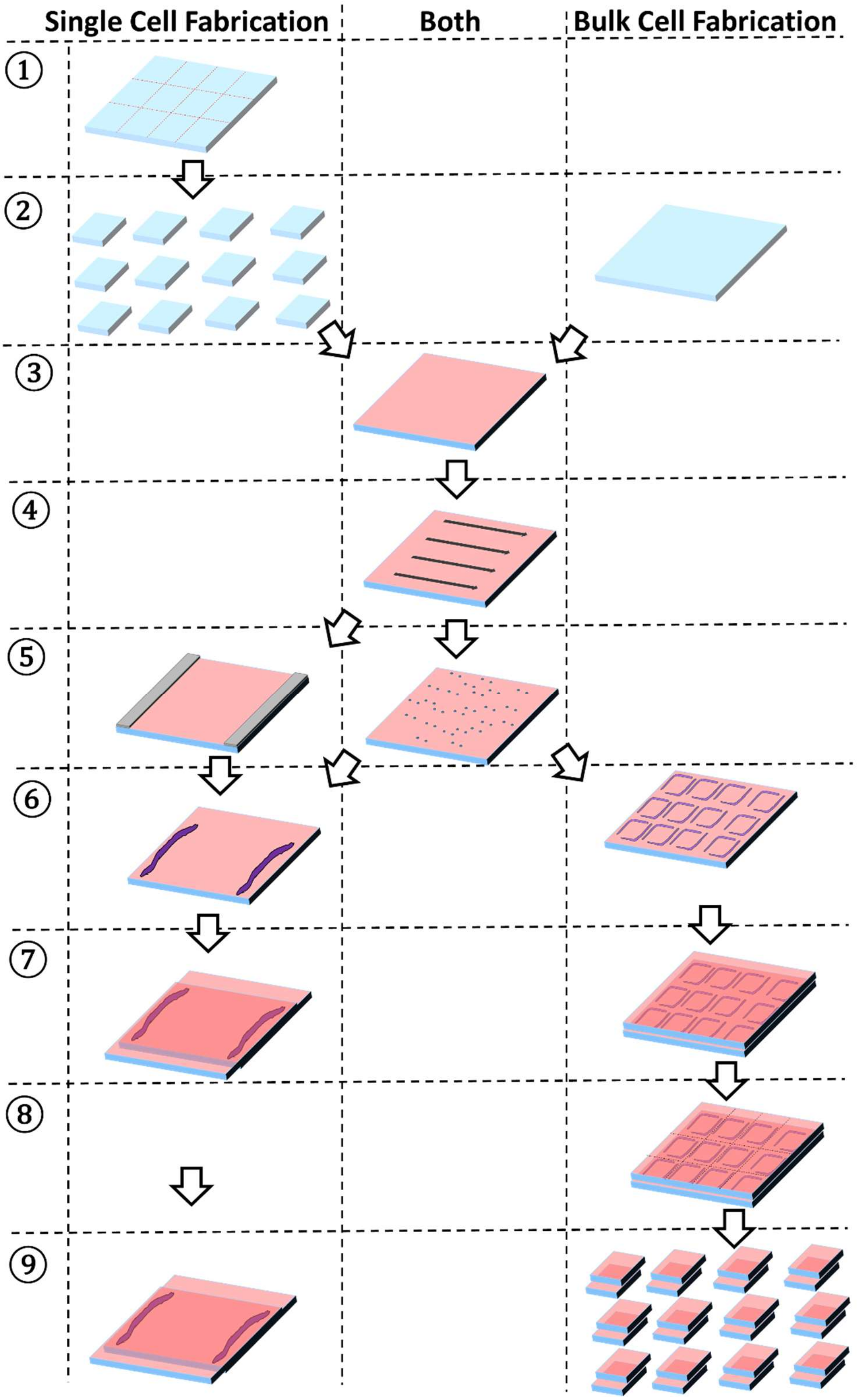

Figure 3.12. An overview of the cell fabrication procedures for single and bulk fabrication. Steps 1-9 are as follows 1) Laminate singulation. 2) Cleaning. 3) PI deposition. 4) Rubbing 5) Spacing 6) Glue deposition 7) Assembly glue curing 8) Singulation and 9) Finished devices. Due to changes in order not all these steps occur at the same point in bulk and single-cell fabrication; thus, an arrow indicates this process is not required.

3.2 Characterization of Liquid Crystal Devices

3.2.1 Polarized Optical Microscopy

3.2.1.a *Setup*

Polarizing optical microscopy (POM) was used extensively to characterise LC devices. The basic premise is that when light is passed through a birefringent sample (such as an LC device) placed between two crossed polarizers (Figure 3.13), the light of certain wavelengths can be transmitted giving information about the sample. This setup may be combined with additional apparatus for example: function generators/amplifiers for applying electric fields, hot stages for controlling temperature and cameras for taking photographs.

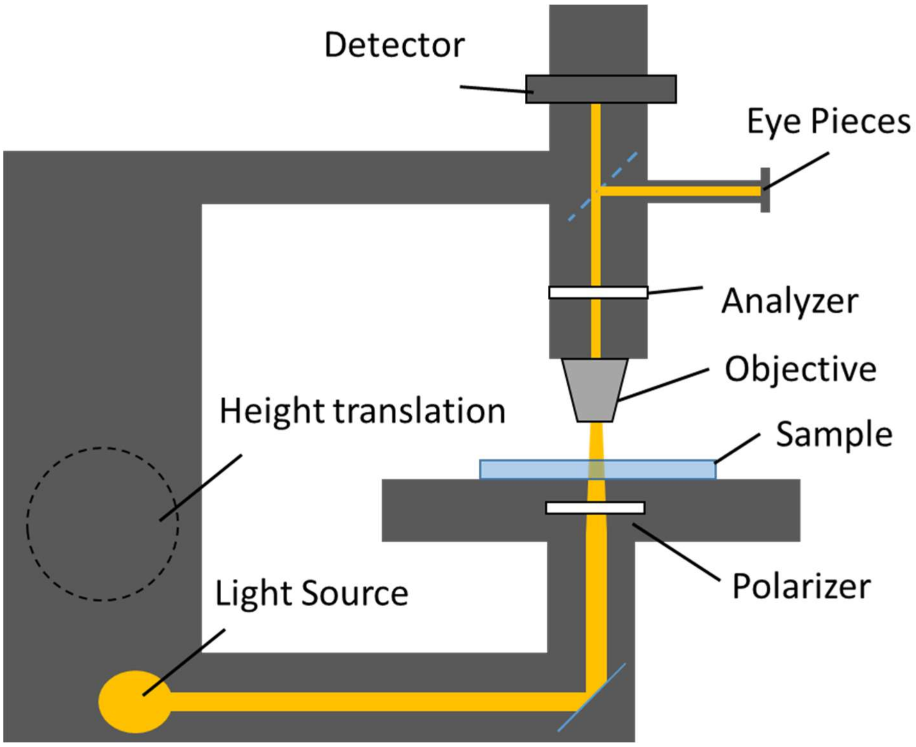

Figure 3.13. Diagram of a polarizing optical microscope.

3.2.1.b *Optics of POM*

The operating principle of POM, relies on the interaction of orthogonal components of light in birefringent media. In order to analyse this often Jones matrices are used[202], here, the unpolarized incident electric field *(E_i)* of light is written as

$$E_i(\boldsymbol{z}) = \begin{pmatrix} E_{x,i} \\ E_{y,i} \end{pmatrix}. \tag{3-6}$$

The transmitted electric field *(E_t),* from E_i passing through two linear polarizers oriented at arbitrary angles θ_1 and θ_2 is written as,

$$E_t(\boldsymbol{z}) = \ \hat{\boldsymbol{p}}(\boldsymbol{\theta_1}) \cdot \hat{\boldsymbol{p}}(\boldsymbol{\theta_2}) \cdot E_i(\boldsymbol{z}), \tag{3-7}$$

where $\hat{\boldsymbol{p}}$ is the Jones matrix corresponding to linear polarizer, defined as,

$$\hat{\boldsymbol{p}}(\theta) = \begin{pmatrix} cos^2\theta & cos\theta sin\theta \\ cos\theta sin\theta & sin^2\theta \end{pmatrix}. \tag{3-8}$$

In POM, the polarizers are typically crossed, meaning $\theta_2 = \theta_1$+90°. This allows no transmittance of light in the absence of an additional element,

$$E_t = \begin{pmatrix} E_x \\ E_y \end{pmatrix} = \hat{\boldsymbol{p}}(\theta_1) \cdot \hat{\boldsymbol{p}}(\theta_2) \cdot E_i \equiv \begin{pmatrix} 0 \\ 0 \end{pmatrix}. \tag{3-9}$$

Physically this represents the first polarizer removing all the light of one polarization, while the second removes all components transmitted by the first.

Aligned NLC materials are birefringent uniaxial materials. The Jones matrix for a uniaxial birefringent slab ($\widehat{\boldsymbol{M}}$) with optic axis aligned an angle θ from *x* is written,

$$\widehat{\boldsymbol{M}} \ = \begin{pmatrix} \cos\theta & -sin\theta \\ sin\theta & \cos\theta \end{pmatrix} \begin{pmatrix} e^{-i\frac{\phi}{2}} & 0 \\ 0 & e^{i\frac{\phi}{2}} \end{pmatrix} \begin{pmatrix} \cos\theta & sin\theta \\ -sin\theta & \cos\theta \end{pmatrix}. \tag{3-10}$$

where ϕ is the difference in optical phase difference between orthogonal components, equal to[203],

$$\phi = \frac{2\pi\left(n_{||} - n_{\perp}\right)d}{\lambda}. \tag{3-11}$$

To investigate a birefringent slab that is placed in a POM setup, $\widehat{\boldsymbol{M}}$ is added between the two crossed polarizers (Figure 3.14),

$$E(\boldsymbol{z}) = \ \hat{\boldsymbol{p}}(\theta_1 = 0°) \cdot \widehat{\boldsymbol{M}} \cdot \hat{\boldsymbol{p}}_{\boldsymbol{2}}(\theta_2 = 90°) \cdot E_i(z) \tag{3-12}$$

$$= \begin{pmatrix} 1 & 0 \\ 0 & 0 \end{pmatrix} \begin{pmatrix} cos\theta & -sin\theta \\ sin\theta & cos\theta \end{pmatrix} \begin{pmatrix} e^{-i\frac{\Delta\phi}{2}} & 0 \\ 0 & e^{i\frac{\Delta\phi}{2}} \end{pmatrix} \begin{pmatrix} cos\theta & sin\theta \\ -sin\theta & cos\theta \end{pmatrix} \begin{pmatrix} 0 & 0 \\ 0 & 1 \end{pmatrix} \begin{pmatrix} E_{x,i} \\ E_{y,i} \end{pmatrix}$$

$$= \begin{pmatrix} E_y cos\theta sin\theta \left(e^{-i\frac{\phi}{2}} - e^{+i\frac{\phi}{2}}\right) \\ 0 \end{pmatrix} = \begin{pmatrix} -2icos\theta sin\theta sin\left(\frac{\phi}{2}\right) E_{y,i} \\ 0 \end{pmatrix}$$

$$= \begin{pmatrix} sin2\theta sin\left(\frac{\phi}{2}\right) E_{y,i} \\ 0 \end{pmatrix}$$

In POM the observable quantity is the transmitted intensity (I_t) found by taking moduli squared of E_t,

$$I_t = |E_x|^2 + |E_y|^2 = sin^2 2\theta sin^2\left(\frac{\phi}{2}\right) E_{y,i} \tag{3-13}$$

Meaning I_t is at a maximum when θ=45° irrespective of λ. This is known as the law of Malus. The value ϕ also determines I_t. Combining equations (3-11) and (3-13), maximum values I_t will be achieved when,

$$\phi = \left(m + \frac{1}{2}\right)\pi = \frac{2\pi\left(n_{||} - n_{\perp}\right)d}{\lambda} \tag{3-14}$$

and minimum when,

$$\phi = m\pi = \frac{2\pi\left(n_{||} - n_{\perp}\right)d}{\lambda} \tag{3-15}$$

where m is an integer. If a white light source is used, different colours will be observed as different λ go through minima and maxima.

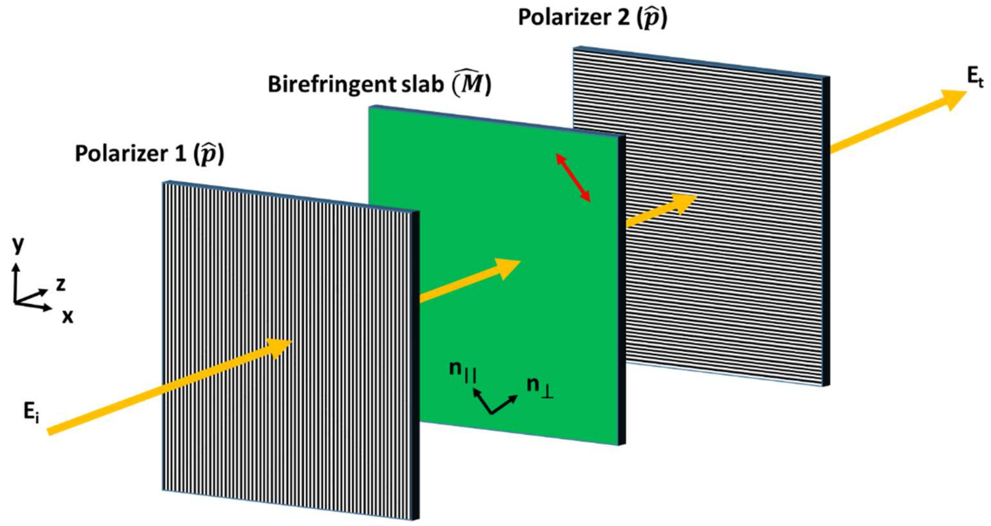

Figure 3.14. Diagram demonstrating the operating principle of POM. Here polarized light is passed through a Birefringent slab($\widehat{\boldsymbol{M}}$), placed between two polarizers oriented at 90° to one another. The birefringent slab is oriented with optic axis at θ=45°, allowing maximum transmission.

3.2.1.c *The Effect of Director Reorientation*

To this point, a birefringent plate with a single unvarying optic axis in the *x, y* plane has been described. For a calamitic liquid crystal, this is representative of perfect PH alignment in a sample with zero pretilt. Here we briefly mention the effect of director reorientation within the *x,y* plane and into the z direction. Firstly, the changes due to the variation in the *x,y* plane can be quantified using the Law of Malus, here deviation from θ=45° simply reduces intensity until eventually black at 0° or 90°, while the colour remains constant. Meanwhile, if the optic axis tilts into the *z*-direction it lowers the birefringence experienced by transiting light. This effective birefringence (Δn_{eff}) at a tilt (ψ) can be written as [204],

$$\Delta n_{eff}\,(\psi) = n_{eff}(\psi) - n_{\perp} = \frac{n_{||}n_{\perp}}{\sqrt{n_{||}^{2}\sin^{2}(\psi) + n_{\perp}^{2}\sin^{2}(\psi)}} - n_{\perp}, \tag{3-16}$$

This changes the colour observed as different wavelengths go through minima and maxima.

3.2.1.d *Thickness Measurements*

LC device spacing was measured prior to filling using a reflection microscope connected to UV-VIS spectrometer. Here, a white light source is used, and the light reflected from the cell normalized to a black background and a mirror .With the cell in place, some light reflects off the interface where light passes from the top substrate into air, then again when it passes from air into the bottom substrate. For specific, λ, this light will constructively interfere if,

$$n\lambda\ = 2d \tag{3-17}$$

and destructively interfere if,

$$\left(n + \frac{1}{2}\right)\lambda\ = 2d \tag{3-18}$$

where *n* is an integer. The reflected intensity as a function of λ was viewed using the spectrometer, where a series of peaks and troughs are seen as these subsequent constructive and destructive processes occur. The distance between the peaks was then used to find the device spacing (*d*), as for two neighbouring peaks (located at λ_1 and λ_2) are related to *d* by ,

$$d = \frac{\lambda_1\lambda_2}{2(\lambda_1 - \lambda_2)}. \tag{3-19}$$

To increase accuracy, peaks across the entire wavelength range of the spectrometer can be used. Here if *m* peaks are used, (3-19) is modified as,

$$d = \frac{\lambda_1 \lambda_m m}{2(\lambda_1 - \lambda_m)}. \tag{3-20}$$

In this work, the cells were measured in five locations (in the middle and four corners), where the *d* value was their average, while the uncertainty (Δd) was their range.

3.2.2 Dielectric Spectroscopy

3.2.2.a *Fundamentals of Dielectric Spectroscopy*

Dielectric spectroscopy is a tool widely used in the analysis of liquid crystals and soft matter systems more generally[85,86]. Fundamentally, when undertaking a dielectric measurement, a sinusoidal voltage ($\tilde{V}$) with angular frequency (ω) is applied across a test cell and a measurement of current ($\tilde{I}$) made. Here if $\tilde{V}$ is written,

$$\tilde{V}(\omega) = |V| e^{i\omega t} \tag{3-21}$$

$\tilde{I}$ lags behind by a impedance phase angle (φ),

$$\tilde{I}(\omega) = |I| e^{i\omega t - \varphi}. \tag{3-22}$$

In an impedance analyser or dielectric bridge, some $\tilde{V}$ is applied between electrodes and the magnitude and phase of $\tilde{I}$ measured. From these values, a number of parameters can be calculated. Firstly, the total complex impedance (Z^*) of the system,

$$Z^* = \frac{\tilde{V}}{\tilde{I}} = \frac{|V|}{|I|} e^{i\varphi} = |Z| e^{i\varphi} = R + iX. \tag{3-23}$$

φ may be written in terms of the real and imaginary parts of impedance (resistance, R, and reactance, X, respectively),

$$tan\varphi = \frac{X}{R}. \tag{3-24}$$

In LC science, it is usual to use dielectric spectroscopy to measure device capacitance (C^*), conductance (G) and capacitance phase angle (δ). Here [205],

$$C^* = \frac{1}{i\omega Z^*}. \tag{3-25}$$

where,

$$C^* = C' + iC'' = |C| e^{i\delta}, \tag{3-26}$$

Thus,

$$tan\delta = \frac{C''}{C'} = \frac{1}{tan\varphi}. \tag{3-27}$$

Meanwhile,

$$G = \frac{1}{R}. \tag{3-28}$$

3.2.2.b *Practical Dielectric Spectroscopy of Liquid Crystal Devices*

In this project dielectric measurements were undertaken to characterize both electronic and viscoelastic properties of materials. Here, LC sandwich devices (of either GR or square electrode type) were connected to a dielectric bridge (Agilent E4980A LCR meter), which allowed the applied frequency to be varied from 20Hz to 2MHz and voltage from 0-20V. The device temperature was controlled with a hotstage (Linkam TMS 93/95). This set up was mounted onto a microscope allowing the sample to be viewed while dielectric measurement was completed.

The values *C'* and *G* were converted into permittivity (ε' or ε) and conductivity (σ) using standard equations for a parallel plate device,

$$\varepsilon = \frac{C'}{C_0} \tag{3-29}$$

and

$$\sigma = \frac{Gd}{A}, \tag{3-30}$$

respectively. Here C_0, d and A are the empty cell capacitance, device spacing and electrode area respectively.

The discussion below demonstrates the data analysis procedure done for a typical NLC (5CB) in a square AWAT device. ε and σ of 5CB as functions of frequency for selected temperature are shown in Figure 3.15a-b. Values corresponding to the plateau values (ε_p and σ_p) were taken, where for this example any frequency in the region 500Hz-2MHz would be appropriate for ε, while 20Hz-10kHz would be appropriate for σ.

As discussed in Chapter 2, the LC director undergoes a Freedericz transition when sufficient voltage is applied across it[32]. Example plots of the real part of ε^* (ε) are shown in Figure 3.15c, where the frequency is chosen such that it is far from any relaxation processes. The intercept of $\varepsilon(1/V)$ gives a value for $\varepsilon(V \rightarrow \infty)$, which for 5CB in a planar cell is $\varepsilon_{||}$. The values $\varepsilon_{\perp}$ and $\varepsilon_{||}$ are compared to $\varepsilon(V=0.05V)$ and $\varepsilon(V=20V)$ in Figure 3.15e.

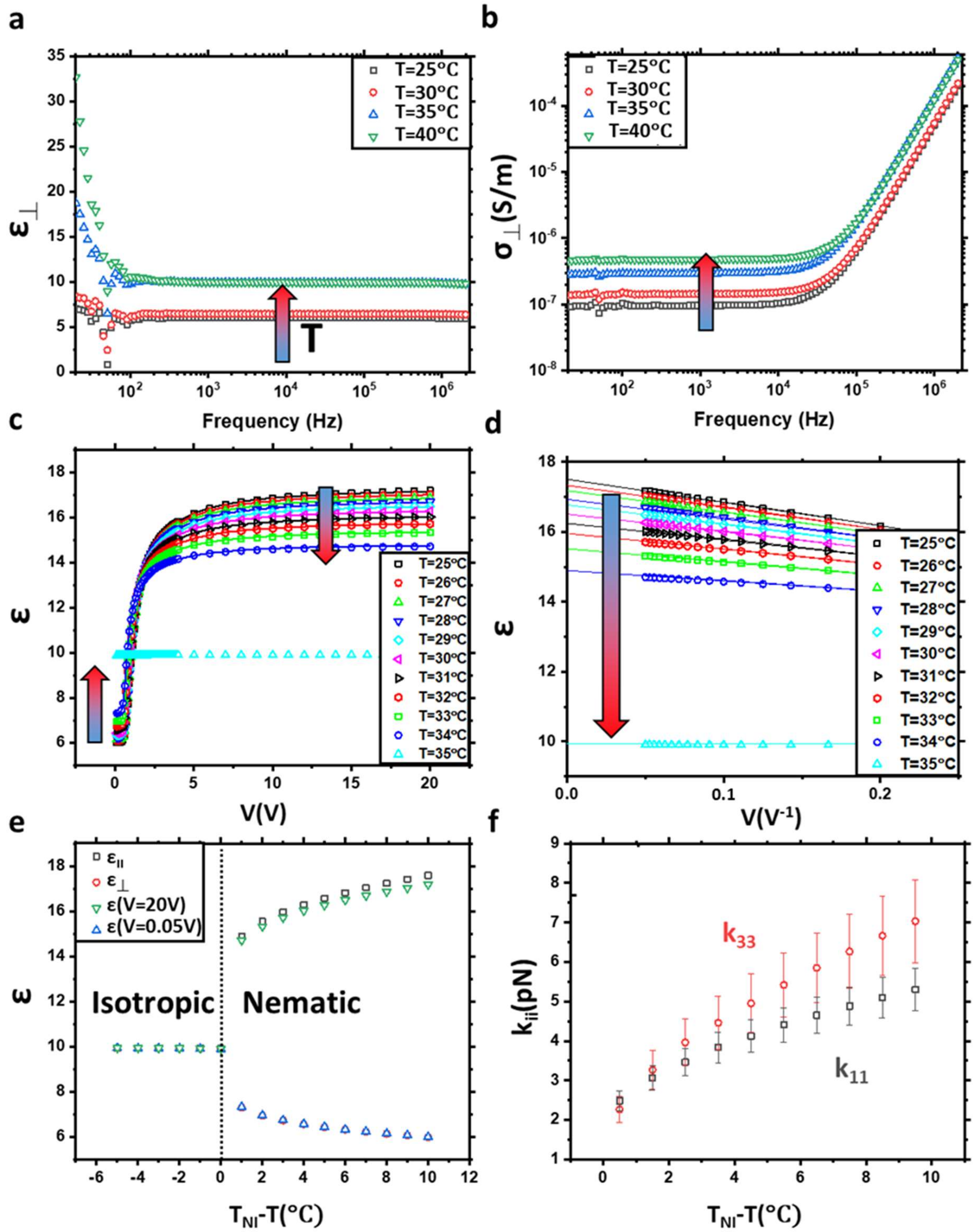

Figure 3.15. Dielectric spectoscopy results from 5CB contained in a planar aligned cell. (a) and (b), show frequency sweeps of ε' and σ. At frequencies lower than 100Hz an increase in ε' is seen which is associated with electrode polarization. At frequencies higher than 10KHz σ starts to increase due to the imperfect ITO electrodes. An arrow indicating increasing temperature is included. (c) The 5CB undergoing a Freedericksz transition. As voltage is increased the director reorients to maximally resist the field. (d) ε as a function of 1/V where the intercept approximately equals $\varepsilon_{||}$. *(e) The values of ε at V=0.05V and V=20V, in addition to the fitted values of* $\varepsilon_{\perp}$ *and* $\varepsilon_{||}$ *(c). (f) Shows the values of the splay (*k_{11}*) and bend (*k_{33}*) elastic constants obtained by fitting (c).*

The curves of *ε(V)* shown in Figure 3.15c were fitted to obtain elastic constants (k_{ii}). This was done using a programme written in Matlab by Brimicombe[206] to fit the equations given in section 2.4.4. for $\Delta\varepsilon>0$ materials in planar cells[100,101]. For a certain *ε(V)* curve the programme aims to put values $\varepsilon_{||}$, $\varepsilon_{\perp}$, k_{11}, k_{33} and θ_p were outputted. Here, as approximate values of $\varepsilon_{||}$ and $\varepsilon_{\perp}$ are already determined from Figure 3.15c-d, the ranges these values can adopt in fitting are set to these values ±5%, while pretilt is permitted to be in the range given by the manufacturer data sheet [73] ±2°. Fittings from this programme are shown in Figure 3.15c, while the outputted elastic constant values k_{11} and k_{33} are shown in Figure 3.15f. Comparing with literature, these values are in reasonable agreement with the error in k_{ii} taken to be around 20% [207], which is likely caused by the square electrodes. Slight modifications were made to the programme for homeotropic cells filled with $\Delta\varepsilon<0$, where the values of k_{11} and k_{33} are switched, as are $\varepsilon_{||}$ and $\varepsilon_{\perp}$[208].

3.2.3 Diffraction Analysis

Diffraction analysis was used to investigate the performance of hydrodynamic Diffractive Optical Elements (DOEs) . The quantities of interest were efficiencies (η_m) and steering angles (θ_m). A diagram of the experimental set up used is shown in Figure 3.16. A polarized laser beam is passed through the device normal to the enclosing glass surfaces, which is then diffracted onto a screen at distance (*D*). Here *D* should be as large as practically possible to ensure conditions of Fraunhofer diffraction are valid [175].

For the set up shown in Figure 3.16 diffraction angles were measured using trigonometry,

$$\tan\theta_m = \frac{x_m}{D}. \tag{3-31}$$

By standard error propagation, the error in θ_m ($\Delta\theta_m$) is calculated to be,

$$\Delta\theta = \frac{\delta\theta}{\delta x_m}\Delta x_m = \frac{\delta\left(tan^{-1}\left(\frac{x_m}{D}\right)\right)}{\delta X}\Delta x_m = \frac{D}{D^2 + {x_m}^2}\Delta x_m. \tag{3-32}$$

Meaning for a diffraction spot at *D*=50cm and x_m=5cm, θ_m=5.7° and $\Delta\theta_m$=0.1° when measured to mm precision.

Measurements of intensity were made either using a single pixel photodiode from Thorlabs (PDA8A/M) or a beam profiler (Thorlabs, BC106N-VIS). Further details will be given section 5.2.6.

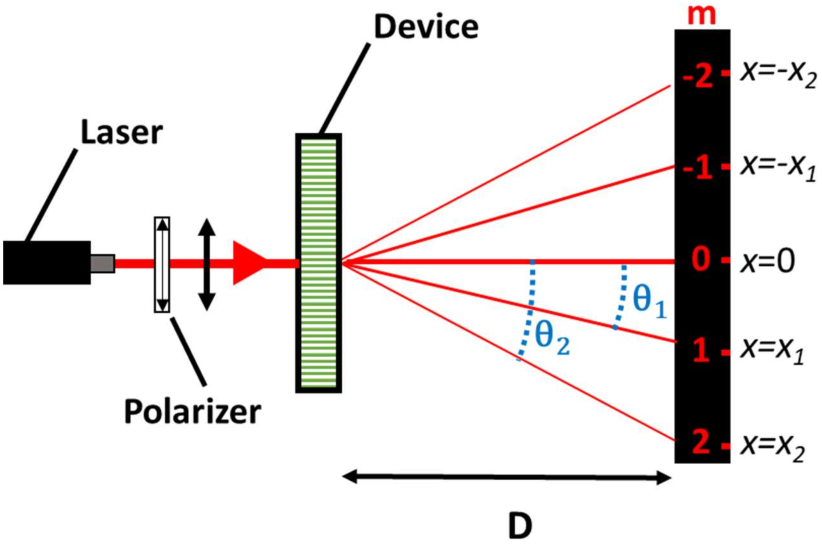

Figure 3.16. Schematic of diffraction experiment. Here the laser passes from the source through a polarizer to ensure desired polarization and through the device. The diffraction pattern is then viewable at a distance D.

3.3 Summary

This chapter introduced some of the general experimental techniques including cell fabrication, optical microscopy, photolithography and dielectric spectroscopy utilized throughout this work. More specialized experimental techniques will be presented where appropriate in subsequent chapters.

Chapter 4 Modelling Diffractive Optical Elements

4.1 Introduction

4.1.1 Chapter Overview and Motivation

As discussed in section 3.2.1, the birefringence, Δn of NLCs means the optical phase difference (ϕ) experienced by transmitted light is dependent upon the relative orientation of the director (***n***) and the light's electric field polarization vector (***E***)[209]. For light of a certain optical polarization, passing through a NLC slab of thickness, *d* in the *z* direction, the $\phi(x,y)$ experienced by light can be written as [203,210],

$$\phi(x,y) = \frac{2\pi}{\lambda}\int_0^d (n_{\text{eff}}(x,y,z) - n_{\perp})dz. \tag{4-1}$$

Here λ is the wavelength of light, $n_{\perp}$ is the refractive index perpendicular to the director and n_{eff} is the effective refractive index. If ***n*** is varying zenithally (Figure 4.1a) the value n_{eff} can be written as[5],

$$n_{\text{eff}}(z) = \frac{n_{||}n_{\perp}}{\sqrt{n_{||}^2 sin^2\psi(z) + n_{\perp}^2 cos^2\psi(z)}}. \tag{4-2}$$

while for radial variations (Figure 4.1b),

$$n_{\text{eff}}(z) = n_{||}^2 sin^2\Omega(z) + n_{\perp}^2 cos^2\Omega(z). \tag{4-3}$$

Here, $n_{||}$ is the refractive index parallel to ***n***, while ψ and Ω are angles shown in Figure 4.1. These optical properties, coupled with ***n*** being controllable with a variety of stimuli allows NLCs to be used to create wide variety switchable diffractive optical elements (DOEs) using both zenithal and radial director control [28,29,33,111,115,136,180,211].

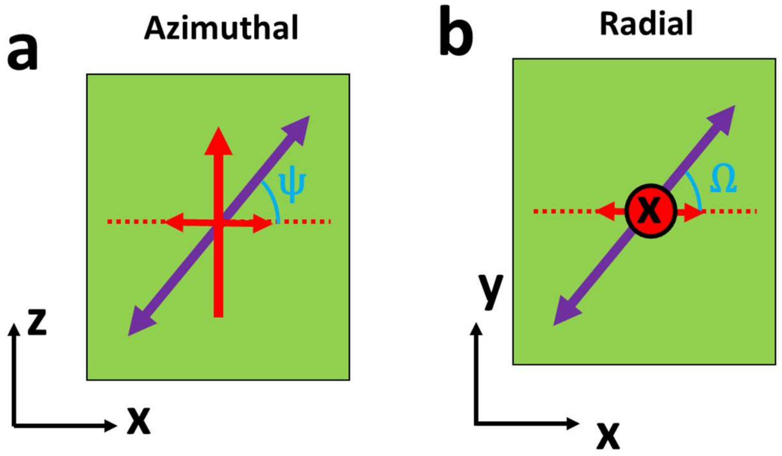

Figure 4.1. Example of director (purple) and light (red, crossbar indicates polarization) geometries. (a) Azimuthal rotation (x-polarized light with the director in the x,z plane). (b) Radial rotation (x-polarised light with the director in the x,y plane).

When creating NLC DOEs, controlling the $\phi(x,y)$ profile arbitrarily across the entire device is a challenging goal, which has been worked towards with a variety of methodologies for many decades[28,29,33,111,115,136,180,211]. Often, different methods employed result in different $\phi(x,y)$ profiles, which are not of a standard type (sinusoidal, square, blazed etc). This means that in order to compare promising avenues, the ability to predict the resultant diffraction efficiencies of any $\phi(x,y)$ structure is highly desirable. This is due to it enabling theoretical limits of imperfect DOE to be estimated before fabrication. This is highly relevant to any industries interested in creating DOEs, including: space[185], virtual/augmented reality [212,213] and smart window[214]. This calculation of theoretical efficiencies of imperfect DOEs will be the central focus of this chapter.

The chapter is structured as follows. Firstly, the background concepts and equations for scalar diffraction theory are introduced. Here, Fraunhofer (far-field) diffraction is assumed as it allows the use of Fourier transforms to calculate resulting diffraction patterns. This is followed by an overview of the modelling programme and the way it operates. To validate the methods and programme, the diffraction spectra of several standard gratings are modelled, where excellent agreement with analytical solutions is obtained. Finally, the techniques are applied to three optical systems relevant to current research in NLC DOEs. Of these more novel systems, the first system "Stepwise Phase Structures in Nematic Liquid Crystals" had previously been investigated by Niv et al [215], however the latter two are not readily available in literature.

4.1.2 Scalar Diffraction Theory

4.1.2.a *Diffraction Angles*

This section starts by introducing the necessary optics of scalar diffraction theory, where the standard text by Goodman has been followed [174,175]. The gratings being considered in this work are optically thin and so of the Raman-Nath (RN) type [173] (see section 2.5.3), meaning the diffraction angles are described using the grating equation

$$m\lambda = \Lambda_{gr} sin\theta_m = \frac{2\pi}{q_{gr}} sin\theta_m, \tag{4-4}$$

where m is the order number, Λ_{gr} is the grating period, q_{gr} is the wavenumber, and θ_m is the diffraction angle.

4.1.2.b *Diffraction Order Intensities*

The intensities of diffractive orders *(I_m),* depend both upon the shape of ϕ (f_{gr}) and its maximum value (ϕ_{max}). For calculation I_m, scalar diffraction theory may be used. Here, the goal is to form an optical field (U_t) on a surface $\Sigma'(x',y')$, and predict the resulting optical field (U_{diff}) on another parallel surface $\Sigma(x,y)$ (separated by distance z, see Figure 4.2). These optical fields (U) are related to the measurable optical intensity (I), by

$$I = |U|^2. \tag{4-5}$$

From an experimental perspective, U_t represents the wave fronts of light having passed through a RN grating. Here, if the optical field before the grating is U_i, U_t may be written [174]

$$U_t(x',y') = t_{gr}(x',y') \cdot U_i(x',y'), \tag{4-6}$$

where t_{gr} is the optical transmittance function of the grating that manipulates U_i in some way.

For a specific U_t, U_{diff} may be calculated (assuming Fraunhofer diffraction) using[174,175]

$$\begin{aligned} U_{diff}(x,y) &= \frac{e^{ikz}e^{\frac{ik}{2z}(x^2+y^2)}}{i\lambda z} \int_{-\infty}^{\infty} U_t(x',y')e^{\left[-i\frac{2\pi}{\lambda z}(xx'+yy')\right]} dx'dy' \\ &= \frac{e^{ikz}e^{\frac{ik}{2z}(x^2+y^2)}}{i\lambda z} \mathcal{F}\{U_t(x',y')\}, \end{aligned} \tag{4-7}$$

where $\mathcal{F}$ represents the Fourier transform operator. A full derivation of (4-7) can be found in Goodman[174,175].

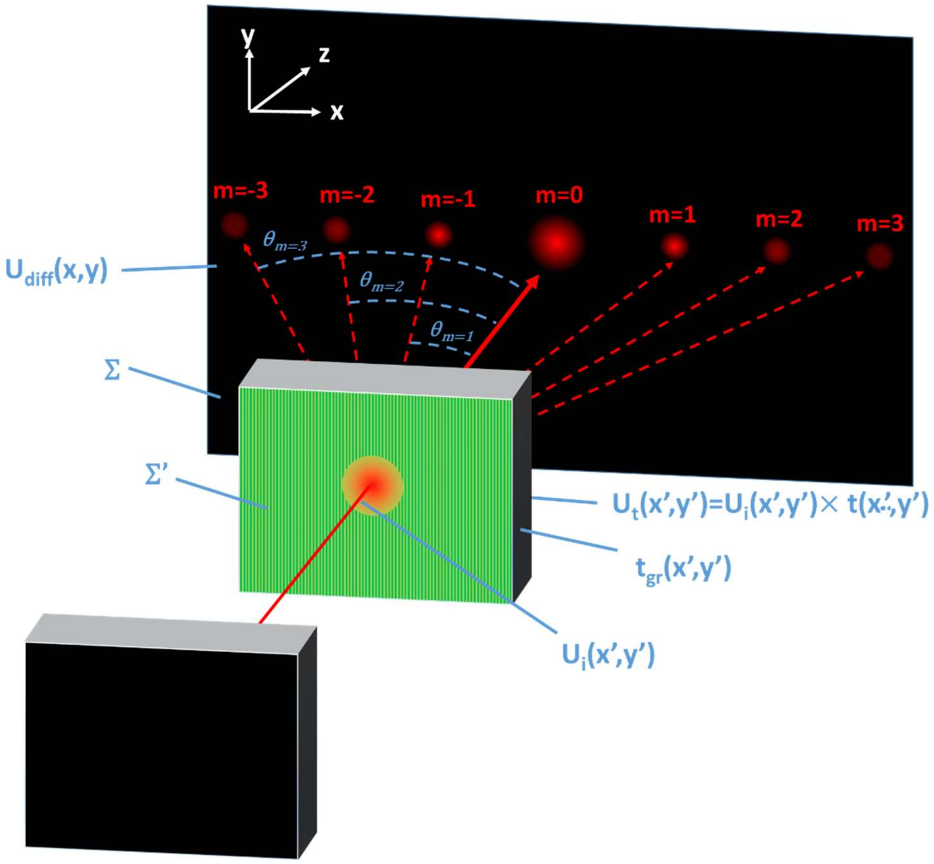

Figure 4.2. Image illustrating Raman-Nath diffraction where parameters U_i, t_{gr}, U_t, θ_m, U_{diff}, Σ and Σ' are shown.

The diffraction pattern from any RN grating in the Fraunhofer regime may be predicted for some U_t by solving equation (4-7). In equation (4-6), U_t is written as a combination of two components, where the input optical field (U_i) will usually be simple (being a laser beam with either a Gaussian or unit amplitude), while the grating's manipulation (t_{gr}) is complicated, but periodic. To calculate U_{diff}, t_{gr} may be written [175]

$$t_{gr} = |\mathrm{t}|e^{i\phi}, \tag{4-8}$$

where values of $|t|$ smaller than unity indicate losses in absolute transmitted optical intensity (amplitude modulation), while changes in ϕ indicate changes of relative optical phase (phase modulation). Thus, the t_{gr} for amplitude-only gratings (t_A) may be written

$$t_A(x',y') = \left(1 - \alpha_{max} \cdot f_{gr}(x',y')\right), \tag{4-9}$$

while for phase-only modulation (t_ϕ),

$$t_\phi(x',y') = e^{i\frac{\phi_{max}}{2}\cdot f_{gr}(x',y')}. \tag{4-10}$$

Here, $f_{gr}(x',y')$ is a function describing the 'shape' of the grating (e.g. sine, square, sawtooth etc) and is a normalised function (between zero and unity) with period Λ_{gr}. Meanwhile, α_{max} and ϕ_{max} are the maximum amplitude and phase modulation of the gratings, respectively. Plots of some examples of f_{gr} for several periodic 1-D diffraction gratings are shown in Figure 4.3. In this work, due to the nature of optical modulation in NLCs, the focus will be on phase gratings.

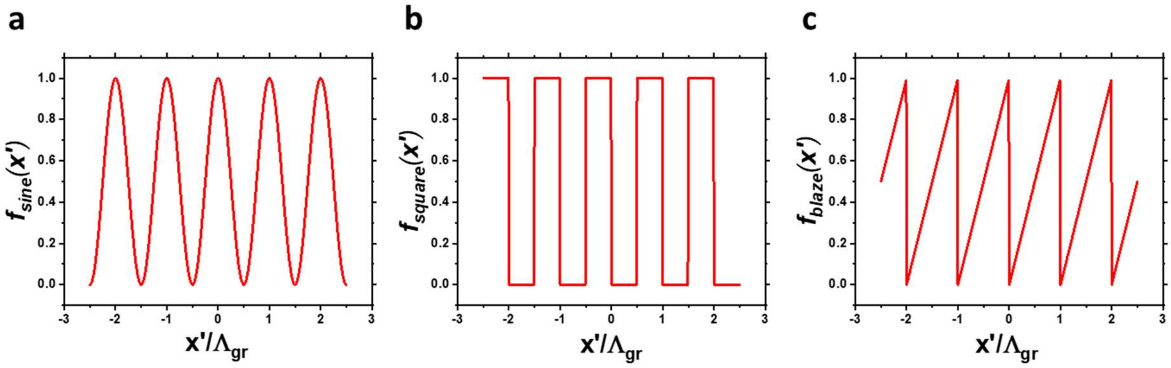

Figure 4.3. Several periods of grating functions f_{gr} which are put into equations (4-9) and (4-10) to create transmittance functions of the amplitude and phase type respectively. (a-c) Sinusoidal, square and blazed gratings, respectively.

For simple t_{gr} gratings (sinusoidal, square etc) equation (4-7) may be solved analytically to obtain expressions for U_{diff}. However, for more complex t_{gr}, the expressions become very complicated. In these cases, equation (4-7) must be solved computationally, which is the approach taken in this work.

Whether solved analytically or computationally, for any periodic t_{gr}, the solution to equation (4-7) will have m regions of strong constructive interference. These are diffraction orders, and their locations are described by the grating equation (equation (4-4)). Their intensities (I_m) can be found by integrating the area under the intensity peaks located at these orders

$$I_m = \iint_{peak} I_{diff}\,dxdy. \tag{4-11}$$

where,

$$I_{diff} = |U_{diff}|^2. \tag{4-12}$$

The values I_m can then be used to measure the absolute (η_m) and relative (ξ_m) efficiencies of the diffraction gratings[174,175],

$$\eta_m = \frac{I_m}{\sum_m I_m}. \tag{4-13}$$

and

$$\xi_m = \frac{I_m}{I_0} = \frac{\eta_m}{\eta_0}. \tag{4-14}$$

4.2 Methods

To perform numerical calculations, a script was written in Python, which allowed the calculation of U_{diff} for any U_t. The steps involved are illustrated in a flow chart in Figure 4.4. Here, the surface Σ' was defined as a 2-dimensional grid of NxN points from $-L/2$ to $L/2$ with the points evenly distributed. This leads to a number density of points (ρ_N), where

$$\rho_N = \frac{N}{L}. \tag{4-15}$$

Generally, the value ρ_N must be high enough relative to Λ_{gr} to describe the desired f_{gr}. For this purpose, a number of points within a single period (N_Λ) is useful to record, where

$$N_\Lambda = \rho_N \Lambda_{gr}. \tag{4-16}$$

For analysis of gratings, U_i was always chosen to be a unit amplitude Gaussian illumination centred on zero:

$$U_i(x', y') = e^{-\left(\frac{x'^2}{2\sigma^2} + \frac{y'^2}{2\sigma^2}\right)}, \tag{4-17}$$

where σ was chosen to be 0.1mm. The choice of Gaussian illumination was made as it significantly simplifies the results (because the Fourier transform of a Gaussian is also Gaussian).

The functions t_{grat} of the phase gratings were defined using equation (4-10), where f_{gr} was varied to examine gratings of different shape. This allowed U_t to be calculated by multiplying U_i elementwise by the chosen t_{gr}. Once U_t was defined, equation (4-7) was solved for U_{diff}. The Fourier transform was performed using the python function “scipy.fftpack.fft2”, and then shifted to the desired grid using “numpy.fft.fftshift” (Documentation of these specific functions can be found in [216], while general usage of NumPy operation can be found in [217]). I_{diff} was then calculated using equation (4-5).

The individual diffraction orders in I_{diff} were then fitted with 1-D Gaussians

$$I_{diff} = |U_{diff}|^2 = H_{\mathrm{m}} e^{-\frac{(x - x_{\mathrm{m}})^2}{2\sigma_{\mathrm{m}}^2}}, \tag{4-18}$$

where the fitting parameters H_m, x_m and σ_{m} give the peak height, position and width of the peaks, respectively. The values θ_m and I_m could then be calculated using

$$\theta_m = tan^{-1}\frac{x_{\mathrm{m}}}{z}, \tag{4-19}$$

and

$$I_m = \sqrt{2\pi}H_0\sigma_m, \tag{4-20}$$

respectively. Once I_m values were obtained, equation (4-13) was used to find values η_m.

The process outlined gives the general process for a single grating with a certain f_{gr} and ϕ_{max}, therefore in order to obtain trends, the process was repeated varying these parameters. This is shown in Figure 4.4, where the pink arrow indicates repeating the process many times.

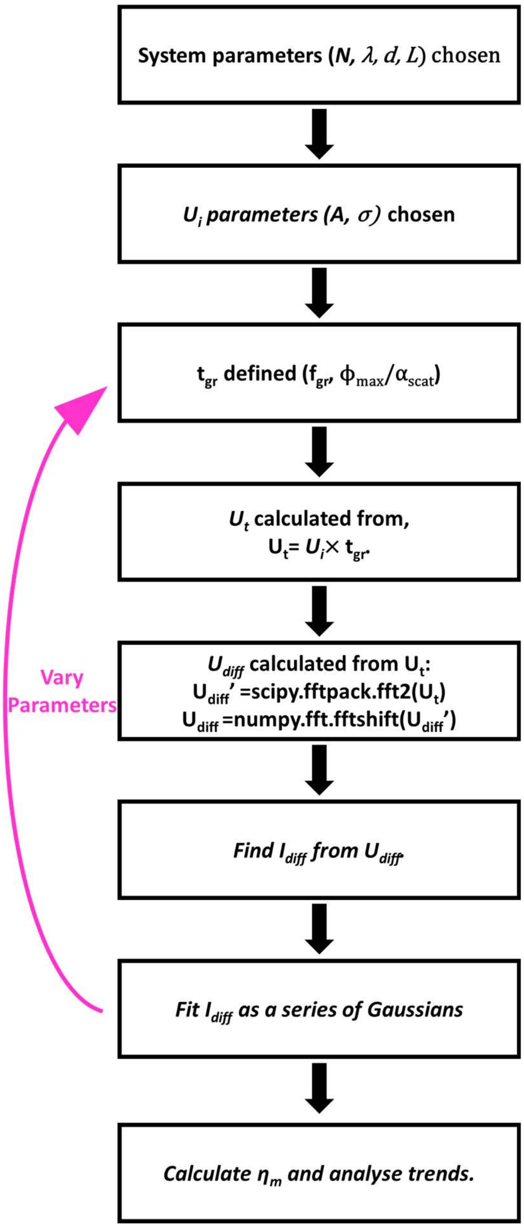

Figure 4.4. Flow chart showing the general operation of the programme designed to use for the analysis of the grating structures in this thesis. The routine can be used to analyse gratings of any standard shape.

4.3 Model Validation with Simple Gratings

4.3.1 Analysis of the Sine Phase Grating

Before applying the programme to more complex diffractive systems and then to liquid crystal device gratings, correct operation was checked by analysing standard gratings, which are well characterised in literature. Here, values of θ_m and η_m were compared to the known analytical solutions.

The first grating discussed is a sinusoidal phase grating. For this, the following system parameters were chosen: N=2000, L=1mm, σ=0.1mm, λ=589nm and z=100mm. The t_{gr} used for this grating ($t_{\phi,sine}$) was defined as,

$$t_{\phi,sine} = e^{i\frac{\phi_{max}}{2}\cdot f_{gr}(x')} = e^{i\frac{\phi_{max}}{2}\sin(q_{gr}x'+\frac{\pi}{2})}. \tag{4-21}$$

Λ_{gr} was chosen to be 20μm giving N_Λ=40.

Figure 4.5a shows an example of the resulting U_t where ϕ_{max}=0.5. Here, the real component, imaginary component and modulus are included. Using equation (4-7), U_{diff} for the sine phase grating is written

$$U_{diff}(x,y) = \frac{e^{\frac{iq_{gr}}{z}(x^2+y^2)}}{i\lambda z}\mathcal{F}\left\{e^{-\left(\frac{x'^2}{2\sigma^2}+\frac{y'^2}{2\sigma^2}\right)} \times e^{i\frac{\phi_{max}}{2}\sin(q_{gr}x'+\frac{\pi}{2})}\right\}, \tag{4-22}$$

which is solved using Python's FFT package.

The U_{diff} and I_{diff} results are plotted against θ_x in Figure 4.5b-c respectively. Here, the $m=\pm1$ orders can be seen on either side of the m=0. These peaks were fitted using equation (4-18) and compared to analytical solutions. Firstly, the period of the grating was varied and the order positions (θ_m) compared to those given by equation (4-4). Results of this are shown in Figure 4.5d, where excellent agreement (within 0.1% error) with the grating equation was found.

The same method was applied for values η_m, where the analytical solution has been be shown to be[175]

$$\eta_m = {J_m}^2\left(\frac{\phi_{max}}{2}\right), \tag{4-23}$$

where J_m is a Bessel function of the first kind of order m. Figure 4.5e-f show results of η_m and ξ_m compared to equation (4-23). Here, the calculated η_m was found to have less than 1% error in the m=0 and m=1 peaks and less than 10% error in m=2-3. These errors are reasonably small for the first two diffractive orders, which are of most interest to this work. They are likely to arise from the finite N_Λ. However, increasing this value rapidly increases the calculation time. In Figure 4.5f, it should be noted that ξ_m may be greater than 100%, this is correct, and simply means that $\eta_m > \eta_0$ which is common for phase only DOEs.

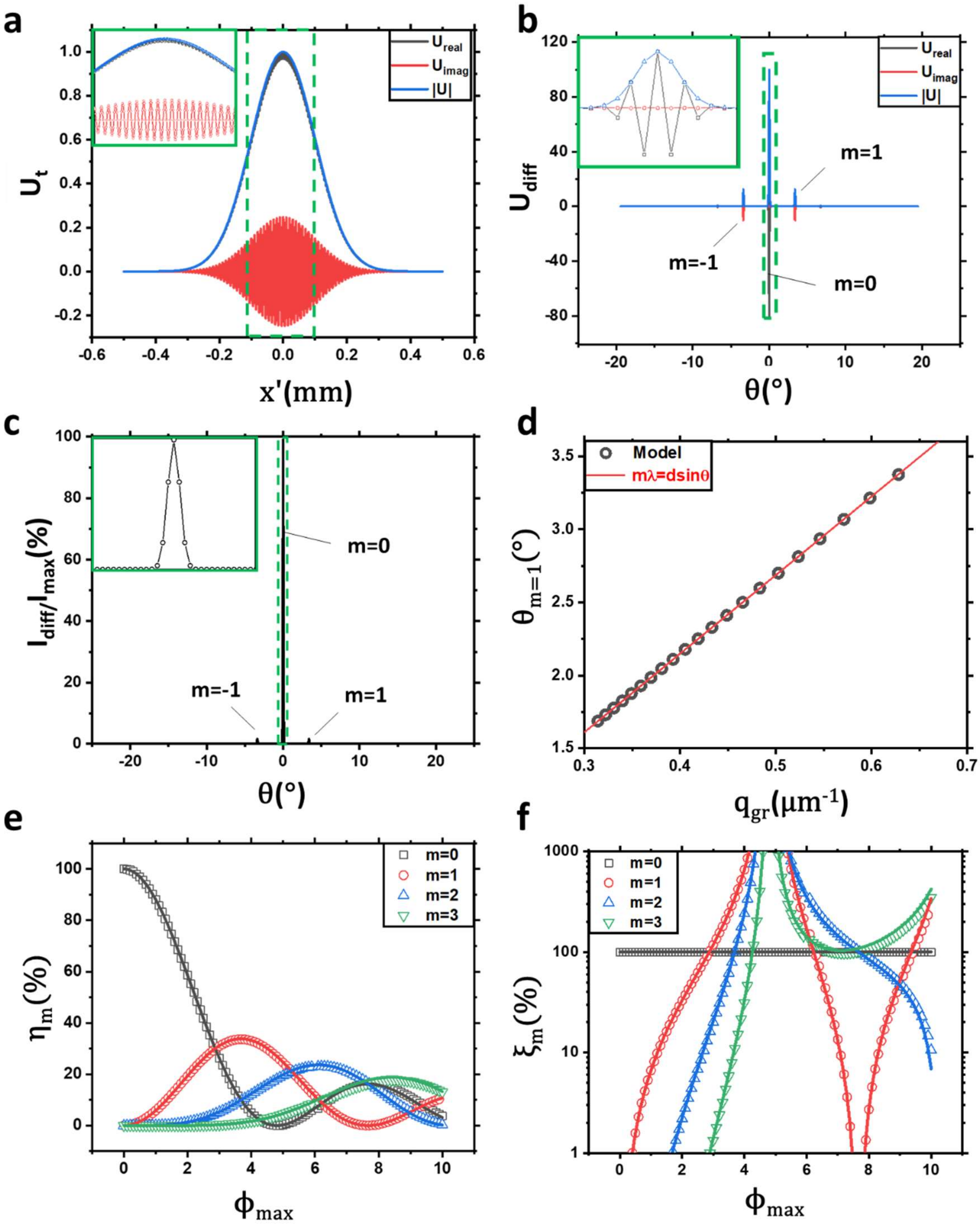

Figure 4.5. Plots related to the calculation of diffraction efficiency for a sinusoidal phase grating. Regions of interest indicated by the dashed green boxes are magnified and plotted in solid green boxes inset top left. (a) Shows the real, imaginary and modulus of U_t. (b) and (c) show U_{diff} and I_{diff} as functions of θ, respectively. Once fitted, (d), (e) and (f) show resulting θ_m, η_m and ξ_m, respectively, where each is compared to the analytical solution (lines).

4.3.2 Other Standard Gratings

The method employed for the sinusoidal grating was extended to other standard grating structures such as square and blazed, using the same system parameters as for the sinusoidal phase grating. Figure 4.6a shows the plot of η_m for a square phase grating, where it is compared to the theoretical [218],

$$\eta_0 = cos^2\left(\frac{\phi_{max}}{2}\right) \tag{4-24}$$

and

$$\eta_m = \frac{4}{\pi^2 m^2} sin^2\left(\frac{\pi m}{2}\right) sin^2\left(\frac{\phi_{max}}{2}\right). \tag{4-25}$$

Here, excellent agreement is observed, where it should be noted equation (4-25) implies all even m have $\eta_m=0$, which was also seen in results.

Similarly, Figure 4.6b shows η_m for a blazed phase grating. Here, due to the asymmetry of the blazed structure, the values η_m for $\pm m$ orders are not equal; this is shown for $m=\pm1$. At $\phi_{max}=2\pi$, $\eta_{m=1}=100\%$; this is a key to many NLC diffractive beam steering devices where practically creating switchable, $\phi_{max}=2\pi$ blazed phase profiles are desirable for efficient wide-angle beam steering [28,29,33,115,136,180,211]. No analytical solution for $\eta_m(\phi_{max})$ in blazed gratings was found in literature to compare to results in Figure 4.6, however, the results appear to agree with calculations recently made by Harvey and Pfisterer in their review of the topic[219].

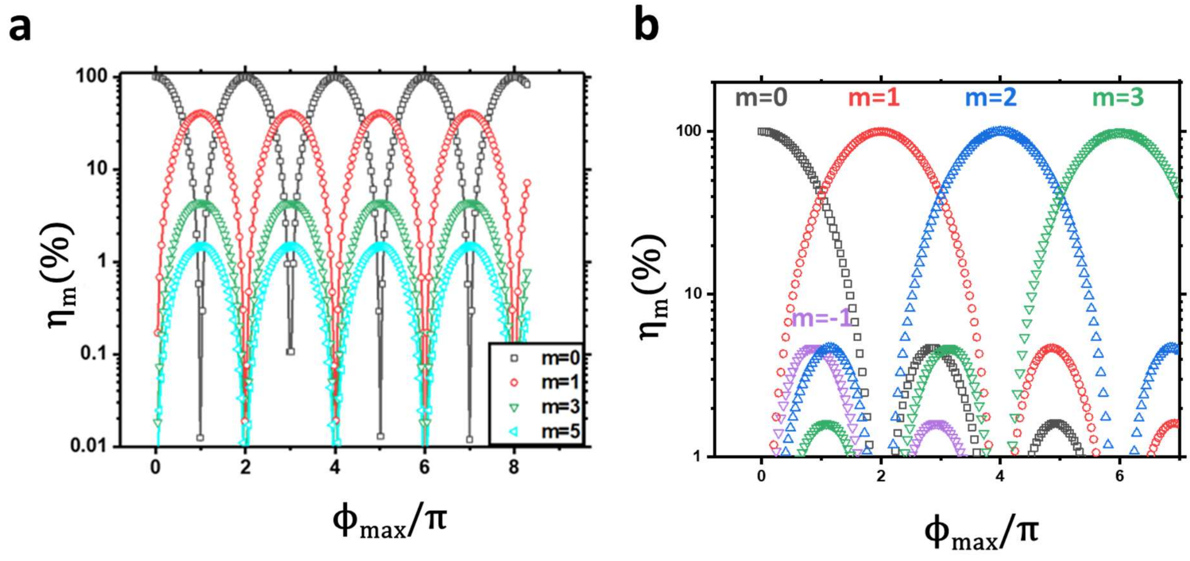

Figure 4.6. Plots of η_m as a function of ϕ in a square (a) and blazed (b) grating. Here in (a), lines are included that plot the analytical solutions for a square phase grating given in equations (4-24) and (4-25).

4.4 Applications of Diffraction Calculations to Liquid Crystal Beam Steering Devices

4.4.1 Introduction

In examining the diffraction from a blazed phase grating in section 4.3.2, their ability to create 100% efficient wide angle beam steering structures has been demonstrated. This leads to them being widely used as beam steering components[219–222], where incorporating LCs to allow for switchable behaviour is a broad field of research[28,29,33,111,115,136,180,211]. Here, although NLCs have excellent switchable behaviour, it is challenging to force them to adopt a perfect blazed grating structure while maintaining the ability to switch. Any imperfections in the blazed structure lead to losses in efficiency, however as the methods of controlling $\boldsymbol{n}$ will usually not lead to a standard ϕ structure, predictions of diffraction efficiencies are often not quoted in the literature. This leads to numerical calculations such as demonstrated in section 4.3 being highly useful in predicting the quantity and nature of these losses, to inform research direction. This will be the focus of the remainder of this chapter, where we will investigate various imperfections which occur in NLC DOEs, explain why they occur and predict losses due to them.

4.4.2 Stepwise Phase Structures in Nematic Liquid Crystals

The first example of an imperfect blazed grating structure is one where ϕ is made up of several digital steps instead of a continuous linear phase ramp. Practically, this optical structure often occurs due to limitations in the practical fabrication of uniform phase ramps. Two examples of where the linear phase ramp becomes digitized in NLC devices are, (1) using digital physical inclusions of different refractive index to encase the NLCs [223] (Figure 4.7a), and (2) using photoalignment to reorient successive patches of NLC alignment to create digital Pancharatnam-Berry structures [180–182,215] (Figure 4.7b).

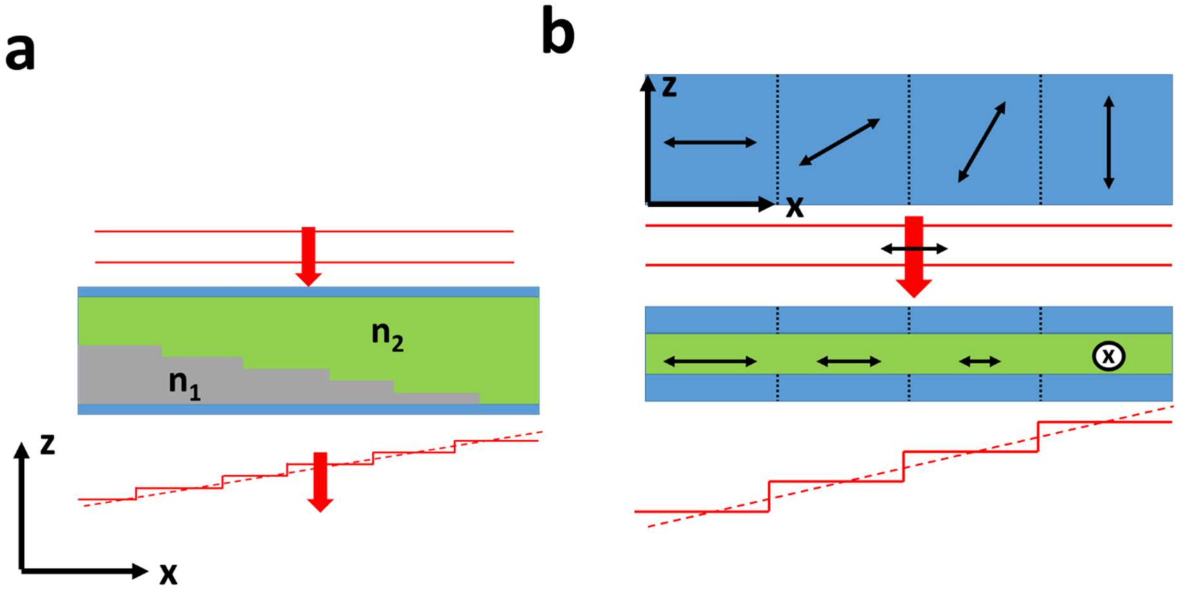

Figure 4.7. How stepwise ϕ profiles can be induced on transient light from several optical components. (a) The effect of digital dielectric structures and (b) a digital director reorientation achieved with techniques such as photoalignment.

The shape of ϕ (f_{gr}) chosen to represent the digital grating is shown in Figure 4.8a, where the blazed grating is approximated by S steps of equal height. This means as S tends to infinity the grating becomes a perfect blazed grating. Here, η_m was found as both S and ϕ_{max} are varied. In 2004, Niv et al. also modelled this system [215], where intuitive increases in $\eta_{m=1}$ towards 100% was seen as S tended to infinity. These results will be compared to those obtained by our calculations, which allows an additional check of calculation accuracy.

The chosen system parameters were: N = 4000, L = 1mm, σ = 0.1mm, λ=589nm, z= 100mm and Λ_{gr}=20µm (giving N_{Λ}=80), and results of the model are shown in Figure 4.8b-d. Here, Figure 4.8b shows the values η_1 for several S as ϕ_{max} is varied from zero to 2π. Here, as expected, the maximum value of η_1 (η_{opt}) increases towards 100% as S increases. Also, the value of ϕ_{max} at which η_{opt} occurs (ϕ_{opt}) increases from ϕ_{opt}= π when S=1 to ϕ_{opt}=2π when S is infinite. This is significant in the effective optical design of digitized diffractive optical components, as it allows the value ϕ_{max} to be tuned in fabrication to ensure highest η_1 for certain S (for example if only 4 steps were practically possible, but ϕ_{max}=2π was used, η_1 would be 70%, while at ϕ_{max}= ϕ_{opt} it would be 85%).

Figure 4.8c-d shows the calculated values of η_{opt} and ϕ_{opt} as functions of S. Here, the error in ϕ_{opt} was taken as half the difference between a value ϕ_{max} and the subsequent value (here $\frac{\pi}{20}$). The error in η_1 was approximated as 1%, as this is the maximum difference seen between the modelled and analytical solutions in section 4.3. In Figure 4.8c, a theoretical plot of ϕ_{opt} against S is shown, which is obtained from:

$$\phi_{opt}(S) = 2\pi\left(1-\frac{1}{n}\right) = 2\pi\left(1-\frac{1}{S+1}\right), \tag{4-26}$$

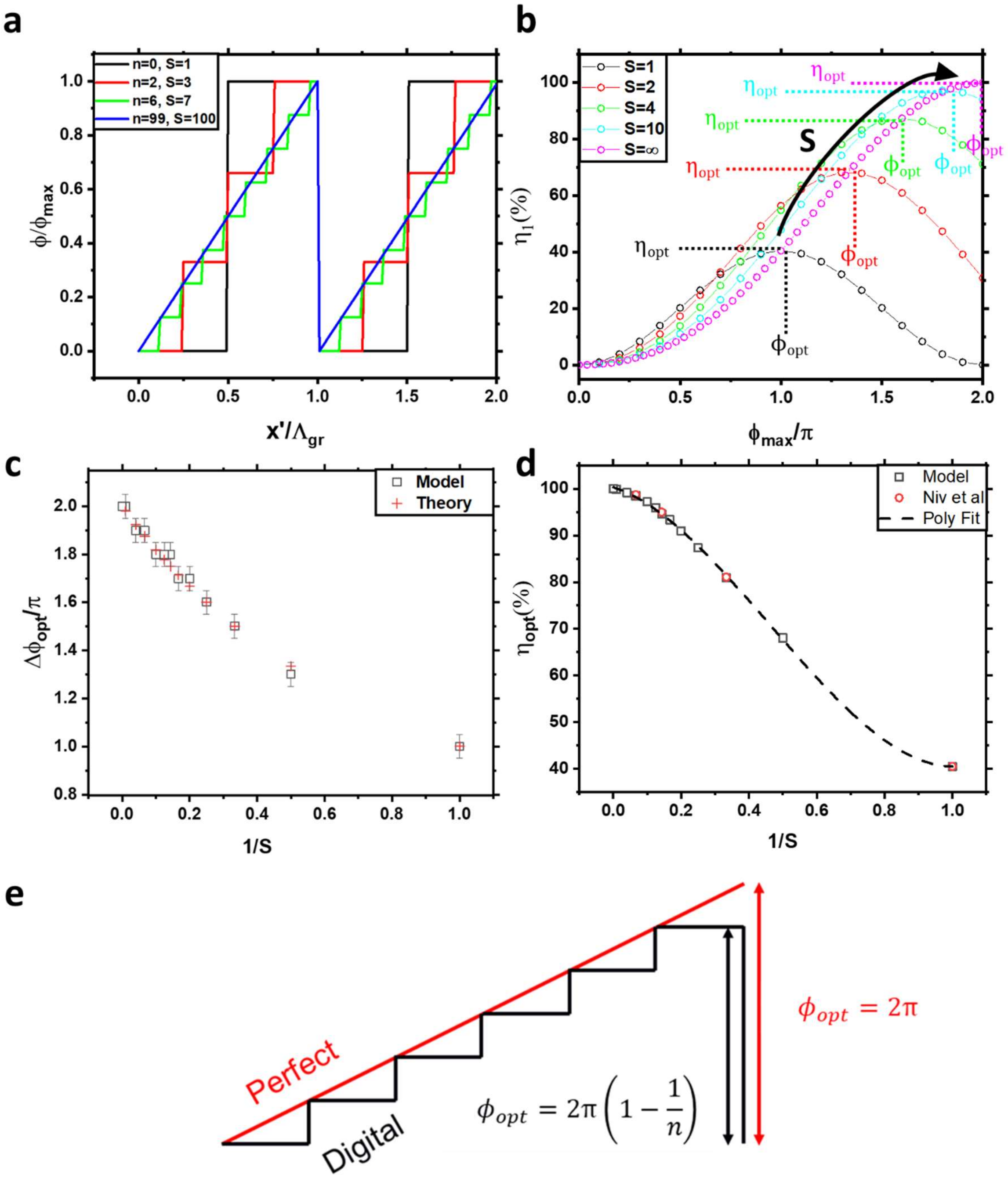

Figure 4.8. The effect of digitizing a blazed grating on resulting diffraction patterns. (a) A blazed gratings $\phi(x)$ split into S individual steps or n levels (not including zero or ϕ_{max}). (b) The efficiency of the m=1 order as ϕ_{max} is increased for several S. η_{opt} and ϕ_{opt} are marked as the maximum values of η_1 and the ϕ_{max} at which they occur. (c) and (d) Show the values η_{opt} and ϕ_{opt} as S is varied, (c) includes equivalent results from Niv et al[215], *where good agreement is found. (d) Includes the fit from 3rd order polynomial fit given in equation (4-27). (e) Illustrates the origin of equation (4-26). The best approximation a digital grating of n levels can make to a blazed grating is shown. To have maximum efficiency (η_{opt}) $\phi < 2\pi$, whereas in a perfect blazed grating $\phi = 2\pi$ would give the highest efficiency.*

here n is the number of individual levels where $\phi/\phi_{max} \neq 0$ or 1 (meaning $n=S$-1, see Figure 4.8a). The reason for the form of equation (4-26) is illustrated in Figure 4.8e, where it is shown that the most accurate approximation of a blazed grating made of n levels, has a ϕ_{max} which is $2\pi/n$ times less than 2π. In Figure 4.8d the results of Niv et al. are also included for comparison[215], which can be seen to be in complete agreement. Here, the behaviour of η_{opt} with S was found to be well described by a 3rd order polynomial fit,

$$\eta_{opt}(S) = k_0 + k_1\left(\frac{1}{S}\right) + k_2\left(\frac{1}{S}\right)^2 + k_3\left(\frac{1}{S}\right)^3, \tag{4-27}$$

where k_0-k_3 were found to be 1.003 ± 0.002, -0.23 ± 0.03, -1.32 ± 0.09 and 0.95 ± 0.07 respectively, by numerical fitting. The 3rd order polynomial was used as significant over-fitting was apparent for 4th order, while 2nd order had significantly higher summed squares.

These results will be most useful to those creating digital blazed grating beam steering components, where the desired grating period (Λ_{gr}) is not far larger than minimum fabrication feature size (w_{fab}). Here, there will be a trade-off between steering angle and efficiency as higher S increases η_1, while smaller Λ_{gr} allows wider steering (equation (4-4)). How this is used will depend on situation and application. For example, if a digital blazed grating is required with θ>11.3° for λ=589nm (Λ_{gr}=3μm), where one fabrication technique offers $w_{fab}=0.2$μm while another has $w_{fab}=0.5$μm, but has some associated advantage (time, cost etc), what will be the loss in efficiency? Here, the maximum S will be 14 and 5 for the 0.2 μm and 0.5 μm methods, respectively. In this case equation (4-27) may be used to find optimum efficiencies for each technique (η_{opt}= 98% and 91%, respectively), while (4-26) will give the ϕ_{max} required to achieve these (1.84π and 1.5π, respectively). Thus, results presented here can not only predict efficiencies but also aid in device fabrication.

4.4.3 Stepwise Phase Structures with Linear Connects

Although the model discussed in section 4.4.2 is a good first approximation of a digital blazed grating, in real NLC diffractive components, it is unlikely to be an accurate description. This is due to the sudden changes in ϕ from step to step, which indicates that the director reorients from one orientation to another within an infinitesimally small width. This does not occur in practice, instead, the director smoothly reorients from one orientation to another. Determining the accurate phase profile of such systems would require significantly more sophisticated modelling than is presented here, as the device spacing, elastic constants, and orientation mechanism would all affect the resulting phase profile.

In this section, the next simplest case is considered to avoid such complexities, where the outgoing phase profile undergoes a linear change between each step, making it discontinuous in gradient only rather than value (see Figure 4.9). This model would be suitable where the method of controlling $\boldsymbol{n}$ is pixelated, but $\boldsymbol{n}$ is allowed to continuously vary from one orientation to the next. For example, in Liquid

Crystal on Silicon devices pixelated electrodes can be used to strongly control ***n*** locally, but it is still free to reorient smoothly between pixels[4,28,136,178,224,225]. Similarly, if a digitally changing alignment layer is used to create the varying ϕ, the director will still smoothly reorient in the bulk[168,180,215,226], somewhat smoothing the shape of f_{gr}.

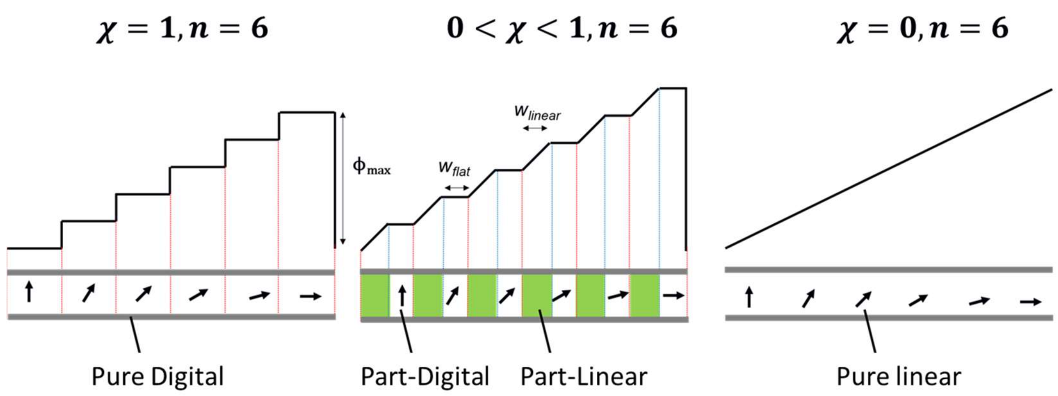

Figure 4.9. The effect of parameter χ on the n=6 digital-linear structure. Left shows a purely digital, right purely linear and the middle an intermediate case.

In this model, the same system parameters as in section 4.4.2 were used. A parameter χ was defined to describe the proportion of each step

$$\chi = \frac{w_{flat}}{w_{linear} + w_{flat}}. \tag{4-28}$$

Here, w_{flat} and w_{linear} are the widths of the flat and linear regions, respectively. These are illustrated in Figure 4.9. From results presented in sections 4.3.2 and 4.4.2, the values of $\eta_{opt}(n)$ and $\phi_{opt}(n)$ in the limits χ=0 and 1 are already known (for χ=0, η_{opt} is always 100% and ϕ_{opt}=2π , for χ=1, η_{opt} and ϕ_{opt} are shown in Figure 4.8).

To examine the intermediate cases, η_{opt} and ϕ_{opt} were found as n and χ were varied. Here, n=6 was examined in detail, with several χ values between zero and one. For n=6, the values of η_{opt} and ϕ_{opt} as χ is varied are shown in Figure 4.10a and b. In Figure 4.10a the value of $\eta_{opt}(\chi)$ was fitted with expression

$$\eta_{opt}(n,\chi) = \eta_{opt}(\chi = 0) - A(n)\chi^2, \tag{4-29}$$

where A is a parameter with a specific value for a certain n. Here a small (~0.3%) discontinuity is found compared to the analytical solution at χ=0. This discontinuity is likely to be caused by finite N_A. The data was renormalized to account for this, so the fitting at χ=0 was 100%. To account for this uncertainty, an error of 0.3% was then used for all points. The new normalized data is shown in Figure 4.10c, where the expression given in (4-29) reduces to

$$\eta_{opt}(n,\chi) = 1 - A(n)\chi^2. \tag{4-30}$$

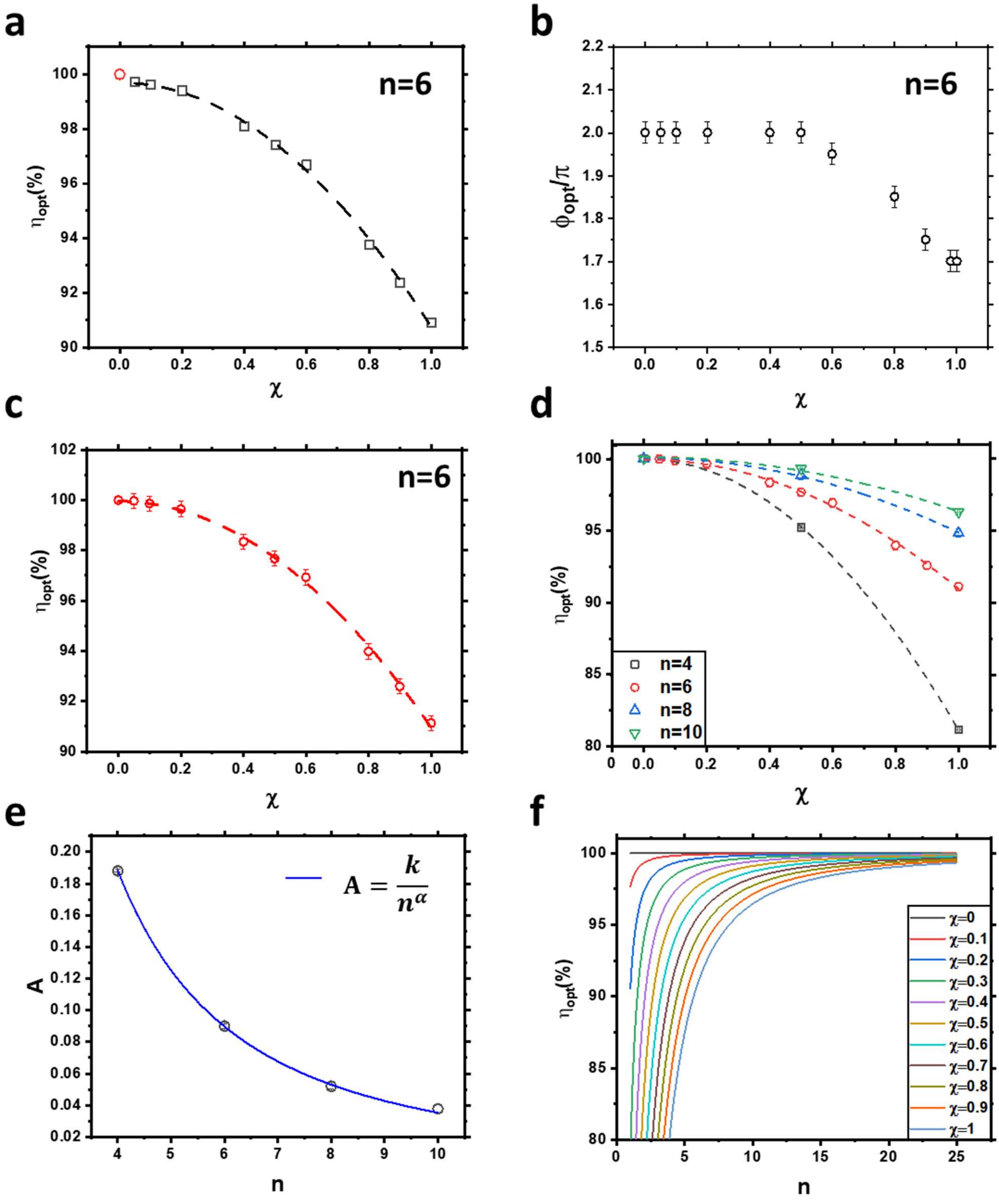

Figure 4.10. Plots of efficiency of the linear-parted staircase. (a) The initial output of η_{opt} when n=6 as χ is varied (black squares). This is compared to the analytical solution (red circle). (b) The value ϕ_{opt} as χ is varied. (c) η_{opt} as χ is varied, where the values shown in (a) have been renormalized so the fit of η_{opt}=100% at χ=0. (d) Data from other n (4,8 and 10) in addition to n=6. (e) Shows A(n) where equation (4-31) was used to fit the data. (f) Shows equation (4-34) plotted out to give $\eta_{opt}(\chi, n)$.

Figure 4.10d shows the data obtained for other n in addition to n=6 with fittings using equation (4-30). From these fits, values of $A(n)$ were obtained as 0.1885 ±0.0005, 0.0906 ± 0.0009, 0.051 ± 0.001 and 0.036 ± 0.002 for n=4, 6, 8 and 10, respectively. The errors were taken from numerical fitting, which is likely to overestimate the level of confidence. These are plotted in Figure 4.10e, where several fitting functions were used to attempt to describe the data, and the best found to be:

$$A(n) = \frac{k}{n^{\alpha}}, \tag{4-31}$$

where k and α are constants found to be 2.37±0.07 and 1.83±0.02, respectively. Again, errors are taken from numerical fitting. It should be noted this function also describes the results given in section 4.4.2. However, as there are comparatively fewer n values used to fit the data, equation (4-31) was considered more appropriate here, as equation (4-27) has a higher number of free parameters, so is likely more prone to overfitting. Combining equations (4-30) and (4-31), the following empirical description of η_{opt} was reached,

$$\eta_{opt}(n, \chi) = 1 - \frac{k\chi^2}{n^{\alpha}}. \tag{4-32}$$

Figure 4.10f shows equation (4-32) plotted for several n. This further enables design of many phase-only diffractive elements where trade-offs between creating linear and digital regions need to be assessed quantitatively. In using equation (4-32), the expression is less accurate for very inefficient systems (for example, if n=1 and χ=1 η_{opt} is negative, which is not physical). This is due to the least efficient data point contributing to the system being a n=4 χ=1 which has η_{opt}>80%. For this reason, (4-32) should only be used when η_{opt}>80% (whenever n>4 or χ<0.3).

These results indicate that the linear regions between the digital steps continuously increase the efficiency between the all-digital and all-linear cases. The trend is non-linear (being fit well by a square relation). In principle, this elevates the potential of NLC materials for beamsteering applications, due to their natural tendency to continuously vary orientation, so that they adopt more efficient phase delays than for example a digitally rotating solid uniaxial crystal.

4.4.4 Smoothed Phase Gratings

The final system examined is a smoothed blazed grating structure. Here, the sharp features seen in previous sections are smoothed. This smoothing often occurs within many NLC DOEs due to the high elastic energy cost of the director undergoing sharp reorientations. Therefore, such smoothed structures are relevant for diffractive LCOS devices based electrode modulation[4,28,136,178,224]. Similarly, the smoothed structures are relevant in Zenithal Bistable Devices (ZBD), where a smoothed blazed grating shape is found to help achieve bi-stability[59,227–229], meaning this system may be highly relevant for understanding bi-stable beam steering components[230].

To examine the effect of smoothing, firstly a suitable f_{gr} is required. Here, the function

$$\frac{\phi(x')}{\phi_{max}} = \kappa(\beta)\frac{1+\tanh(2\beta x')-2x'}{2}, \tag{4-33}$$

within limits -0.5 and 0.5 is used to describe a single period, where $\kappa(\beta)$ is a coefficient that normalizes the rest of the function between the limits zero and unity. $\phi(x')/\phi_{max}$ is plotted for several β within these limits in Figure 4.11a. Equation (4-33), approaches a perfect blazed grating as β tends to infinity, meanwhile when β is some finite value, it represents a more smoothed optical structure. The function can also be seen to be approximately periodic, where

$$\frac{\phi(x'=0.5)-\phi(x'=-0.5)}{\phi(x'=0.5)} \times 100\% < 0.1\%, \tag{4-34}$$

provided $\beta > \approx 4.5$.

η_m was found as β and ϕ_{max} were varied to examine the effect of smoothing. N=8000 and other system parameters were kept unchanged ($N_\Lambda = 160$). The results of η_{opt} and ϕ_{opt} are shown in Figure 4.11b and c, respectively. Here the reduction of η_{opt} can be seen to be approximately linear with $1/\beta$. The results are fitted with expression

$$\eta_{opt} = 1 - \frac{m}{\beta}, \tag{4-35}$$

where m was found from fitting to be 2.00 ± 0.04.

The behaviour ϕ_{opt} is adequately described by an exponential decay

$$\phi_{opt} = 2\pi e^{\frac{-w}{\beta}}, \tag{4-36}$$

where w was fitted to be 1.66 ± 0.04. It should be noted both (4-35) and (4-36) are chosen for simplicity, and from results of Figure 4.11c-d can be seen to start to breakdown at values $1/\beta$ of around 0.15.

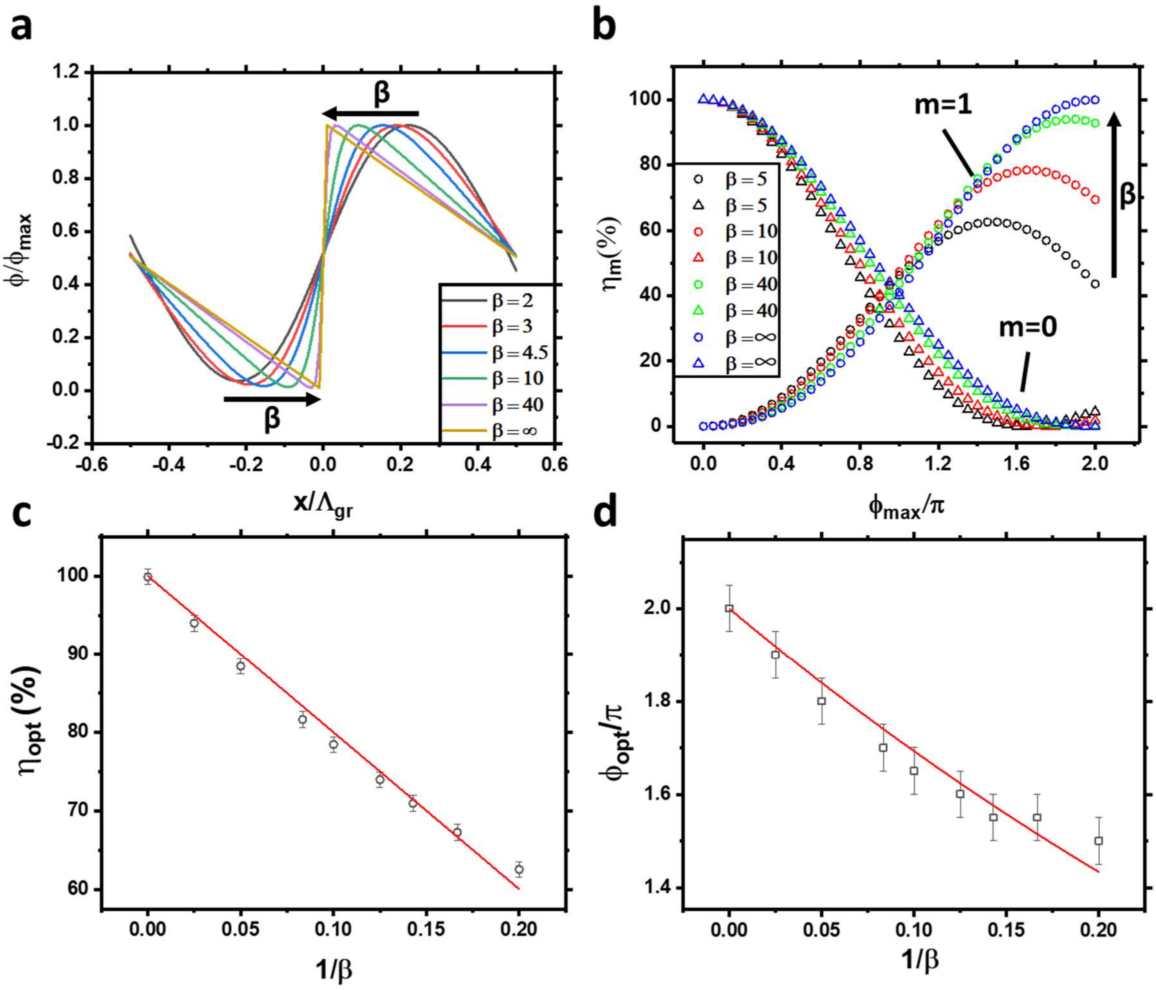

Figure 4.11. Plots relating to the smoothed blazed grating diffraction. (a) The effect of varying β on grating shape. (b) The effect on diffraction efficiencies of the m=0 (triangles) and m=1 (circles) orders as ϕ and β are varied. (c) and (d) the calculated values η_{opt} and ϕ_{opt}, respectively as β is varied. They include fits using equations (4-35) and (4-36) respectively.

These results have shown the losses in efficiency due to the curving of outgoing phase profile away from the perfect blazed case. As stated, this commonly occurs within NLC devices, so results may be useful to predict the limits for example of a ZBD bi-stable beam steering component. Interestingly, they can also be used in reverse, to garner information about a device form the resulting diffraction pattern. For example, if a ZBD surface relief structure of known refractive index (n_{ZBD}) was fabricated, and had a shape described by a certain β but was of unknown thickness(d_{ZBD}) this analysis could be used. If $\eta_{m=1}$ is measured practically, the corresponding value ϕ_{max} can be found and used to obtain the maximum thickness of the grating (d_{ZBD}), using a slightly altered form of equation (4-1),

$$d_{ZBD} = \frac{\phi_{max}\lambda}{2\pi(n_{\mathrm{ZBD}} - 1)}. \tag{4-37}$$

This could be useful as it allows quick approximate measurements of d_{ZBD}, avoiding the necessity for Scanning Electron microscopy which is usually necessary[231].

4.5 Summary

In this chapter, numerical methods that can be used to predict resulting diffraction efficiencies and angles of Raman-Nath diffraction gratings were presented. The necessary optics equations were introduced and the way they were put into a computer programme outlined. After this, the efficacy of the programme was established, by examining some well-characterised examples, then, it was used to examine the benefits and limitations of using NLCs to create blazed grating structures. Here, three systems were examined, where in each case the more the system deviated from the linear blazed profile, the more inefficiency was observed. In each section the application of these results has been discussed, where they can: (1) Aid device design (for example tuning ϕ_{max} such that it equals ϕ_{opt}), (2) Give maximum predicted efficiencies for a particular approach and (3) analyse devices created to determine their structures.

Although the results presented for these asymmetric gratings did not represent the gratings which were practically fabricated in this work (which were symmetric), it gives a thorough understanding of what is necessary for efficient devices. These ideas will be discussed further in Chapter 9, where after the intermediate chapters present work completed on hydrodynamic gratings, methods of optimizing their potential function as DOEs will be examined.

Chapter 5 Electrohydrodynamic Instabilities in Nematic Liquid Crystals

5.1 Introduction

This and the following chapter presents the results of using hydrodynamic patterns in Nematic Liquid Crystals (NLCs) to create ordered grating structures. In both chapters, ionic effects are used to induce well-defined electrohydrodynamic patterns, which are then assessed as diffractive optical elements (DOEs). The majority of results found in this chapter are published in reference [232] and those in Chapter 6 in reference [114]. This chapter provides the results of the effect of ionic conductivity, temperature and device spacing on the formation of electrohydrodynamic patterns. Chapter 6 presents an investigation of the role of elastic constants in the phenomenon.

5.1.1 Electrohydrodynamics and Electroconvection

Electrohydrodynamics is the study of the dynamics of fluids containing charged particles being placed under electric fields [233]. It is a broad topic with applications in biology[234,235], energy storage[236] and astrophysics[237]. A simple and relevant example of electrohydrodynamic phenomena is electroconvection in an isotropic fluid containing ions. Here, when a voltage above some critical value (V_C) is applied across the material, a net ion movement occurs, as under the Coulomb force the ions move to the oppositely charged electrode to resist the applied field (Figure 5.1a) [91,238,239]. This time dependence can be described relative to a charge relaxation timescale (τ_q)[240],

$$\tau_q \approx \frac{\varepsilon_0 \varepsilon}{\sigma}, \tag{5-1}$$

where ε is the relative permittivity, ε_0 is the permittivity of free space and σ is the material conductivity. The ions movement will be resisted by a viscous drag, which in addition to slowing the ions movement, induces flow within the material [241,242]. These flows are subject to dissipative processes, where the material redistributes the energy evenly to reach thermodynamic equilibrium[243].

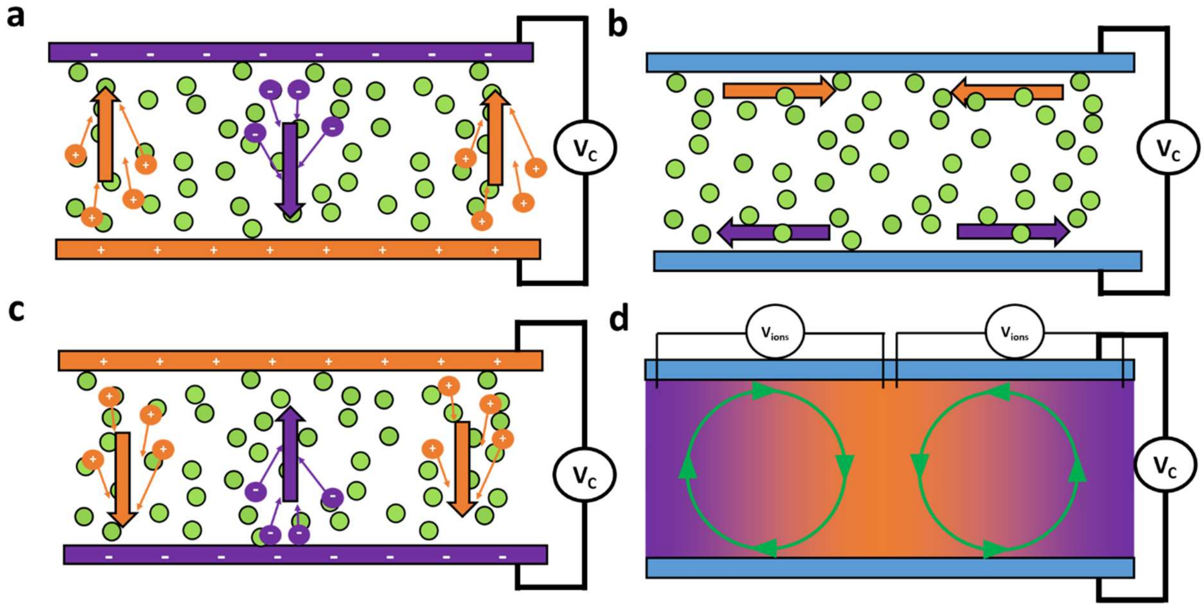

Figure 5.1 The formation of electroconvective rolls in isotropic fluids. (a) Ions within a thin layer of dielectric material with a critical voltage (V_c) applied. The ions (orange and purple arrows) move to the opposite electrodes to oppose the applied field. (b) The point where the polarity of the applied signal is switching, where the ions spread laterally at the surfaces of the device (c) The device with switched polarity where ions now move to the other electrode. (d) A snapshot of a 2D cut of the system after several such cycles. Here, hydrodynamic rolls have formed with macroscopic charge separation (symbolized by V_{ions}). These remain provided the AC voltage across the device is applied.

If, instead of DC, an AC voltage of frequency ω is used, where,

$$\omega \ll \frac{1}{\tau_q}, \tag{5-2}$$

the ions then move to the other electrode when the voltage polarity switches. Here, the value V_C is a function of ω as a larger Coulomb force is required to move the ions within a smaller time period. Over several cycles of switching polarity (Figure 5.1b-c), the ions often adopt hydrodynamic domains to optimize their transport through the fluid (Figure 5.1d)[244]. This also has the effect of creating charge separation within the material, which in turn creates an in-plane electronic potential difference (marked as V_{ions} in Figure 5.1d)[22,23,245]. These patterned vortices can be varied in shape (1-D lines, 2D grids etc.), where their exact nature is the result of small fluctuations at the point of formation (similar to those seen in other patterned forming phenomena such as Rayleigh Bernard Convection and Taylor-Couette flows)[243,246]. However, at V_C, isotropic fluids usually adopt flow patterns with honeycomb-like hexagonal unit cells[243–245].

5.1.2 Electrohydrodynamic Instabilities in Nematic Liquid Crystals

5.1.2.a *Anisotropy in Electroconvection*

Due to NLC's anisotropy of physical properties and the director (***n***) reorienting during the process [240,247,256,248–255], electroconvection in NLCs is significantly more complex than isotropic fluids. Here, due to the destabilising of ***n***, the processes are often known as Electrohydrodynamic Instabilities (EHDI).

The first observations of EHDI domains in NLCs were made by Williams [20,34] and Kapustin and Larinova in 1963[257]. NLC sandwich devices of planar homogenous (PH) alignment were filled with a NLC of negative permittivity anisotropy ($\Delta\varepsilon<0$) and positive conductivity anisotropy ($\Delta\sigma>0$). When a voltage (V) is applied to such devices, no Fréedericksz transition occurs due to the maximum ε already resisting the applied field[32]. However, at some critical voltage (V_C) ordered 1-D domains form when viewed with Polarized Optical Microscopy (POM). These domains are caused by ***n*** tilting out from the aligned PH orientation, due to a combination of viscous drag and charge separation [22,23] (the different components of which are shown in Figure 5.2a-b).

The anisotropy of the NLC phase can influence pattern directionality, as ions flow more easily along the axis of highest σ. This directionality can manifest in a number of ways, leading to different anisotropic patterns. One pattern is the Normal Roll (NR) mode, where the roll wave vector ($\boldsymbol{q_C}$) is parallel to the rubbing direction of ***n***(Figure 5.2c). This NR mode is the focus of our investigations.

For comparison, Figure 5.2d shows the case of a positive $\Delta\varepsilon$ NLC in a homeotropic (HT) aligned device. Here, the observed domains have no clear directionality, and are similar to those seen in isotropic fluids, due to lack of preferential direction of ion flow at the point of formation[239,243,258,259].

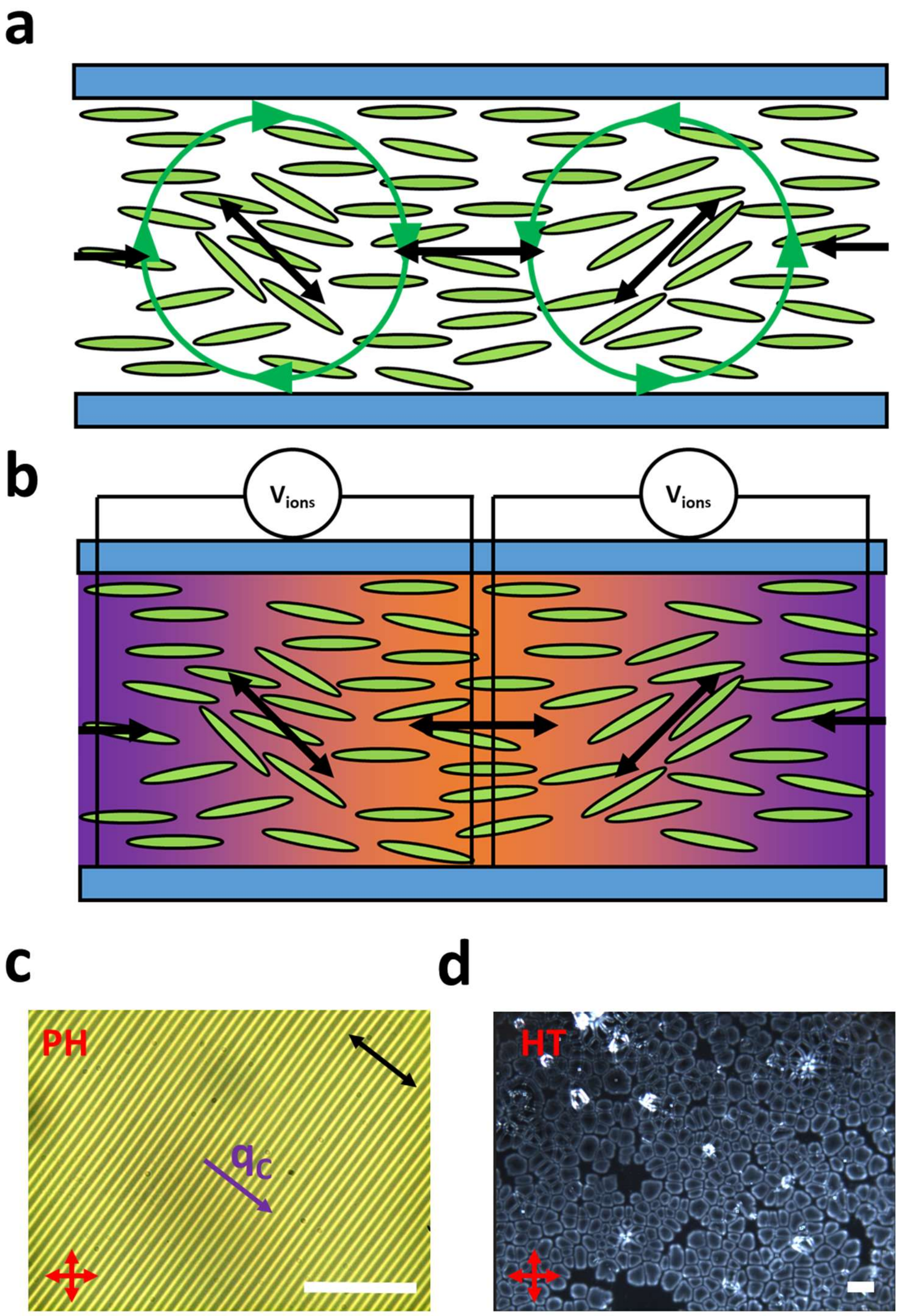

Figure 5.2. EHDI in NLCs. (a) and (b) show cartoons of the director field, where dual forces of viscous flow (a) and electric potential (b) act to reorient a NLC with negative $\Delta\varepsilon$ and positive $\Delta\sigma$. (c) A photograph of the Normal Roll (NR) mode in a PH NLC device. The domains are well ordered with q_C pointing in the device alignment direction (black arrow). (d) The equivalent domains in a NLC HT cell. As no preferential direction exists for the domains, they form a more hexagonal pattern more typical of isotropic fluids. In both the white line is $100\mu m$.

5.1.2.b *Map of the Frequency Voltage Space*

The NR mode is one of many patterns which may occur as the frequency *(f)* and voltage *(V)* applied to a PH *($\Delta\varepsilon<0$, $\Delta\sigma>0$)* device are varied. A typical map of the different textures is shown in Figure 5.3[249,253]. Here, flexoelectric effects are neglected due to such effects not being seen to manifest in the presented work. This is likely due to the high conductivities dominating EHDI behaviour making such effects negligible. The frequency space is typically divided into conduction ($f<f_{diel}$) and dielectric ($f>f_{diel}$) regimes, where[260,261],

$$f_{diel} \approx \frac{1}{\tau_q}. \qquad (5\text{-}3)$$

The patterns usually observed are listed below:

i. **Normal Rolls (NR)** are uniformly aligned with q_C parallel to the rubbing direction. They appear at V_C in the frequency range: $f_{lif} < f < f_{diel}$. At lower frequencies within this range[249,255],

$$q_C = |\boldsymbol{q_C}| \approx \frac{d}{\pi}, \qquad (5\text{-}4)$$

and increases in value with f[240].

ii. **Oblique Rolls (OR)** are similar to NR rolls in appearance, but have a helicoidial flow pattern which leads to two degenerate $\boldsymbol{q_C}$ at angles $\pm\alpha$ to the rubbing direction[262,263]. As f increases α reduces until they become the NR mode at f_{lif}.

iii. **Undulating Rolls (UR).** At a voltage slightly above V_C, both the NR and OR patterns start fluctuating, which degrades their uniformity [263].

iv. **Grid Pattern (GP).** At higher V, ion flow perpendicular to the director will also be of great enough magnitude to reorient the NLC. This leads to a grid pattern, with two wave vectors parallel and perpendicular to $\boldsymbol{n}$ ($\boldsymbol{q}_{\parallel}$ and $\boldsymbol{q}_{\perp}$)[264,265].

v. **Dynamic Scattering Modes (DSM).** At higher V, the pattern features become smaller and flicker with time[2,102,254,266]. These lead to much lower transmissibility due to increased scattering of light by $\boldsymbol{n}$ varying in space[267,268].

vi. **Pre-Wavy Pattern (PWP).** This is the first texture to appear as voltage is increased in the dielectric regime. It appears similar to the NR mode, but the domains (of wavevector $\boldsymbol{q_{PW}}$) are typically wider than the NR mode[269,270].

vii. **Chevron Patterns (CP).** At higher voltages close to f_{diel} the PWP incorporates twisted conductive rolls within them, forming a chevron pattern[253,269,270]. Here, three wavevectors exist simultaneously $\boldsymbol{q_{PW}}$ for the rolls and $\boldsymbol{q}_+$ and $\boldsymbol{q}_-$ from the two chevron orientations.

viii. **Dielectric Rolls.** Above V_C in the dielectric regime, short pitch, low contrast rolls form which can also have chevron like structures[253,260,261]. Here, the coupling between the director and the oscillatory applied field, leads to charge separation causing periodic director modulation.

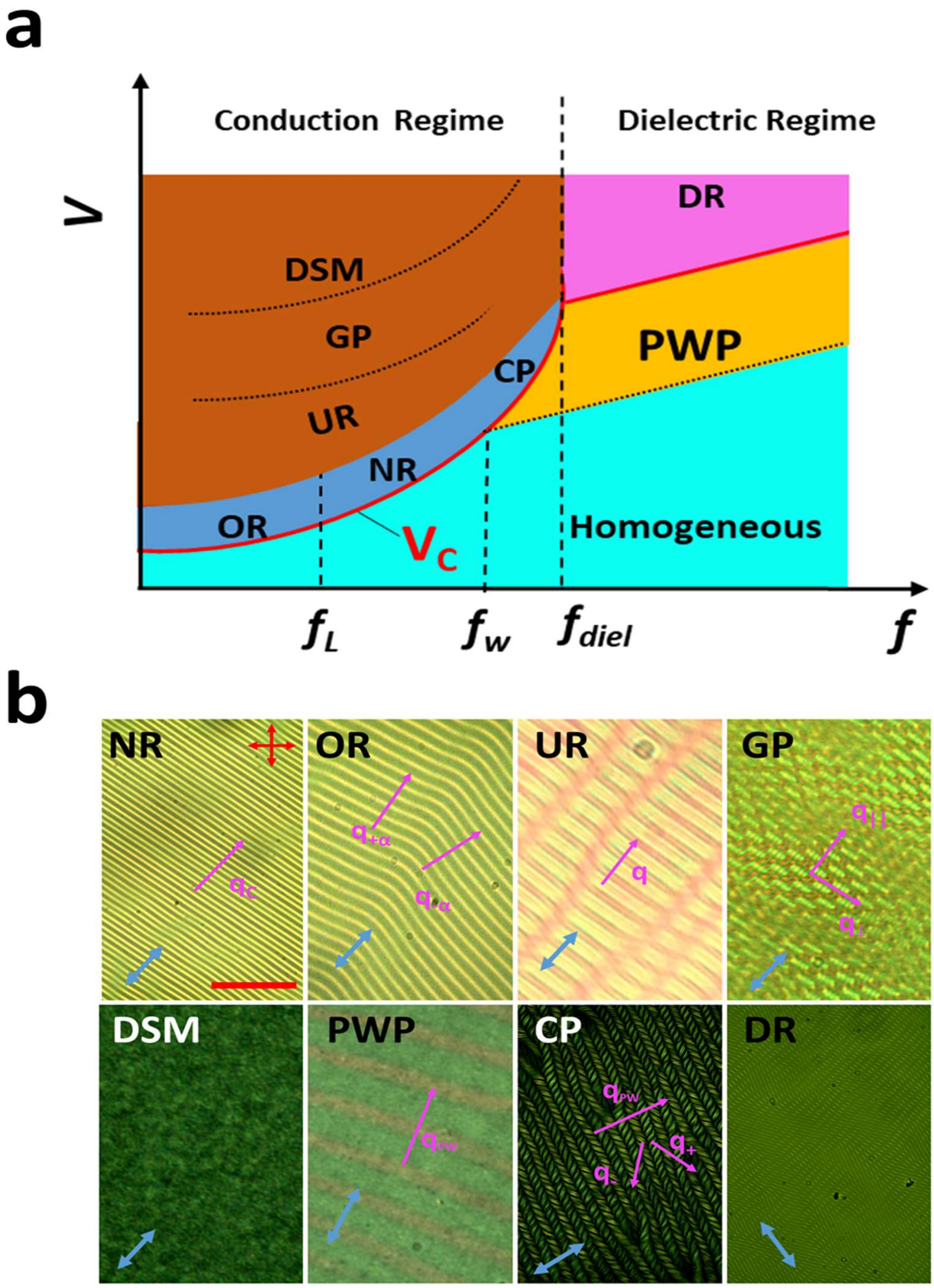

Figure 5.3.a). a) The map of different textures for a PH device filled with negative Δε material, based on mappings given in references [249,253]. *b) Photos of the different patterns, taken during this project. Here the red scale bar (100µm) applies to all photos other than CP. The crossed polarizers are applicable to all the photos.*

5.1.2.c *Applications of EHDI in NLCs*

The most famous application of EHDI is the use of the DSMs to create electrically addressable optical shutters for the first Liquid Crystal Displays (LCD) [2,102,254,266]. Their use in displays were short lived, as relatively soon after their discovery, the superior twisted nematic replaced this as the standard operation mode for the LCD [1]. More recently the DSMs have been extensively investigated for use in smart window technology[271–273].

The goal of this chapter is to investigate EHDIs operation as diffractive optical elements (DOEs). Of the patterns shown in Figure 5.3b, the most promising for creating high efficiency and variable pitch diffraction gratings is the NR mode [274–276]. The controlled formation of the NR mode and its optical properties are discussed in the following section.

5.1.3 Theoretical Descriptions of the NR Mode

5.1.3.a *Threshold of the NR Mode*

Description of EHDIs in general has developed over many decades, where one of the first and most successful models was developed by Carr and Helfrich in 1969[22,23]. This model attributed the processes of director modulation to the accumulated effects of charge separation and viscous flow (as shown in Figure 5.2a-b). Since then, further refinements have been added to "The Carr-Helfrich mechanism" to generalize it for as broader range of systems as possible [188,240,279–281,247,248,253,255,256,262,277,278].

To describe the formation of the NR mode we follow the summary of many of these works written by of Kramer and Pesch in 1996[240]. Here, the frequency dependence for V_C in the NR mode is written as,

$$V_c{}^2 = A\frac{(1+\omega'^2)q'^2_C}{\left(\omega'^2-\omega^2_{diel}\right)}, \tag{5-5}$$

where,

$$q'_C = q_C\left(\frac{d}{\pi}\right), \tag{5-6}$$

$$\omega' = \omega\tau_\perp\left(\frac{D}{S}\right), \tag{5-7}$$

$$A = \frac{\pi^2 k_{33}\sigma_{||}{}^2}{\varepsilon_0^3\varepsilon_{||}\varepsilon_\perp\Delta\varepsilon}, \tag{5-8}$$

$$D = \left(\frac{\varepsilon_{||}}{\varepsilon_{\perp}}\right) q'_C + 1 \tag{5-9}$$

$$S = \left(\frac{\sigma_{||}}{\sigma_{\perp}}\right) q'_C + 1 \tag{5-10}$$

$$\tau_{\perp} = \frac{\varepsilon_0 \varepsilon_{\perp}}{\sigma_{\perp}} \tag{5-11}$$

and

$$\omega_{diel}^2 = \frac{\sigma_{||}}{\varepsilon_0^2 \varepsilon_{\perp}} \left[\frac{|\alpha_2|}{\eta_1} \left(\frac{\sigma_{||}}{\varepsilon_{||}} - \frac{\Delta\sigma}{\Delta\varepsilon} \right) - \frac{\sigma_{\perp}}{\varepsilon_{\perp}} \right], \tag{5-12}$$

where d is the device spacing, τ_q is a charge relaxation time, subscripts || and $\perp$ indicate parallel and perpendicular to ***n*** respectively, k_{33} is the bend elastic constant and α_2 and η_1 are viscosity coefficients introduced in section 2.3.

Here, in equation (5-5) if ω is set to zero, an expression,

$$V_0{}^2 = -A \frac{q'^2_0}{\omega_{diel}^2}, \tag{5-13}$$

is obtained, where V_0 and q_0 are the values of V_C and q_C as ω tends to zero. Combining this with equation (5-8) gives,

$$A = \frac{\pi^2 k_{33} \sigma_{||}{}^2}{\varepsilon_0^3 \varepsilon_{||} \varepsilon_{\perp} \Delta\varepsilon} = -\frac{V_0{}^2}{q'^2_0} \omega_{diel}^2. \tag{5-14}$$

and so,

$$\frac{V_c{}^2}{V_0{}^2} = \frac{q'^2_C}{q'^2_0} \frac{(1 + \omega'^2)\omega_{diel}^2}{\left(\omega_{diel}^2 - \omega'^2\right)}. \tag{5-15}$$

5.1.3.b *The Director Profile of the NR mode*

Let us examine the effect the formation of the NR mode has upon ***n***. Following the treatments by Carr, Helfrich and Dubois Violette et al. [22,23,247], a 1-D solution for the tilt of ***n*** from the x orientation into the z direction (ψ) is assumed to have a sinusoidal form (Figure 5.4a-b),

$$\psi(x) = \psi_{max} \cos(q_c x) \sin\left(\frac{\pi z}{d}\right), \tag{5-16}$$

where ψ_{max} is the maximum tilt.

To investigate the dependencies of ψ_{max} on system properties, the total torque experienced by $\boldsymbol{n}$ (Γ_T) is[247],

$$\Gamma_T = \Gamma_{visc} + \Gamma_{el} + \Gamma_{Fred}, \tag{5-17}$$

where Γ_{visc}, Γ_{el} and Γ_{Fred} are torques associated with: viscous drag, director elasticity and the total electric field both due to applied and induced electric fields, respectively. In reference [247] terms for Γ_{el} and Γ_{Fred} are obtained through differentiating the relevant part of the Frank free energy (discussed in section 2.2.1) with respect to ψ,

$$\Gamma_{el} = \frac{\delta F_{el}}{\delta\psi} = \frac{1}{2}\frac{\delta}{\delta\psi}\left(k_{11}\,(\nabla.\boldsymbol{n})^2 + k_{22}(\boldsymbol{n}.\nabla\times\boldsymbol{n}) + k_{33}(\boldsymbol{n}\times\nabla\times\boldsymbol{n})\right), \tag{5-18}$$

$$\Gamma_{Fred} = \frac{\delta F_{Fred}}{\delta\psi} = \frac{\delta\Delta\varepsilon\varepsilon_0(\boldsymbol{E_{app}}\cdot\boldsymbol{n})^2}{\delta\psi}. \tag{5-19}$$

From these, reference [247] obtains first order expressions (for small ψ),

$$\Gamma_{el} = -k_{33}\frac{\partial^2\psi}{\partial x^2} = -k_{33}q_c^2\psi, \tag{5-20}$$

and

$$\Gamma_{Fred} = -\frac{\Delta\varepsilon\varepsilon_0}{4\pi}{E_{app}}^2\left(\psi + \frac{E_{ions}}{E_{app}}\right) \tag{5-21}$$

where $\boldsymbol{E_{app}}$ is the electric field from the applied voltage, $\boldsymbol{E_{ions}}$ is the induced field due to charge separation and k_{ii} are elastic constants. Γ_{visc} is written [247] as,

$$\Gamma_{visc} = \gamma_1\left[\frac{\partial\psi}{\partial t} - \frac{\gamma_1-\gamma_2}{2\gamma_1}\frac{\partial v_z}{\partial x}\right], \tag{5-22}$$

where v_z is the velocity field in the z direction. To simplify Γ_{visc}, we assume v_z at $z=d/2$ to has sinusoidal form (Figure 5.4c),

$$v_z\left(x, z = \frac{d}{2}\right) = v_{max}\sin(q_c x) \tag{5-23}$$

and take only the steady state solution ($\frac{\partial\psi}{\partial t} = 0$), which simplifies equation (5-22) to,

$$\Gamma_{visc} = \left(\frac{\gamma_2-\gamma_1}{2}\right)q_c v_{max}. \tag{5-24}$$

In the steady state Γ_T will equal zero, meaning equation (5-17) can be written as,

$$0 = \Gamma_{visc} + \Gamma_{el} + \Gamma_{Fred} \tag{5-25}$$
$$= \left(\frac{\gamma_2 - \gamma_1}{2}\right) q_c v_{max} - k_{33} q_c^2 \psi_{max} - \frac{\Delta\varepsilon\varepsilon_0}{4\pi} E_{app}^2 \left(\psi_{max} + \frac{E_{ions}}{E_{app}}\right).$$

This gives an expression for ψ_{max},

$$\psi_{max} = \frac{\left(\frac{\gamma_2 - \gamma_1}{2}\right) q_c v_{max} - \frac{\Delta\varepsilon\varepsilon_0}{4\pi} E_{app} E_{ions}}{\left(k_{33} q_c^2 + \frac{\Delta\varepsilon\varepsilon_0}{4\pi} E_{app}^2\right)}. \tag{5-26}$$

This is useful to give the expected trend of ψ_{max} with various physical parameters, where it will: increase with v_{max}, decrease with k_{33} and decrease or increase with $\Delta\varepsilon$ depending on the relative sizes of E_{ions} and E_{app}.

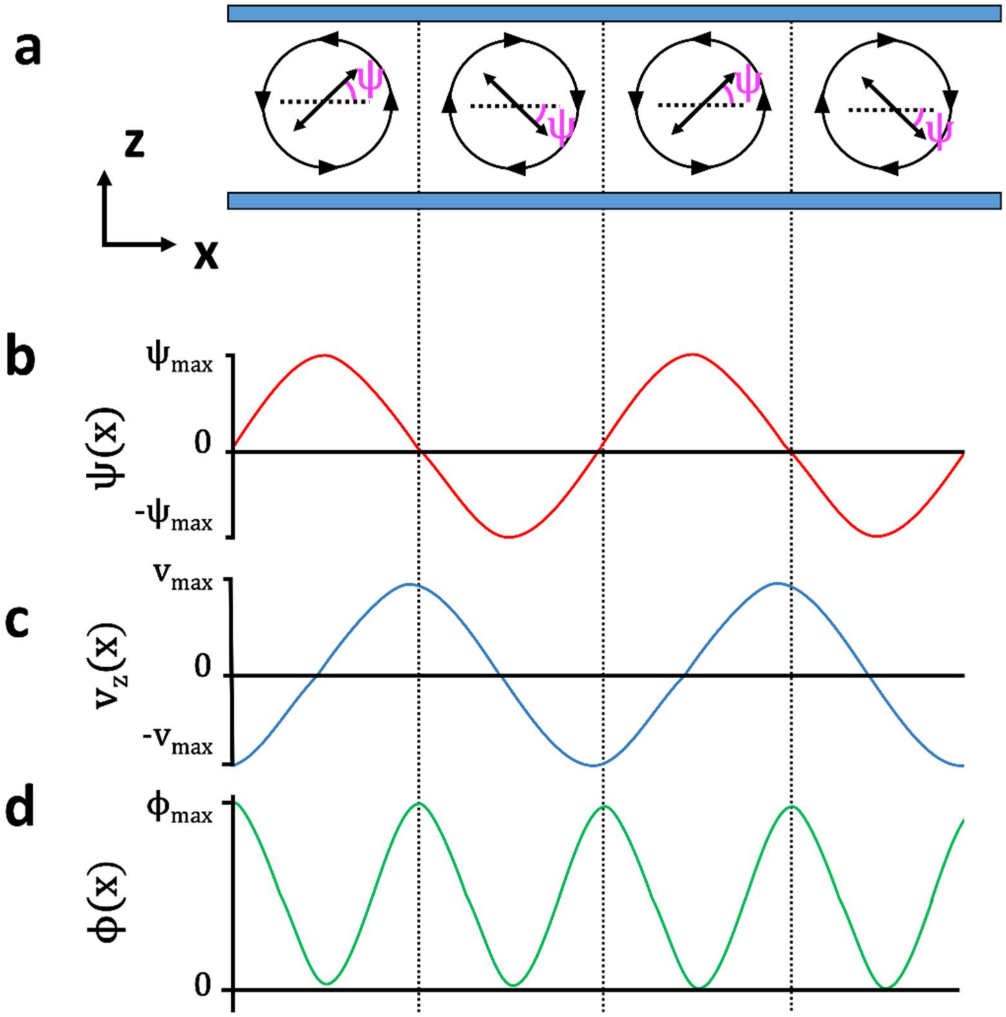

Figure 5.4. Properties of an NLC in the NR mode. (a) The roll configuration with ψ marked. (b-c) Plot of ψ(x) and $v_z(x)$ where in both cases z=d/2. (d) Shows the optical path difference as a function of x.

5.1.3.c *Optics of the NR Mode*

Treating the NR mode as a Raman-Nath optical phase grating, diffraction efficiencies can be predicted. Here, the optical phase difference *(ϕ)* due to an NLC may be written as,

$$\phi(x) = \frac{2\pi}{\lambda}\int_0^d n_{eff}(\psi) - n_{\perp}\, dz. \tag{5-27}$$

where,

$$n_{eff}(\psi) = \frac{n_{||}n_{\perp}}{\sqrt{n_{||}^2 sin^2\psi + n_{\perp}^2 cos^2\psi}}. \tag{5-28}$$

These can be combined with the director profile given in (5-16) to obtain a complex integral. However, instead we take the approximate result from John et al[274],

$$\phi(x) = \phi_{max}\cos(q_{opt}x). \tag{5-29}$$

where,

$$\phi_{max} = \frac{\pi}{4}\frac{d}{\lambda}\frac{n_{||}\left(n_{||}^2 - n_{\perp}^2\right)}{n_{\perp}^2}\psi_{max}^2 \tag{5-30}$$

and

$$q_{opt} = 2q_c. \tag{5-31}$$

This allows the absolute diffraction efficiencies of the grating (η_m) to be calculated as being of sinusoidal shape[175],

$$\eta_m = {J_m}^2\left(\frac{\phi_{max}}{2}\right), \tag{5-32}$$

where J_m is a Bessel function of the first kind of order m. Combining equations (5-30) and (5-32) η_m is plotted as functions of ϕ_{max} and ψ_{max} in Figure 5.5. From this it can be seen that the maximum $\eta_{m=1}$ is 34% and will occur at $\psi_{max}=34°$. This is problematic, as the theoretical treatments presented throughout this chapter have assumed small deviations of $\boldsymbol{n}$ [240,247,274], meaning their interpretation may be limited for creating efficient EHDI gratings. Another issue with this treatment is that we have assumed the EHDI grating to be of Raman-Nath type. This is not true, as due to the layer thickness, beams undergo significant deviations with Gradient Index (GRIN) effects during their travel through the material (discussed in detail in [274]).

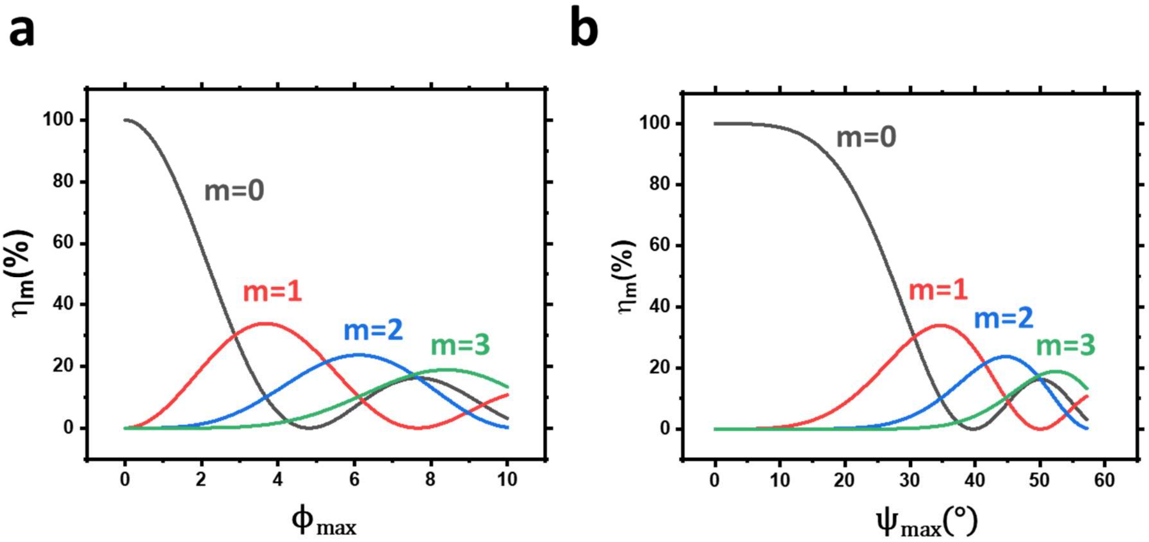

Figure 5.5. η_m *against* ϕ_{max}*(a) and* ψ_{max}*(b). For (b) typical parameters of* d*=20μm,* $n_{||}$*=1.7,* $n_{\perp}$*=1.5,* λ*=589nm were used.*

5.2 Methods

5.2.1 Overview of Work

The goal of this chapter is to evaluate NLCs in a state of EHDI as variable pitch DOEs. Simplistically, in order to create efficient gratings a large ϕ_{max} is required, while to make them wide-angle a large q_{opt}. From the literature[240,247–254,282], it is apparent that many factors affect the values of ϕ_{max} and q_{opt} including: the device geometry, the driving field, and the viscoelastic and dielectric properties the NLCs. This work investigates several of these factors including driving frequency and voltage, material conductivity, temperature and device spacing.

5.2.2 Materials

The mesogenic compound chosen to perform the work was MLC 2081(Provided by Merck Chemicals UK). This has standard elastic constants for a calamitic nematic (which are measured in Chapter 6), negative $\Delta\varepsilon$, positive $\Delta\sigma$ and wide nematic range (-40°C to108°C). The material was found to have very low intrinisic conductivity. This was increased by adding Tetra-Butyl-Ammonium-Tetra-Phenyl-Borate (TBATPB, Figure 5.6).Similar materials have been shown to increase conductivity when added to liquid crystals [283,284].

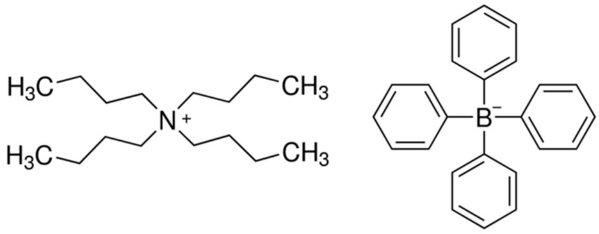

Figure 5.6. Molecular diagram of Tetra-Butyl-Ammonium-Tetra-Phenyl-Borate.

5.2.3 Devices

Sandwich devices of spacing 5, 10 and 20μm were used to observe EHDI (purchased from AWAT). These had planar homogenous (PH) alignment achieved using rubbed layers of SE130 polyimide [73]. Devices with a homeotropic (HT) alignment (SE1211) were also used to characterise materials, however when significant voltages were applied to devices containing TBATPB, the HT alignment was seen to degrade rapidly. For this reason, only the 0% and 0.3% TBATPB homeotropic devices were examined in this work (where only voltages of 0.05V were used).

5.2.4 Dielectric Spectroscopy

The electronic properties of the devices were measured using broadband dielectric spectroscopy (Agilent E4980A). Here, the device temperature *(T)* and oscillation frequency *(f)* was varied with a voltage *(V)* of 0.05V. The measured capacitance (*C*) and conductance (*G*) were converted to permittivity ($\varepsilon_{\perp}$) and conductivity ($\sigma_{\perp}$) using standard equations for a PH cell,

$$\varepsilon_{\perp} = \frac{C}{C_0} \tag{5-33}$$

and

$$\sigma_{\perp} = \frac{Gd}{A}. \tag{5-34}$$

where C_0 is the empty cell capacitance and *A* is the electrode area. Here, the pretilt (θ_p) was assumed to be negligible. From the Nissan data sheet θ_p=1-2°, resulting in a systematic error of 2-3% in values. In addition, the devices had square electrodes, which can increase the tendency of fields to fringe at the corners. Due to this experimental errors were taken to be 5% of measured values.

5.2.5 Optical Microscopy

Characterisation of the EHDI thresholds was made through measurement of parameters V_c and q_{opt} as applied frequency (*f*) was varied. Here, q_{opt} is related to q_c using equation (5-31) and was chosen due to the focus of work being optical gratings. To measure V_C, a certain *f* was set and the voltage increased until a pattern was observed. Here, at times the patterns were distributed unevenly through the material. For this reason, the same location was used for the same sample and an error for V_C of ± 0.1V was given. The period of the grating (λ_{opt}) was measured using a stage micrometre, which was converted to q_{opt} using,

$$q_{opt} = \frac{2\pi}{\lambda_{opt}}. \tag{5-35}$$

Here, usually the number of λ_{opt} measured *(N)*, was 10. The errors in λ_{opt} ($\Delta\lambda_{opt}$) and q_{opt} (Δq_{opt}) were approximated as,

$$\Delta\lambda_{opt} = \frac{\lambda_{opt}}{2N}. \tag{5-36}$$

and

$$\Delta q_{opt} = \frac{q_{opt}}{2N}, \tag{5-37}$$

respectively.

5.2.6 Diffraction Analysis

Diffraction experiments were used to measure steering angles (θ_m) and absolute efficiencies (η_m) of the gratings. A helium neon (632.8nm) laser was used, and all experiments were performed at ambient temperatures (T=17±2°C). Similar to POM measurements, f was set and the voltage was increased until a diffraction pattern was formed. When the EHDI was in NR mode, the diffraction pattern was 1D and had odd-even characteristics (see Figure 5.7a), where for example $\eta_{m=2} > \eta_{m=1}$. This is typical of the NR mode and is explained by an additional amplitude modulation of period $2\lambda_{opt}$, caused by lensing [21,276]. At other locations in the frequency voltage space, other patterns were observed, where for example diffraction patterns from grid and oblique rolls are shown in Figure 5.7a.

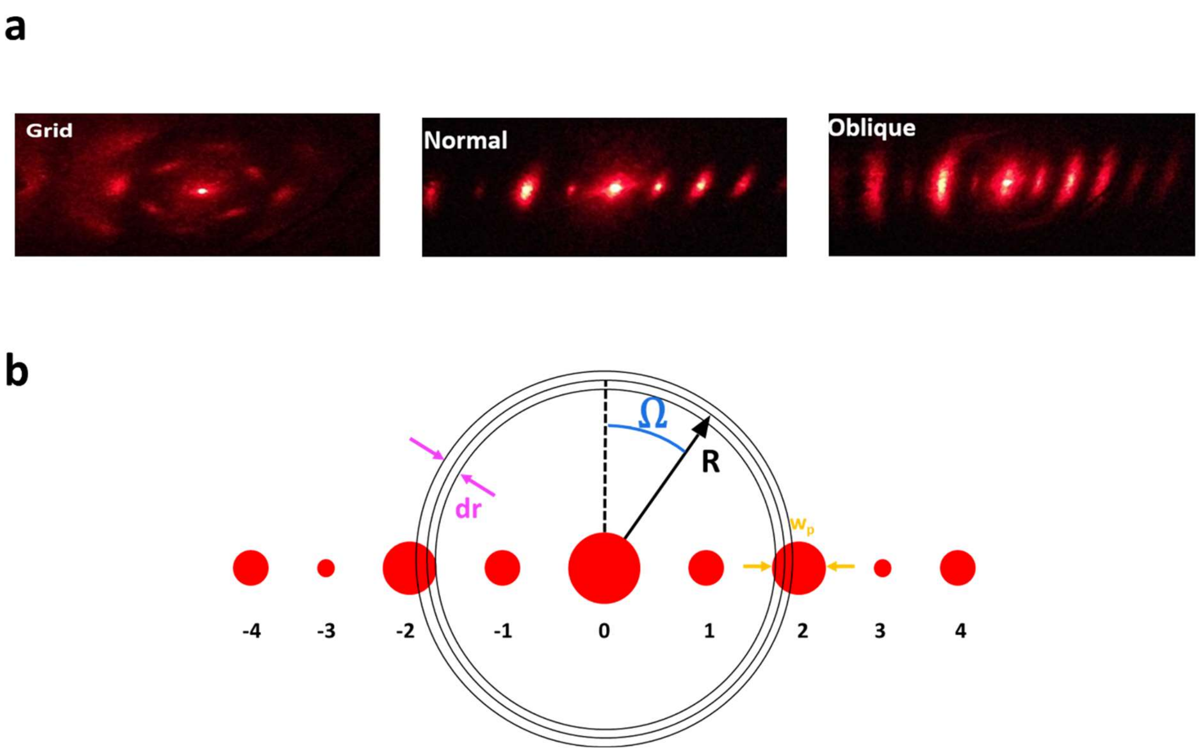

Figure 5.7. Diffraction patterns from EHDI. (a) Shows photographs of patterns from various EHDI textures. In the NR mode $\eta_{m=2} > \eta_{m=1}$. (b) A diagram showing variables associated with measurement of η_m.

A beam profiler (Thorlabs, BC106N-VIS) was used to measure η_m, at times the sensor was positioned such that the diffraction pattern could be viewed. This outputted x-y mappings of intensity $(I(x,y))$, which were converted into radial coordinates $(I(R,\Omega))$, where R=0 was at the centre of the zeroth order.

$I_\Omega(R)$ was then obtained by integrating radially around consecutive rings of width $dr=5\mu m$ (see Figure 5.7b),

$$I_\Omega(R) = \int_0^{2\pi} (I(R,\Omega) - I_0)d\Omega, \tag{5-38}$$

where I_0 was the background noise. The intensity of the peaks (I_m) were found by integrating I_Ω about the location of the peak (centred on R_p of width w_p),

$$I_m(R) = \int_{R_p-\frac{w_p}{2}}^{R_p+\frac{w_p}{2}} I_\Omega dR. \tag{5-39}$$

η_m was then found using,

$$\eta_{m=2} = \frac{I_{m=2}}{2I_{diode}} \tag{5-40}$$

where

$$I_{diode} = \int_0^\infty I_\Omega dR. \tag{5-41}$$

The factor 2 in (5-40) comes from averaging the ±2 orders.

At other times , due to refining of techniques, the beam profiler was used to measure the orders directly. Here, any discrepancies between techniques were found to be within calculated experimental errors.

5.3 Results and Discussion

5.3.1 Effect of TBAPTB on NLC Properties

5.3.1.a *Frequency Dependency*

The addition of TBATPB to MLC 2081 increased the conductivity of the liquid crystal, as expected. Figure 5.8a-d show the dielectric results comparing the pure material (0% TBATPB) to 1% TBATPB.

In the pure sample, the value $\varepsilon_\perp$ did not vary considerably with frequency, other than a small increase in measured value at low frequencies and high temperatures. This small increase was taken to be due to a small amount of ionic impurities in the material, which corresponds with the $\sigma_\perp$ measurements, where at low frequencies below around 50kHz, $\sigma_\perp$ increases in value with temperature (attributed to increased ionic transmittance). At higher frequencies ($f > 300$ kHz), all $\sigma_\perp$ plots coalesce. This is commonly seen in LC cells and is usually attributed to: ITO not being a perfect metal, lengthy thin wires and oxidisation at electrode interfaces.

In the 1% sample, comparatively larger increases in low frequency $\varepsilon_\perp$ were seen. These appeared to undergo Debye-like relaxation process (a plot of a Debye relaxation is shown in Figure 5.8c, which fits observations well). The behaviour $\sigma_\perp$ was similar to the pure material, but had far larger values (by a factor between 100 and 1000). At high temperatures and low frequencies, a decrease in $\sigma_\perp$ was seen. This was taken to be due to electrode polarization forming double layer structures, trapping the ions [86]. From these graphs the ‘plateau values’ (ε_p and σ_p) were obtained (Figure 5.8d). These plateaus occurred either at the same frequency each time or varied in location with temperature (black dashed lines in Figure 5.8).

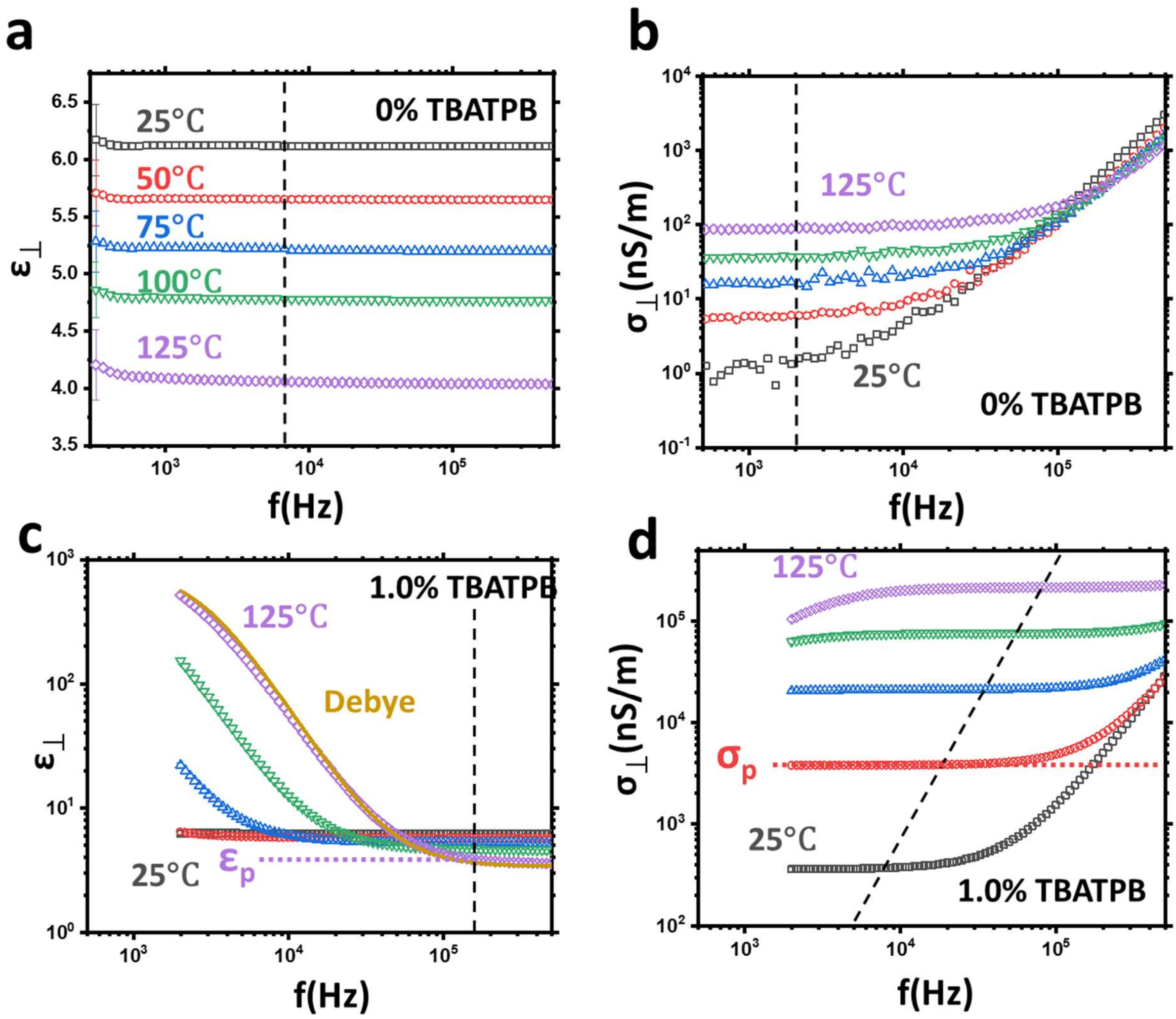

Figure 5.8. Dielectric spectra of MLC 2081 with and without TBATPB. (a) and (b) show the values of $\varepsilon_\perp$ *and* $\sigma_\perp$ *at several temperatures in pure MLC 2081, respectively. (c) and (d) show similar for MLC 2081 with 1% TBATPB. In (c) a Debye model is included to show the ionic relaxation is well described as such (yellow line). The black dashed lines in all figures show appropriate locations to measure the values* ε_p *and* σ_p*, where in some cases a single frequency can be used while for others it will migrate with temperature.*

5.3.1.b *Temperature Dependency*

To examine temperature dependency, the values ε_p and σ_p were obtained from frequency dependent plots (such as those in Figure 5.8), and taking the average of ten consecutive points on the plateau.

Figure 5.9a shows values of ε_p (from here labelled ε for conciseness) of the 0% and 0.3% TBATPB materials in the HT and PH devices. Here, in both materials the values $\varepsilon_\perp$ increase and $\varepsilon_{//}$ decrease as T is increased. At T_{NI} they coalesce within error. This is standard behaviour for a negative $\Delta\varepsilon$ material and is caused by the decreasing order parameter of ***n*** *(S)*. The addition of TBATPB appears to have increased both $\varepsilon_\perp$ and $\varepsilon_{//}$ by a factor of approximately 0.5. Figure 5.9b plots the values $\Delta\varepsilon$ as functions of T-T_{NI} which indicates the addition of TBAPTB does not appear to have changed $\Delta\varepsilon$ within error.

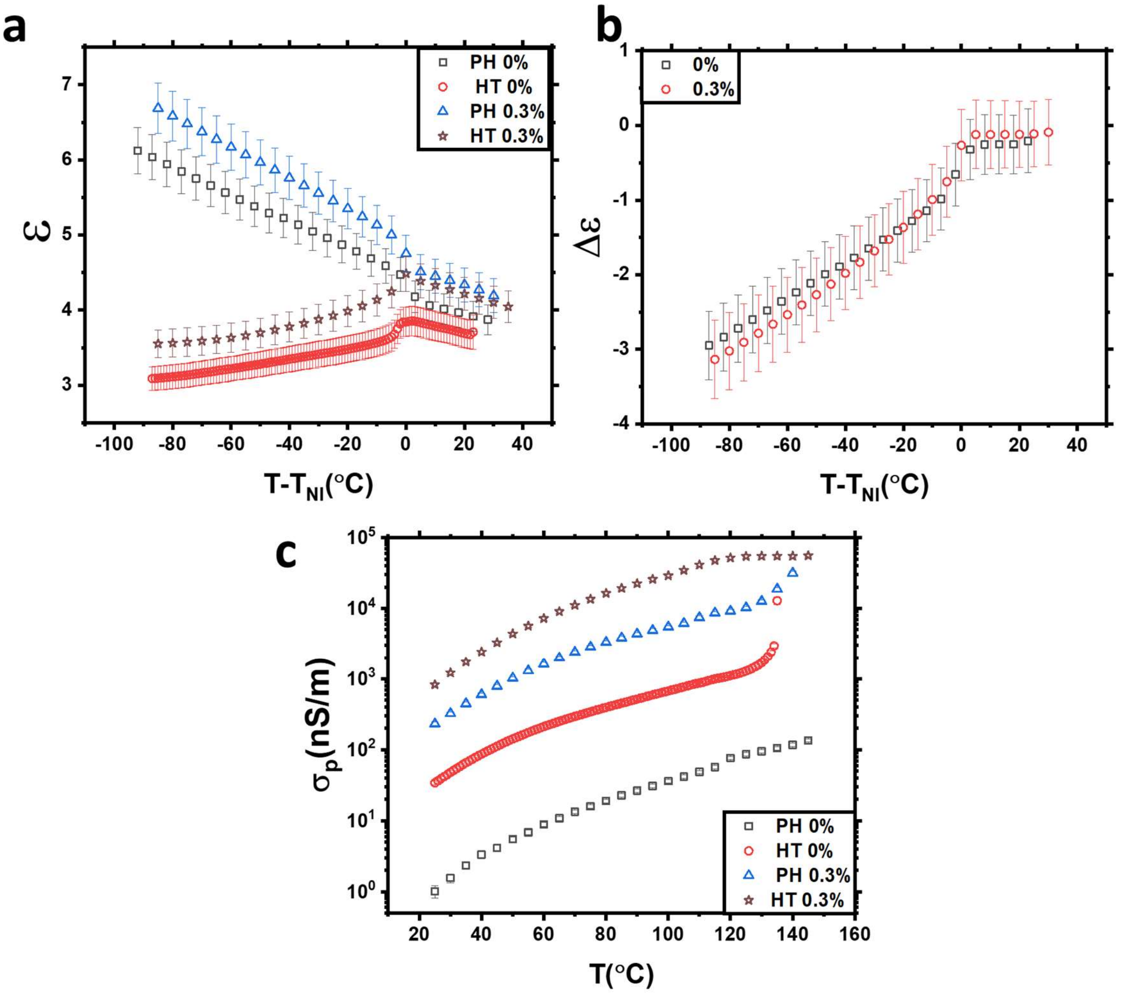

Figure 5.9. Comparison of PH and HT cells filled with MLC 2081 with 0 and 0.3% TBATPB. (a) ε as a function of T_{NI}-T (b) same as (a) where doped samples have 0.5 subtracted from their values. (c) σ_p as a function of T.

In both the PH and HT devices of both concentrations, the values of σ_p are not equal above T_{NI} (Figure 5.9c). The cause of these differences is uncertain, however as the materials should be identical above T_{NI}, it seems likely to be caused by difference in the devices not materials. As the prominent device difference was the alignment layers, it may be the PH alignment layer, is somehow supressing σ_p compared to the HT devices. The observation of degradation of HT alignment with high voltage low frequency driving could be related to similar ions-alignment layer interactions.

Figure 5.10a-b compares all PH devices measured ε and σ_p as functions of temperature. Here, all materials showed similar trends in value with temperature. In ε value, all devices apart from 0.6% and 2.3% were within error of one another. A possible trend of increasing ε with ion concentration can be seen, however the effect is small, similar to the results shown in Figure 5.9a-b. The reason for the differences in 2.3% and 0.6% are unknown. The 2.3% had an anomalously large C_0 measurement, meaning a different C_0 from a similar device was used. Meanwhile, the 0.6% device was 10μm, if the ions are interacting with alignment layers, it may be that this effect is larger in the thinner device due to a larger electrode surface area per volume of NLC.

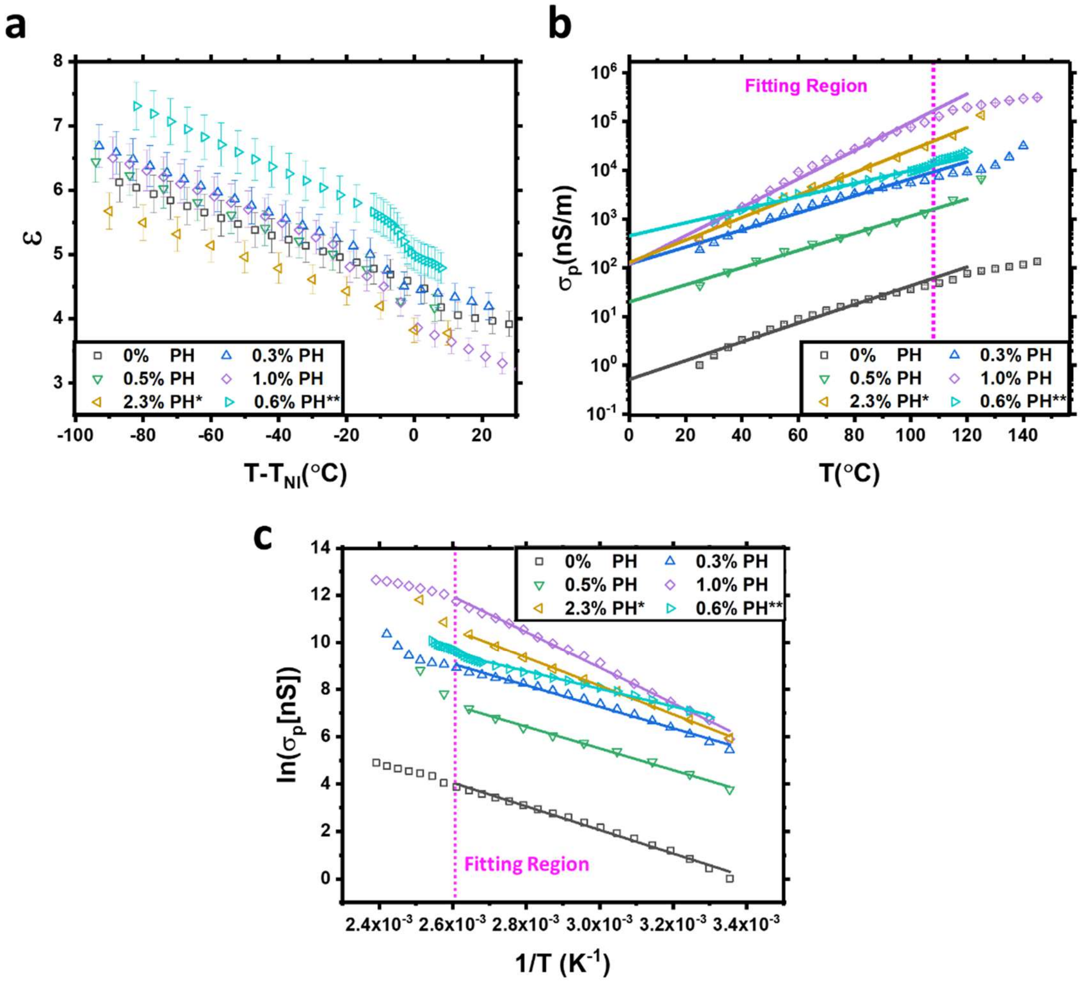

Figure 5.10. Dielectrics of PH devices filled with various amounts of TBATPB (shown as %) as functions of temperature. The values ε (=ε_p) *(a) and* σ_p *(b) were taken from graphs similar to those seen in Figure 5.8.All device spacing's are 20μm, apart from 0.6% which is a 10μm. The 0.6% PH and 2.3% devices appear to be anomalous in magnitude ε. In (b) a fittings* σ_p *is obtained using equation (5-42). (c) shows an Arrhenius plot of the same data given in (b), fitted with equation (5-43). Fitting are given in Table 5-1.*

The σ_p values were dramatically increased by the addition of TBATPB. For later sections it is useful to obtain expressions for $\sigma_p(T)$. To do so the σ_p data in Figure 5.10b was fitted with an empirical exponential expression,

$$\sigma_p(T) = \sigma_0 e^{mT}, \tag{5-42}$$

where T was taken in °C rather than Kelvin for ease of use. Figure 5.10c shows the same data replotted on an Arrhenius plot. This data was fitted using,

$$ln[\sigma_p(T)] = ln[\sigma_\infty] + \frac{E_A}{k_B T}, \tag{5-43}$$

where σ_∞ is the value σ_p as T tends to infinity, E_A is an activation energy and k_B is Boltzmann's constant. The fitting parameters obtained for equations (5-42) and (5-43) are given in Table 5-1.

Table 5-1. Details of the devices and fitting parameters obtained for PH devices filled with MLC2081 with various concentrations of TBATPB. All devices were coated with SE130 polyimide (by AWAT). T_{NI} were measured at time of dielectric spectroscopy. σ_0 and m are fitting parameters from equation (5-42).

ϕ_{ions}(%)	**0**	**0.3**	**0.5**	**1.0**	**2.3***	**0.6****
***d*(µm)**	19.6 ±0.2	18.9 ±0.3	19.2 ±0.2	19.1 ±0.2	18.9 ±0.1	10 ±0.2
T_{NI}(°C)	112 ±2	118 ±1	119 ±1	114 ±2	115 ±2	112 ±2
σ_0(nS/m)	0.52 ±0.06	120 ±20	20 ±2	120 ±20	130 ±10	450 ±20
m (°C^{-1})	0.044 ±0.001	0.040 ±0.001	0.040 ±0.001	0.067 ±0.002	0.053 ±0.001	0.0305 ±0.0006
$\sigma_\infty(S)$	0.024 ±0.009	1.1 ±0.4	0.23 ±0.08	54000 ±22000	230 ±60	0.21 ±0.04
$E_A(k_B)$	5000 ±100	4500 ±100	4600 ±100	7500 ±100	6000 ±80	3720 ±60

5.3.1.c *Long Term Effects of Ions*

Over large time periods the T_{NI} was measured to change over time from device filling. Measured T_{NI} (using POM) is plotted as a function of time (t) in Figure 5.11, where it can be seen to consistently increase in all devices. It is unclear whether this effect has any relationship with the addition of TBATPB or not, as the pure material can also be seen undergo the effect. The MLC 2081 directly from the bottle, was checked after a year and found to still have T_{NI}=112°C indicating this effect is likely due to the application of relatively low-frequency, high-voltage signals across the materials, which may be causing degradation of one or more of the mixture components. For these reasons, T_{NI} was always measured before EHDI measurements were undertaken.

The increase in T_{NI} over time is unexpected, as it would be more standard to see T_{NI} reduce as material breaks down. This odd behaviour is hypothesized to be caused by asymmetric breakdown of mixture components, where for example those with low T_{NI} are breaking at a higher rate than those with T_{NI} leading to a net increase in T_{NI}. Confirmation of this hypothesis is challenging due to unknown components of the MLC 2081.

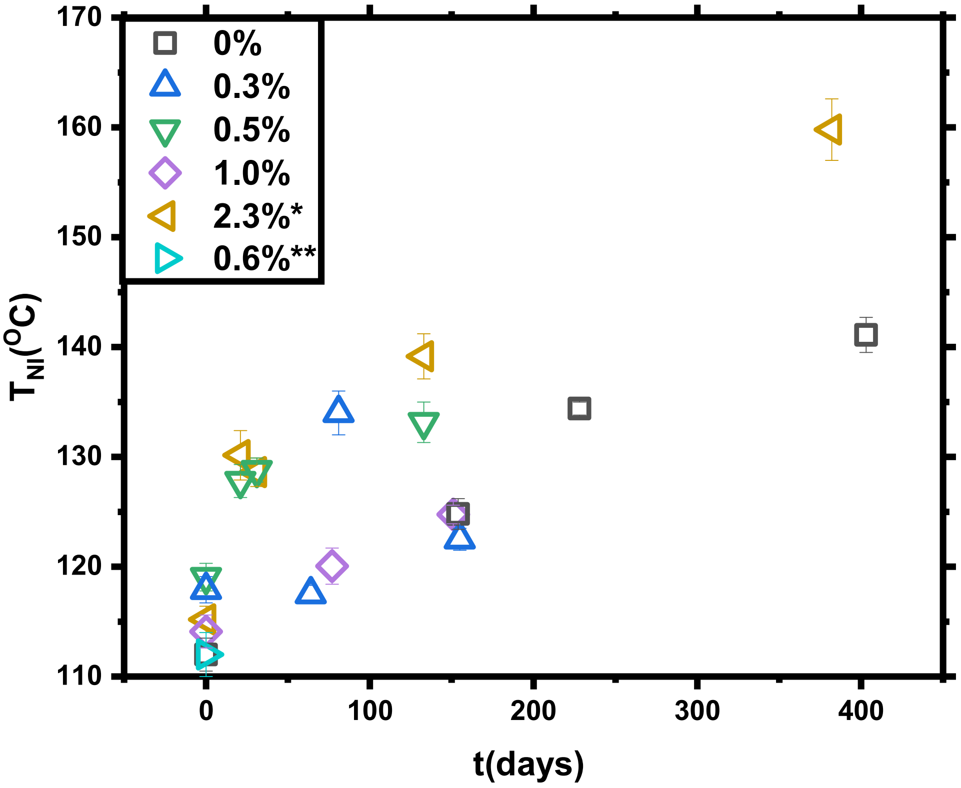

Figure 5.11. T_{NI} measured in devices as function of time since filling.

5.3.2 Effect of Conductivity and Temperature on EHDI

5.3.2.a *Microscopy Characterization of the NR Mode*

The values V_C and q_{opt} for the NR mode were measured in all 20 µm PH devices as functions of frequency using POM. Pictures of the NR mode (at V_C) are shown at two frequencies in Figure 5.12a-b. Here, the higher frequency patterns have an increased value q_{opt}. This may be due to either of the situations shown in Figure 5.12b, where the roughly circular rolls at low frequencies could be becoming more ellipsoidal or shrinking in size.

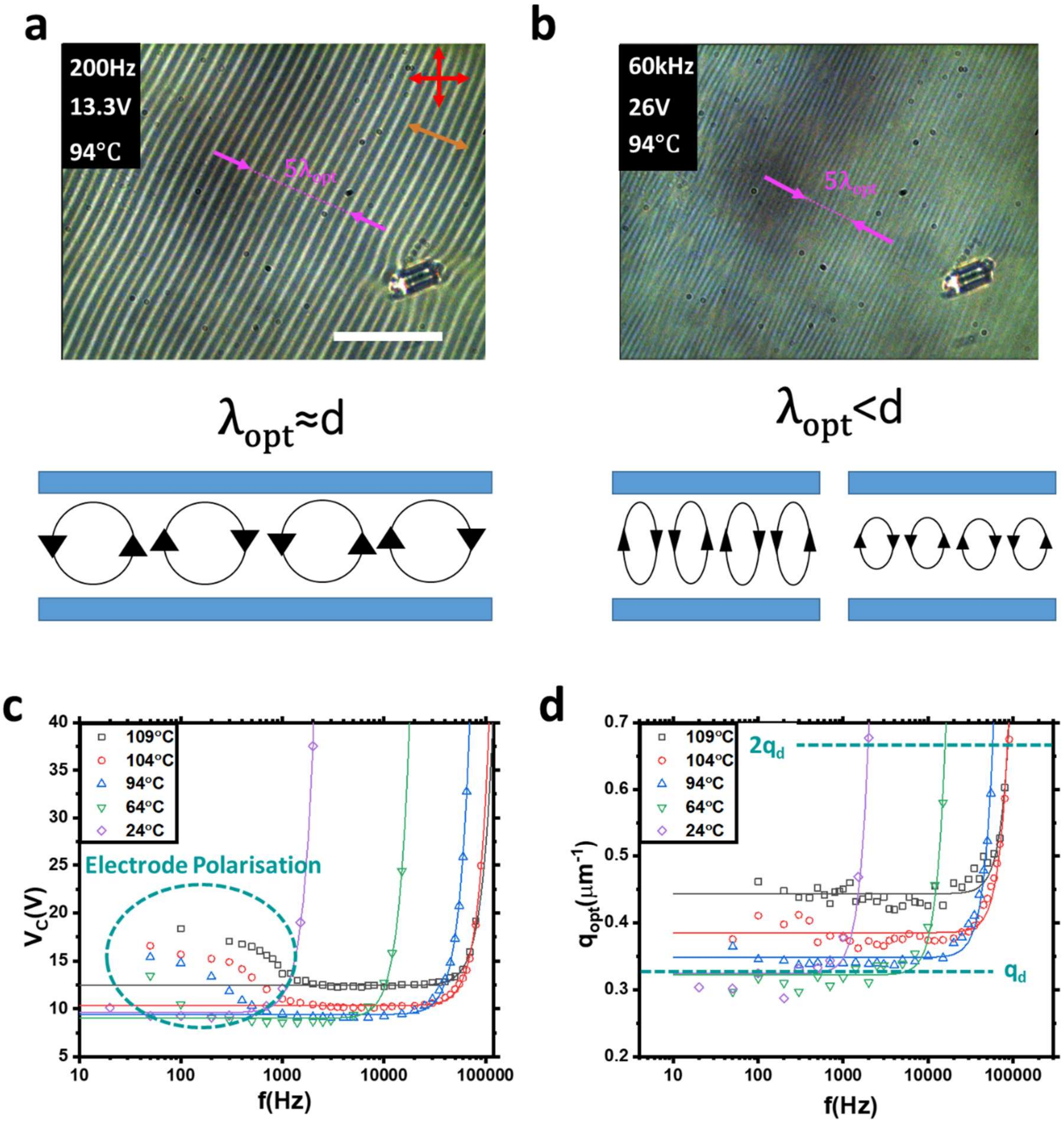

Figure 5.12. The NR threshold as functions of frequency. (a) and (b) show shrinking λ_{opt} (increasing q_{opt}) as frequency is increased. For this to occur, the hydrodynamic rolls must either become more oval or maintain their circular shape but reducing in radius. (c) and (d) give V_C and q_C as functions of frequency at several temperatures. The sample was MLC2081 with 1% TBATPB, where the T_{NI} at the time of measurement was 114℃.

Figure 5.12c-d, shows an example data set of V_C and q_{opt} measurements as functions of frequency. Here, this data is well described by the empirical expressions,

$$V_C(f) = V_0\left(1+\left(\frac{f}{f_{crit,\ V}}\right)^4\right) \tag{5-44}$$

and

$$q_{opt}(f) = q_0\left(1 + \left(\frac{f}{f_{crit,\ q}}\right)^4\right). \tag{5-45}$$

Where V_0 and q_0 are low frequency values of their respective parameters and $f_{crit,V}$ and $f_{crit,\ q}$ are frequencies where they are doubled.

At the coldest temperatures it was noted that in all samples,

$$q_0 \approx \frac{2\pi}{d}, \tag{5-46}$$

which has been previously observed[249]. Meanwhile when q_{opt} approached a value $\frac{4\pi}{d}$ the required V_C would rapidly increase, and a chevron pattern (CP) would form. This may give an indication of the behaviour of roll shape as frequency is increased, as if the rolls were maintaining circular form this may be the point where two rolls may form on top of one another. This was outlined as a potential solution to the electrohydrodynamic equations by Penz and Ford in 1971 [282], and similar 'double rolls' are observed in Rayleigh Bernard convection with extreme temperature gradients [285]. This will be discussed in more detail as a future research direction in section 9.3.3.

Data sets such as those five shown in Figure 5.12c-d, were fitted in all four of the doped devices (ranging from T_{NI}-T=5 to room temperature). This data was fitted with equations (5-44) and (5-45), respectively, where the values V_0, q_0, $f_{crit,\ V}$ and $f_{crit,\ q}$ were used to normalize the data. These are all plotted in the master curves shown in Figure 5.13. One region where (5-44) did not describe behaviour well, was at low frequencies in the most conductive samples (especially at high T, see Figure 5.12). This was taken to be due to electrode polarisation, and these data points were omitted in the fitting.

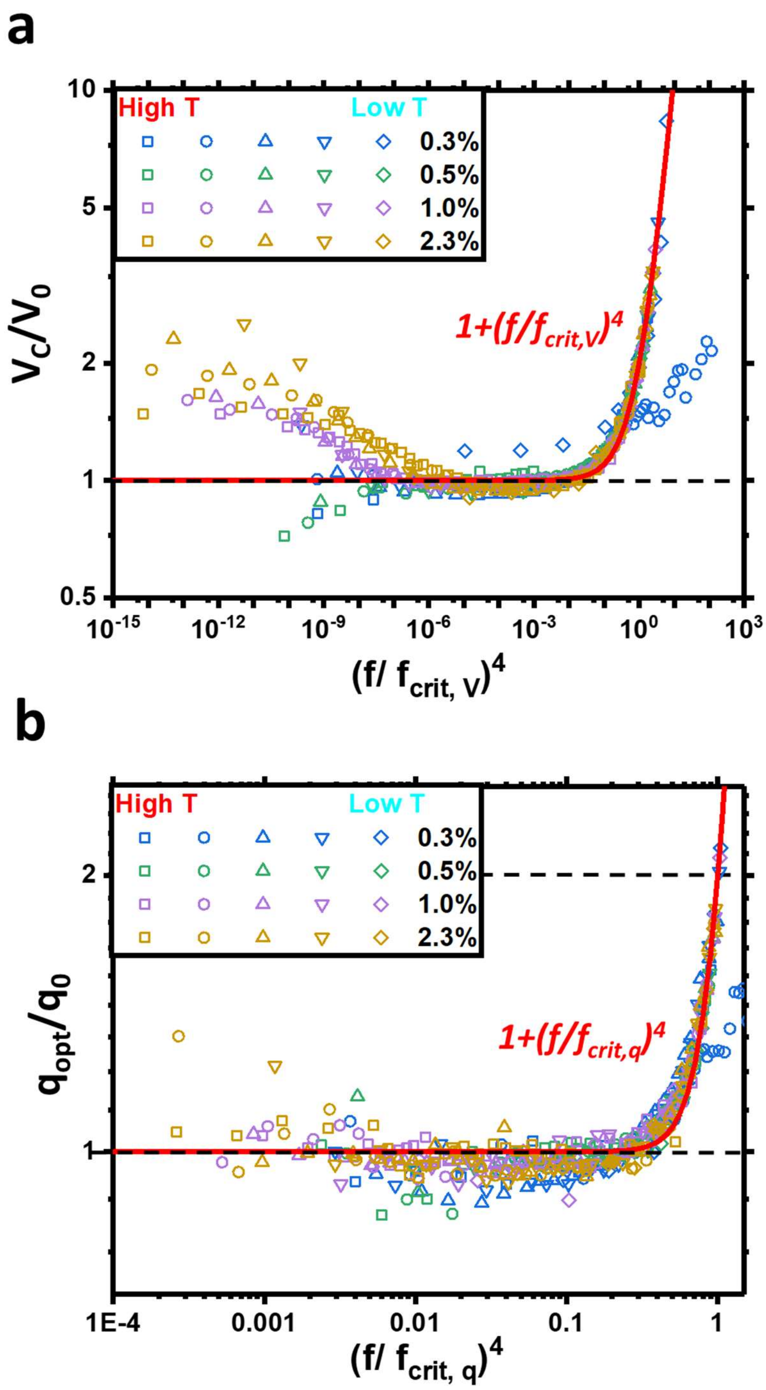

Figure 5.13. Master curves of all data for V_C/V_0 and q_{opt}/q_0 (a and b respectively). All four 20µm devices are included where the data was obtained at five different temperatures. T_{NI} values at time of measurement were 117, 129, 114 and 129℃ for 0.3-2.3% TBATPB, respectively.

The expressions given in (5-44) and (5-45) were identified as part of this project, where in reference [114] it is argued the form may be understood by a relatively simple model of circular motion. Here, if the fluid is treated as a series of particles of mass, m, undergoing circular motion of radius, r at velocity, v. The centrifugal force (F_C) can be written as,

$$F_C = \frac{mv^2}{r} = m\omega^2 r, \tag{5-47)}$$

where,

$$q_C \sim \frac{1}{r} \sim \omega^2, \tag{5-48)}$$

And

$$V_C \sim F_C \sim \omega^2. \tag{5-49)}$$

All results given indicate that V_C and q_C appear to mutually increase at the same frequency, indicating (which is also given in predicted in theory of (5-15)),

$$V_C \sim q_C. \tag{5-50)}$$

Combining these relations, gives,

$$V_C \sim q_C \omega^2 \sim \omega^4. \tag{5-51)}$$

and

$$q_C \sim V_C \omega^2 \sim \omega^4. \tag{5-52}$$

Although simple, this model does appear to describe the observed trends in frequency. However, investigations with a wider variety of materials would be required to confirm the dependencies. It may be for example; this simple rotational behaviour is only seen in very conductive samples.

To examine the effect of temperature and conductivity on the parameters V_C and q_C the fitting parameters from (5-44) and (5-45) were compared to the temperature and conductivity of the materials. Values V_0 were not found to vary significantly between devices, where no clear trend with conductivity was seen. However, it does vary significantly with temperature. This is shown in Figure 5.14a where it appears to be at a minimum value in the region of 60±20°C in all samples. This behaviour is likely caused by the complex effect of temperature on EHDI, where it changes many parameters simultaneously. Here, increasing T will decrease the system elasticity, but it will also increase the thermal dissipation of coherent flows [243]. It is probable that this causes the local minimum in V_0, where the interplay between reducing elasticity and increasing dissipation are balanced. The behaviour seems unlikely to be caused by differences in conductivity, as we have demonstrated these samples have highly varied σ_p values, but we observe little coherent variance between them. It is likely these effects also have some dependency on ε, however this behaviour is difficult to predict, as it is unknown which of the competing electric fields (E_{app} and E_{ions}) are dominating in this system. The results for q_0 as a function of temperature (Figure 5.14b) show a similar lack of difference between devices, however it increases with T. This likely has a similar cause, where the wider rolls cannot form at higher temperatures due to increased thermal dissipation.

In contrast, the values $f_{crit,\ V}$ and $f_{crit,\ q}$ do show strong correlations with conductivity (Figure 5.14c-d). These are reasonably linear in the log-log plots, meaning,

$$log_{10}(f_{crit}) = mlog_{10}(\sigma_p) + c, \tag*{5-53)}$$

for each $f_{crit.}$ The fitting parameters obtained using equation (5-53) were c=0.82±0.03 and 0.80±0.03 for $f_{crit,\ V}$ and $f_{crit,\ q}$ respectively, while in both m= 8.2±0.2. This behaviour can be understood as being due to the materials with more abundant charge carriers being able to maintain the EHDI process at higher frequencies.

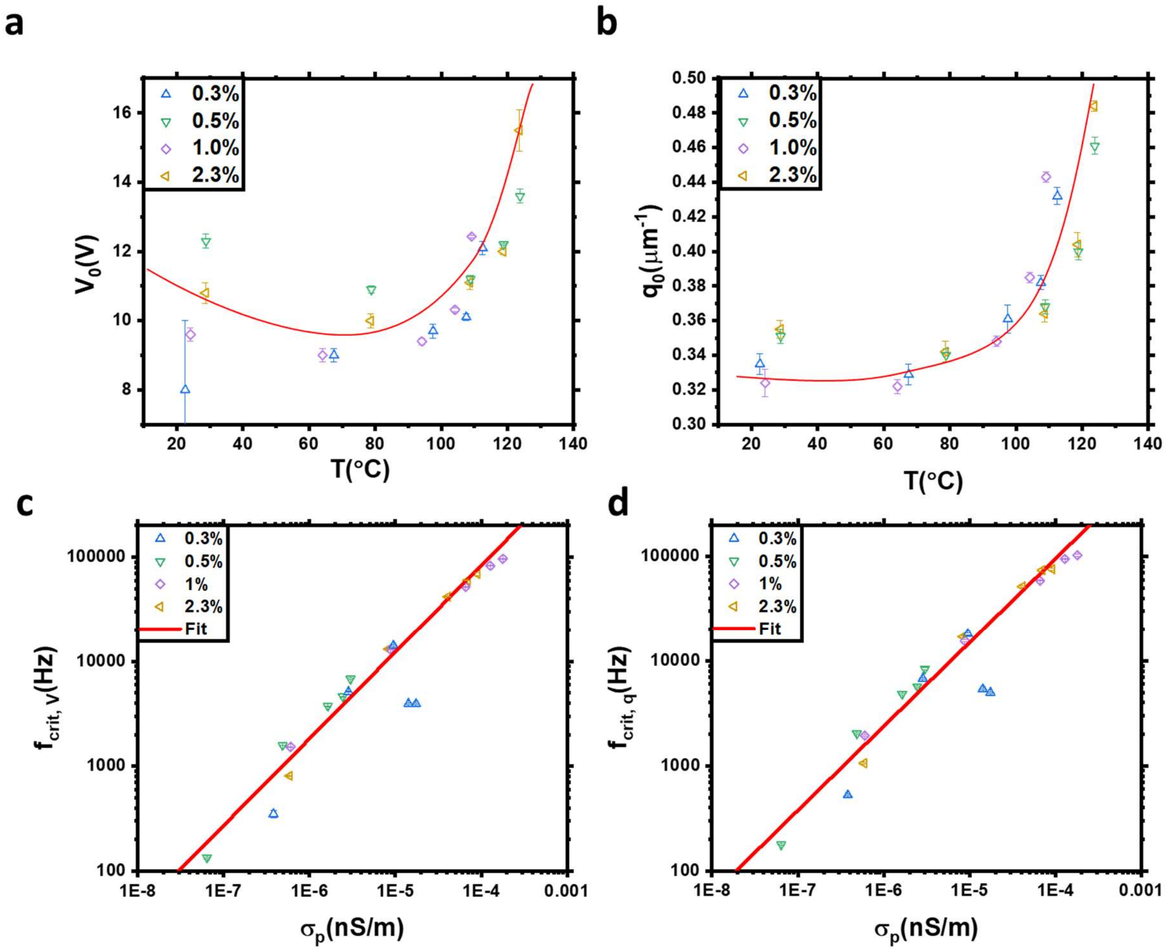

Figure 5.14. Fitting parameters obtained from fitting data using equations from (5-44) and (5-45). (a) V_0 against temperature, (b) q_0 against temperature. In both red lines are included as a guide to the eye. (c) and (d) show $f_{crit,\ V}$ and $f_{crit,\ q}$ as functions of the measured conductivity plateau (σ_p). These were fitted with equation (5-53).

The only PH device that did not display the behaviour describable by equations (5-44) and (5-45) was the pure MLC 2081. Here, the first textured structures observed as V was increased (at T=28°C), were highly oblique rolls at very low frequencies (f<1Hz) and chevrons at higher frequencies (f>3Hz, see Figure 5.15a-b). These textures indicate, other than the oblique rolls seen at sub-Hz frequencies, this device is being driven in the dielectric regime [269], which was confirmed by the linear dependency of V_C with f (Figure 5.15c) [251]. Here, f_{diel}≈1Hz and demonstrates the need for TBATPB in this work.

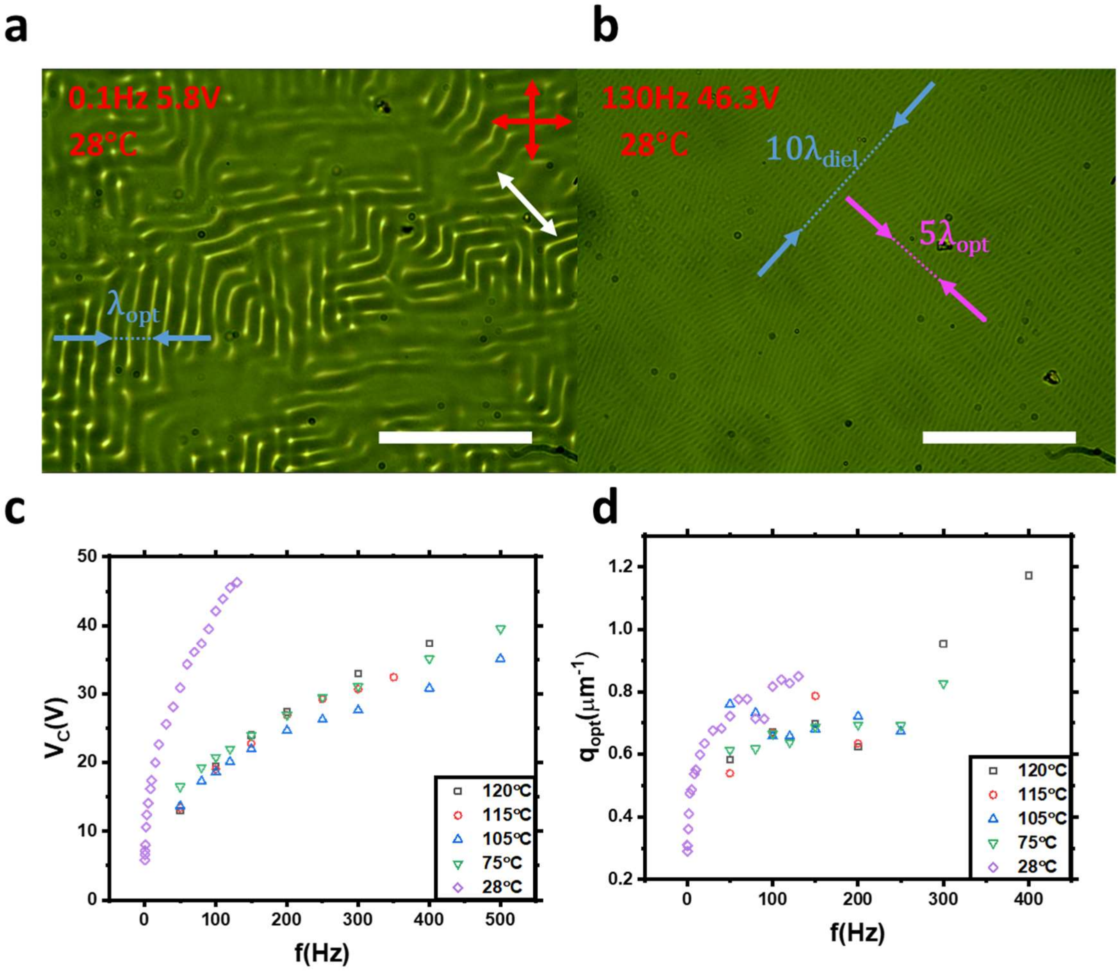

Figure 5.15. Results from the undoped 20 μm sample. The electroconvection was significantly different to the doped samples. Patterns at low and high frequencies are shown in (a) and (b) respectively, where highly oblique rolls and dielectric rolls are shown respectively. (c-d) V_C *and* q_C *as functions of frequency at several temperatures. The shape of the data and patterns indicate being close to* f_{diel}.

5.3.2.b *Diffractive Properties*

To assess the EHDI patterns as DOEs the devices were investigated with diffraction spectroscopy. The measured values θ_m are plotted in Figure 5.16a, where a fitting of,

$$sin\theta_{m=2} = sin\theta_{0,\ m=2}\left(1+\left(\frac{f}{f_{crit,\theta}}\right)^4\right), \tag{5-54}$$

is used (this can be directly derived from equation (5-39) and the grating equation). The fitted values $f_{crit,\ \theta}$ are plotted as functions of σ_p in Figure 5.16b, where similar behaviour to other f_{crit} is observed.

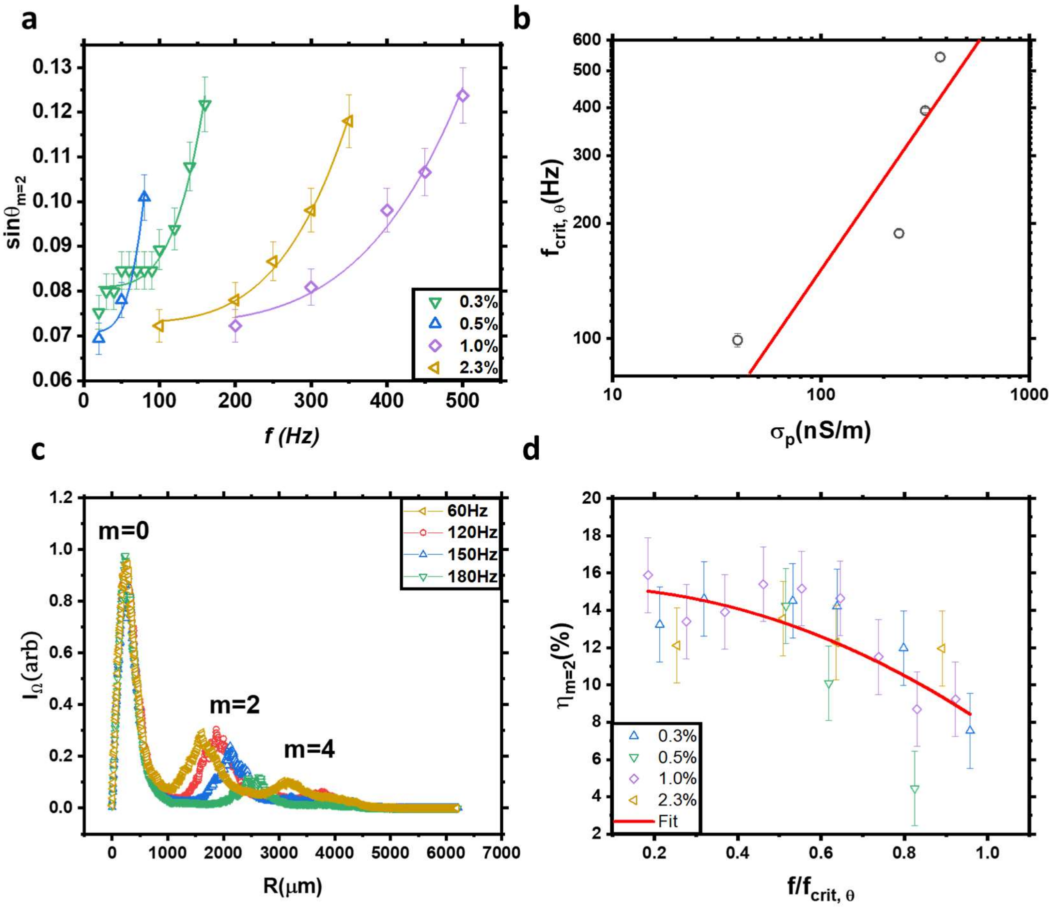

Figure 5.16 Results from diffraction experiments on 20μm spaced devices, taken at T≈17℃. (a) Results of measured angle of the m=2 order. This was fitted with equation (5-54). (b) $f_{crit,\ \theta}$ as a function of σ_p values. (c) Example output from the beam profiler (0.3% TBAPTB). (d) Values $\eta_{m=2}$ as normalized frequency is varied. The data is fitted with equation (5-55).

In measuring diffraction efficiencies, an example data set from the beam profiler output is shown in Figure 5.16c, where the summed radial intensity (I_Ω) is plotted as a function of distance from the centre of the pattern (R). As frequency was increased the m=2 peak migrates to wider angles, while the odd m orders were too faint to be detect. Figure 5.16d shows the values $\eta_{m=2}$, in all 20μm devices as normalized frequency was varied. A general trend of decreasing value with increased frequency is observed, which fits a quadratic expression,

$$\eta_{m=2} = \eta_{max}\left(1 - k\left(\frac{f}{f_{crit,\theta}}\right)^2\right). \tag{5-55}$$

A concatenated fit of all data gave η_{max} =15.3±0.7% and k= 7±2. From the assumption of the pattern acting as a sinusoidal Raman-Nath grating, the result of η_{max}=15% gives the predicted tilt angle of around 22° (see Figure 5.5b). The reduction in efficiency with increased frequency may have 3 possible causes (1) The value of θ_{max} is reduced, (2) the roll height is shrinking (3) scattering is increasing in the device. This was further investigated by looking at several similar devices of different d.

5.3.3 Effect of Device Spacing

Devices of spacing 5µm and 10µm filled with MLC 2081 doped with 0.6% TBATPB were compared to the 20µm device filled with 0.3% TBATPB (this was chosen due to similar conductivity to 0.6% TBATPB, see Figure 5.10). Figure 5.17a-b shows the values V_c and q_c as f was varied (measured using POM). Here, little difference is seen between devices V_C value as functions of normalized frequency (±1V at low f). Meanwhile, the q_{opt} values appear to be strongly effected by device spacing. Here, as frequency is increased q_{opt} increases from $\frac{2\pi}{d}$ to a maximum value $\frac{4\pi}{d}$. Larger q_{opt} values than $\frac{4\pi}{d}$ were not seen, where when they approached this value the chevron pattern would form.

Diffraction experiments were performed on these devices, where instead of the entire diffraction pattern being analysed simultaneously by the beam profiler, each order was individually measured for intensity. Despite this change in technique, the 20µm device saw similar results for $\eta_{m=2}$, where as the frequency was increased a reduction in value from 15% to 5% was observed. Meanwhile, the 10µm device appeared to reduce from a value of around 5% down to 1-2%. The 5µm device could not be examined with diffraction analysis, as at ambient temperatures it could not be forced to adopt a state of EHDI. So to compare q_c values were obtained using POM and the resulting angles predicted Figure 5.17c shows $\sin\theta_{m=2}$ as a function of normalized frequency in the 10 and 20µm devices, where the values θ_0 were 8.5±0.2° and 4.4±0.2° respectively.

These results give indicate that the changing values q_{opt} are caused by rolls maintaining their circular shape, but reducing in radii, as the low frequency 10µm device appeared to have similar optical properties to the high frequency 20µm device. Importantly, these devices also see the formation of the chevron pattern at the point where, q_{opt}=$\frac{4\pi}{d}$. This enhances further earlier observations that it if the rolls becoming less than half the device spacing, which allows their overlaying into chevron patterns (Figure 5.17d).

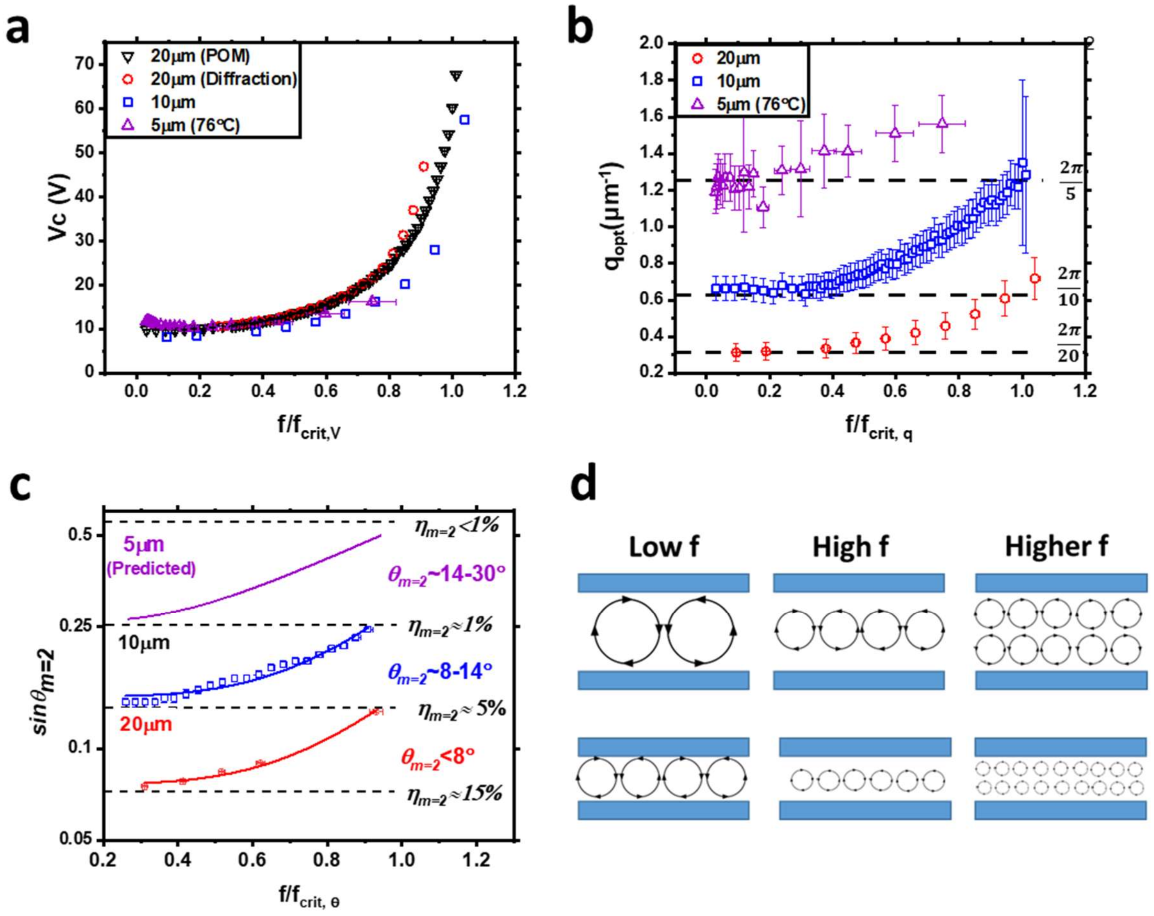

Figure 5.17. Effect of device spacing, d. (a-b) V_c and q_C values as functions of normalized frequency taken with POM. All sample q_C values were seen within the limits $\frac{2\pi}{d}$ and $\frac{4\pi}{d}$.As they approached $\frac{4\pi}{d}$ the V_C value rapidly increased and the dielectric regime begun. (c) Measured diffraction angles of the 20 and 10μm devices as well as the predicted ones for the 5μm. Here, the efficiency of the 20μm at high frequencies is very similar to the 10μm at low frequencies. (d) Diagram giving the inferred behaviour. Here, as frequency is increased the rolls first shrink to $q_{opt}=\frac{4\pi}{d}$then adopt a new more complex pattern of the chevron type.

5.4 Conclusions

This chapter presents the results of an investigation of several NLC systems in states of EHDI. Particularly the function of the NR mode as a variable pitch diffraction grating, was examined. The key parameters were the attainable steering angles, the breadth of continuous steering and the efficiency of diffractive orders. From the results presented, we have shown that for this NLC material the attainable q_{opt} values (which dictate steering angles) are limited to the range of approximately $\frac{2\pi}{d}$ and $\frac{4\pi}{d}$, meaning the angles and the breadth of steering are determined almost exclusively by d. The efficiency of the orders are also seen to reduce as wider angles are attained. Here, we have argued this is likely due to the reduction in the overall phase contrast as the hydrodynamic rolls shrink while maintaining circular form. Our results indicate that these limits cannot be changed through modulation of material conductivity.

These observations accumulatively do not indicate EHDI in NLC are promising as DOEs. However, in these investigations we have focussed on a calamitic material with standard elastic constants. In work published as part of this project[232], we posited the idea of potentially varying the shape of the rolls using NLC materials of novel elastic constants. This will be the focus of the following chapter, where a dimeric mixture was created, which was predicted to promote ovular rolls (high optical path difference, short pitch)[114].

Chapter 6 Electrohydrodynamic Gratings in Materials of Unusual Elastic Constants

6.1 Introduction

In the previous chapter, Nematic Liquid Crystals (NLCs) in a state of Electrohydrodynamic instability (EHDI) were investigated as optical gratings. It was found that in the standard calamitic liquid crystal, MLC 2081, the wavevectors (q_{opt}) of the Normal Roll (NR) mode obey the relation,

$$\frac{2\pi}{d} < q_{opt} < \frac{4\pi}{d}. \tag{6-1}$$

If NLCs in a state of EHDI are to be used as Diffractive Optical Elements (DOEs), widening the range of attainable q_{opt} values is highly desirable. A possible method of improving the range of q_{opt} is through creating mixtures with tailored elastic constants. From the deformation in NLC structure induced by EHDI, it was hypothesized during this project that greater q_{opt} values may be attainable if the bend elastic constant (k_{33}) is reduced. This is illustrated in Figure 6.1, where due to lowered bend resistance, it was predicted that the optimised EHDI pattern would alter, reducing in period (λ_C) increasing q_{opt}[232]. This is the subject of this chapter, where through using a mixture of unusual elastic constants the role of the elastic constants in determining q_{opt} is examined. The results and discussion contained in this chapter has been published in reference [114].

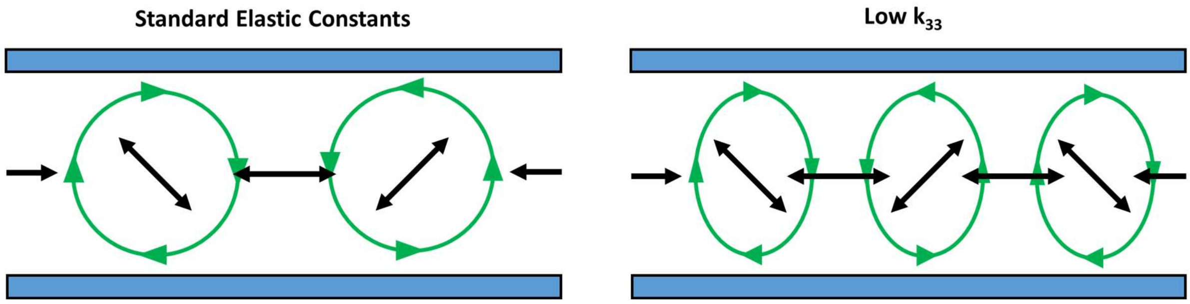

Figure 6.1. Proposed method to reduce the pitch of EHDI gratings. By lowering k_{33}*, the director can bend out the plane more, which leads to hydrodynamic patterns becoming more ovular.*

6.1.1 Elastic Constants of Bent Liquid Crystal Mesogens and their Mixtures

Two classes of materials which often form novel liquid crystal phases are bent dimeric (BD)[12,46,291–297,47,52,53,286–290] and bent core (BC) [12,48,304,49,50,298–303] mesogens. In their nematic temperature range these materials often display unusual ratios of elastic constants

[47,49,53,290,293,298,305]. Even in standard calamitic materials elastic constants very close to T_{NI} can adopt unusual ratios, however at T_{NI} - T>5°C usually the elastic constants obey the following relation[45,306],

$$k_{22} < k_{11} < k_{33}. \tag{6-2}$$

Meanwhile, the NLC phases made up of BD and BC mesogens often have [46–48,297,298],

$$k_{33} < k_{11}. \tag{6-3}$$

BC and BD mesogens often do not exhibit nematic phases at ambient temperatures, leading to difficulties in utilizing them in devices. A way to overcome this, while maintaining unusual elastic constant ratios, is through mixing BC or BD mesogens with calamitic materials [307–316]. A relevant example of this was published by Parthasarathi et al. in 2016[312], where calamitic material 7OCB was mixed with various quantities of bent dimer CB7CB (Figure 6.2a). The values of measured k_{11} and k_{33} at various molar concentrations of CB7CB (M_{CB7CB}) published by Parthasarathi et al. [312] are plotted as a function of T_{NI}-T in Figure 6.2b-c. At high M_{CB7CB} in 7OCB mixtures, k_{33} is seen to initially increase with reduced temperature before reducing. This effect has been the subject of previous studies and it is believed to be caused by a changing ratio of different CB7CB conformers [46,52,53,287,289,292,303,317,318]. Taking the values at T_{NI}-T=10°C (Figure 6.2d), k_{11} and k_{33} can both be seen to vary with M_{CB7CB} in a 'hockey stick' shape. Here, at M_{CB7CB} < 90% k_{33} is seen to reduce approximately linearly with M_{CB7CB}. This method of mixing dimers with standard calamitic NLCs was used to lower k_{33} in this work to examine the effect on EHDI.

It should be noted that often when combining calamtic (nematic-forming) mesogens with either BC or BD materials, more complex effects than variation of elastic constants can occur. For example when BD mesgoens are mixed into a nematic phase made up of calamitic molecules, the constituent phase will often adopt a twist bend nematic (N_{tb}) conformation with certain thermodynamic ranges [309,312]. Additionally, phase seperation is often observed in the mixtures of either BD or BC molecules with calamitic ones [319–321].

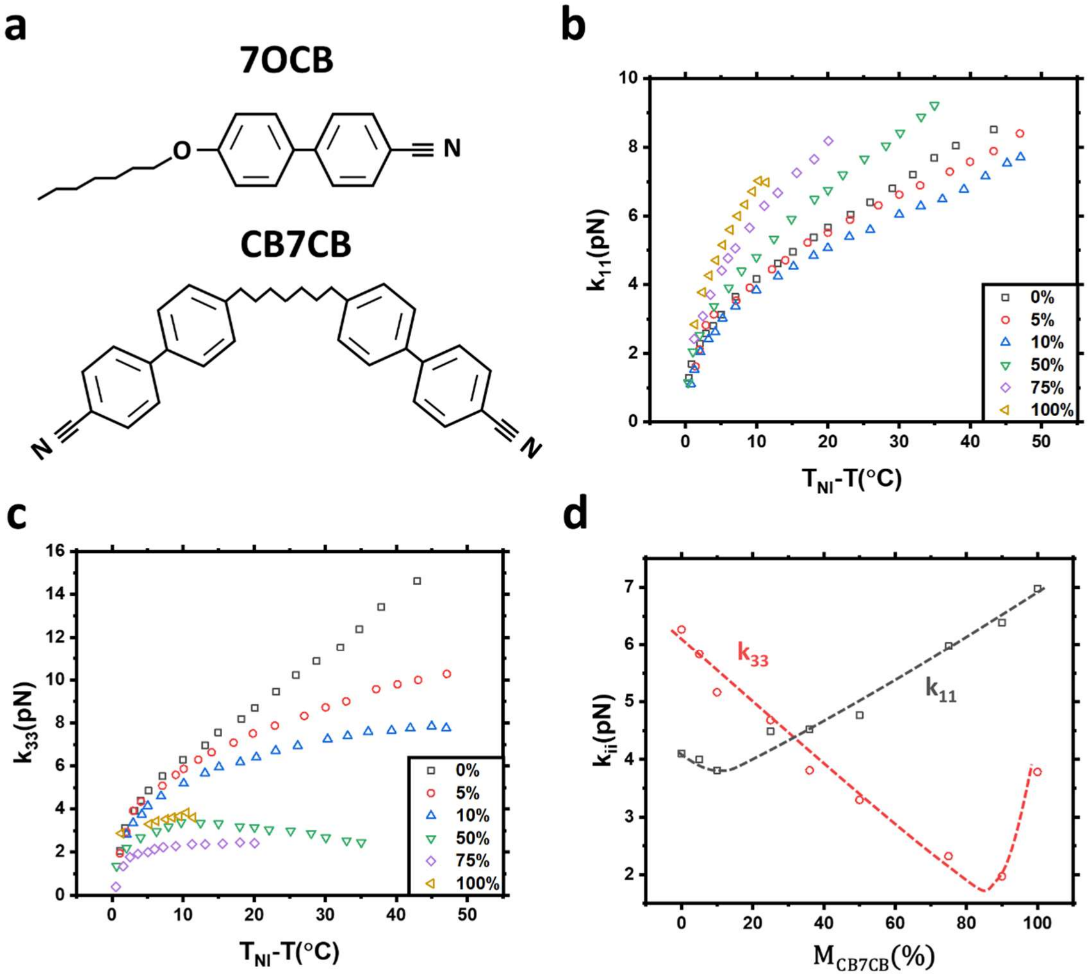

Figure 6.2. Splay and bend elastic constants in binary mixtures of 7OCB and CB7CB. (a) Chemical structures of components. (b) and (c) the splay and bend elastic constants as a function of reduced temperature. Here the % refers to M_{CB7CB}. (d) Splay and bend elastic constants as function M_{CB7CB} at T_{NI}-T=10℃. Data taken from reference [312].

6.1.2 Electroconvection in Bent Liquid Crystal Mesogens and their Mixtures

Previously studies have been undertaken examining electroconvection in BC[299,322–324] and BD[325,326] materials. Often, due to the sharply contrasting properties of the BC and BD phases, the EHDI behaviours exhibited are often significantly different to those of calamitic materials. These differences are attributed to: (1) materials often having the unusual property of negative conductivity anisotropy ($\Delta\sigma<0$)[322], (2) larger molecular sizes tending to lead to dielectric relaxation processes at lower frequencies[327], (3) odd elastic constant ratios[46,327] and (4) larger flexoelectric terms[278,281,328–330].

References [322,324,329,331] report on the results for threshold of EHDI's as function of frequency in BC materials. In reference [322] the general the form shown in Figure 6.3 is reported. Here, LR are longitudinal rolls, which are similar to the Normal Roll (NR) pattern, however the rolls normal ($\hat{\boldsymbol{q}}_C$) is perpendicular rather than parallel to the director (***n***). This can be understood to be caused by the BC material being used having negative dielectric and conductivity anisotropies ($\Delta\varepsilon<0$, $\Delta\sigma<0$)[322,332]. The Prewavy Patterns (PWP) are both similar to PWP discussed in the previous chapter, where $\boldsymbol{q}_{PWP}$ is parallel to initial ***n***.

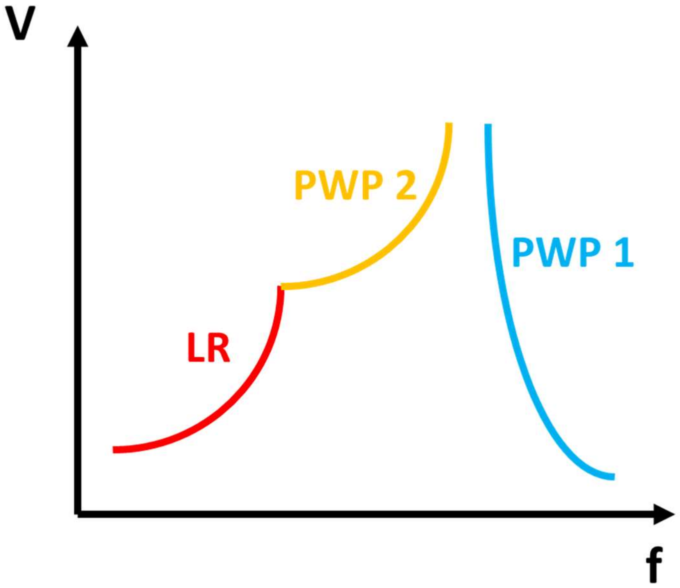

Figure 6.3. General patterns seen at threshold of EHDI in BC systems.

Limited similar experiments have been undertaken to investigate electroconvection in dimeric materials with the only examples found in literature references[325,326,333,334]. In these, no mappings of the frequency-voltage space were presented. Such will not be provided in this work, however it is important to note that in studies of EHDI in both the BC and BD materials, a low frequency roll regime (similar to the NR mode) exists.

The differences in resulting textures from EHDI in pure BC and BD materials, makes their comparison to the standard calamitic materials challenging. In this work, a material of unusual elastic constants, which undergoes standard EHDI, was created for this purpose.

6.2 Methods

6.2.1 Devices

Two kinds of device were used for this work:

- **GR.** 10 µm Guard ring devices fabricated with methods outlined in section 3.1. The alignment layers used were rubbed SE2170 for PH alignment and SE1211 for HT.
- **AWAT.** 20 µm spaced cells purchased from AWAT with square electrodes (similar to those used in the previous chapter). These have a SE130 PH alignment.

6.2.2 Materials

The LC materials used in this work were various mixtures of MLC 2081, CB7CB and TBATPB. CB7CB has phase sequence: *Iso* (116°C) *N* (102°C) N_{tb} [53,293], and as shown in Figure 6.2 can lower k_{33} when mixed into calamitic materials[312]. Issues with using this material are its positive Δε (≈2[46,309]) and propensity to form the N_{tb} phase. To avoid such, sufficient MLC 2081 was needed to supress N_{tb} and maintain a negative $\Delta\varepsilon$. The work of Trbojevic et al. [309] was used to inform the ratios, where typically N_{tb} phases exist if the concentration of CB7CB is greater than 50%. Due to these properties, a mixture of 60% MLC 2081 and 40% CB7CB was created. This was compared to MLC 2081 with various quantities of TBATPB. The format $\phi_{MLC2081:CB7CB:TBATPB}$ is used to describe the concentration of the components of each material, where the subscripts are ratios of one another (i.e. $\phi_{60:40:0}$ is 60% MLC2081, 40% CB7CB and 0% TBATPB).

6.2.3 Dielectric Analysis

Both pure MLC 2081 ($\phi_{100:0:0}$) and dimeric mixture ($\phi_{60:40:0}$) were placed in HT and PH GR devices to perform dielectric spectroscopy, where $\varepsilon_{\perp}$, $\varepsilon_{||}$, k_{11} and k_{33} were measured as functions of temperature (T)[100,101,206]. For capacitance measurements, the oscillation frequency was held at 50 KHz for one minute, while for conductivity measurements plateau values were obtained as discussed in section 5.3.1.a. Between HT and PH devices a small offset (~5%) in ε values was observed, which was attributed to slight differences in alignment layer thicknesses (d_{AL}). These were approximated to affect the measured permittivity of the LC (ε_{LC}) and the voltage applied (V_{LC}) by,

$$\varepsilon_{LC} = \frac{\varepsilon_m}{1 - 2\frac{d_{AL}\varepsilon_{LC}}{d_{LC}\varepsilon_{AL}}}, \qquad (6\text{-}4)$$

and

$$V_{LC} = \frac{V_{app}}{1 + 2\frac{d_{AL}\varepsilon_{LC}}{d\varepsilon_{AL}}}, \tag{6-5}$$

where ε_m is the measured permittivity, ε_{AL} is the alignment layer permittivity (3.1[73]) and V_{app} is the applied voltage. The values of d_{AL} used for this are given in Table 6-1 and were obtained through comparing the data sets to literature from Merck and ensuring $\varepsilon_{\perp} = \varepsilon_{//}$ both above T_{NI} and at T=63°C (in $\phi_{60:40:0}$). The difference due to this rescaling leads to small differences in the magnitude of ε (~5%) and smaller changes to elastic constants (k_{ii}), however add significant clarity to results.

Table 6-1. Devices used for dielectric investigations.

Material	$\phi_{100:0:0}$	$\phi_{100:0:0}$	$\phi_{60:40:0}$	$\phi_{60:40:0}$
Device Type	GR	GR	GR	GR
Alignment/Polyimide	PH/SE2170	HT/SE1211	PH/SE2170	HT/SE1211
d(μm)	10.6±0.2	10.5±0.5	10.6±0.4	10.5±0.5
d_{AL}	60	210	180	40

6.2.4 EHDI Characterization

Polarized Optical Microscopy (POM) was used to measure V_C and q_C as functions of frequency in a similar manner to measurements performed in the previous chapter. Here, comparison between $\phi_{100:0:X}$ and $\phi_{60:40:0}$ allowed the effects of changing elastic constants to be observed. Table 6-2 lists devices used to investigate EHDI. Additionally, diffraction analysis was performed on the 20 μm devices, to confirm q_{opt} behaviour through measurement of the diffraction angles (θ_m).

Table 6-2. Devices used for EHDI experiments.

Material	$\phi_{100:0:0.5}$	$\phi_{100:0:1}$	$\phi_{100:0:0.6}$	$\phi_{60:40:0}$	$\phi_{60:40:0}$
d(μm)	19.2±0.3	19.1±0.2	10.0±0.2	10.6±0.4	18.9±0.2
Device Type	AWAT	AWAT	AWAT	GR	AWAT
Alignment/Polyimide	PH/SE130	PH/SE130	PH/SE130	PH/SE2170	PH/SE130

6.3 Results and Discussion

6.3.1 Material Analysis

6.3.1.a *Transition Temperatures and Behaviour $\Delta\varepsilon$*

Pure MLC 2081($\phi_{100:0:0}$) is a negative $\Delta\varepsilon$ NLC material between 112±2°C and ambient temperatures (T_{amb}), thus its Fréedericksz transition was probed in the HT device. The dimer mixture ($\phi_{60:40:0}$) had more complex behaviour of $\Delta\varepsilon$ as a function of T, where when cooled from T_{NI} (102±2°C) at approximately T=63°C the material switched from being positive to negative. This meant both PH and HT devices were used to measure the transition (below and above 63°C, respectively).

Examples of fitting $\varepsilon(V)$ are shown in Figure 6.4. In the pure material (Figure 6.4a), $\Delta\varepsilon$ continuously decreases with T, until T_{NI} where $\Delta\varepsilon$=0. Meanwhile, Figure 6.4b-c show the same for the dimeric mixture below and above 63°C (when negative and positive). In Figure 6.4b $\Delta\varepsilon$ continuously decreases with T, however in Figure 6.4c it increases then decreases.

The odd behaviour of the dimer mixture likely arises from the molecular chemistry of CB7CB, where results have been previously presented indicating as temperature is varied the proportion of "hairpin" and "banana" conformers changes [53,295,296,318]. Considering these conformers (Figure 6.4d), it is apparent the hairpin will have a larger ratio of dipole moments (δ)[318],

$$\delta = \frac{\mu_{||}}{\mu_{\perp}}, \tag{6-6}$$

where $\mu_{\perp}$ and $\mu_{//}$ are dipole moments perpendicular and parallel to the director (***n***) respectively. Dunmur and Luckhurst [318] report that more hairpins occur at higher temperatures, which may account for positive $\Delta\varepsilon$ at high T, negative $\Delta\varepsilon$ at low T.

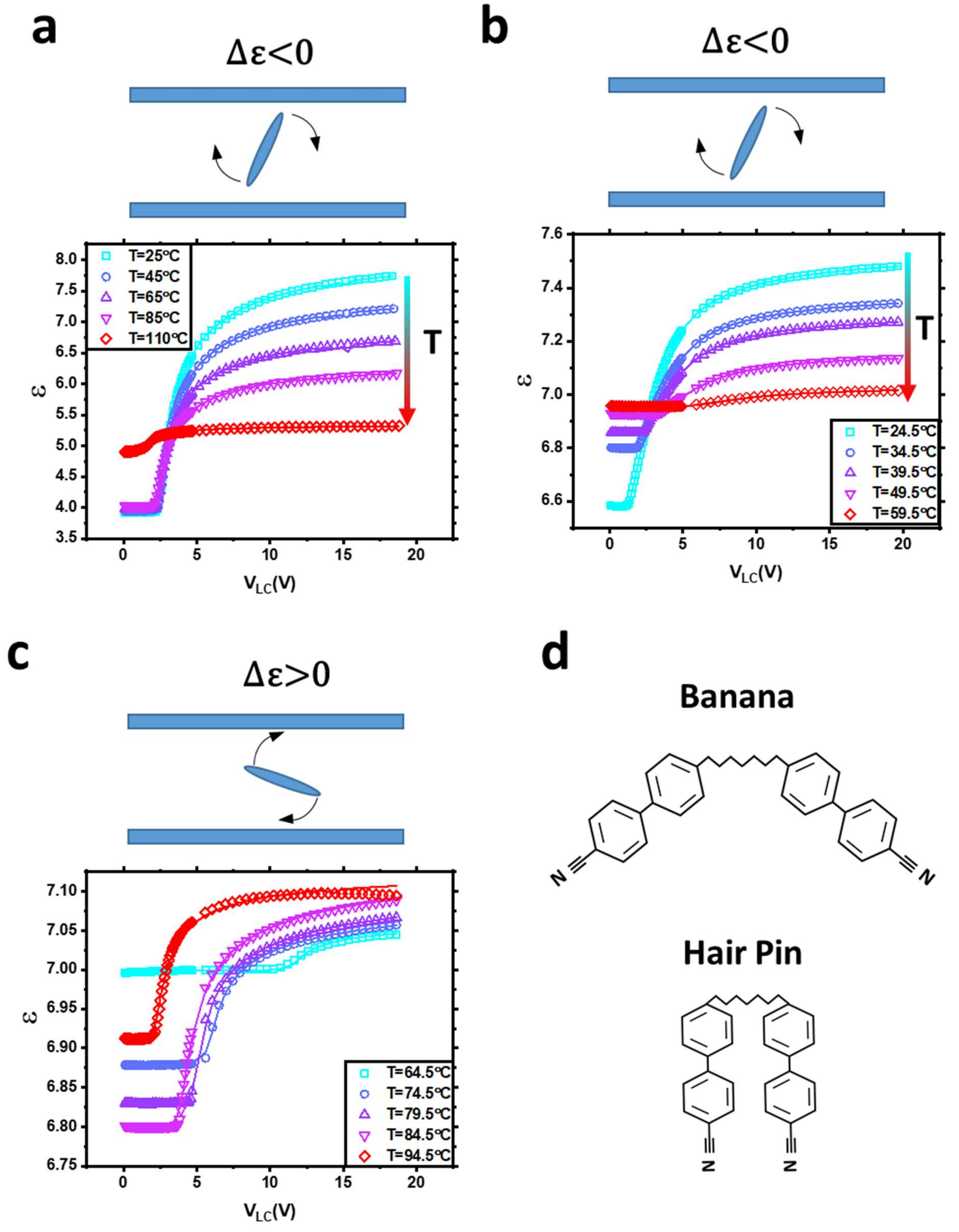

Figure 6.4. Permitvity (ε) as function of voltage (V_{LC}) at several temperatures. (a) MLC 2081 in HT device (b) Dimeric mixture in HT device (T<63℃) (c) Dimeric mixture in PH device (T>63℃). (d) the conformers of CB7CB leading to its odd dielectric behaviour.

6.3.1.b *Permitivities and Elastic Constants of MLC 2081*

Figure 6.5 shows dielectric results for MLC 2081. Figure 6.5a gives graphs of $\varepsilon_\perp$, $\varepsilon_{//}$ and $\bar{\varepsilon}$, where,

$$\bar{\varepsilon} = \frac{\varepsilon_{||} + 2\varepsilon_{\perp}}{3}. \tag{6-7}$$

Here, the errors (5% in $\varepsilon_\perp$ and $\varepsilon_{//}$) are taken from the rescaling process described in equations (6-4) and (6-5), and are for the magnitude of ε rather than the trend which is more certain. As T is varied, the material displays the same behaviour as discussed in the previous chapter, where, on cooling from T_{NI} the order parameter meter *(S)* increases, leading to increasing $\Delta\varepsilon$. Figure 6.5b compares the elastic constants k_{11} and k_{33} in MLC 2081 as a function of T_{NI} - T. To demonstrate the small effect of the rescaling described in equations (6-4) and (6-5) the calculated k_{ii} without this processing are included (marked as k_{ii}'). Usual behaviour for a calamitic NLC is observed with k_{33}>k_{11}. Figure 6.5c replots these results as functions of T/T_{NI}, this is fitted to an approximate form of Haller's equation[42,335],

$$k_{ii} = k_{ii}^{0}\left(1 - \frac{T}{T_{NI}}\right)^{n_{hal,ii}}, \qquad i = 1,3 \tag{6-8}$$

where the fitted values of the rescaled data are given in Table 6-3.

Table 6-3. Details of elastic constant fits as a function of temperature. Here, different fits have assosiated fitting parameters.

Material	**Fitting Eq**	**Parameters**			
$\phi_{100:0:0}$	**(6-8)**	k_{11}^{0}**(pN)**	$n_{hal,11}$	k_{33}^{0}**(pN)**	$n_{hal,ii}$
		34.4±0.8	0.55±0.01	57±2	0.60±0.02
$\phi_{60:40:0}$	**(6-9)**	***K*(pN)**	m_{11}***(pN/K)***	K_{33}^{0}**(pN)**	m_{33}***(pN/K)***
		37±4	0.09±0.01	-16±2	0.059±0.005

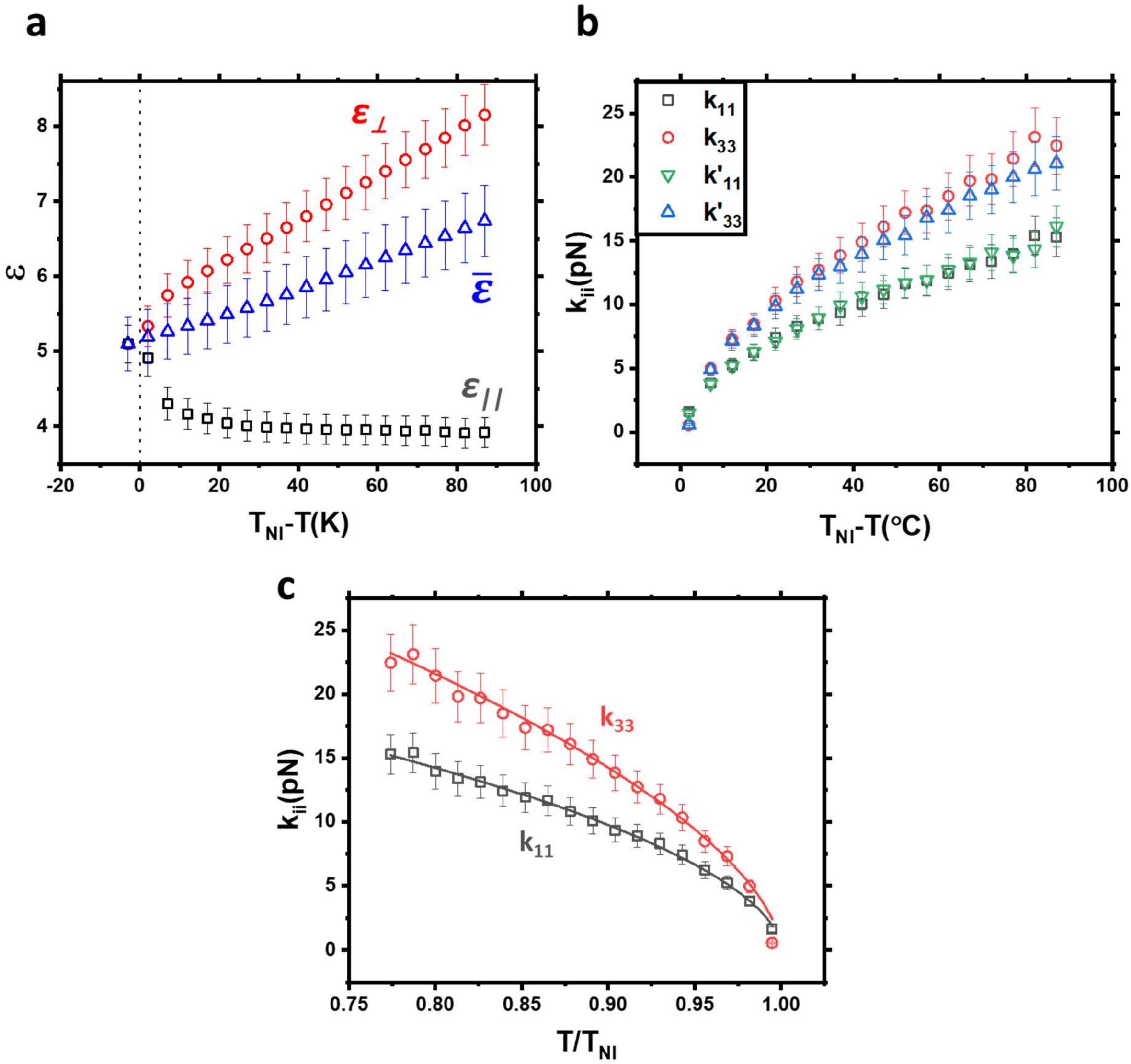

Figure 6.5. Dielectric analysis of MLC 2081. (a) $\varepsilon_\perp, \varepsilon_{//}$ and $\bar{\varepsilon}$ as function of T_{NI}-T (T_{NI}=112±2℃). (b) Splay (k_{11}) and bend (k_{33}) elastic constants as function of T_{NI}-T. Here, as stated in the text k_{ii}'≈ k_{ii}, showing the treatment given in in equations (6-4) and (6-5) does not greatly effect values. (c) k_{ii} plotted as a function of T/T_{NI} fitted with equation (6-8).

6.3.1.c *Permitivities and Elastic Constants of Dimer Mixture*

Figure 6.6 shows results from dielectric investigation of the dimeric mixture. Figure 6.6a shows values of $\varepsilon_\perp$, $\varepsilon_{//}$ and $\bar{\varepsilon}$, where the positive to negative transition at 63°C may be seen. As discussed, this is attributed to conformational changes of the dimer (section 6.3.1.a). The errors in Figure 6.6a are large compared to the value $\Delta\varepsilon$, however these are for the absolute value rather than the trend which is more certain and confirmed through applying electric field while performing POM. Figure 6.6b shows elastic constant behaviour, where raw and rescaled values can be seen to be similar, but the rescaled ones show a more continuous trend in the region close to 63°C, where $\Delta\varepsilon$ is very small (these are filled in for k_{11} and k_{33}, to identify their larger associated errors). Figure 6.6c shows the rescaled elastic constant values, where continuous change above and below 63°C (taken in PH and HT devices respectively) is observed. Of most relevance to this work is the region where $\Delta\varepsilon$ is negative, as this allows EHDI to be compared to that of pure MLC 2081. This is below 63°C, a region shown in Figure 6.6d. Here the behaviour of both k_{11} and k_{33} are reasonably linear, and is fitted with,

$$k_{ii} = K_{ii}^{0} + mT(K)\,, \qquad i = 1{,}3 \tag{6-9}$$

where fitting parameters are given in table Table 6-3.

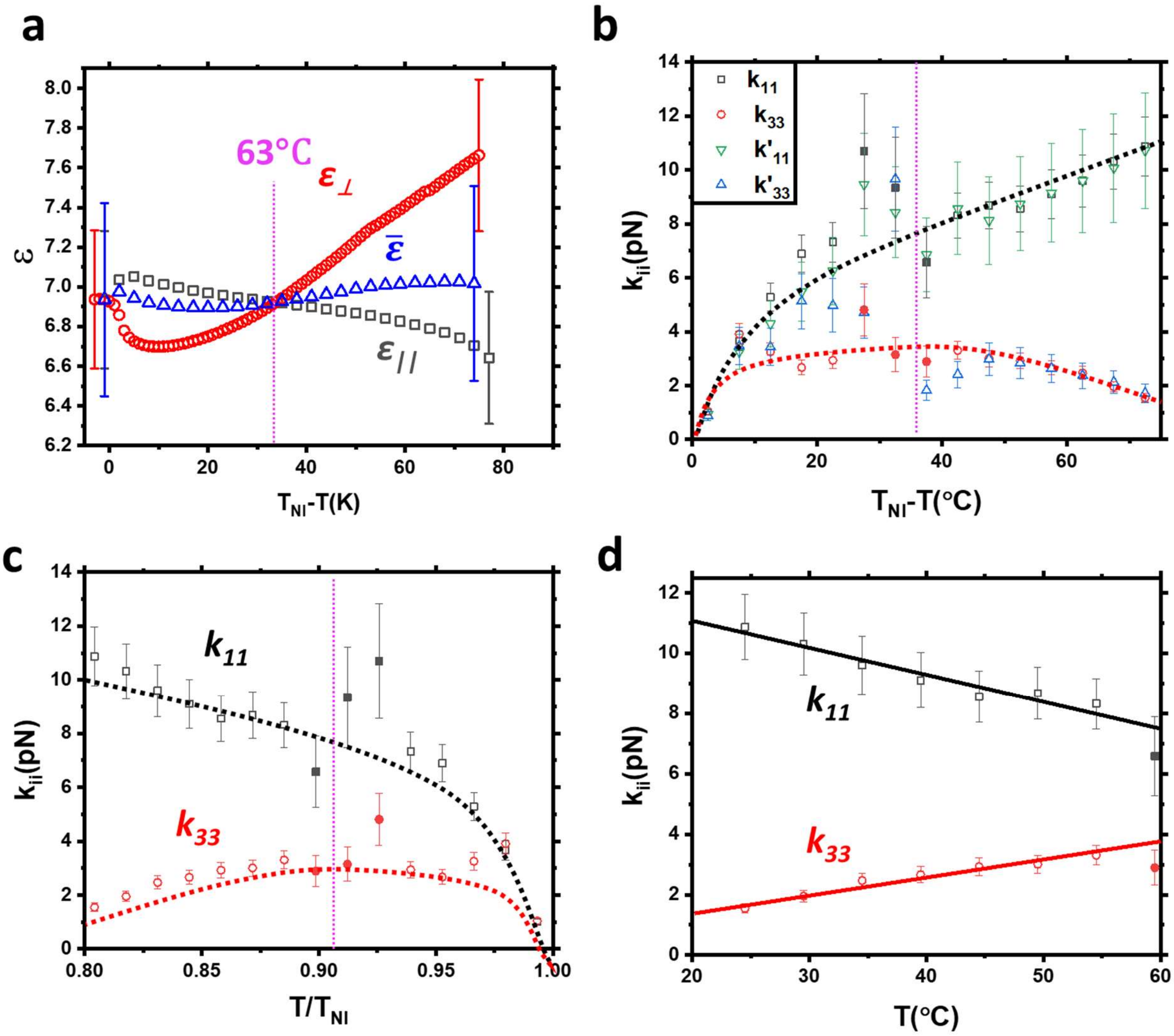

Figure 6.6. Dielectric analysis of dimer mixture ($\phi_{60:40:0}$) as temperature is varied. (a) Permitivity as function of T-T_{NI}. (b) k_{11} and k_{33} as functions of temperature, both using raw (k'_{ii}) and rescaled data (k_{ii}).Data data points close to 63 ℃(Pink lines) are filled in due to being more erroneous. This is caused by the $\Delta\varepsilon$ becoming close to zero. (c) Rescaled elastic constants as a function of T/T_{NI}. (d) k_{11} and k_{33} in the temperature range where $\Delta\varepsilon$<0. Behaviour well described by linear fit (equation (6-9)). Red and black dotted lines are guides for the eye.

6.3.1.d *Material Suitability for Experiment*

The goal of this chapter is to assess the role of elastic constants in shaping the hydrodynamic rolls formed within NLCs in a state of EHDI. To do so a novel dimer mixture was created to compare with the standard material MLC 2081. For the dimer mixture desirable properties are:

- ***i.*** Negative $\Delta\varepsilon$.
- ***ii.*** Positive $\Delta\sigma$.
- ***iii.*** Lower k_{33} than MLC 2081.
- ***iv.*** Similar ε and $\Delta\varepsilon$ to MLC 2081.
- ***v.*** Similar σ and $\Delta\sigma$ to MLC 2081.
- ***vi.*** Similar viscosity to MLC 2081.

From results presented in Figure 6.5 and Figure 6.6 we have shown that $\phi_{60:40:0}$ achieves the properties ***i-iii*** when below 63°C. Property ***iv*** is partly satisfied, with similar ε, but with $\Delta\varepsilon$ in MLC 2081 being around four times larger at ambient temperatures. To investigate ***v***, Figure 6.7 plots the measured conductivities as function of T (taken in the same manner as Chapter 5). Here, similar conduction magnitude is seen in the dimer mixture as the device filled with $\phi_{100:0:0.5}$. This is unexpected and indicates that the CB7CB used has significant ionic contamination, however in this case it is useful as it allows the material to be used for EHDI experiments in the absence of TBATPB. Results from Figure 6.7 also show at T<63°C $\Delta\sigma$ is positive. For ***vi*** the viscosities are unknown, which is an uncertainty moving forward given their importance for hydrodynamic phenomena.

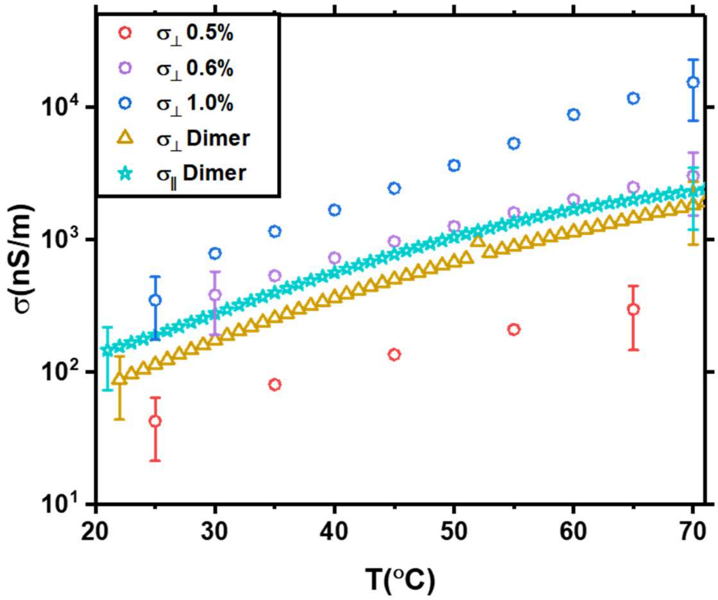

Figure 6.7. Conductivity of dimer mixture compared to MLC 2081 doped with TBATPB. Three devices from the previous chapter are plotted against the dimer (circles) with concentration TBATPB given in key. The values $\sigma_\perp$ and $\sigma_{||}$ in $\phi_{60:40:0}$ are shown as triangles and stars respectively. These results were all taken in 20µm AWAT devices.

6.3.2 V_C and q_C as Functions of Frequency

As voltage and frequency were varied similar behaviours were seen as described in the previous chapter in both doped MLC 2081 ($\phi_{100:0:0.5}$) and the dimeric mixture ($\phi_{60:40:0}$). Figure 6.8 shows several observed patterns in the dimer mixture as frequency *(f)* and voltage *(V)* are varied. Similar to the MLC 2081 results, the Normal Roll (NR) mode forms in the conduction regime when a critical voltage (V_C) is applied. When the frequency increases to f_{diel} the NR mode transfers to the chevron pattern (CP) or prewavy pattern (PWP), depending on voltage. This is standard behaviour[270,336], indicating the material is behaving in a comparable way to the MLC 2081, rather than displaying the non-standard electroconvection often seen in BC materials.

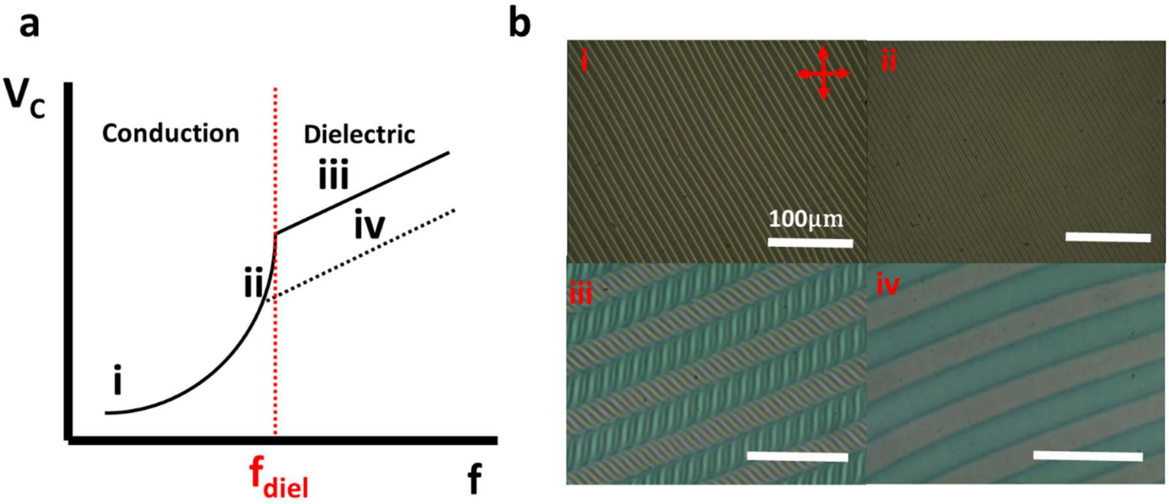

Figure 6.8. (a) Mapping the observed textures as voltage and frequency are varied in the dimeric mixture. (b) Images of: (i) NR mode at low f, (ii) NR mode at high frequency (iii) chevron pattern and (iv) prewavy pattern.

Figure 6.9 shows plots V_C and q_C as functions of frequency *(f)* at several *T* in both salt doped MLC 2081 ($\phi_{100:0:0.5}$) and dimeric mixture ($\phi_{60:40:0}$). They are fit with the same expressions used in the previous chapter,

$$V_C(f) = V_0\left(1 + \left(\frac{f}{f_{crit,\ V}}\right)^4\right) \tag{6-10}$$

and

$$q_{opt}(f) = q_0\left(1 + \left(\frac{f}{f_{crit,\ q}}\right)^4\right) \tag{6-11}$$

which describe the behaviour in all cases but dimeric mixture at 60.3°C (where Δε is very small).

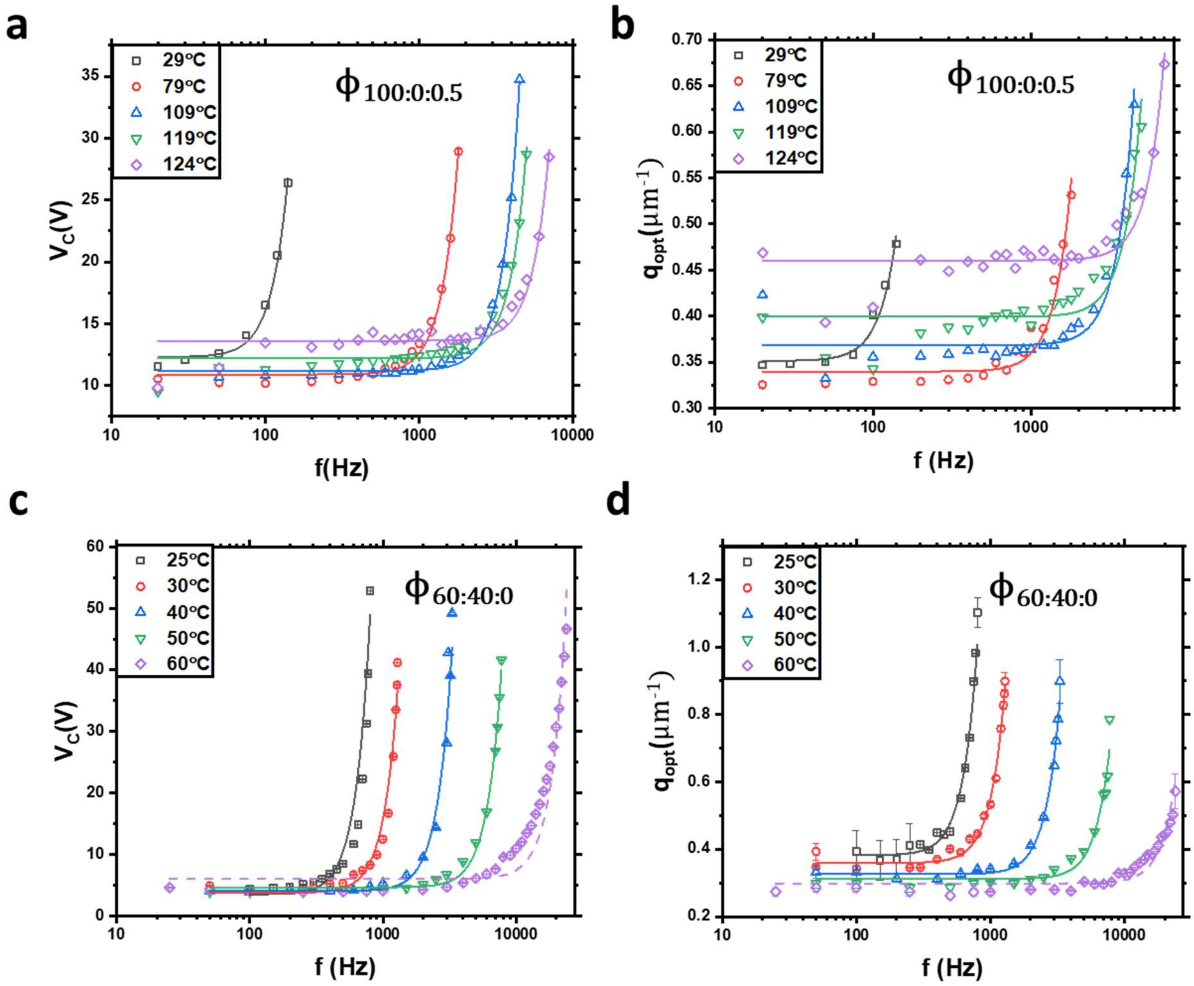

Figure 6.9. Plots of V_C and q_C as functions of frequency. (a) V_C in $\phi_{100:0:0.5}$ (b) q_{opt} in $\phi_{100:0:0.5}$ (c) V_C in $\phi_{60:40:0}$ (d) q_C in $\phi_{60:40:0}$. These are fited with equations (6-10) and (6-11). At the time of measurement T_{NI} in $\phi_{100:0:0.5}$ was 129±2℃, and in $\phi_{60:40:0}$ was 102±2℃.

One of the key conclusions from the previous chapter was that f_{crit} values appear to be determined by sample conductivity. V_0 and q_0 as functions of T are plotted in Figure 6.10 to see differences between materials. In Figure 6.10a V_0 is seen to continually increase with T in the dimer mixture, while in the MLC 2081 it slightly reduces then increases again. For MLC 2081 we repeat the explanation made last chapter regarding the competition between reductions in material elasticity[207,247,249] and increasing thermal dissipation[243] as T is increased. For the dimer mixture, V_0 appears to increase with T only, with no local minimum. This is likely to be caused by the unusual positive gradient of k_{33} with T at low temperatures, meaning both thermal dissipation and elastic resistance act to increase V_0, rather than opposing one another (as in the calamitic material).

Figure 6.10b shows dissimilar effects of T on q_0 between the two materials, where the dimer mixtures value reduces with T while MLC 2081 again displays a minimum before increasing. This reduction in the dimeric material is promising for the hypothesized mechanism illustrated in Figure 6.1, as in this region T is proportional to k_{33}, meaning as k_{33} reduces q_0 is becoming larger. At some point we predict this behaviour would eventually reach a local minimum and start to increase again (as does the MLC 2081), either as thermal dissipation becomes dominant or k_{33} starts to reduce again (see results in Figure 6.6). These observations indicate that elastic constants play an important role in determining V_0 and q_0. To examine the limits of q_{opt} in more detail the next section investigates the limits of this parameters as functions of the measured elastic constants.

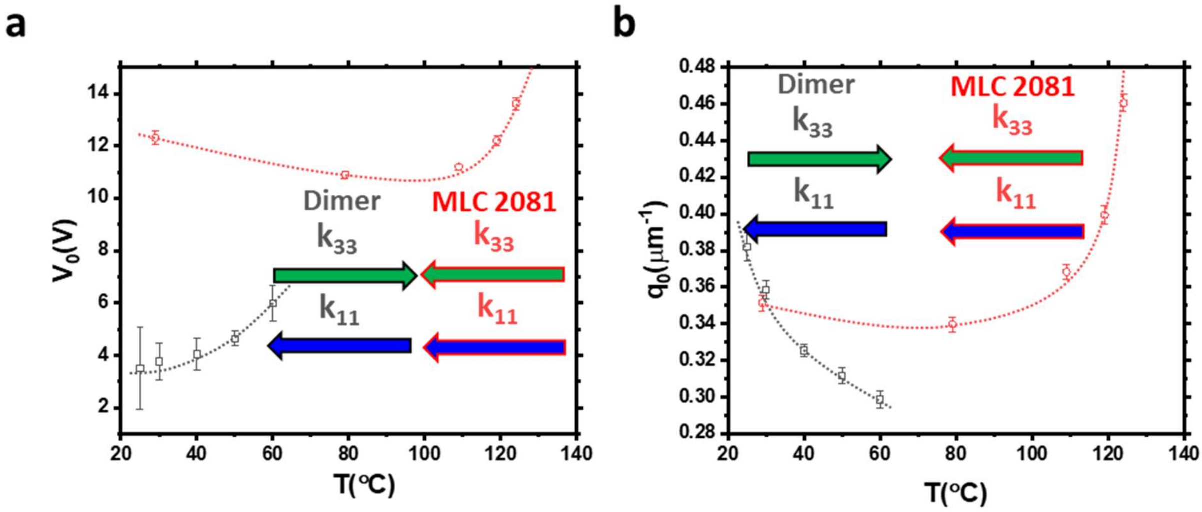

Figure 6.10. V_0 and q_0 from fittings shown in Figure 6.9 using equations (6-10) and (6-11) as functions of T. The arrows are included showing the temperature dependency of elastic constants k_{11} and k_{33} (in Figure 6.6) taken from . For example in the examined temperature range for the dimer mixture k_{33} increases with T (right-facing arrow) while k_{11} decreases (left- facing arrow). Meanwhile in the MLC 2081 both k_{11} and k_{33} reduce with T (left-facing arrows).

6.3.3 Limits of q_C

This section aims to understand the role of elastic constants in dictating the observed q_{opt} values. Here, the temperature was varied to obtain different elastic constant values and ratios, using elastic constant fits presented in section 6.3.1. As discussed in the previous chapter, MLC 2081 doped with TBATPB appeared to change T_{NI} as experiments went on. For this reason, T_{NI} was measured at the start of each experiment and it was assumed that elastic constants at T_{NI}-T were the same as pure MLC 2081. Key parameters to the possible application of EHDI gratings are the maximum (q_{max}) and minimum (q_{min}) q_{opt} values observed for a certain T (which determines ratio of elastic constants). As devices of different spacing (d) were investigated it is useful to look at the dimensionless factors $\frac{q_{max}}{q_0}$ and $\frac{q_{min}}{q_0}$, where,

$$q_0 = \frac{2\pi}{d}. \tag{6-12}$$

Figure 6.11 plots $\frac{q_{max}}{q_0}$, $\frac{q_{min}}{q_0}$ and $\frac{q_{max}}{q_{min}}$ as functions of k_{11}, k_{33} and their ratio. As the method of controlling elastic constants was changing sample T, conclusions are challenging due to many parameters (viscoelastic and dielectric) changing simultaneously. To try to clarify these effects, arrows showing direction of increasing T are shown in Figure 6.11.

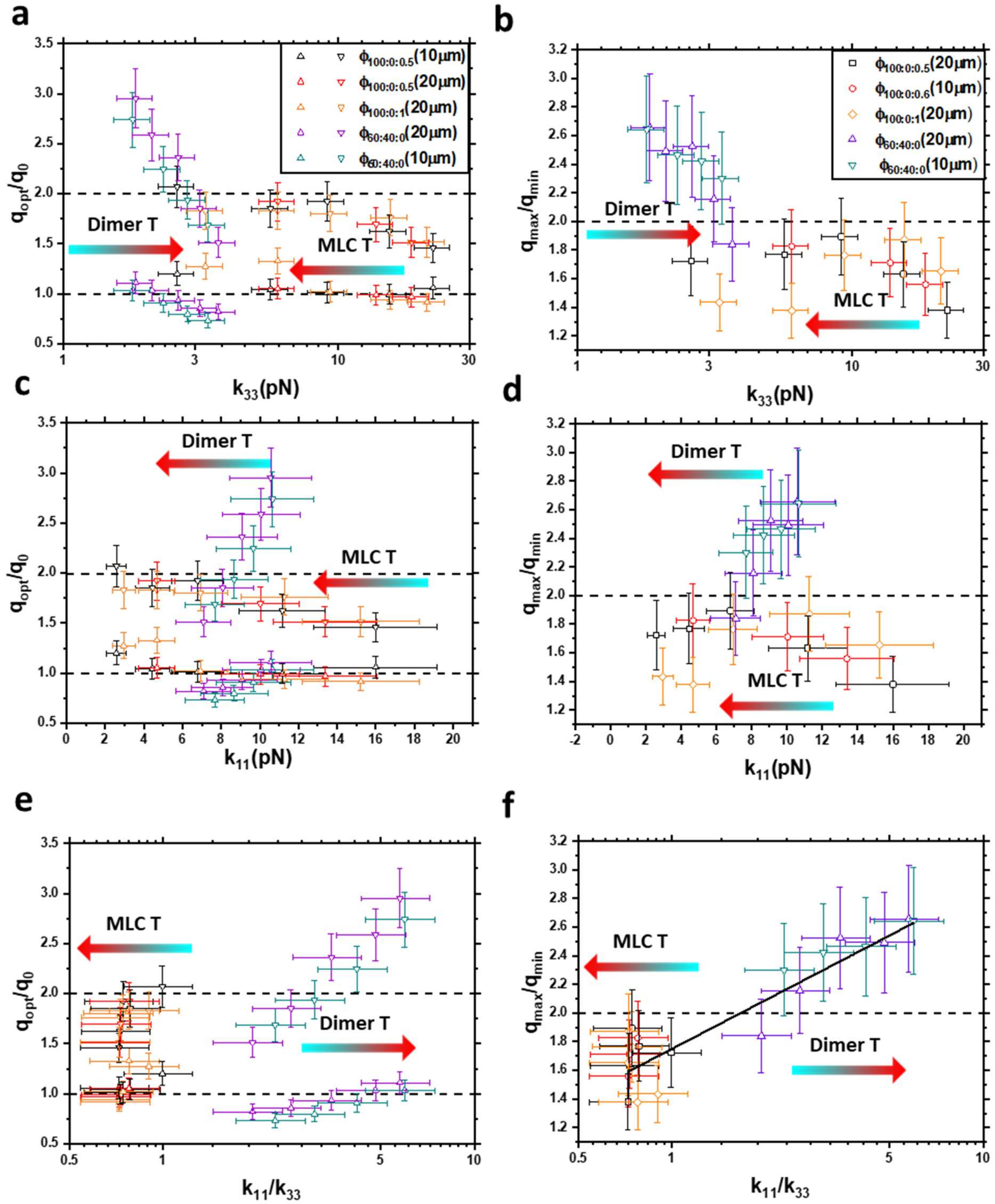

Figure 6.11. Differences between the values q_{opt} displayed by the dimeric and salt doped samples in states of EHDI. (a), (c) and (e) show the normalized minimum (upwards triangles) and maximum (downwards triangles) observed values of q_{opt} as functions of k_{33}, k_{11} and k_{11}/k_{33}. (b), (d) and (f) show the breadth of wavevectors observed as functions of these same elastic constants and their ratios. (f) is fitted with a linear fit through all points. Keys for left and right sides are given in (a) and (b). Arrows indicate direction of increasing temperature. Here, similiarly to Figure 6.10 the arrows of temperature show the directionality of relevant elastic constant or ratio with temperature. These can be seen to vary between mixtures (from results in in Figure 6.6).

For MLC 2081 the previously observed limits of

$$\frac{q_{min}}{q_0} > 1, \tag{6-13}$$

$$\frac{q_{max}}{q_0} < 2, \tag{6-14}$$

and

$$\frac{q_{max}}{q_{min}} < 2, \tag{6-15}$$

are obeyed in all cases. Meanwhile the dimeric mixture does not follow the same behaviour, displaying q_{min} values as small as $0.75q_0$ and q_{max} values as large as $3q_0$ (at highest and lowest k_{33}, respectively). In Figure 6.11a a clear correlation between the limits q_{opt} and $\frac{1}{k_{33}}$ is observed in all devices. This alleviates uncertainties as the temperature dependency of k_{33} are opposite in the MLC 2081 and dimeric mixture. This means although the factors Δε and Δσ are varying, they are doing so in opposite direction, while a negative correlation of q_{opt} limits with T and k_{33} occurs. This indicates the dielectric properties and thermal dissipation effects are only weakly effecting the observed behaviours, while viscoelastic properties dominate. Similar arguments can be used in Figure 6.11b, where if the MLC 2081 data points close to T_{NI}(at lowest k_{33}) are omitted a consistent correlation in $\frac{q_{max}}{q_{min}}$ can be seen. This is taken as evidence that the effects of thermal dissipation only become important at high T. In Figure 6.11c-d, correlations between k_{11} a q_{opt} limits are seen in both samples, where in the MLC 2081 q_{opt} limits decrease with k_{11} while in dimeric mixture they increase. In Figure 6.11e-f the parameters are plotted against the ratio $\frac{k_{11}}{k_{33}}$. This ratio changes little in the MLC 2081 samples, while in the dimer is varies considerably. Here, similar trends are seen with k_{33} alone, however, Figure 6.11f shows slightly more continuous behaviour between samples, where the black line is a concatenated fit between all points of,

$$\frac{q_{max}}{q_{min}} = A\left(\frac{k_{11}}{k_{33}}\right)^n, \tag{6-16}$$

where A and n were fitted to be 1.73±0.04 and 0.24±0.03. This behaviour may indicate that the breadth of q_{opt} values displayed is mainly determined by $\frac{k_{11}}{k_{33}}$ and d, however more evidence from a wider range of systems would be required to confirm this.

To confirm the behaviours of q_{opt} as frequency is varied, the angles of the $m=\pm 2$ $(\theta_{m=2})$ diffraction orders were measured using diffraction analysis at ambient temperature (T=22°C). This was done in the two 20 μm devices filled with $\phi_{100:0:1}$ and $\phi_{60:40:0}$. Combining the grating equation,

$$m\lambda = \Lambda_{gr} sin\theta_m, \tag{6-17}$$

with equations (6-13) and (6-14), the predicted angles of the m=2 order (θ_m) for calamitic mixtures obey,

$$\theta_{min} < \theta_{m=2} < \theta_{max}, \tag{6-18}$$

where θ_{min}=3.8° and θ_{max}=7.6°. These and the values $\theta_{m=2}$ as functions of frequency are plotted in Figure 6.12. $\phi_{100:0:1}$ obeys (6-18), while larger angles are seen in the device filled with $\phi_{60:40:0}$, where, θ_{min}=4.8±0.3° and θ_{max}=10±1°.

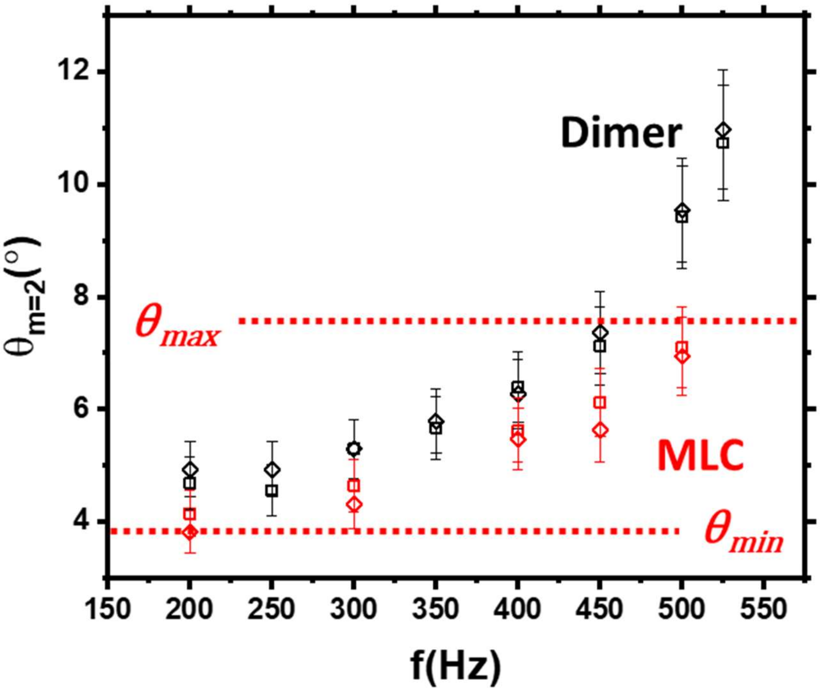

Figure 6.12 Diffraction angles of the m=2 order as functions of frequency in MLC 2081 ($\phi_{100:0:1}$) and dimer mixture ($\phi_{60:40:0}$). Square points indicate positive orders, diamonds negative. The values θ_{min} and θ_{max} from equation (6-18) are marked, where MLC 2081 appears to obey these limits, but the dimeric mixture does not.

6.4 Conclusion

This chapter presented the analysis of the relationship between elastic constants and EHDI patterns. Both the dielectric analysis and the reduced values of V_C, indicated that the addition of CB7CB to MLC 2081 has had the desired effect of greatly reducing k_{33} in the composite material compared to the pure MLC 2081. Also, the addition of CB7CB decreased k_{11}, increased conductivity, reduced $\Delta\varepsilon$ and reduced T_{NI}. This makes direct comparisons complex, due to many parameters being simultaneously varied.

In examining the EHDI characteristics of the dimeric mixture, significantly shorter pitch gratings (by a factor of around 1.5) were observed than seen in MLC 2081 with TBATPB at any temperature or concentration TBATPB. This indicates the change in behaviour is unlikely to be caused by the magnitude of permittivity, conductivity, viscosities or elastic constants, but rather their anisotropic ratios. Of these, the origin of the changed behaviour does not seem likely to be caused by dielectric properties, as all evidence shows these have lower anisotropies in the dimeric mixture than in MLC 2081, which would be a similar situation to MLC 2081 close to T_{NI}. These discussions indicate that the changes in attainable q_{opt} values are caused by varying viscous and elastic properties of the material. This work shows that both $1/k_{33}$ and k_{11}/k_{33} have positive correlations with the values q_{opt} as predicted at the start of the chapter. Often theoretical models of EHDI assume a single isotropic elastic constant[240], hence this behaviour might have been missed in many of those theoretical studies. It is also possible that the origin of this changing behaviour is due to changing viscosity. From theoretical treatments the parameters α_3, γ_1 and γ_2 are particularly important in EHDI formation (see section 5.1.3) [240]. The change in these quantities have not been quantified in this work, meaning their measurement would be useful in confirmation of the dominant cause of changes observed.

To conclude, Chapter 6 has aimed to investigate whether through creating novel materials the attainable wave vectors of systems in states of EHDI can be increased. This has been successful, where clear increases in both the breadth and absolute values of achievable q_{opt} have been demonstrated. Certainty that this result is due to changes to material elastic constants only, cannot be confirmed without measurements of material viscosity, however the results presented indicate at least a partial dependency on k_{33}.

The increases in observed q_{opt} are moderate, with the maximum observed increase in q_{opt}'s value and range being around 50% despite a factor of 10 change to k_{33}. It may be that further increases in q_{opt} can be achieved through further elastic constant tuning, however it is likely such improvements will be incremental. Additionally, the fundamental issue within the EHDI diffractive devices of not being able to induce blaze is not addressed using these methods. Further discussion of EHDI performance as a diffractive optical element is presented in Chapter 9, where the theoretical limits of an optimized device will be presented, in addition to ideas to improve the devices further.

Chapter 7 Measurement of the Speed of Sound in Nematic Liquid Crystals

This and the following chapter concern acoustic properties and phenomena in NLCs. This chapter (Chapter 7) introduces the key concepts of acoustics in general soft matter but focuses on lower acoustic power where the ultrasonic irradiance is insufficient to alter the macroscopic properties of the material. The chapter includes measurement of the speed of sound in the NLC mixture E7. Chapter 8 continues with acoustics, but focusses on larger powers of ultrasonic irradiance, where changes to the orientation of the NLC director are induced.

7.1 Fundamentals of Acoustic Waves

7.1.1 The Wave Equation for Acoustics

Acoustic waves are pressure waves, obeying the wave equation,

$$\nabla^2 p - \frac{1}{v_s^2}\frac{\partial^2 p}{\partial t^2} = 0, \tag{7-1}$$

where p is the pressure, v_s is the speed of sound and t is time. A useful solution to (7-1) for a single wave propagating along the z-axis may be written as,

$$p = \begin{bmatrix} p_x \\ p_y \\ p_z \end{bmatrix} e^{i(\omega t - k_A z)} = \begin{bmatrix} p_x \\ p_y \\ p_z \end{bmatrix} e^{2\pi i\left(ft - \frac{z}{\lambda_A}\right)}, \tag{7-2}$$

where p_r are the complex amplitudes of the pressure wave in the direction r, k_A is the wave's wavenumber, λ_A is the acoustic wavelength, ω is the angular frequency, and f is the linear frequency. Unlike electromagnetic waves, acoustic waves have polarized components in the three Cartesian polarisation directions, as they can be longitudinal and transverse. Schematics of both transverse and longitudinal waves are shown in Figure 7.1.

When an acoustic wave passes through a medium, the amplitude reduces in value over time and space. This is due to the dissipation of energy into the medium, known as attenuation. The attenuated pressure (p_α) can be written as,

$$p_\alpha = \begin{bmatrix} p_x e^{-\alpha_x t} \\ p_y e^{-\alpha_y t} \\ p_z e^{-\alpha_z t} \end{bmatrix} e^{i(k_A z - \omega t)} \tag{7-3}$$

where α_r are known as attenuation coefficients.

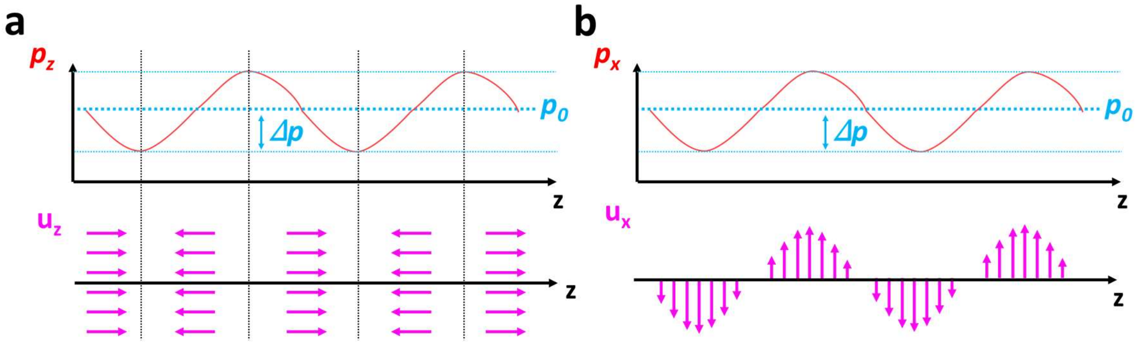

Figure 7.1. The different polarisations of acoustic waves. The pressure (p, red lines) and resulting velocity fields (u, pink arrows).(a) A longitudinal wave. (b) A x- polarized transverse wave.

7.1.2 Bulk Acoustic Waves in Simple Materials

Within materials, acoustic waves may be split into two types: those which pass through the bulk of the material and others which pass along an interfacial surface. This chapter only considers the interaction of Bulk Acoustic Waves (BAWs) with NLCs.

7.1.2.a *Newtonian Fluids*

One of the simplest materials to describe BAW propogation within are Newtonian fluids. Within these materials, no elastic forces exist between the constituent particles, and the propagation of acoustic waves is caused by localised increases in density due to the applied pressure. Usually, these materials only support the transmission of longitudinal waves over significant distances. As they have no inter-particle bonds, transverse acoustic modes have very high attenuations[337]. In these materials, the speed of sound, v_s for the longitudinal mode can be approximated with Urick's equation[338],

$$v_s = \sqrt{\frac{B}{\rho}} \tag{7-4}$$

where B is the bulk modulus of the fluid (a measure of a material's resistance to compression) and ρ the unperturbed density.

7.1.2.b *Elastic Solids*

In elastic solids, both longitudinal and transverse acoustic wave modes are supported. This difference can be understood by solid materials generally possessing intermolecular bonds. A simple model for an elastic solid material is a construct of many masses (molecules) connected by springs (bonds). Here, if either a transverse or longitudinal vibration is applied to a particle, the wave transmits through the material.

For longitudinal waves in elastic solids v_s may be written as,

$$v_s = \sqrt{\frac{B + \frac{4}{3}G}{\rho}}, \tag{7-5}$$

Where G is the shear modulus (a measure of a material's resistance to shearing). Meanwhile, for the transverse waves the v_s is written as,

$$v_s = \sqrt{\frac{G}{\rho}}. \tag{7-6}$$

7.1.3 Generation of Ultrasonic Acoustic Waves using the Piezoelectric Effect

7.1.3.a *The Piezoelectric Effect*

In this thesis, ultrasonic waves are solely generated using the piezoelectric effect. The piezoelectric effect is defined as the inducement of a macroscopic charge due to some externally applied stress[339]. In tensor form, a non-piezoelectric elastic material, a material's stress ($\boldsymbol{T}$) and strain ($\boldsymbol{S}$) can be written as,

$$\boldsymbol{S} = \boldsymbol{sT} \tag{7-7}$$

and the dielectric displacement ($\boldsymbol{D}$) may be written as,

$$\boldsymbol{D} = \boldsymbol{\varepsilon E} \tag{7-8}$$

where $\boldsymbol{s}$ is the material compliance, $\boldsymbol{\varepsilon}$ the permittivity and $\boldsymbol{E}$ the electric field. For a piezoelectric material, $\boldsymbol{D}$ and $\boldsymbol{S}$ are coupled to one another, where,

$$\boldsymbol{S} = \boldsymbol{sT} + \boldsymbol{\delta}^T\boldsymbol{T} \tag{7-9}$$

and

$$\boldsymbol{D} = \boldsymbol{\varepsilon E} + \boldsymbol{\delta T} \tag{7-10}$$

where $\boldsymbol{\delta}$ and $\boldsymbol{\delta}^T$ are the piezoelectric tensor and its transpose. The piezoelectric effect is reversible, meaning when an electric potential is applied across a piezoelectric material, it will distort its shape. Therefore, by applying an oscillating electric potential, piezoelectric materials can vibrate to produce acoustic waves.

Many materials exhibit piezoelectricity [339–343] where the absolute requirement is that the crystalline structure is non-centrosymmetric[344]. The most commonly used piezoelectric material is Lead Zirconate Titanate (PZT) [345]. PZT has a perovskite atomic structure, where a central cation (zinc or titanium) is surrounded by 6 anions (oxygen) then a further 8 cations (lead)[344]. A unit cell of PZT above the Curie temperature (T_C) (shown in Figure 7.2a), does not exhibit piezoelectricity due to it being centrosymmetric. However, below T_C, the central cation moves to a new minimum energy position off the centre of the lattice. This leads to the unit cell exhibiting a permanent dipole and stretching into a cuboid shape (Figure 7.2b). If cooled below T_C with no electric field applied, these unit cells will be randomly distributed in orientation, meaning there is no bulk polarisation in the macroscopic material. However, if a large electric field (≈2-4 kV/mm)[346] is applied as the material is cooled from above T_C, the dipoles align to resist it, creating a material with a macroscopic permanent dipole (This is known as "poling"). For a poled material, when an appropriately aligned electric field is applied across the structure, the central cation moves to resist the applied field, dilating the unit cells. This leads to the macroscopic material flexing and vibrating when DC and AC fields are used, respectively (Figure 7.2c-d).

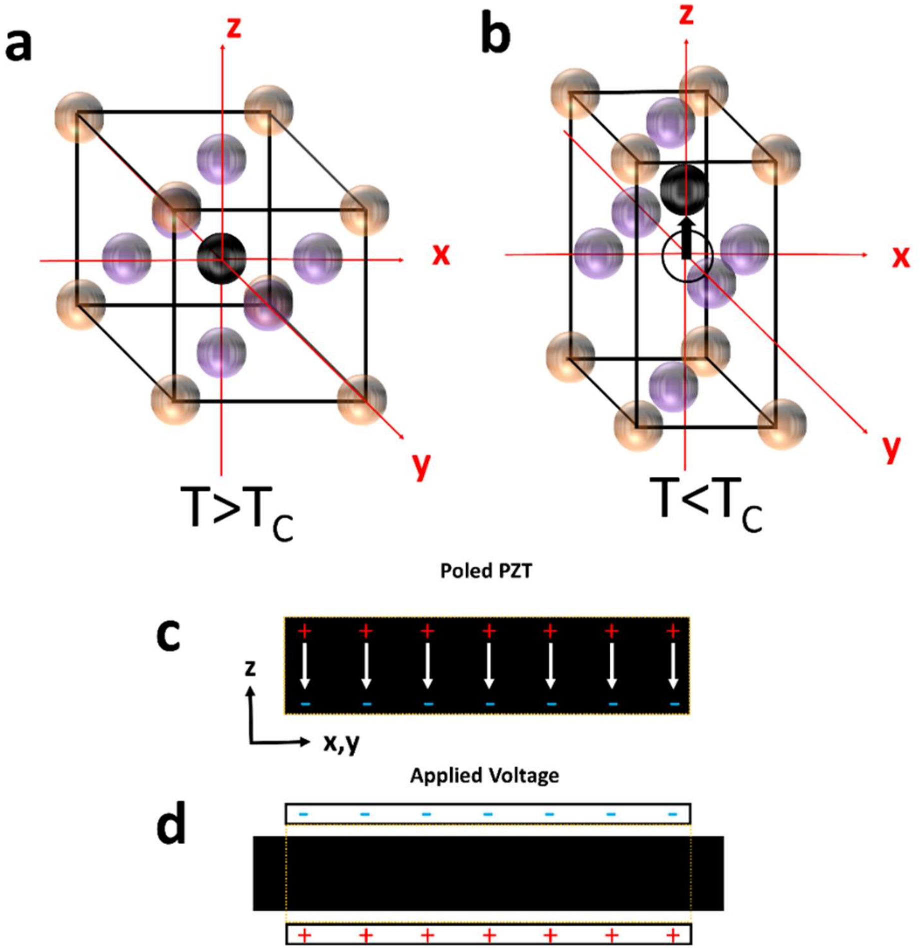

Figure 7.2 Origins of piezoelectricity in PZT. (a) A standard Perskovite unit cell where a central cation (black) is surrounded by 6 anions (purple) in the centre of each face and 8 more cations (orange) in each corner. (b) The crystal structure below T_C, where the central cation moves slightly off-centre, and unit cell stretches in the z-direction. (c) A poled PZT material, where a macroscopic permanent dipole moment exists. (d) The case when an electric field is applied to the poled PZT, where the central cation moves under the applied field, flexing the macroscopic shape.

7.1.3.b *Resonance*

Usually, piezoelectric devices show strong dispersions, where, as the applied frequency is varied, the material undergoes several resonance processes. Figure 7.3 shows an example of dielectric spectra of a poled PZT disk (taken using the Agilent E4980A LCR meter on a disk from Precision Acoustics, Dorset). Here, close to the resonance frequency (1MHz), the measured impedance of the system (Z^*) is very small. This is due to the energy being efficiently transferred into ultrasonic irradiance within the device. This is the frequency where the maximum acoustic intensity is achieved.

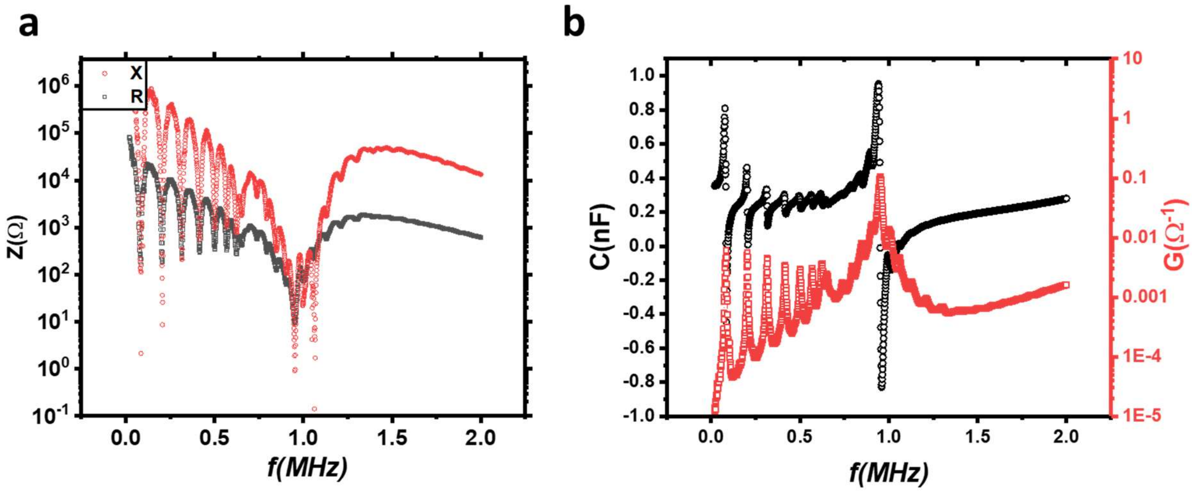

Figure 7.3. (a) The real and imaginary parts of impedance (R and X respectively) of a PZT disk as the applied frequency is varied. (b) The corresponding capacitance (C) and conductance (G).

7.2 Speed of Sound Measurements in Soft Materials

7.2.1 The Pitcher & Catcher Method

The speed of sound (v_s) is a highly important parameter to understand acoustic interactions within materials. For this this work it was found to be critical for understanding the NLC acoustic interactions reported in Chapter 8. Due to the material's viscoelasticity and anisotropy, v_s is a complex parameter to measure in NLCs. These complexities will be introduced in this section, so that results presented may be better understood.

A standard method of measuring v_s is the Pitcher and Catcher (P&C) method [338]. Here, two piezoelectric transducers are used, which are separated by some distance (d). The cavity between the two transducers is then filled with the material to be studied (see Figure 7.4). A voltage pulse is applied to one of the transducers (the Pitcher), which transfers it into a longitudinal acoustic pulse. This pulse moves through the distance d and is received by the other transducer (the Catcher), which transfers it back as an electric signal. This allows direct measurement of v_s if the time spent within the distance d (t_d) is known as [338,347],

$$v_s = \frac{d}{t_d}. \tag{7-11}$$

The measurement of t_d is not trivial, as the total time between an input pulse and output pulse (Δt) is the sum of times spent in the transducer casing and buffer rod (d_b, see Figure 7.4) in addition to d. Therefore for similar pitcher and catcher transducers,

$$\Delta t = t_d + 2t_b. \tag{7-12}$$

Also, for thin samples, d may not be known to a high degree of accuracy. This can be overcome by either measuring a well-characterised reference material (usually water[338]) or taking measurements at several d values.

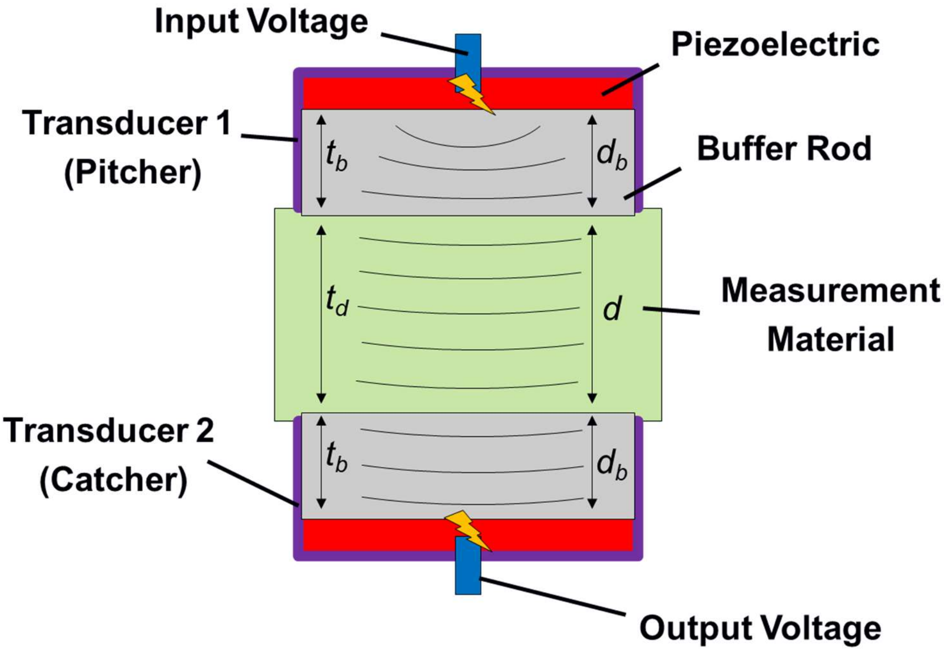

Figure 7.4.Schematic of Pitch and Catch method's operation.

Often within the P&C measurements, more information than v_s can be obtained. Usually, the signal attenuation (A) is measured, defined as,

$$A = 10\, log_{10}\left(\frac{I_f}{I_i}\right). \tag{7-13}$$

Here, I_i and I_f are the intensity before and after the attenuation, respectively. A can be converted into a material attenuation coefficient (α) by,

$$\alpha = \frac{A}{d_\alpha \cdot f_A}, \tag{7-14}$$

where d_α is the distance over which the attenuation took place (in P&C d_α=d).

7.2.2 Speed of Sound Measurements in Non-Liquid Crystals

7.2.2.a *Accuracy of P&C Measurement*

Generally, the P&C measurements of isotropic liquids are highly accurate at obtaining values of v_s, where errors are often quoted in the range 0.01-0.0001%[348–350]. The main uncertainties of such measurements are maintaining uniform temperature and pressure across the sample, rather than the P&C method itself.

To a large extent, the accuracy of value v_s is determined by d, as thicker samples reduce the relative errors of both d and Δt in (7-11). For example, Povey et al. [351] reported an uncertainty of 0.1ms^{-1} in the measurements isotropic molecular liquid samples. Here a 50mm thick sample was used. Taking this example and making a first-order approximation, a reasonable minimum expected error for a v_s measurement (δv_s) may be written,

$$\delta v_s = 0.1ms^{-1}\frac{50}{d[mm]}. \tag{7-15}$$

This means that in simple fluids if a value of δv_s smaller than 10 ms^{-1} is desired, a minimum layer thickness of around 500μm is required. This is important for LC material measurement as usually only small quantities of material will be available.

7.2.2.b *Influence of Relaxation Processes on Ultrasonic Measurements*

Although equations (7-4) and (7-5) can be used to describe v_s of longitudinal waves in simple solids and fluids, respectively, they are generally over-simplified. A critical behaviour that is missed in these simple relations is dispersion, where often as the frequency of the transmitted acoustic wave is varied, v_s changes. This is due to physical relaxation processes within the material, which as the frequency increases, have insufficient time to respond to the oscillations of the acoustic wave (becoming relaxed). This is characterised by a critical frequency, ω_0, where the process changes from being in its dynamic to inertial frequency range. The effect of an acoustic relaxation can often be described to affect the value v_s using [352],

$$v_s^2 = v_0^2 + (v_\infty^2 - v_0^2)\frac{\left(\frac{\omega}{\omega_0}\right)^2}{1+\left(\frac{\omega}{\omega_0}\right)^2}, \tag{7-16}$$

where v_0 and v_∞ are the values v_s in the dynamic and inertial range, respectively. At ω close to ω_0 the attenuation coefficient (α) also tends to increase in value [352],

$$\alpha = \alpha_0 + \alpha_R, \tag{7-17}$$

where α_0 is some base attenuation constant far from relaxation and α_R is the increase close to relaxation. For a single relaxation process, this is approximately quantified as,

$$\alpha_R = f\frac{\left(v_\infty^2 - v_0^2\right)\left(\frac{\omega}{\omega_0}\right)}{v_0^2\left(1+\left(\frac{\omega}{\omega_0}\right)^2\right)+\left(v_\infty^2 - v_0^2\right)\left(\frac{\omega}{\omega_0}\right)^2}. \tag{7-18}$$

This increase in α can be understood as being caused by increased energy absorption due to it being close to a mechanical resonance.

As stated above, the origin of relaxation processes are varied. Some are thermal and caused by the relaxation of the vibrations of intermolecular bonds [352,353]. A simple example of such thermal relaxation is observed in fluorine gas[352], which was probed by Shields in 1962 [353]. The results for v_s and α of the fluorine are shown in Figure 7.5. Here, the data is fitted accurately using equations (7-16) and (7-18) indicating the process can be described as a simple single process mechanical relaxation (Figure 7.5a and b).

Another relaxation process of particular importance to soft matter systems is viscous relaxation[354]. A viscous material behaves as an elastic spring at high frequencies, and displays a viscous response at low frequencies (see section 2.3.1). This can be understood qualitatively using Maxwell's standard model of viscoelasticity (see Figure 7.5c)[355], where two springs (of spring constant k_1 and k_2) are put into a mechanical circuit with a piston (of elastic resistance R_1). At low frequencies ($\omega \ll \omega_0$) the effective system elastic constant (k_T) will equal k_2 as the branch of the system containing k_1 has sufficient time to respond viscously($\omega \ll \omega_0$). At high frequencies ($\omega \gg \omega_0$) there is insufficient time for the viscous response, so k_T will be the summation of k_1 and k_2. The effect of viscous relaxation was investigated in several highly viscous fluids by Isakovich and Chaban in 1966[354], where reasonable qualitative agreement with equation (7-16) was found (shown in Figure 7.5d). The lower quality of fit in Figure 7.5d compared to Figure 7.5a is caused by the complexity of glycerol's viscous behaviour compared to Fluorine's simple diatomic thermal relaxation. Similar methods to those used to generalize the Debye equation for describing a wider range of dielectric relaxations using the Havrilliak-Negami exponents (see section 2.4.2)[87,88], can be used here to generalise (7-16) to fit a wider variety of mechanical relaxation curves[356].

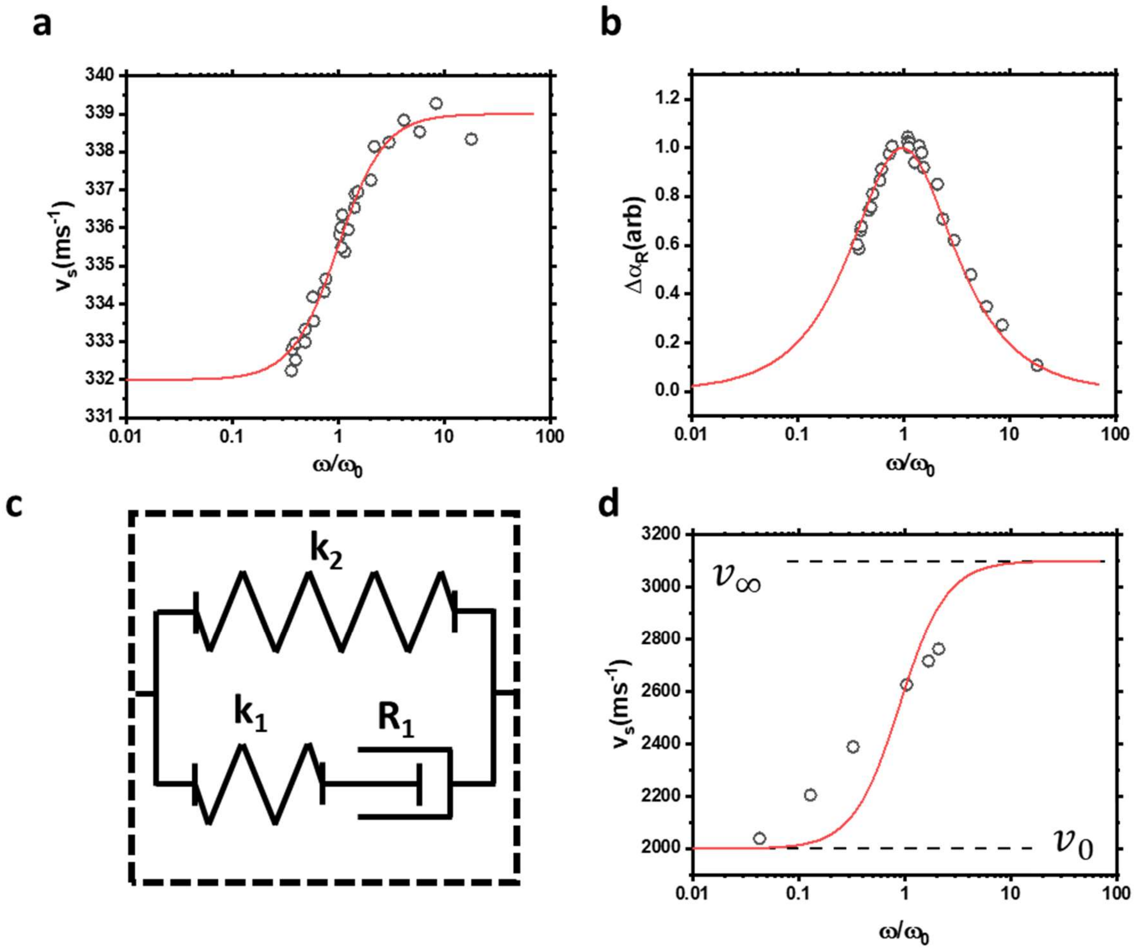

Figure 7.5. Relaxations of processes which contribute to v_s. (a) The thermal relaxation of v_s in Fluorine gas, taken by Shields[353] *(fitted with equation (7-16, ω_0=93.5kHz) (b) The corresponding α_R fitted with equation (7-18) (c) Maxwell's model of viscoelasticity. (d) Measurements of v_s in glycerol at T=-14°C from Isakovich and Chaban* [354].

7.2.2.c *Influence of Scattering in Ultrasonic Measurements*

Other complexities in ultrasonic measurements are caused by scattering phenomena. These are often described analogously to optical scattering events[267,268,357–359], where a wave is deflected from its trajectory by an interface or object. In both optical and acoustic scattering, if a bulk sample is made up of two dispersed phases, the amount of scattering depends upon: *(i)* the volume fractions (ϕ_n) of each phase, *(ii)* the contrast in transmission properties of the two phases (ε and μ for electromagnetic waves, B and ρ for acoustic waves), *(iii)* The size (d_{dom}) and shape of the domains that make each phase, *(iv)* the sharpness of the domain interfaces and *(v)* the acoustic wave frequency and wavelength [360–364].

An important manifestation of acoustic scattering in P&C measurements is when the technique is used to measure v_s in colloidal systems. Due to the huge interfaces between the two phases per unit volume within a colloid, scattering occurs to a large extent. This manifests in a number of ways, for example when v_s is measured in a colloidal system, often [338,361,365,366],

$$v_s < \phi_1 v_1 + \phi_2 v_2. \tag{7-19}$$

The cause of this difference in measured v_s is illustrated in Figure 7.6. Here, despite the same values ϕ_n and v_n, Figure 7.6a has a significantly higher v_s values than Figure 7.6b. This is caused by many more scattering events occurring in the colloidal system as the pulse moves through the material. This scattering increases the measured α,

$$\alpha > \alpha_1 \phi_1 + \alpha_2 \phi_2. \tag{7-20}$$

Here α_n are the α of the two the pure phases. This allows a quantification of the material scattering attenuation (α_s, if the attenuation of the two constituent phases are known) [359],

$$\alpha_s = \alpha - (\alpha_1 \phi_1 + \alpha_2 \phi_2). \tag{7-21}$$

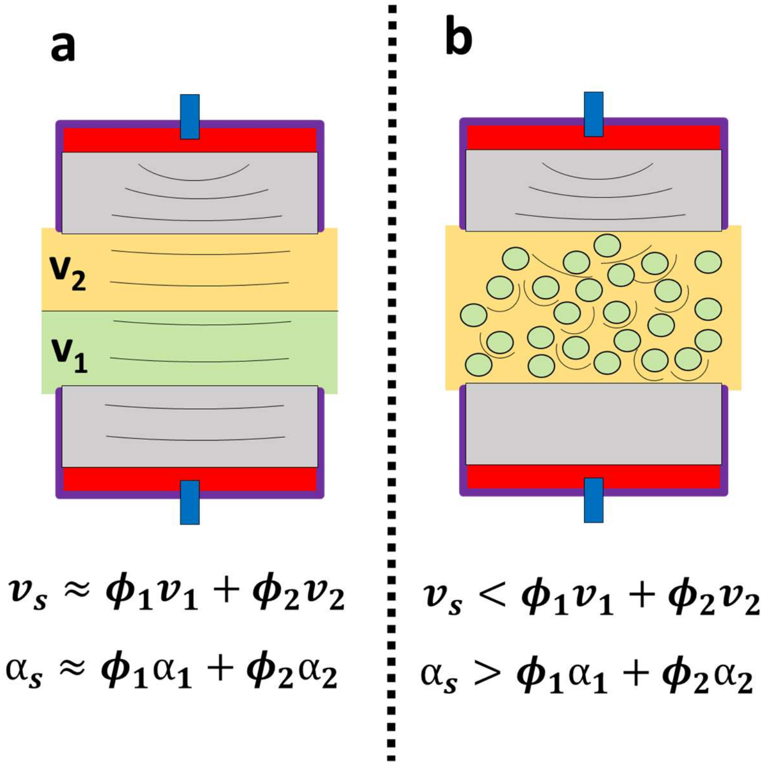

Figure 7.6. An example of a biphasic system with the same v_n and ϕ_n. (a) A separated case where the waves move through undisturbed by interfaces. (b) A colloidal system where many scattering events will occur as the waves move through, reducing v_s and increasing α.

7.2.3 Speed of Sound Measurements in Nematic Liquid Crystals

7.2.3.a *Previous Measurements of v_s using P&C*

Several P&C measurements have been reported on NLCs[367–372], where the measurements of v_s and α were found as a functions of temperature *(T)*, acoustic frequency *(f_A)* and director orientation. Here, on cooling the NLC from its isotropic phase, an increased α and a reduction in v_s is observed close to the T_{NI}. The results of v_s and α in a NLC (MBBA) taken by Eden et al. (in a configuration similar to Figure 7.4) is shown in Figure 7.7. In Figure 7.7a the v_s decreases with T with an approximately constant gradient both sufficiently above and below the T_{NI}. Closer to T_{NI} a sudden reduction in value occurs, particularly when measured with a lower acoustic frequency. This decrease in v_s typically coincides with a spike in α (shown in Figure 7.7b).

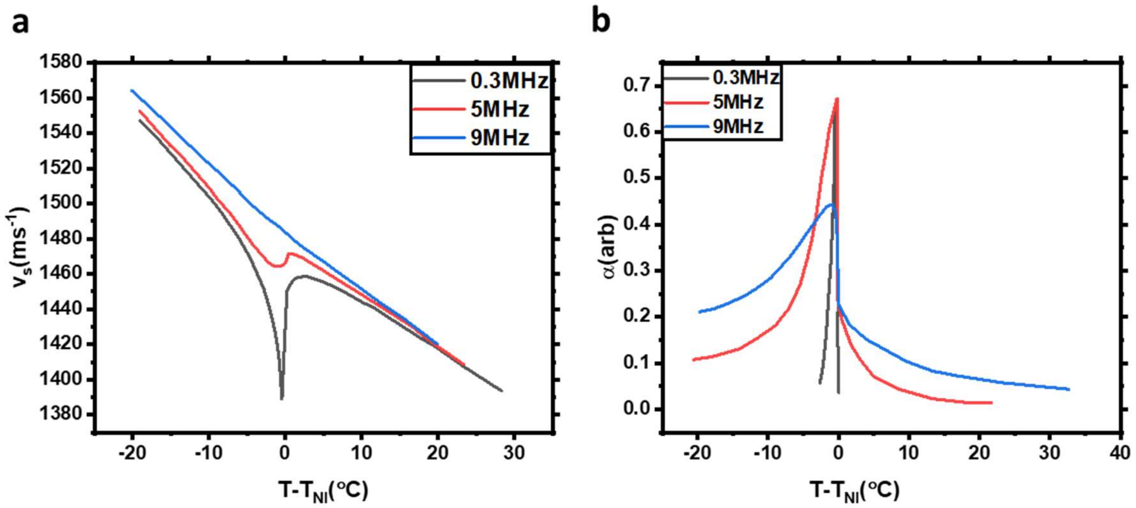

Figure 7.7 Speed of sound (a) and attenuation (b) measurements in p-methoxybenzylidine- p-n-butylaniline (MBBA)taken from Eden et al[367]. *Here no aligning magnetic field was used.*

7.2.3.b *Acoustic Dispersion in NLCs*

From Figure 7.7, a clear dispersion can be seen in v_s and α between the frequencies of 0.3 and 9 MHz[367]. The origin of this is discussed in some detail by Nagai et al. [368], where they argue that the dispersion is not only due to the viscous response of the NLC (which would occur in any viscous isotropic material), but also due to coupling between fluctuations in the nematic director and the transmitted acoustic pulse[347,373]. These director fluctuations are largest close to T_{NI}, meaning the strongest attenuation occurs here[347]. The attenuation coefficient of a NLC (α_{LC}) may be written as a sum of several processes[368],

$$\alpha_{LC} = \alpha_n + \alpha_v + \alpha_T + \alpha_\infty. \tag{7-22}$$

where α_n, α_v, α_T and α_∞ are attenuations associated with the director fluctuations, viscous response, thermal response and the high frequency static value, respectively. Here, all but α_∞ vary with frequency, similar to the equation (7-18). The equation (7-22) is a simplified picture as each term in this equation is made up of series of functions. When ω is far greater than all ω_0 all processes will be in their static rather than dynamic ranges, meaning both v_s and α will tend to v_∞ and α_∞, respectively.

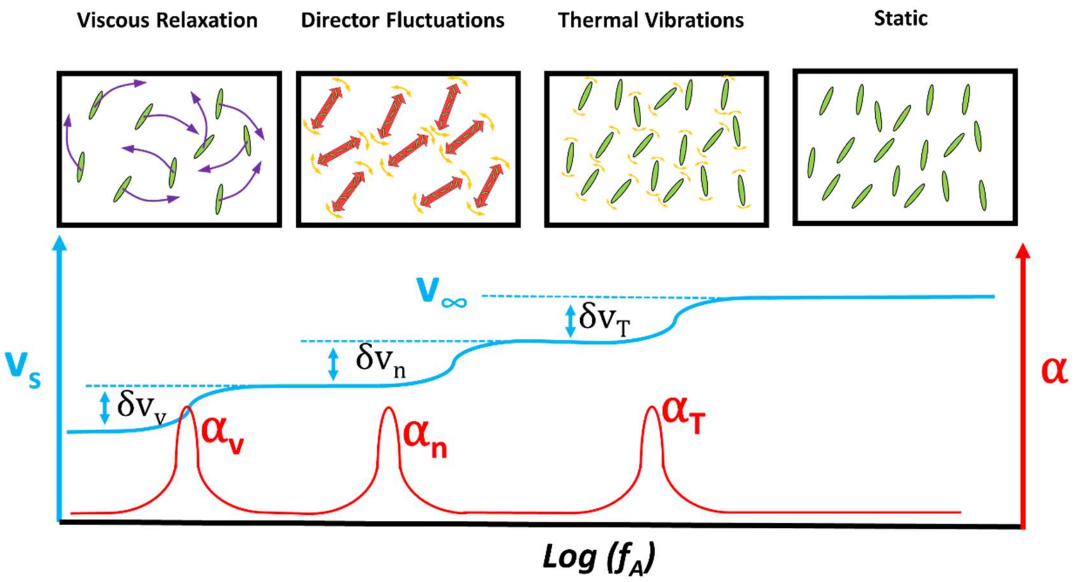

Figure 7.8. A simplified illustration of the dispersion of vs in a NLC. This is similar to what would be expected in a usual viscous fluid; but with director fluctuations. Purple single-headed arrows indicate the flow of molecules within the sample, and the yellow double-headed arrows indicate thermal fluctuations of the director. As the frequency increases to infinity, v_s tends to the value v_∞.

7.2.3.c *The Influence of Alignment and Anisotropy of NLCs on Ultrasonic Measurements*

Generally, the cylindrical symmetry of NLCs leads to two v_s and α values at a given frequency, one set perpendicular ($v_\perp$, $\alpha_\perp$) and one parallel ($v_{||}$, $\alpha_{||}$) to ***n***. For standard calamitic NLCs, generally, these are found to obey [374,375],

$$v_{||} > v_\perp. \tag{7-23}$$

and [368],

$$\alpha_{||} > \alpha_\perp. \tag{7-24}$$

This anisotropy in v_s and α leads to potential difficulties in performing P&C measurements including the requirement of the LC thickness greater than 500μm for accurate measurements as discussed in section 7.2.2.a. Such a thick layer of NLC is problematic to align with alignment layers alone. This can be overcome by using a large magnetic field to homogeneously align the director [32]. Mullen et al. [369]and Bacri [376], independently measured the anisotropy in v_s (Δv) and α ($\Delta\alpha$) as a functions of temperature. Results from reference [369] are shown in Figure 7.9a. Here, the NLC was MBBA and the magnetic field was varied from zero to 40000A/m across the sample, where at around 4000A/m the value v_s stopped changing value (interpreted as ***n*** aligning completely will the field). Similar was done in reference [376], where measurements of $\Delta\alpha$ were included (here a field up to 1.2T was used).

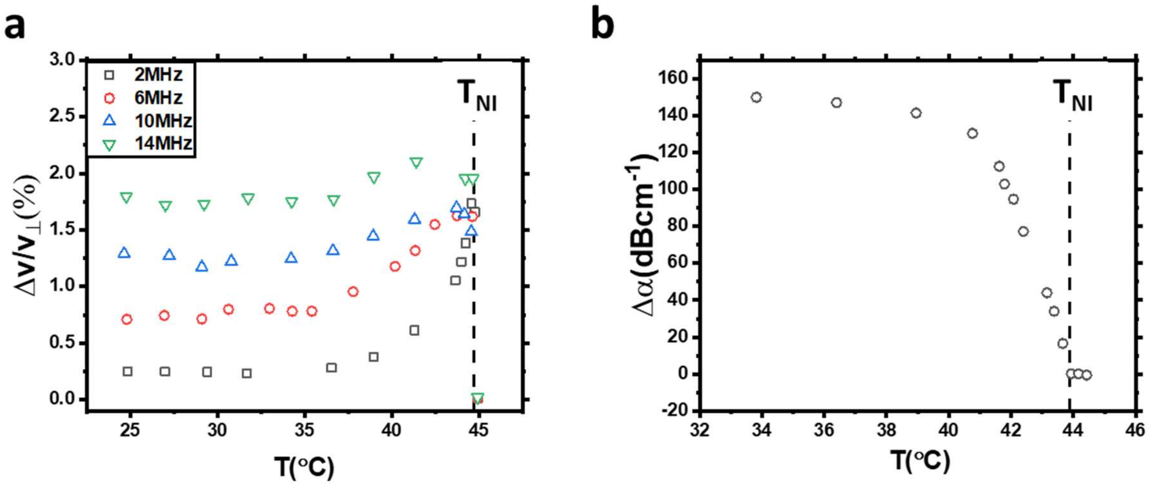

Figure 7.9. Acoustic measurements of Δv (a) and Δα (b) for MBBA as function of temperature. The data from (a) and (b) were taken from [369] *and* [376] *respectively.*

The acoustic results obtained in this chapter were obtained in the absence of any external magnetic field. The absence of such field leads to uncertainties in acoustic scattering due to inhomogenous director orientation within the sample. It is, however, reasonable to assume this scattering is negligible in this work given the small values of Δv and $\Delta\alpha$[369,376].

7.2.3.d *Brillouin Light Scattering*

Another standard method of measuring v_s in LCs is Brillouin Light Scattering (BLS), a technique utilizing the scattering of light off thermal phonons within the material[372,375,377–379]. Although this is not used in this work, it is important to note that the method has distinct advantages over P&C measurement, particularly as it can be used to find the v_s within thinner sandwich devices, which allows better control of the LC alignment. Bradberry and Clarke studied the anisotropy of v_s in the nCB series liquid crystals using the BLS [375]. Their results of $v_\perp$ and $v_{||}$ are shown in Table 7-1, where the reported difference in values are fairly small (>4%), particularly when compared to, for example, permittivity anisotropy of the materials.

Table 7-1. Measurements of vs perpendicular ($v_\perp$) or parallel ($v_{||}$) to the director taken by Bradberry and Clarke. All measurements were taken at TNI-T=5°C, except for 9CB where T=TNI-1.5°C[375].

nCB	T_{NI}(℃)	$v_{\|\|}$ (ms^{-1})	$v_\perp$ (ms^{-1})	$v_\perp/v_{\|\|}$(%)
5CB	35	1740	1680	96.6
6CB	29.1	1776	1712	96.4
7CB	42.6	1682	1623	96.5
8CB	40.6	1675	1640	97.9
9CB	49.5	1596	1545	96.8

An associated disadvantage of BLS is that it is indirect and relies on phonons scattering the optical field. Generally, it operates in the GHz range, and much of the relaxation dynamics at lower frequencies are not observable. Grammes et al. [372], compared values of v_s measured with 1MHz ultrasonic techniques and BLS in 5CB. They found that far from T_{NI} the values obtained by BLS was approximately 15% higher than using ultrasonic techniques, while close to T_{NI} it was significantly more. This is similar to the effect of increasing frequency shown in Figure 7.7a, but more pronounced due to larger difference in probe frequency.

7.3 Methods

7.3.1 P&C Set Up

The results of v_s in NLCs obtained in this chapter were measured using the P&C method, set up as part of the project. In order to conduct these measurements, two piezoelectric transducers of resonant frequency 500KHz were used (Precision Acoustics, Dorset). These acted as the ‘Pitcher’ and ‘Catcher’ transducers. They were arrayed as shown in Figure 7.10, where a fitted PTFE bowl was attached to the Pitcher to contain the fluid. The Catcher was attached with a spring-loaded mechanical micrometre stage. Here, variations in distance d to a minimum of 10 µm precision were possible using a grub screw. The Pitcher was addressed by a MP215 Ultrasonic Pulser TM500 System (MetroTek), which created electrical pulses of frequency 500KHz. These pitched pulses were recorded by an oscilloscope (GDS-1102A-U, Instek), which also recorded the caught pulses to measure Δt. No methods of aligning the LCs (alignment layers, magnetic or electric fields) were used, meaning it is likely the measurement is of some combination of $v_\perp$ and $v_{||}$. From the results of Bradberry and Clark given in Table 7-1[375], this gives an approximate minimum uncertainty due to unknown orientation of 4%.

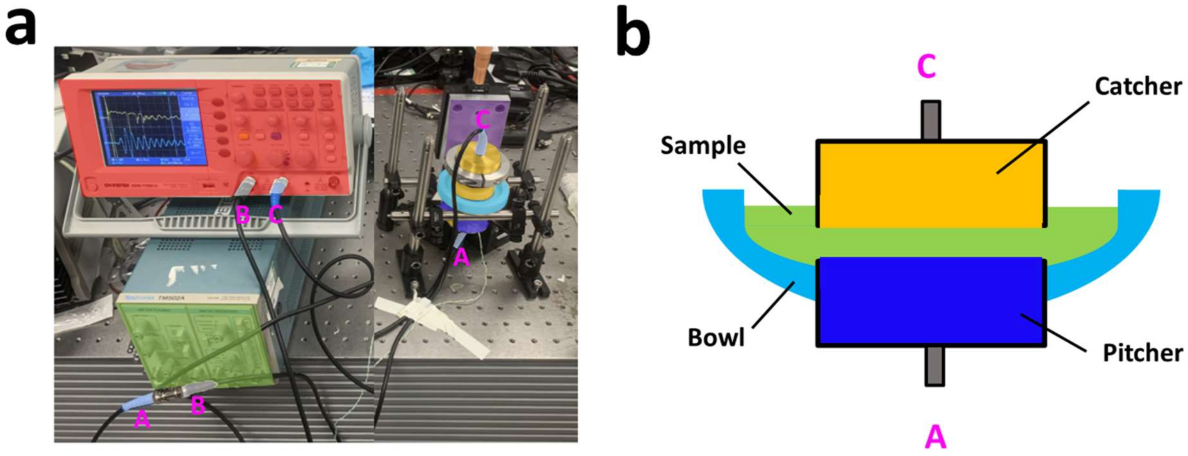

Figure 7.10. The P&C experimental set up. (a)A photograph of the experimental set up with the pulse generator (green), the oscilloscope (red), the Pitcher transducer (dark blue), the Catcher transducer (yellow), sample bowl (light blue), micrometre stage (purple), micrometre handle (orange). It also shows the three electrical connections (A, B and C), where A applies the pulse to the Pitcher, B measures the input pulse on the oscilloscope and C goes from the Catcher to oscilloscope. (b) A schematic of the sample holder and Pitcher and Catcher. The sample fills the bowl allowing the measurement to be made.

7.3.2 Procedure

To obtain a measure of v_s the bowl was first filled with the material of interest. Then, the micrometre position (p) varied as Δt was recorded. Due to the configuration of the micrometre stage, an increase in p decreased d. An example of this measurement is shown in Figure 7.11a, where at $p\approx16$mm the two transducers collide ($d\approx0$) preventing further changes to Δt. A more intuitive representation of the data is shown in Figure 7.11b. This was obtained by fitting graphs of Δt *vs* p using a linear fit,

$$\Delta t = m \cdot p + \Delta t_0, \tag{7-25}$$

then Δt was plotted against x where,

$$x = -p - \frac{\Delta t_0}{m}. \tag{7-26}$$

By definition, the linear region (7mm<x<15mm) in Figure 7.11b will have an intercept of zero. The value v_s can be obtained from either graph from,

$$v_s = \frac{-1}{m}. \tag{7-27}$$

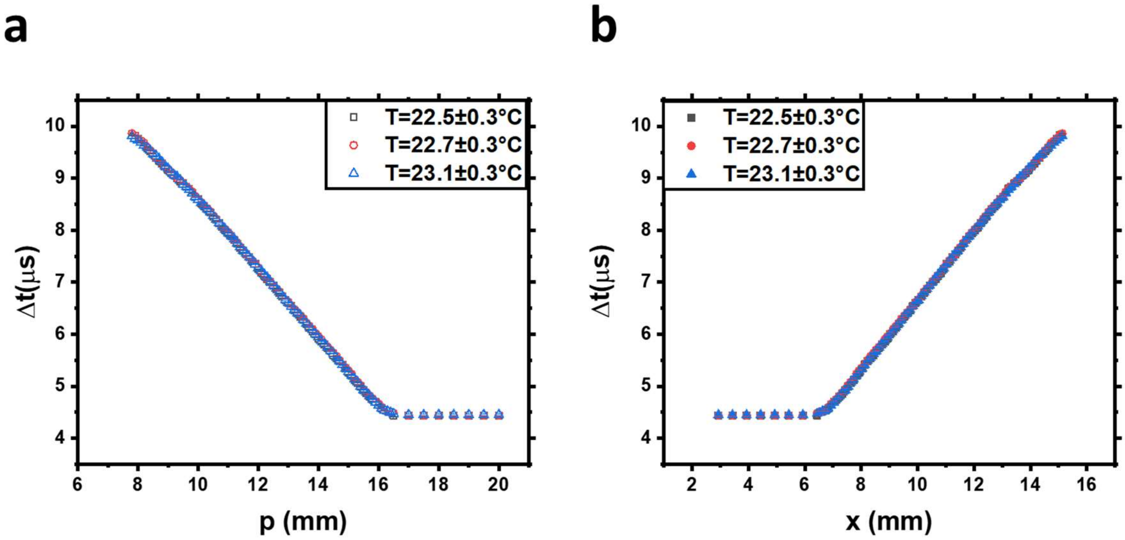

Figure 7.11. Δt as the distance between the piezos was varied. The example sample is water and was repeated 3 times at the indicated temperature. (a) Δt as the readout p was varied. (b) The same data, shifted into a more intuitive form (as a function of x) where now increases in x increases Δt and $\Delta t=0$ when x=0.

7.3.2.a *Validation*

To validate the experimental technique, v_s was first measured in several well-characterised materials: water, methanol and IPA. Figure 7.12 shows the obtained graphs of Δt against x in these. The values compared to literature are shown in Table 7-2, where all values were within 1% of those previously reported.

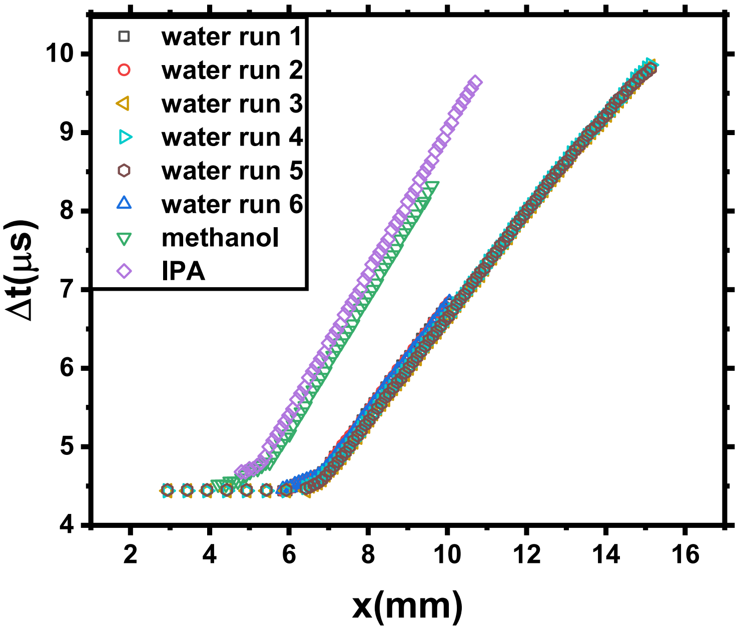

Figure 7.12. Δt as a function of x in several isotropic liquids.

Table 7-2. Values from of vs in some simple isotropic liquids. Here the literature values are compared to those obtained in this work. The difference in % value is quoted in the final column.

Liquid	Literature v_s(ms^{-1}) at T=20°C	Obtained v_s(ms^{-1})	% Difference
Water	1482.343 ([380])	1479±7 (T=22.7±1.0°C)	0.2%
Methanol	1125 ([351])	1113±5 (T=19.9°C)	1%
IPA	1157([348])	1153±5 (T=20.6°C)	0.3%

7.3.3 Temperature Control

The sample temperature was varied using an insulated aluminium box with an internal variable heating element (Bosch, GHG 23-66 heat gun 2300W). Ice was used to cool the box below ambient temperatures. When a thermocouple was placed inside the box (attached to one of the transducers), these techniques allowed variation in the probe temperature (T_p) from around 10°C-100°C. It should be noted that T_p is not necessarily equal to the sample temperature (T_{LC}).The setup used to do this is shown in Figure 7.13.

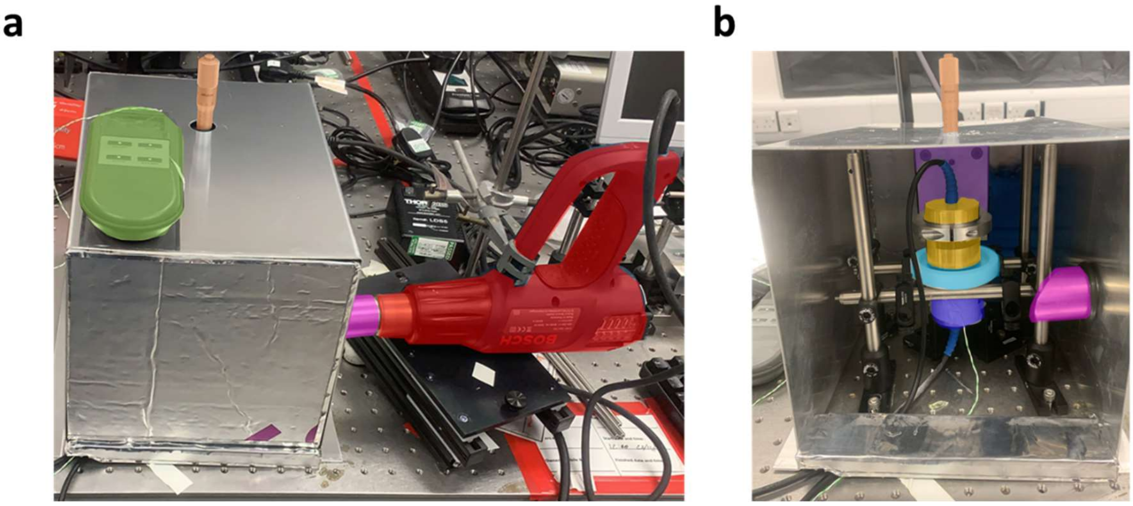

Figure 7.13. Photographs of the set up used to control temperature while undertaking P&C measurements. Colours correspond to those in Figure 7.10. Here the Bosch Heat gun (red) sends hot air through the feed tube (pink) into the aluminium chamber. The temperature is then measured by a digital thermocouple (green) which was attached to the Pitcher transducer. (a) The chamber when shut, while (b) shows it with one of the walls removed to see the inner experimental apparatus.

7.3.4 Measurements of the Speed of Sound in NLCs

Using the outlined techniques, v_s was measured in the positive Δε NLC E7 (T_{XN}=-55°C[381], T_{NI}=78±2°C (measured with POM)). 2ml of material was used, which allowed Δt to be measured as p was varied over a range of around 5mm. From the results of the isotropic fluids, it was found that small distances between the data points p (Δp) were essential to obtaining accurate values. Firstly, runs were conducted with a relatively small value Δp of 50 µm. These were done at several temperatures in three cooling or heating runs:

- **Run #1.** Decreases T_p from 28°C using ice, taking measurements at T_p=28, 25, 19 and 14°C.
- **Run #2.** Increased the temperature from 20°C to 72°C using the heat gun, taking measurements at T_p=52, 65, 72°C.
- **Run #3.** Reduced the temperature from 72°C to 20°C by turning off the heat gun, taking measurements at T_p=42 and 36°C.

For each temperature greater than 30°C the heat gun was programmed to a specific heating setting and left for 30 minutes to allow the sample to thermally equilibrate before a measurement was taken. This was similar for placing ice on top of the box for temperatures lower than T_{amb}. Errors in T_p (ΔT_p) were recorded as the difference in T_p at the start and end of the experiment.

In addition to the Δp=50µm experiments, a cooling run was completed where the sample was heated to T_p close to 100°C and left heating for around 1 hour. After this time, the heater was turned off, and the sample was allowed to naturally cool as measurements were taken. Here, the measurements had to be completed quickly due to the constant cooling, meaning a larger Δp of 500µm was used. This coarser measuring technique allowed measurement at a broader range of T_p. Once the sample reached T_{amb}, ice was used to cool the samples further to a T_p of around 10°C.

7.4 Results

7.4.1.a *Temperature scans with Δp=50µm*

Figure 7.14 shows results from Δp=50µm measurements at several temperatures. Figure 7.14a shows the raw data of Δt vs p where a linear relationship was observed between p=13mm and p=15.5mm in all cases. In this range, the data was fitted using a linear fit, and using equation (7-26). Figure 7.14b shows v_s as T_p was varied. Here a pink line is included as a guide to the eye to demonstrate the possible highly similar behaviour to Eden's results on MBBA[367], where a reductions in v_s was observed close to T_{NI} (Figure 7.7). Here, the approximate T_p where the nematic isotropic transition occurs ($T_{NI, p}$) is marked in addition to that more accurately measured using polarized microscopy ($T_{NI, opt}$). It can be seen error bars in T_p are much larger at higher temperatures than ambient ones. This is due to its value would change more rapidly. The errors in v_s were obtained by numerical fittings of Figure 7.14a.

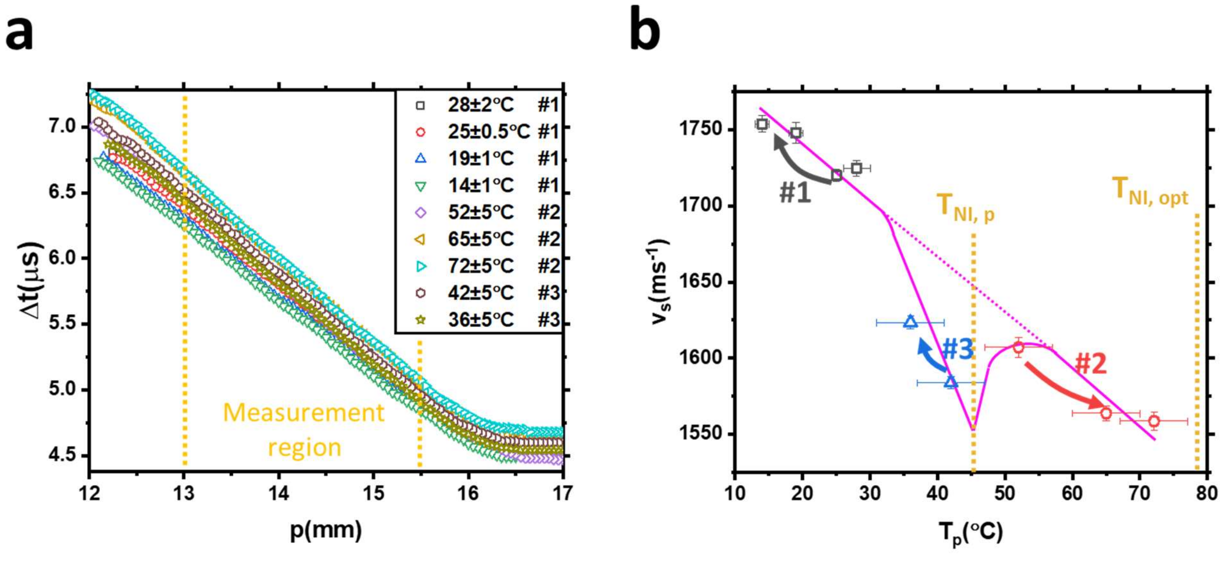

Figure 7.14. Results from the Δp=50µm experiments at several temperatures from runs #1,#2 and #3. (a) Δt as p is varied. (b) The calculated values of vs as T_p was varied. The different runs are colour coded and the arrows give the direction of temperature change as the measurements were taken. The pink lines indicate an interpretation of this data, where the apparent reduction in v_s around T_p=45°C is considered to be real and not due to experimental noise.

7.4.1.b *Temperature scans with Δp=500µm*

Figure 7.15 shows the results from the Δp=500µm measurements. Comparing Figure 7.15 with Figure 7.14, the effect of the larger Δp can be seen. The behaviour of v_s shown in Figure 7.15b is similar to that observed in previous studies [367,368], where the v_s is fairly linear aside from in the region where the isotropic nematic transition occurs (T_p≈53°C). The blue points have been fitted with a linear fit,

$$v_s = m_T \cdot T_p + v_0, \tag{7-28}$$

where v_0 is the speed of sound at T_p=0°C and m_T is the rate of change of v_s with T_p. This fit obtained, v_0 = 1696±9ms^{-1} and m_T= -3.3±0.2ms^{-1}°C^{-1}. The most notable deviations from this behaviour is at high temperatures when the uncertainty in T_p is largest.

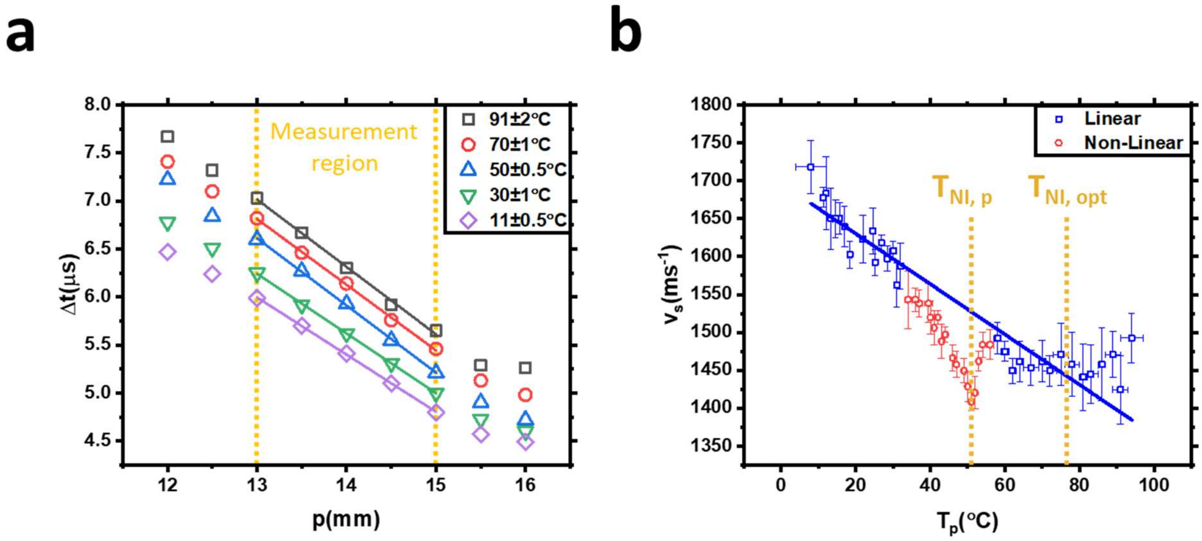

Figure 7.15. Similar graphs to Figure 7.14 but for the Δp=500μm case which is coarser, but provides more temperature dependent data. (a) Examples of several calculations of Δt as p was varied. The region where the fits were obtained is shown. (b) The calculated values v_s. The data points close to T_{NI} are coloured red, while those away are blue. The blue points are fitted with equation (7-28).

7.5 Analysis and Discussion

This section combines results from Δp=50 μm and 500 μm data sets. Figure 7.16a shows the graph of comparison of the two sets of results, where a systematic decrease in measured v_s was found for the Δp=500 μm compared to Δp=50 μm. The ratio of the values v_s for Δp=50μm and 500μm (v_{50}/v_{500}) are shown in Figure 7.16b, where an average value of 0.94±0.02 was found. As Δp=50μm results are likely more accurate than Δp=500μm, these results were divided by 0.94. This shifted the results to the values shown in Figure 7.16c, where additional errors have been added due to uncertainty in the shifting process.

To convert T_p to T_{LC} it was assumed that at T_{amb} T_p=T_{LC} and that when T_p=53°C, T_{LC}=78°C. Using these two points T_{LC} was assumed to take the form,

$$T_{LC} = m_T T_p + T_0, \tag{7-29}$$

where m_T and T_0 were, 1.8±0.2 and -15±6 respectively. As there was no transition to rescale to below T_{amb}, here it was assumed that $T_{LC} = T_p$. The error in temperature naturally deviates further from T_{amb}, meaning the error in T_{LC}(ΔT_{LC}) was approximated as,

$$\Delta T_{LC} = \left|T_{LC} - T_p\right| \frac{\Delta m_T}{m_T}. \tag{7-30}$$

Here Δm_T is the fitting error in m_T. Figure 7.16d shows results from this analysis where v_s is shown as a function of T_{LC}, where the behaviour typically associated with the nematic to isotropic transition can be observed at T_{NI}. The data of v_s in runs #1 and #3 are fitted with a linear fit (shown as the pink line in Figure 7.16d). Here the gradient was found to be -2.3 ± 0.1ms^{-1}°C^{-1} and the intercept 1770± 10ms^{-1}.

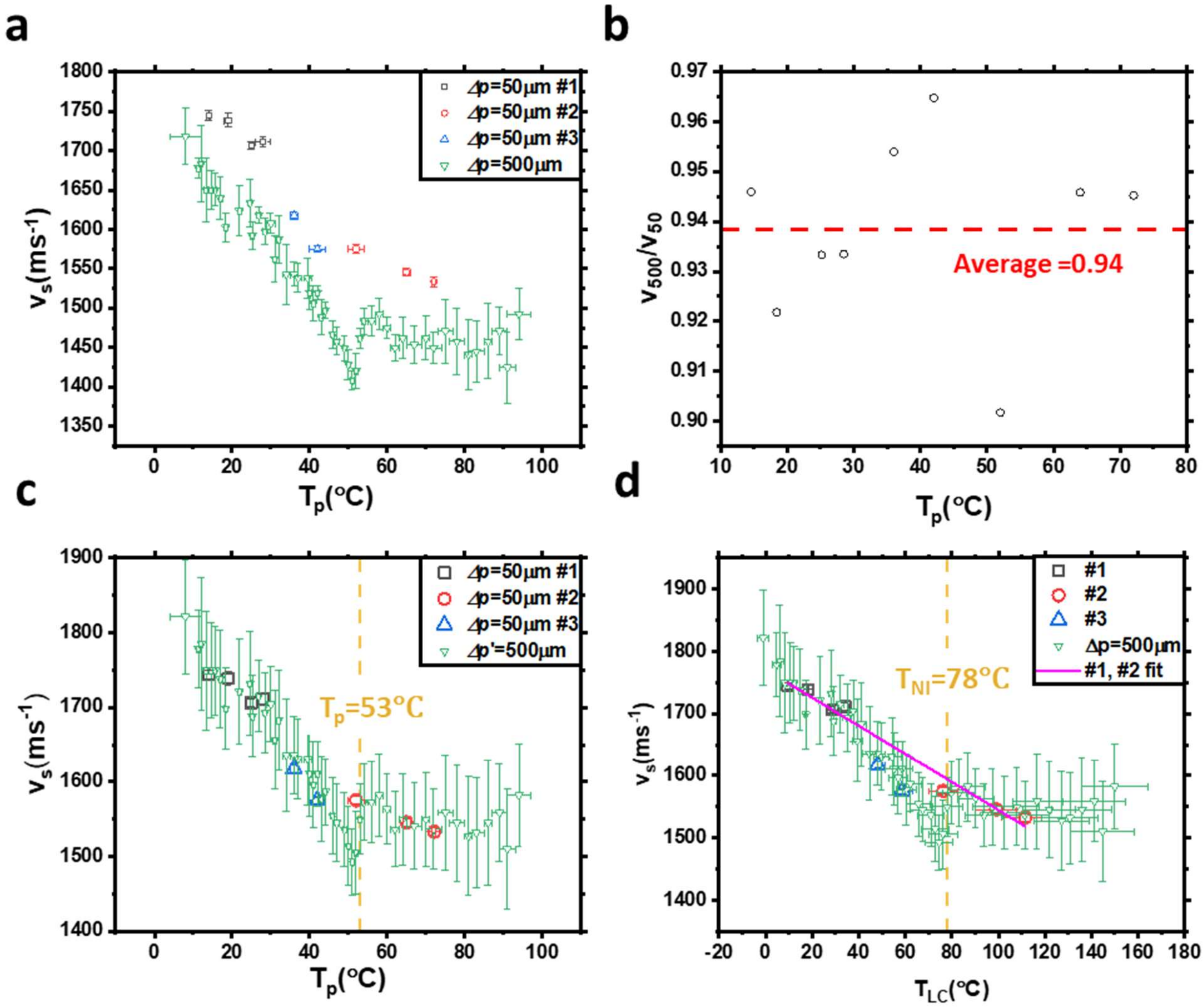

Figure 7.16. Plots showing how the combination of results from Δp=50μm and Δp=500μm experiments. (a) Shows the raw data comparison where an offset between measurements can be seen where Δp=50μm measurements are all above the Δp=500μm. (b) The values of v_s for Δp=500μm divided by Δp=50μm where data was available. Here the average value is shown. (c) The same data as (a), however now the Δp=500μm has been divided by the average shown in (b). (d) v_s as a function of T_{LC}. The x and y error bars for the Δp=500μm and x error bars in Δp=50μm are large due to amount of analysis undertaken.

No values for v_s for the nematic mixture E7 have previously been published making a direct comparison of the results obtained here to other literature difficult. Therefore, the values for v_s in the components of E7 were found to assess whether the experimental values obtained are reasonable.

E7 is a mixture composed of 51% 5CB, 25% 7CB, 16% 8OCB and 8% 5CT[382]. Ultrasonic v_s measurements in both 5CB and 8OCB have been published previously as functions of temperature in references [372] (f_A=1MHz) and [383] (f_A=2MHz), respectively. No examples of measurements of v_s in 7CB using ultrasonic methods were found in literature, however using Brillouin scattering it was found to have a very similar v_s to 5CB [367]. 5CT has not been previously been measured for v_s. Therefore it was assumed that

$$v_{5C} \; = \sqrt{\frac{\rho_{5CB}}{\rho_{5CT}}} \times v_{5CB} = 1.097 \times v_{5CB}, \tag{7-31}$$

(see equation(7-4)). Here v_{5CB} and v_{5CT} are the velocity of sound in 5CB and 5CT materials and ρ are their densities. These values of v_s as function of temperatures are shown in Figure 7.17a. The figure shows the reported values for 5CB, 8OCB, which are fitted with linear fits for data points far from T_{NI}. From the values for 5CB and equation (7-31), the predicted value for 5CT is also shown. A simple model of how v_s could be expected to behave in E7 is included here,

$$v_{E7} = (\phi_{5CB} + \phi_{7CB})v_{5CB} + \phi_{8OCB}v_{8OCB} + \phi_{5CT}v_{5CT} \tag{7-32}$$

where ϕ are the respective components volume fractions.

Equation (7-32) is compared to experimental data in Figure 7.17b. Here it can be seen that the model predicts lower v_s values than both the Δp =50 and 500μm results, however the experimental values are within the acceptable region ($\pm$200ms^{-1}). Moreover, the model is too simplified, as for example it takes no account of the influence of order parameter or the non-linear characteristics of LC mixtures[384,385]. It is unlikely that the difference is due to the difference in acoustic frequencies, as the 5CB and 8OCB studies used higher frequencies compared to ours. This would usually lead to higher value of v_s, where here the opposite was observed. It is also likely that E7 and 5CB undergoes acoustic relaxation processes at similar frequencies, as broadband dielectric studies both find their dipole reorientations relax at approximately 10MHz[386,387].

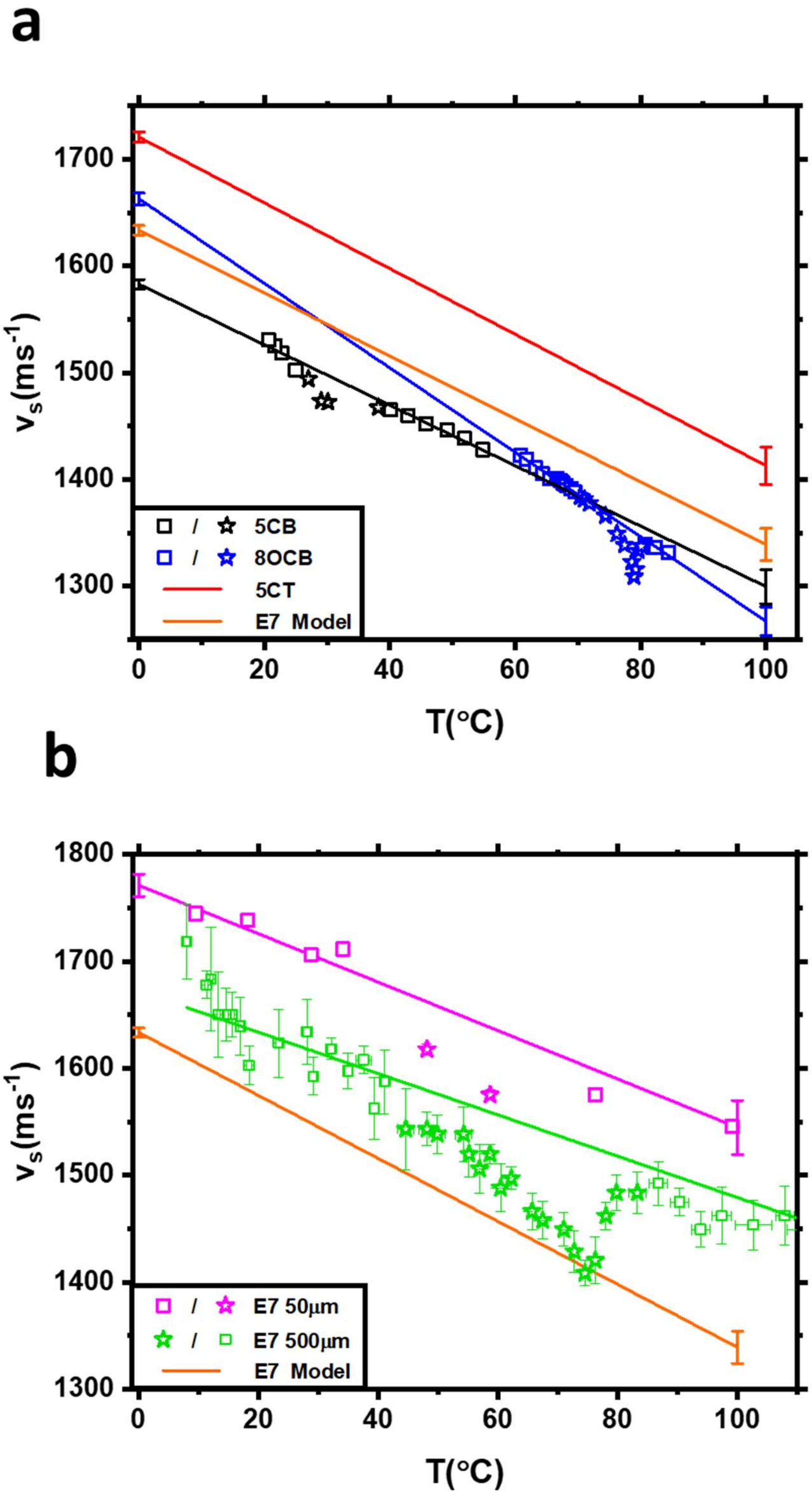

Figure 7.17. Figures comparing equation (7-32) to experimental data. (a) The experimental data for v_s in 5CB and 8OCB taken from references [372] and [383], respectively. Starred points are close to T_{NI}, squared are far away. The square points are fitted to linear fits which are shown. The linear fit for 5CT was obtained using the result for 5CB and equation (7-31). The orange line shows the predicted behaviour of E7 using equation (7-32). (b) Comparison of (7-32) to experimental data. The Δp=50μm and Δp=500μm (before normalising to the Δp=50μm data) points are included.

7.6 Conclusions

In this chapter the acoustic properties of NLCs have been introduced with a focus on techniques used to measure the speed of sound. In the context of speed of sound measurement, the complexities arising from the viscoelastic and anisotropic nature of NLC materials have been discussed, with examples of how they manifest when ultrasonic measurements are performed.

This chapter has firstly reported upon a customised experimental apparatus designed to measure v_s for unusually small quantities of material. It then is demonstrated to be capable of measuring v_s in simple isotropic fluids within 1% of other published values. v_s is then measured in the NLC mixture E7. These results appear to be of reasonable magnitude compared to similar materials previously studied, and display similar trends as a functions of temperature; with a tendency for v_s to decrease with T and a sharp dip occurring close to T_{NI}. These results were compared to a simple theoretical model of what the v_s in E7 might be expected to be from knowledge of its components. This model does not accurately present the data (giving a lower v_s by a factor between 5-10%), however is of the correct magnitude and gives a similar gradient to the probably more accurate Δp=50μm results. For further validation of the results presented, a measurement of a larger quantity of material with more uniform temperature control would be advised.

The most important results presented here for this thesis are the values v_s in E7 at ambient temperatures, as these will be used extensively in the next chapter to understand the interaction of the materials with surface acoustic waves. For this purpose we take the value v_s at ambient temperatures (18-28°C) to be v_s=1720±70ms^{-1} where the error incorporates both the range of results given in run #1 and the typical anisotropy of around 4% seen between $v_\perp$ and $v_{//}$ Brillouin scattering studies[375]. The next chapter will return to the creation of DOEs, this time utilizing acoustic waves. In addition to the value of v_s in E7, the discussion of acoustic transport given in this section will used.

Chapter 8 Acoustohydrodynamic Gratings in Nematic Liquid Crystals

In the previous chapter, the complexities of low intensity ultrasonic wave transmission in NLCs was discussed. In this chapter, NLCs are investigated under higher acoustic pressures, where the intensity is sufficient to influence the orientation of the NLC director.

This chapter is split into two by the types of acoustic field applied to NLCs. Firstly, section 8.1 discusses NLC interactions with longitudinal Bulk Acoustic Waves (BAW), where the theory of such interactions and some preliminary experimental results are discussed. Sections 8.2-8.4, then go on to discuss the effect of Surface Acoustic Waves (SAW) on NLCs more thoroughly. The reason for this focus, is that SAW-NLC interactions have previously been shown to create hydrodynamic gratings similar to those observed in EHDI[24,25,27,388], however unlike BAWs are still a relatively unexplored research space.

The results from this chapter will then be combined with results from Chapters 4, 5, 6 and 7, in Chapter 9 to discuss hydrodynamic patterns in NLCs in the broader context of NLC diffractive optical elements.

8.1 Structural Transformations Due to Bulk Acoustic Waves

8.1.1 Acousto-Optical Phenomena in Nematic Liquid Crystals due to Bulk Acoustic Waves

In this section, results from previous studies investigating high power BAWs interacting with NLCs are discussed. Due to the orientation of the NLC changing as the acoustic field is applied, the phenomena are fundamentally non-linear, requiring relatively complex theoretical descriptions[372,373,389–392]. Good reviews on the both experimental and theoretical aspects are given in references [27,189,388,393]. To understand the interaction of materials with both BAWs and SAWs, the relationship between the acoustic wavelength (λ_A), frequency *(f)* and speed of sound *(v_s)*

$$\lambda_A f = v_s, \tag{8-1}$$

is fundamental and will prove crucial throughout this chapter.

A common configuration used to examine NLC interactions with BAWs is shown in Figure 8.1a, where a NLC sandwich device is placed in contact with a BAW transducer. This transducer is then driven to create longitudinal waves of wavevector $\boldsymbol{q_L}$, which pass through the device[394,395]. Several phenomena have been observed within such devices, such as: director reorientation, narrow domain formation, defect formation and light scattering. These are described below and are in increasing order of the acoustic intensity that is usually required:

i. **Director Reorientation.** This phenomena is understood to be caused by a direct coupling between $\boldsymbol{n}$ and the incident acoustic field (Figure 8.1b), the free energy of which is minimized when $\boldsymbol{q_L}\cdot\boldsymbol{n}=0$[27,391,393,395–400]. It is this director coupling, which is thought to be responsible for the sharp increase in attenuation close to T_{NI} observed when undertaking P&C measurements (see Chapter 7)[373,390,391]. Often, in the experimental configuration shown in Figure 8.1a, the director coupling observed tends to have some spatial periodicity, leading to it often being referred to as wide domain formation. This periodicity is usually explained as either being caused by the acoustic field setting up standing waves [395,400], inducing viscous flow within the material[393,394,401,402] or a combination of both[27,403,404]. Each of these mechanisms place spatially dependent torques upon $\boldsymbol{n}$, which create domains of the order of millimetres[395,399]. They are predicted to have a period (λ_{dom}) related to λ_A by[388,395],

$$\lambda_{dom} \approx \frac{\lambda_A}{4}. \tag{8-2}$$

ii. **Narrow Domain Formation.** Shorter domains highly similar to those seen in electrohydrodynamic instabilities (EHDI) have also been observed[27,392,407,393–395,398,401,402,405,406]. These can be explained by the formation of vortices in the NLC[388,392,402] (Figure 8.1c), and are observed more clearly under shear oscillations [408] as opposed to longitudinal BAW. It may therefore be their appearance in BAW is due to intense longitudinal acoustic waves being transferred to shear waves at interfaces.

iii. **Defect Formation.** As acoustic intensity increases, visible flow can be observed within the devices distorting the domains[393]. This can lead to the creation of disclinations within the material.

iv. **Light Scattering Mode.** At even higher intensities flow and defects can lead to the material adopting a dynamic light scattering (DLS) state [393]. This is similar to the DSM modes seen in EHDI[2,249,271], and are caused by $\boldsymbol{n}$ rapidly fluctuating on short length scales, leading to the material appearing optically milky [267,268].

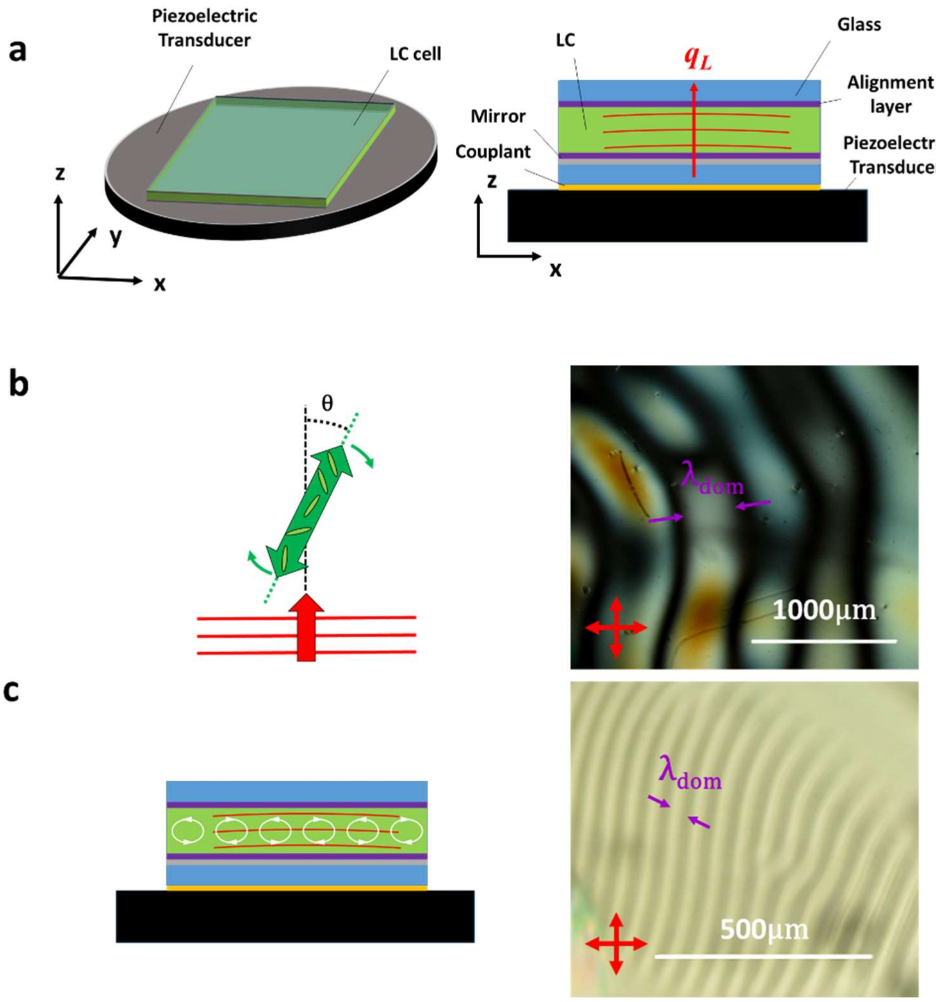

Figure 8.1Diagrams illustrating acousto-optical effects in NLCs. (a) A device configuration used in our work and reference [395]. *(b) Diagram and photograph of the phenomena of director reorientation due to a longitudinal acoustic field. (c) Diagram and photograph of the formation of short hydrodynamic domains due to the application of BAW.*

In this section preliminary investigations into the interaction of BAWs with NLCs will be presented. The goal of this research was to create DOEs, thus a focus will in finding methods of creating uniform periodic structures.

8.1.2 Method

8.1.2.a *Fabrication*

Cells of type shown in Figure 8.2 were created, comprising one 0.7mm ITO coated glass substrate and one 1-1.1mm aluminium-coated glass substrate (either coated in house or purchased from Dynasil Corp). These allowed application of voltage across the NLC and clear viewing of the device in reflection Polarized Optical Microscopy (POM). Mylar films were used to control the device spacing (*d*), as it was found that spacer beads would scatter under applied acoustic fields. The alignment layers used to achieve planar homogenous (PH) and homeotropic (HT) alignment were SE2170 and SE1211 (Nissan

Chemicals), respectively. The devices were filled with either an electrically positive (E7) or negative (MLC 2081) NLC mixture, which allowed control of ***n*** through a Fréedericksz transition [32,98]. The devices were firstly sealed with UV glue (UVS93), then several layers of two part adhesive epoxy (Araldite, RS Components) were added to prevent leakage (which was found commonly when applying acoustic fields to similar cells).

The piezoelectric transducers used were Lead Zirconate Titanate (PZT) disks with longitudinal mode resonant frequencies of 1MHz (purchased from Precision Acoustics, Dorset). These disks were placed into contact with the LC cell through a layer of acoustic couplant (UTX5000, Cordex), where this contact was maintained either with bulldog clips or tape. All electrodes were attached using indium solder.

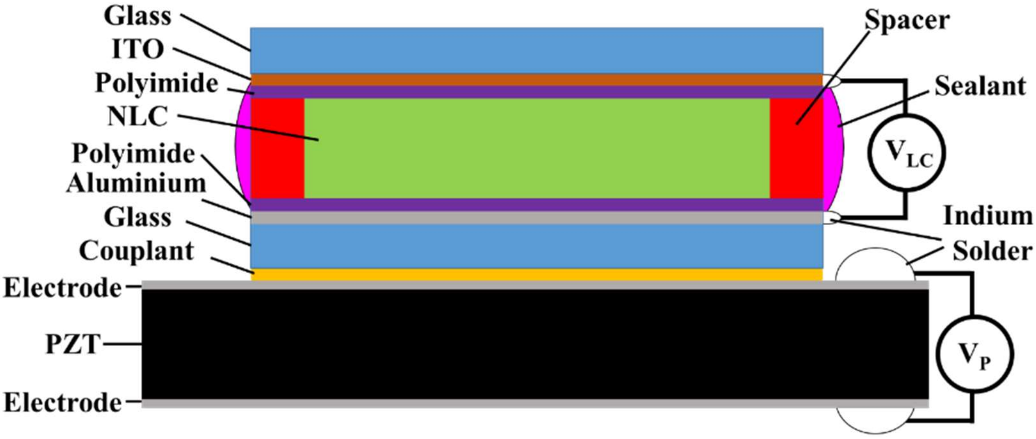

Figure 8.2. Diagram of the devices created, which consist of standard LC cell placed onto a PZT piezoelectric transducer.

8.1.2.b *Addressing*

Using the ITO and aluminium layers as electrodes, voltages were applied across the LC layer (V_{LC}). This allowed both the Fréedericksz transition and dielectric measurements to be performed. The PZT disks were addressed with a piezo voltage (V_p), either directly from a function generator (TGA12100, Aim TTi, allowing 1MHz driving up to 7.1V), or through an amplifier (allowing up to 100kHz driving at 34V).

8.1.2.c *Overview*

The previous chapter described a number of physical processes important to the transmissions of BAWs through NLCs. In this chapter we undertake experiments at higher intensities where the aim is to change the director orientation. For clarity, the results in this chapter are split into three studies:

- **Study One.** Investigates the optical effect of PZT disks driven directly by a function generator at 1MHz on NLCs in devices with either PH or HT alignment.

- **Study Two.** Investigates the effect of PZT disks driven by the amplifier at 100kHz on rubbed HT devices filled with E7 of varying *d*.
- **Study Three.** Expanded Study One by also applying voltages across the NLC, to measure capacitance and observe changes in the Fréedericksz transition.

Details of the devices used in these studies are given in Table 8-1.

Table 8-1. Details of the devices used for various studies, including how they will be referred to (code), which studies they were used for, the alignment type/polyimide used[73] and d.

Code	Study	Alignment / PI name	LC	*d* (µm)
PH-17-E7	1,3	PH/2170	E7	17±1
HT-19-MLC2081	1,3	HT/1211	MLC2081	19±1
HT-18-MLC2081	3	HT/1211	MLC2081	17.7±0.3
HT-17-E7	2	HT/2170	E7	17±1
HT-33-E7	2	HT/2170	E7	33±2
HT-65-E7	2	HT/2170	E7	65±5

8.1.3 Results and Discussion

8.1.3.a *Study One: Longitudinal BAW at 1MHz*

In this study, the effect of increasing V_P at 1MHz (while V_{LC}=0) was examined in devices PH-17-E7 and HT-19-MLC2081, while taped to piezoelectric transducers. Photographs of the NLC textures are shown in Figure 8.3. In the HT sample, wide domains of λ_{dom}=450±50µm were seen at V_p >1.6V. Their size indicate good agreement with equation (8-2) which predicts λ_{dom}≈430µm (using v_s=1720±70ms^{-1}, f_A=1MHz) for the wide domains. As V_p was increased, these domains became more birefringent while λ_{dom} did not change significantly. At higher acoustic intensity (V_p=5.1±0.2V), defects were seen to form within the material. These disclinations would move turbulently within the materials during application of the acoustic field, and create regions that appeared to resemble planar (PL) alignment. In these 'planar' regions, short pitch domains would often appear, usually between two disclination lines (see highlighted pink box in Figure 8.3). These domains were often also seen near other interfaces (e.g. glue seals), indicating they may not be formed by the longitudinal acoustic wave, but instead secondary waves created by scattering. This is supported by results given in reference[408], where similar domains are observed due to shear oscillatory driving. When the acoustic field was removed the disclinations would move together, shrinking the 'planar' regions and eventually annihilate on the timescale of seconds. In the PH sample, little interaction was seen until V_p=3.5±0.5V, at which point defects formed and flowed throughout the sample. Similarly the regions inside these disclination lines were slightly different in colour to those outside of it, indicating ***n*** is reorienting to overcome the small pretilt (~2°[73]). Generally, these results concur with previous studies using similar geometries[393,395], however previous reports of these 'planar' regions forming have not been reported.

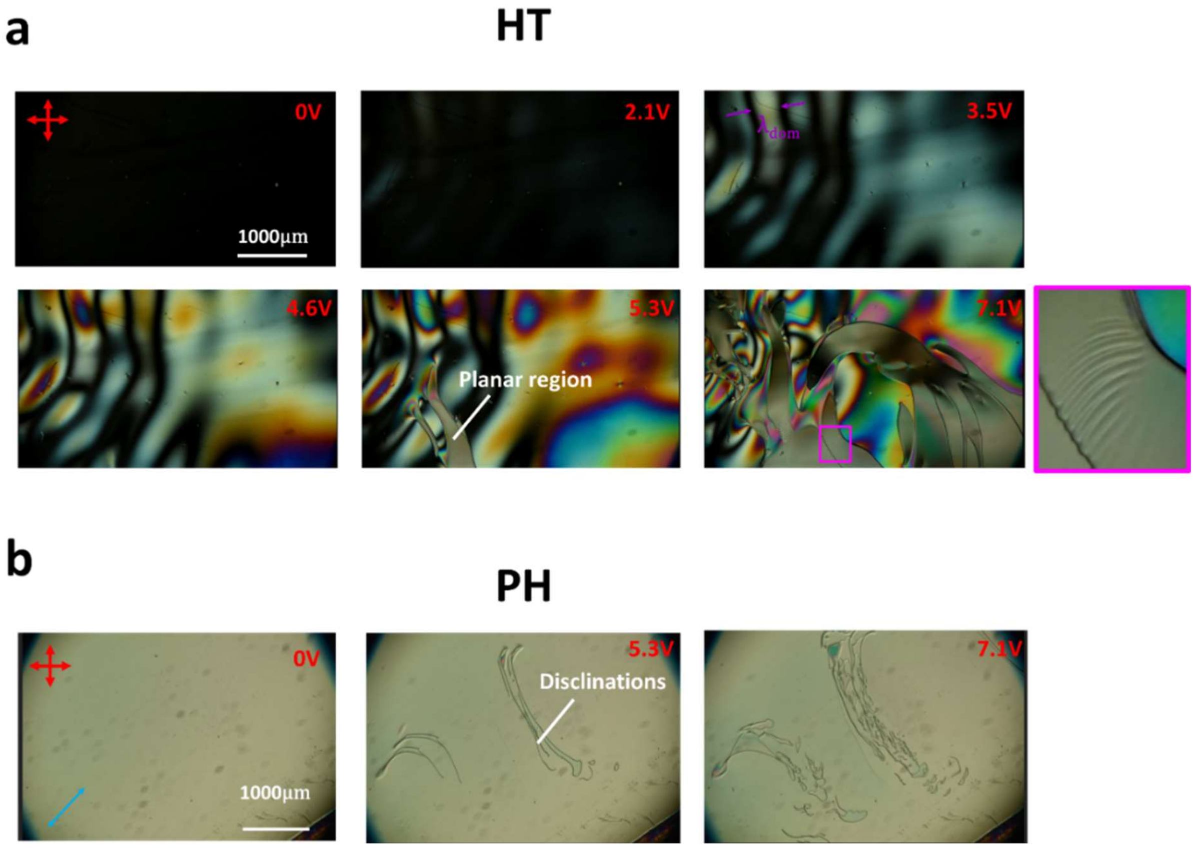

Figure 8.3. Images of HT-19-MLC2081 (a) and PH-17-E7 (b) cells under longitudinal acoustic driving. In (a) as the voltage increases director reorientation is seen with a wide domain. Then defect formation occurs were regions between defects appear. At high intensities short domains between the disclinations are seen (shown in 7.1V image where the pink box shows the region of interest zoomed in). T=25 ±1°C. In (b) little director reorientation occurred however defects forms at approximately the same intensity as in the homeotropic case. T=16 ±1°C.

8.1.3.b *Study Two: Clipped Devices at 100 kHz*

In Study Two, several rubbed homeotropic devices were created (HT-17-E7, HT-33-E7 and HT-65-E7), where it was hypothesised that giving a preferred director orientation would align the domains similarly to those observed in the NR mode of EHDI. The devices were attached to the piezoelectric disks with bulldog clips and driven using the amplifier setup (at f= 98, 93 and 105kHz respectively) to maximize power into the NLC. Photographs of the NLC texture at several voltages are shown in Figure 8.4. Large interaction occurred only in the 33 and 65μm devices. In these devices, director reorientation occurred forming wide domains with $\lambda_{dom}\approx$ 2mm (the correct order of magnitude as that predicted by equation (8-8), which gives $\lambda_{dom}\approx$4mm). Unlike the Study One, the short domains here reliably formed at the higher intensities, where λ_{dom} was measured to be 30±5µm and 70±10µm for the 33 and 65 µm devices, respectively (giving the possible expression $\lambda_{dom} \approx d$). Without further experiments, it is unclear whether the formation of these domains is due to the lower frequency, the larger values d, the higher V_p or the fact the devices were clipped to the PZTs. However, the most likely explanation is that the disk is not being driven at its 1MHz longitudinal resonance, instead in the usually lower frequency radial mode (vibration oscillating disk diameter rather than thickness[409]). This supports results from Study One and reference[408], that short period ($\lambda_{dom} \approx d$) domains are created when the ultrasonic field has a significant shear component.

The reason the 17 µm device showed such little interaction is also unknown; however it may be that the stronger anchoring strength relative to the amount of NLC, means the acoustic field is insufficient for large scale interaction.

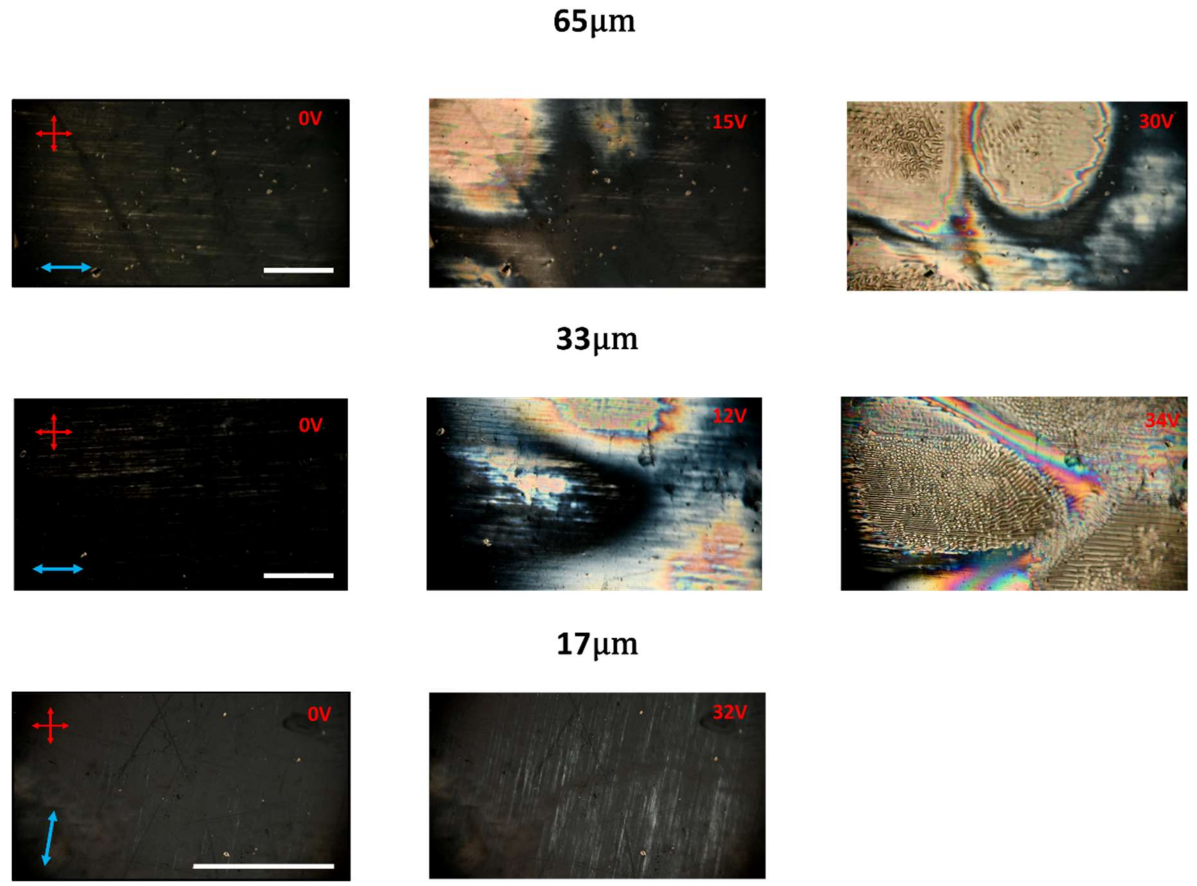

Figure 8.4. Images of rubbed HT devices of different spacing. Here all scale bars are 1mm (white) and the rubbing direction is indicated by the double-headed blue arrow.

8.1.3.c *Study Three: BAW and the Fréedericksz Transition in PH Device*

Study Three investigated the interplay between acoustic irradiance and the Fréedericksz transition[32]. Devices PH-17-E7, HT-18-MLC2081 and HT-19-MLC2081 were used, and both V_P and V_{LC} were varied. Similar experiments were performed using SAW by Anikeev et al. in 1989[410], where significant reduction in the threshold of the Fréedericksz transition (V_{fred}) of a HT aligned cell was observed due to the applied acoustic pressure (f_A=1MHz). These experimental results are split across sections 8.1.3.c-f.

Figure 8.5a shows photos of PH-17-E7 as V_P and V_{LC} were varied. It was observed that V_P effected the optical threshold of the Fréedericksz transition, significantly reducing homogenuity throughout the field of view. At locations throughout the cell the threshold of the Fréedericksz transition (V_{fred}) reduced by a measurable amount. This is plotted in Figure 8.5b, where a reduction of over 50% was observed in localized regions. At V_p>3.5±0.5V, defects were seen to form in the NLC when $V_{LC}=0$. As V_{LC} was increased, the defects would reduce in number and stop moving turbulently until at some value (V_{def}), the field of view was reasonably static. The value V_{def} was seen to increase with V_P (see Figure 8.5b).

To examine the Fréedericksz transition in the absence of defects, dielectric runs were performed on the NLC device as V_p was increased up to 3.75V. The measured capacitance *(C)* as a function of V_{LC} is shown in Figure 8.5c. Only very small changes in C were found as V_p increased at any V_{LC}. This indicates that although the effect of the acoustic fields noticeable changes director reorientation when viewed in localised regions using POM is very clear (for example shown in V_p=3V, V_{LC}=3V in Figure 8.5a) it does not significantly change the orientation of ***n*** when averaged across the entire device. This means that either the total director deviation due to the acoustic field ($\Delta\psi_A$) is either very small or is positive at points and negative at others summating in a net small change in C (as shown in Figure 8.5d).

To examine the orientation of ***n***, the birefringence observed in the photographs taken when V_{LC}=3V and V_P=0V or 3V were compared using the Michel Levy chart. This indicates the optical path difference *(Γ)* for the green colour is ≈1900nm, while in the adjacent pink and purple regions it is ≈2100nm and 1700nm respectively. This gives the change in Γ due to the acoustic field ($\Delta\Gamma_A$) of ±200nm. From this, an approximate value for $\Delta\psi_A$ is obtained. Assuming a tilt profile of,

$$\Delta\psi_A(z) = \Delta\psi_{max}\sin\left(\frac{\pi z}{d}\right), \tag{8-3}$$

Gives an average $\Delta\psi_A(\Delta\psi_{av})$ across the device of $2\Delta\psi_{max}/\pi$. Then using relation,

$$\Gamma = \left(n_{eff} - n_{\perp}\right)d. \tag{8-4}$$

a approximate of $\Delta\psi_{av}$ is obtained using,

$$\Delta\Gamma_A \approx \left(\frac{\left(n_{||} + n_{\perp}\right)}{2} sin(\Delta\psi_{av})\right) d \tag{8-5}$$

Which gives $\Delta\psi_{av}$ *of* 0.4° and $\Delta\psi_{max}$ 0.6°. This angle is smaller than the pretilt of planar polyimide, adding credibility to the explanation shown in Figure 8.5d.

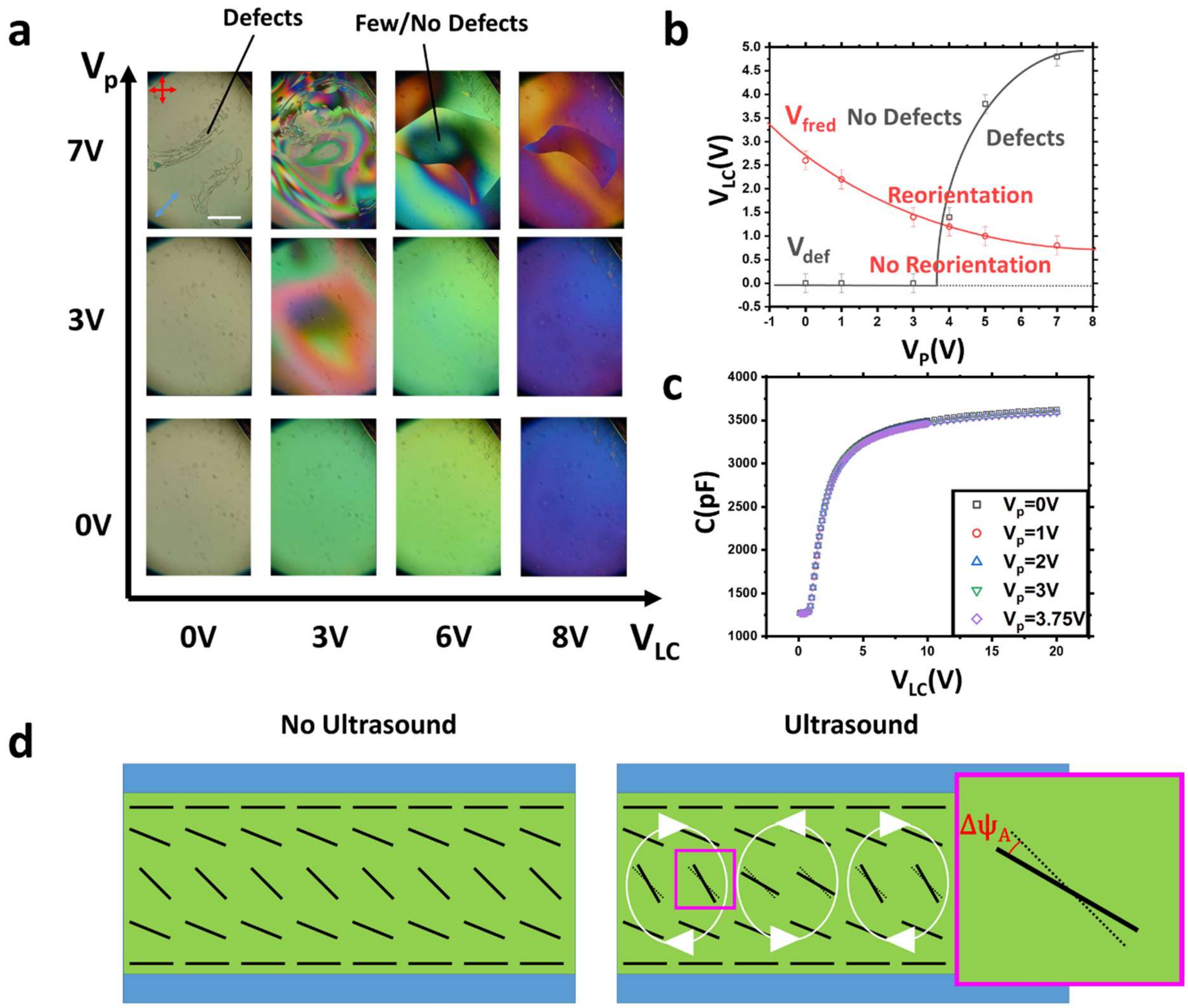

Figure 8.5 Results from device PH-17-E7. (a) Photographs of the different textures as V_p and V_{LC} are varied where T=16 ±1°C. (b) V_{fred} and V_{def} plotted against V_p. Lines are included for guides to eye. (c) The capacitance graphs vs V_{LC} measured at several V_p where no significant change is seen. Here T=21.5 ±0.5°C. (d) A possible explanation for the lack of dependency of C on V_p while POM images clearly show differences, where the C in the no ultrasound and ultrasound cases would be very similar.

8.1.3.d *Study Three: BAW and the Fréedericksz Transition in HT Device*

Homeotropically aligned devices (HT-18-MLC2081 and HT-19-MLC2081) were similarly examined. Figure 8.6a shows photographs of V_p and V_{LC} being varied. In HT-19-MLC2081, when V_P<2.9V the application of a BAW field was insufficient to reorient the director itself, but noticeably changed the resulting Schlieren texture when the Fréedericksz transition was performed. As V_P was increased, the brushes of the Schlieren texture were noted to have less defects and longer brusher strokes between them. Over time, it is usual for Schlieren textures to reduce the amount of defects over time as those of opposite strength anihilate [411], however, the acoustic field did not appear to be simply decreasing the number of defects but also the shape of brush strokes between them.

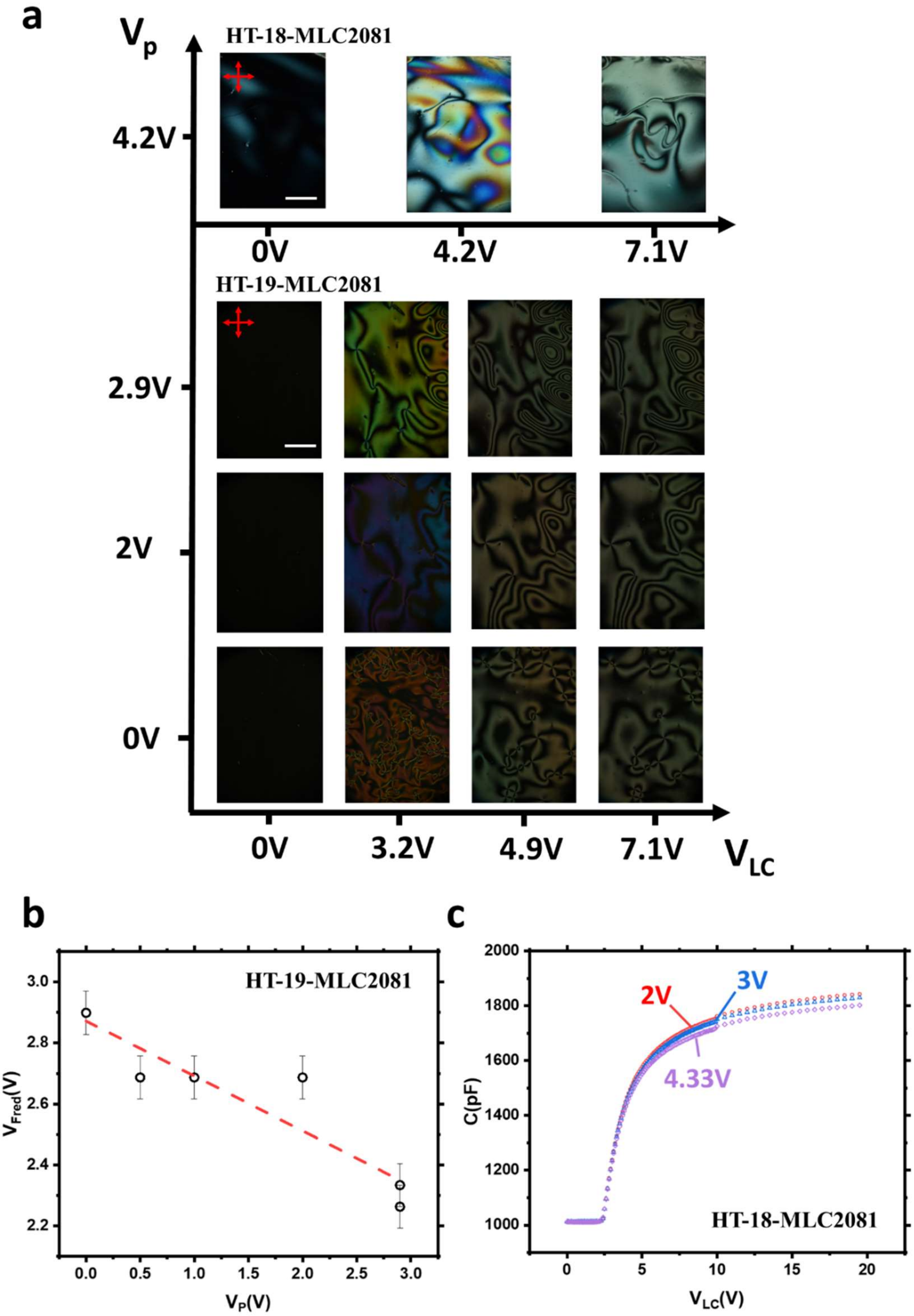

Figure 8.6 Results from HT-18-MLC2081 and HT-19-MLC2081. (a) Photos at several V_p and V_{LC} in both the 17 and 18μm devices at $T=25\pm1°C$. (b) The local optical Fréedericksz threshold plotted as a function of V_p. (c) Capacitance of the device at several V_p as a function of V_{LC}, where $T=18.3\pm0.5°C$.

In these devices V_{fred} was also obtained optically and is plotted in Figure 8.6b, where the general trend of reducing value of V_{fred} as V_p was increased can be seen. The fact V_{fred} is lowered in both HT and PH devices, indicates these effects are not due to director coupling, but instead the director experiencing an additional torque due to viscous flow induced ultrasound field (similar to Figure 8.5d).

It is also noted that the electric and acoustic fields do not appear to add linearly to reorient the NLC. For example in HT-19-MLC2081 the acoustic domains would appear at V_p=3V and V_{LC}=0, but when V_p=2.9V V_{fred} was only reduced by a factor of approximately 20%. This further confirms that the observed acoustic process is hydrodynamic in nature rather than an interaction between the ultrasound and the director. Similar experiments were undertaken on HT-18-MLC2081. For that device, the threshold for domains was slightly higher, where when V_{LC}=0 the threshold was V_P=4.2V. In this device C (V_{LC}, V_P) was measured (Figure 8.6c), similarly to results shown in Figure 8.5c, a slight reducing in the value C was seen at high V_{LC} with increasing V_p.

8.1.3.e *Study Three: Effects BAW on Dielectric Measurements*

The effect of V_p on C measurements during the Fréedericksz transition can be seen from Figure 8.5c and Figure 8.6c to be quite small, where the explanation of this being due to positive and negative changes happening simultaneously due to hydrodynamic flow have been introduced (Figure 8.5d). To examine the effect further, Figure 8.7a-b plots differential capacitance parameters (ΔC_{PH} and ΔC_{HT}) respectively, where,

$$\Delta C_{PH}(V,V_p) = \frac{C_{PH}(V_{LC},V_p) - C_{PH}(V_{LC},V_p = 2V)}{C_{PH}(V_{LC},V_p = 2V)} \times 100\% \tag{8-6}$$

and

$$\Delta C_{HT}\left(V,V_p\right) = \frac{C_{HT}\left(V_{LC},V_p\right) - C_{HT}\left(V_{LC},V_p = 2V\right)}{C_{HT}\left(V_{LC},V_p = 2V\right)} \times 100\%, \tag{8-7}$$

for PH-17-E7 and HT-18-MLC2081 respectively. Figure 8.7a-b plots these differential capacitances, while Figure 8.7c-d plots their values at several V_{LC} (0.1V, V_{fred} and 20V) as a function of V_P. Here lines are included fitting the fairly noisy data to illustrate the generally positive or negative gradients.

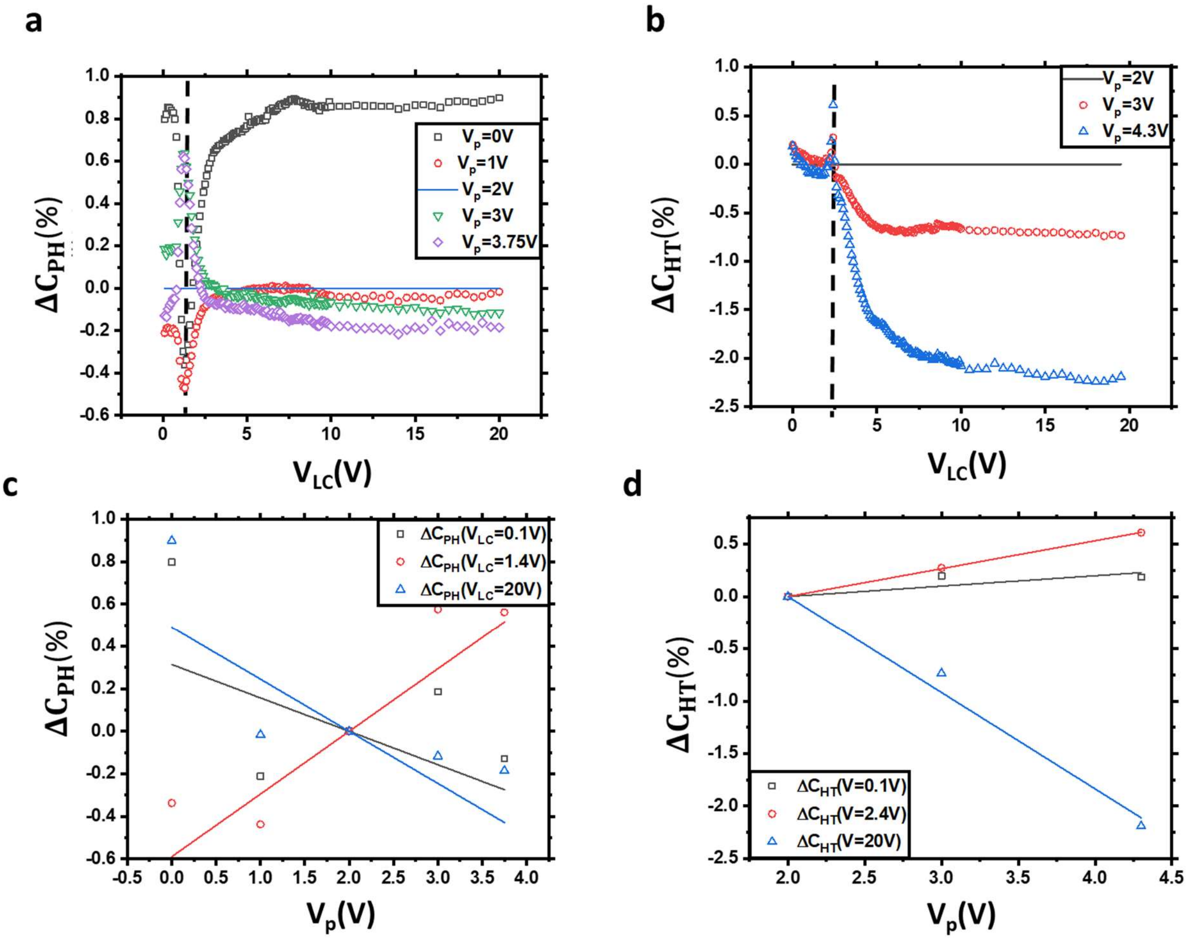

Figure 8.7. Results from examining dielectric runs with parameter ΔC_{PH} (a) and ΔC_{HT}(b). (c) and (d) Shows the values of ΔC at different V_{LC} where lines are intended as a guide to the eye only, to show positive or negative general dependency.

To explain the results given in Figure 8.7, two effects of the acoustic waves on the NLC are considered: (1) vortices formation within the material and (2) director coupling to the acoustic field. To describe the effect of hydrodynamic flows the qualitative model shown in Figure 8.5d is used. At low voltages little change is expected due to $\Delta\psi_A$ being smaller than pretilt angle (see calculations in equations (8-3)-(8-5)) allowing both positive and negative changes to director tilt. Meanwhile, the hydrodynamic flow is expected to increase C in both HT and PH cases at the Fréedericksz transition, as the threshold is locally reduced due to the addition of the additional torque (confirmed by POM measurements). At high voltages the hydrodynamic effect would reduce C in both HT and PH devices as they are then aligned with maximum ε aligned with the electric field, meaning any deivation will reduce C. For director coupling, the predicted effect of V_p is negative on C for all PH cases and positive for all HT, as the longitudinal field reorients the LC perpendicular to the direction of travel of the acoustic wave[390]. These predicted dependencies are summarised in Table 8-2.

Table 8-2. Results summarising results of ΔC's dependency on V_p during the Fréedericksz transition. Columns three and four give the predicted effects, while coloumn five gives the observed effect (from Figure 8.7).

Alignment	**Voltage range**	**ΔC vs V_P trend**		
		Vortices Formation	**Director Coupling**	**Observed**
PH	**$V \ll V_{fred}$**	Neutral	Negative	Weak Negative
	$V \approx V_{fred}$	Positive	Negative	Positive
	$V \gg V_{fred}$	Negative	Negative	Negative
HT	**$V \ll V_{fred}$**	Neutral	Positive	Weak positive
	$V \approx V_{fred}$	Positive	Positive	Positive
	$V \gg V_{fred}$	Negative	Positive	Negative

Comparing the predicted behaviours to the observed behaviours in Table 8-2, the behaviour of ΔC (V_P)can be explained by a dominating effect of vortices formation and a smaller effect of director coupling. This is due to times where director coupling opposes vortices formation in their effect on ΔC, vortice formation always dominating (leading to changes in ΔC *of* ≈1-2% magnitude*)*. The only times the director coupling effect is seen is when the vortices formation effect is expected to be net neutral, here, only small changes are observed (≈0.3%).

8.1.4 Conclusions

This section discusses a preliminary investigation of interactions of BAWs with NLCs. The work has demonstrated the complexities of experimental studies of ultrasound induced structural transformations in NLCs, where numerous interactions between the acoustic field and the director can occur. These effects are further complicated by the addition of electronic stimuli. When combined, these effects do appear to influence one another, however do not combine to reorient the director in a linear fashion.

For the systems investigated, results appear to be explainable by the model of combined weak director coupling and stronger vortices formation discussed in section 8.1.3.e. Considerable further results would be required to confirm and quantify these effects, where shaped (preferably guarded) electrodes would help increase clarity of dielectric results. Additionally varying device spacing d would be most interesting, as it is likely that the dominant effect at some point transfer from vortices formation to director coupling at small d. Experiments to higher V_p values would also be advantageous, and filling E7 and MLC 2081 into HT and PH cells respectively and performing similar experiments.

Despite these interesting further avenues, the work on BAW was concluded here as the aim of the project was to create controllable pitch gratings. The longituinal BAW did not reliably induce short period domains (similar to those seen in EHDI) in either HT or PH devices. For this reason the focus of the project moved to creating gratings using SAW, which will be the focus of the remainder of the chapter.

8.2 Introduction to Surface Acoustic Waves

8.2.1 Surface Acoustic Waves

Unlike BAWs, SAWs only exist at interfaces between materials, with their amplitude rapidly decaying deeper into the bulk. SAWs may possess elements in the longitudinal and transverse directions simultaneously, where the transverse types can exhibit motion either within the surface plane or out of it. Two examples of SAW are shown in Figure 8.8a-b, where Rayleigh SAW (R-SAW) possess both longitudinal and out of plane components, whereas Love SAW (L-SAW) possess motion within the plane's surface perpendicular to the direction of travel only[412,413]. Within many materials, these different kinds of wave will be anisotropic in propagation speed; however, as waves, for a specific propagation direction and polarisation they will obey the wave equation (8-1).

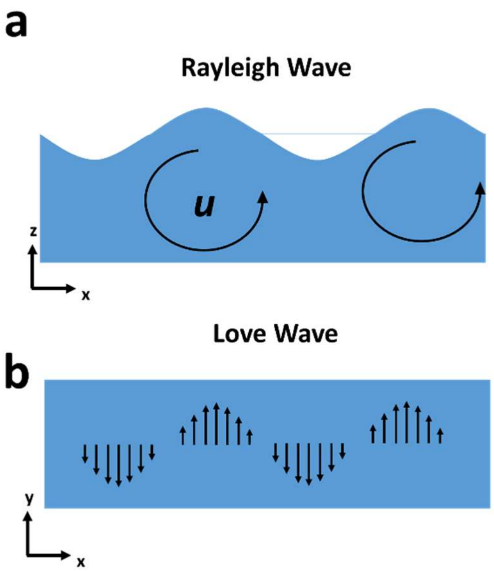

Figure 8.8.Diagrams of various kinds of SAW. (a) and (b) show Rayleigh and Love waves, respectively.

8.2.2 Producing SAW

A standard method for producing uniform SAWs is using a set of Interdigitated Transducers (IDTs) placed upon a piezoelectric crystal[412,414,415] (see Figure 8.9a). When a voltage is applied to the IDTs, the piezoelectric will flex, creating acoustic waves. Two parallel sets of transducers are often be included in a device (as shown in Figure 8.9a), which, similar to P&C measurements (Chapter 7) allow an acoustic wave to be produced and analysed. The type of wave produced is determined by the piezoelectric material the IDTs are placed upon, and their orientation relative to the crystal axis. In this work, SAW devices were fabricated by placing aluminium electrodes (oriented perpendicular to the -direction) onto Black 128° Y-cut Lithium Niobate ($LiNbO_3$) wafers, which produce R-SAW[413,414,416].

Similar to BAW transducers, SAW devices undergo resonance behaviour as the frequency of the applied electric potential is varied. For a device composed of uniformly spaced IDTs (Figure 8.9a), a single resonance occurs at f_{res}, where[413],

$$f_{res} = \frac{v_s}{\lambda_A} = \frac{v_s}{4w}. \tag{8-8}$$

Here, λ_A is the acoustic wavelength, v_s is the speed of sound and w is the width of both the IDTs and the gaps between them.

Often, SAW devices require a wider bandwidth (Δf_{res}) of frequencies at which resonance occurs. This can be achieved using chirped IDT structures (Figure 8.9b)[413,417,418]. Here, there are many w within a single device, each of which, when driven at their respective f_{res} produce different λ_A. If the w values are spaced such that their resonances start to overlap, these chirped devices can approximate a continuous broadband device (Figure 8.9c). When the number of finger electrodes is constant, this increase in bandwidth tends to reduce the maximum efficiency of the device, as they are not be able to all resonate at the same f_A.

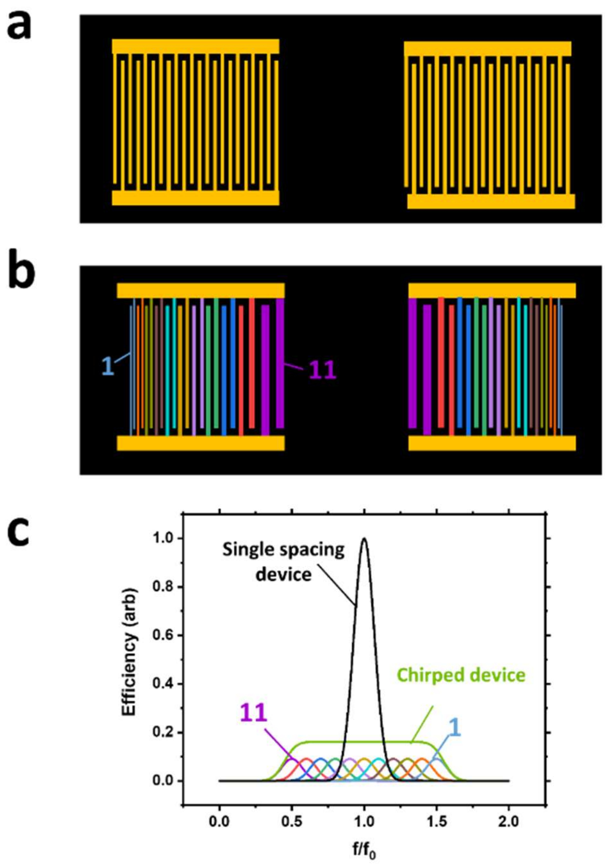

Figure 8.9. Illustrations of SAW devices and their operation. (a) Two sets of uniformly spaced IDT's (yellow) placed upon a piezoelectric wafer (black). (b) A chirped IDT SAW device. The fingers are shown as different colours to represent changing width. (c) Illustrates the difference in device efficiency as frequency is varied. The small multi-coloured peaks accumulate in the total chirped device spot. These peaks are colour coded and numbered as in (b) for clarity.

8.2.3 Fluid Interaction with SAW

8.2.3.a *Isotropic Fluids*

When a SAW propagates along an interface between solid and fluid materials, the wave will attenuate due to the energy leaking into the fluid[419]. The amount of attenuation that occurs depends upon both the type of SAW (for example, R-SAW tends to attenuate more strongly than L-SAW[413]) and the fluid with which they are in contact (attenuation from liquids tends to be orders of magnitude larger than gases[415]). When this energy passes into the fluid, many phenomena occur due to inducing flow and pressure fields within the fluid[419–422].

Figure 8.10 shows one of the most studied SAW-fluid systems, where a R-SAW travels along a substrate, on which a droplet of isotropic liquid is placed. This injects momentum both the direction of travel and perpendicular to the surface into the fluid, which can induce acoustic streaming. The flow pattern is dictated by a number of parameters, but important parameters are often: λ_A, the intensity of the SAW (I), the thickness of the droplet (d), and the fluids kinematic viscous penetration depth (λ_v) [420,421,423–427], where

$$\lambda_v = \sqrt{\frac{\eta_K}{\pi f_A}}, \tag{8-9}$$

and η_K is a kinematic viscosity. For a water droplet with a typical SAW frequency (10MHz-1GHz) will give λ_v<1μm. When droplets have $d>>\lambda_v$, the typical flow pattern observed is shown in Figure 8.10a. Vortices are induced by the SAW creating flow within the fluid at the Rayleigh angle (θ_R), where[423,427],

$$sin\theta_R = \frac{v_{liq}}{v_{sub}}. \tag{8-10}$$

Here, v_{liq} and v_{sub} are the speeds of sound in the liquid and wafer respectively. In addition to streaming, R-SAW have been shown to cause droplets to atomise into the air or translate across the substrate (Figure 8.10b-c) [421,425,428]. These generally occur at higher acoustic intensities.

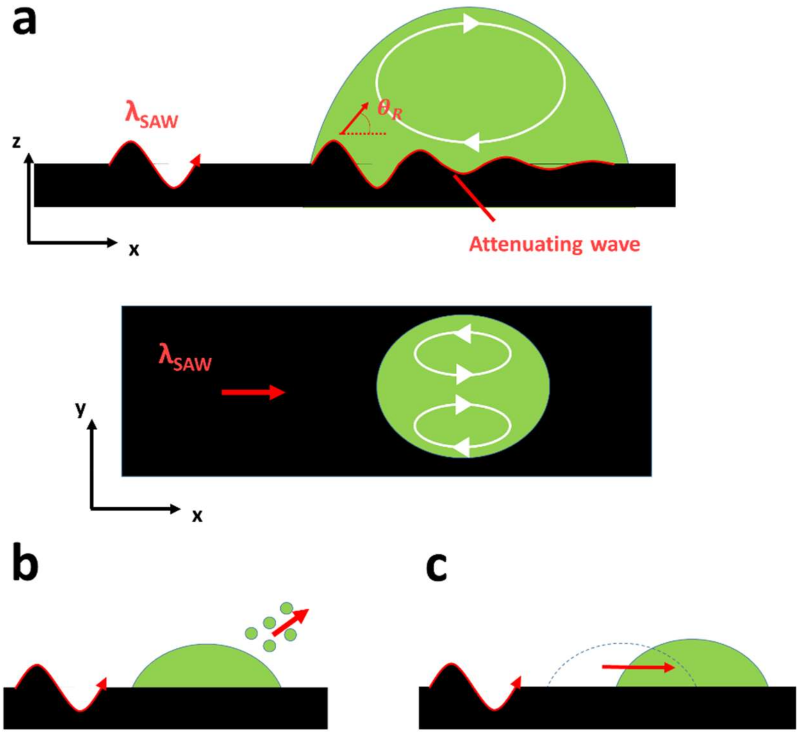

Figure 8.10. SAW interactions with isotropic fluid. (a) Acoustic streaming where flow is induced in the droplet. (b) The process of atomisation where increased evaporation of fluid is observed under the influence of SAW. (c) Translation, where the droplet moves in location due to the applied SAW.

An important system for this work is shown in Figure 8.11a, where a fluid is placed inside a cuboidal capillary made of thickness d. The values I, d, λ_A and λ_v dictate the observed fluid flow behaviour in this system [425,429]. Experiments and theoretical modelling have observed single vortices similar to droplets[430], switching of circular helicity in thin capillaries [425,429] and periodic vortices formation[431,432] (Figure 8.11b-d, respectively).

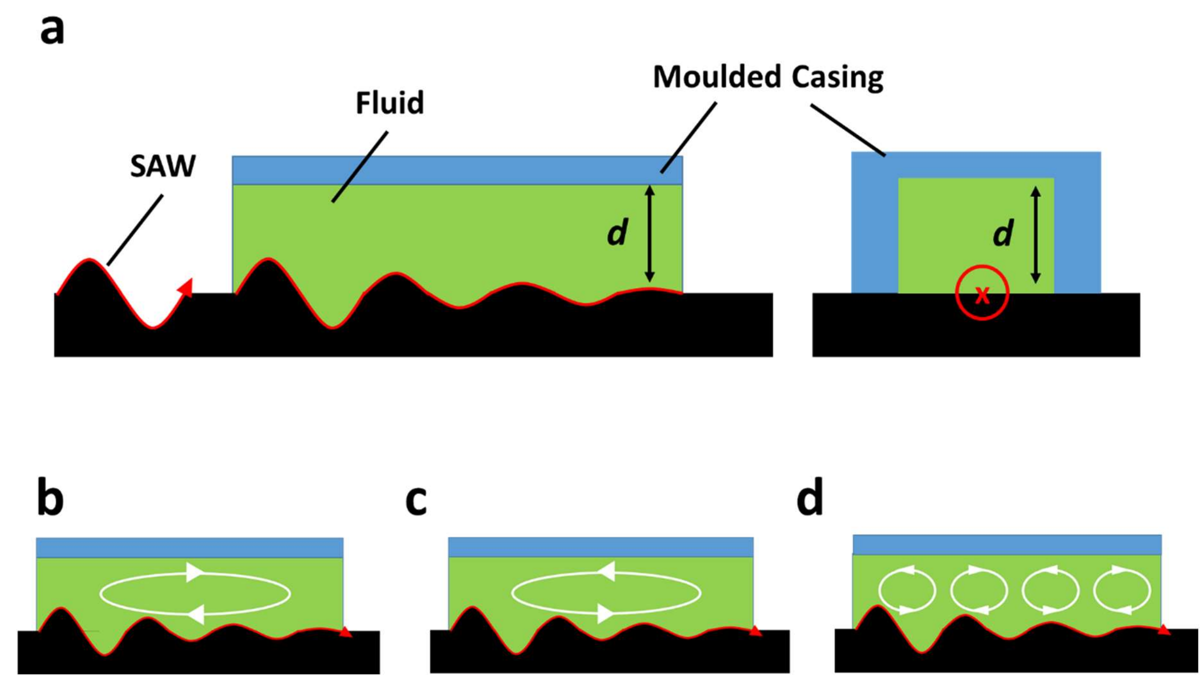

Figure 8.11. Possible flow patterns induced in fluids within capillaries by SAWs. (a) The configuration from the side and front, where a square capillary filled with fluid has SAW applied to it. (b-d) Several possible flow patterns (white arrows).

8.2.3.b *Nematic Liquid Crystals*

Several studies have been conducted investigating the interactions between SAW and both standard NLCs[24–26,189,388,433–436] and more novel LC composite materials[437–441]. Applications being investigated include smart windows[437] and ultrasound lenses[442]. A common experimental setup is shown in Figure 8.11a, where a cavity is filled with a NLC, one of the surfaces of which has a SAW wave passed along it[24–27,388,433,435,436].

For the setup shown in Figure 8.11a, different types of SAW can be used[189,413]. This results in different patterns, where Figure 8.12a-c shows examples due to R-SAW[24,25], L-SAW[436,443,444] and unpolarised SAW (u-SAW) [435,442].

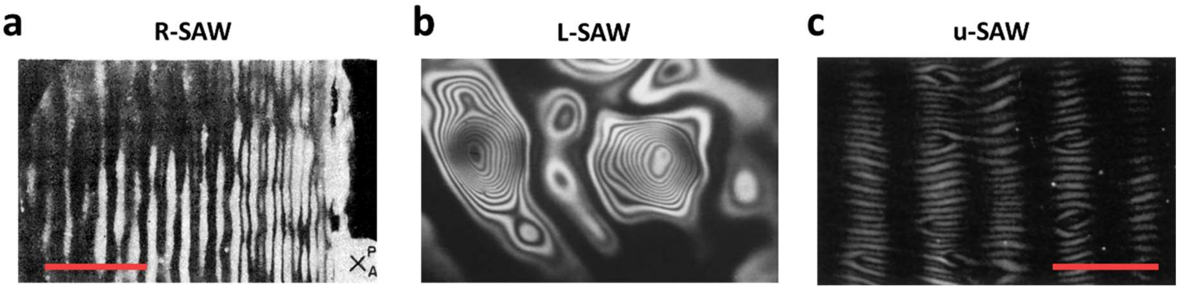

Figure 8.12 NLC patterns formed by different kinds of SAW taken with POM. (a) Homeotropic aligned NLC R-SAW [25] (b) Homeotropic aligned NLC with L-SAW [189]*(c) Planar homogenous NLC with u-SAW* [435]*. All red scale bars are 500μm.*

Of the patterns shown in Figure 8.12, the most promising for variable pitch diffractive structures is the R-SAW. Here, a uniform 1-D diffractive grating is seen of period λ_{dom}. Detailed studies of this and other relevant systems were conducted by Miyano and Shen in 1978-1979 [24,25], Sato and Ueda in 1981 [433] and Inoue, Moritake and Toda in 2000 [435]. From combining the results from these studies, several conclusions can be made:

- Firstly, the value λ_{dom} is relatively unaffected by NLC alignment, whether HT, PH paralell to the SAW or PH perpendicular to the SAW[24,25,433]. It is noted that for a set intensity more director reorientation occurs in homeotropic samples.
- Secondly, it is found that λ_{dom} increases with the thickness of the LC layer (*d)*[24,25]. λ_{dom} as a function of *d* is shown in Figure 8.13*a* where a relatively weak dependency on layer thickness is seen (200% increase in *d* yields around 50% increase in λ_{dom}).
- Thirdly, a linear relationship between λ_{dom} and λ_A is observed, where the relation[189],

$$\lambda_{dom} = \frac{\lambda_A}{\left(\frac{v_{sub}}{v_{LC}} - 1\right)} = \frac{v_{sub} v_{LC}}{f_A (v_{sub} - v_{LC})}, \tag{8-11}$$

can be used, where, v_{LC} is the speed of sound in the liquid crystal. This is shown in Figure 8.13b, where the v_s theory plot comes from using a literaure value for v_{LC} (1550ms^{-1}[367]). The origin of (8-11) comes from taking the difference in the respective wavevectors of the acoustic wave in the LC (q_{LC}) and the substrate (q_{sub}) [189],

$$q_{dom} = \Delta q = |q_{sub} - q_{LC}|. \tag{8-12}$$

When combined with the wave equation (8-1), this results in,

$$\lambda_{dom} = \left|\frac{\lambda_A \lambda_{LC}}{\lambda_{LC} - \lambda_A}\right| = \left|\frac{\lambda_{sub} v_{LC}}{v_{LC} - v_{sub}}\right| = \left|\frac{\lambda_A}{\left(1 - \frac{v_{sub}}{v_{LC}}\right)}\right| = \frac{\lambda_A}{\left(\frac{v_{sub}}{v_{LC}} - 1\right)}. \tag{8-13}$$

- Fourthly, at higher intensities, these domains break down where too much flow occurs within the system for the domains to maintain their uniformity[24,25]. This is presumably a precursor to the DLS state observed at high BAW intensities[393].

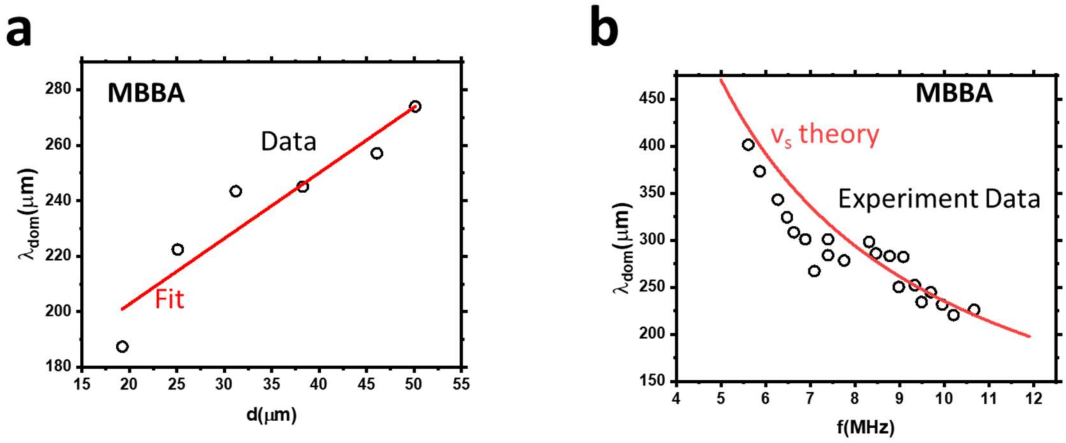

Figure 8.13. (a) Dependency of λ_{dom} on d in MBBA (taken from reference [25]). Here the alignment was homeotropic, f_A=12.3MHz, $v_{sub}\approx 4540ms^{-1}$ and $\lambda_A\approx 370\mu m$. The red line shows a linear fit through points as a guide for the eye.(b) Dependency of λ_{dom} on f in MBBA (data taken from reference [435]*). The alignment was planar homogenous, d = 25μm and $v_{sub}\approx$ 4540 ms^{-1}. The red line shows the predicted value from equation (8-11) using v_s=1550ms^{-1}.*

From the earliest research, the strong similarities of these SAW induced domains to those observed in electroconvection were noted [20,24,25,27,433]. These findings led collectively to the domains being explained using the picture shown in Figure 8.14, where the domains are caused by inducing periodic vortices within the NLC that induce hydrodynamic torques upon ***n*** [388]. Assuming no attenuation, this director orientation (θ) can be written as,

$$\theta = \theta_{max}\cos(q_{dom}x)\sin\left(\frac{\pi z}{d}\right), \tag{8-14}$$

where θ_{max} is the maximum reorientation.

Similar to the treatment of EHDI in Chapter 5 the torque balance equation of this system may be written as,

$$\Gamma_T = \Gamma_{visc} + \Gamma_{el} \tag{8-15}$$

where Γ_T is the total torque, and Γ_{visc} and Γ_{el} are the components associated with the viscous drag and material elasticity, respectively. Dubois Violette, De Gennes and Parodi found the following expressions for these torques for small deviations of ***n***[247],

$$\Gamma_{visc} = \gamma_1\left[\frac{\partial\theta}{\partial t} - \frac{\gamma_1-\gamma_2}{2\gamma_1}\frac{\partial v_z}{\partial x}\right]. \tag{8-16}$$

and

$$\Gamma_{el} = -k_{eff}\frac{\partial^2\theta}{\partial x^2} = -k_{eff}q_{dom}^2\theta. \quad (8\text{-}17)$$

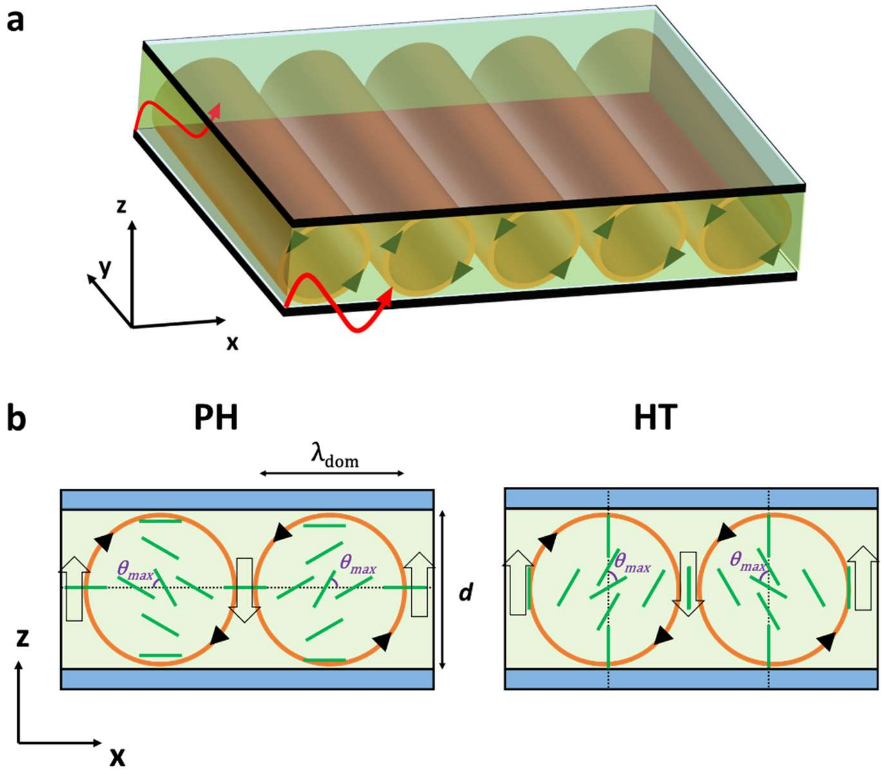

Figure 8.14. Images of hydrodynamic vortices induced in nematic liquid crystals by SAW. (a) A 3D sketch of the flow pattern (shown as orange cylinders with arrows showing rotation direction). (b) The effect on the director (green lines) of the vortices flow when the surface alignment is PH and HT respectively.

Here, γ_1 is the rotational viscosity, γ_2 is the torsional viscosity, k_{eff} is the effective elasticity of the NLC and v_z is the velocity field in the z-direction. Combining equations (8-15), (8-16) and(8-17), while assuming a steady state solution ($\frac{\partial\theta}{\partial t}$ and Γ_T equal zero), allows θ to be found in terms of a v_z,

$$\theta = \frac{\gamma_1 - \gamma_2}{2k_{eff}q_{dom}^2}\frac{\partial v_z}{\partial x}, \quad (8\text{-}18)$$

from which it can be seen that

$$\theta_{max} \propto \frac{\gamma_1 - \gamma_2}{2k_{eff}q^2}. \quad (8\text{-}19)$$

Here, $k_{eff} \approx k_{33}$ for the homeotropic case while in planar homogenous geometry $k_{eff} \approx k_{11}$. Usually, as $k_{33} > k_{11}$ explaining the difficulty in observing domains in planar devices compared to homeotropic [24,25].

As the treatment in reference [247] was intended to describe electroconvection rather than SAW interactions with NLCs, one factor lost in this treatment is the attenuation of the SAW wave. To describe such equation (8-14) can be adjusted to decay in amplitude with distance x (as shown in Figure 8.14a),

$$\theta = \theta_{max} \cos(qx) \sin\left(\frac{\pi z}{d}\right) e^{-\alpha x}, \tag{8-20}$$

where α is the attenuation coefficient. This is significant for diffractive applications as large α values would significantly reduce potential maximum aperture sizes.

8.3 Methods

8.3.1 Fabrication of SAW Devices

To examine the effect of SAW on NLCs, new device fabrication techniques were developed as a part of the project. The Piezoelectric substrates used were Black 128° Y-cut $LiNbO_3$ wafers (circular substrates with 100mm diameter and 0.5mm thickness, purchased from Roditi), onto which aluminium electrodes were deposited. A diagram of a finished device and a photo are shown in Figure 8.15a and Figure 8.15b, respectively. A summary of the final fabrication method defined is outlined below and illustrated in Figure 8.15c.

i. **Cutting.** The wafers were cut down to appropriate sizes (1.75cm×3cm) using diamond wafer scribes, with the long axis oriented in the x direction, which when voltage is applied, will produce R-SAW.
ii. **Cleaning.** The wafers were cleaned using processes given for glass in section 3.1.2.b. They were then placed on a hot plate at 120^{O}C for 5 minutes to remove moisture.
iii. **Lift Off Resist Spinning**. After allowing wafers to cool, the substrates were placed upon a spin coater (WS-650-MZ, Laurell Corp). Several millilitres of Lift-Off Resist A (LOR-A, Microresist Technology) was deposited onto the substrates, which was wetted with the side of the pipette. After this, the spin coater underwent a spinning programme of 0 to 2500rpm at 50rpms^{-1} then 2500rpm to 4500rpm at 100rpms^{-1}. It was then held at 4500rpm for 60s. After spin coating, the LOR-A was soft baked at 125°C then 175°C both for 5 minutes on hotplates. The samples were then left for 30 minutes before Shipley deposition.
iv. **Shipley Resist Spinning.** Shipley Photoresist 1813 (S1813, Microresist Technology) was deposited onto the wafers in the same manner as LOR-A. The spin programme was 0 to 2500rpm at 50rpms^{-1} then 2500rpm to 4000rpm at 100rpms^{-1}, where it was held for 60s. After this, a soft bake was performed for 1 minute at 110^{o}C. The samples were then left at least 30 minutes before exposure.

v. **Exposure.** Samples were selectively exposed to UV light (405nm) using Direct Write Lithography (DWL, section 3.1.2.d). A dosage of 300 ± 30mJ/cm^2 was found to produce the best results.

vi. **Development.** At least one hour after exposure, samples were developed using Shipley Developer MF319. It was found greatly improved features were achieved when puddling was used. A puddle of developer was placed on the sample for 20s, removed through spinning, then another puddle added for 20s before being removed by spinning, while spraying deionised water onto the sample[445].

vii. **Mounting.** Wafers were mounted on 1.1mm glass microscope slides to add rigidity and allow mounting in evaporation step. This was done using a two-part adhesive epoxy (Araldite, RS Components).

viii. **Metallic Evaporation.** 60-150nm of aluminium was deposited onto the wafers using an evaporator (Edwards 306 Vacuum Thermal Evaporator). Samples were loaded into a chamber which is evacuated (below 2×10^{-6} Bar), then a aluminium sample (held within a Molybdenum boat) is heated by a large current until it evaporated. The evaporation rate was measured by a quartz microbalance and was held to 0.1-0.2nms^{-1} by controlling applied voltage. The thickness was checked by other group members using a Dektak Surface Profiler, which gave accuracy of evaporated thickness within 5µm of that given by the evaporator.

ix. **Lift-off.** Aluminium was lifted off through submerging the sample in a beaker of PG remover (Microresist Technology) heated to 60°C. Between samples dramatic differences in required time for lift off were noted (20-120 minutes). For this reason, samples were checked periodically (every 15 minutes) and removed once the aluminium was fully removed. Once complete, wafers were rinsed with water, acetone and IPA, being blown dry between each rinse. The smallest lateral features that were achieved for an entire device using these methods was 6 µm.

x. **Addressing.** Due to the high operational frequencies of the SAW devices (10-40MHz), wires and electrodes of the type used for LC devices were inappropriate for SAW devices. Instead, very short(<5mm) wide gauge (>1mm) wires were used to attach electrodes to solderable BNC jacks (RS Components). Wires were soldered to the SAW devices using Indium solder, where to reduce thermal gradient the entire process was completed on a hot plate at 110°C. The connection to the BNC jack was a silver loaded epoxy (CW2400, Farnell), which was found capable of transmitting the high frequency voltages.

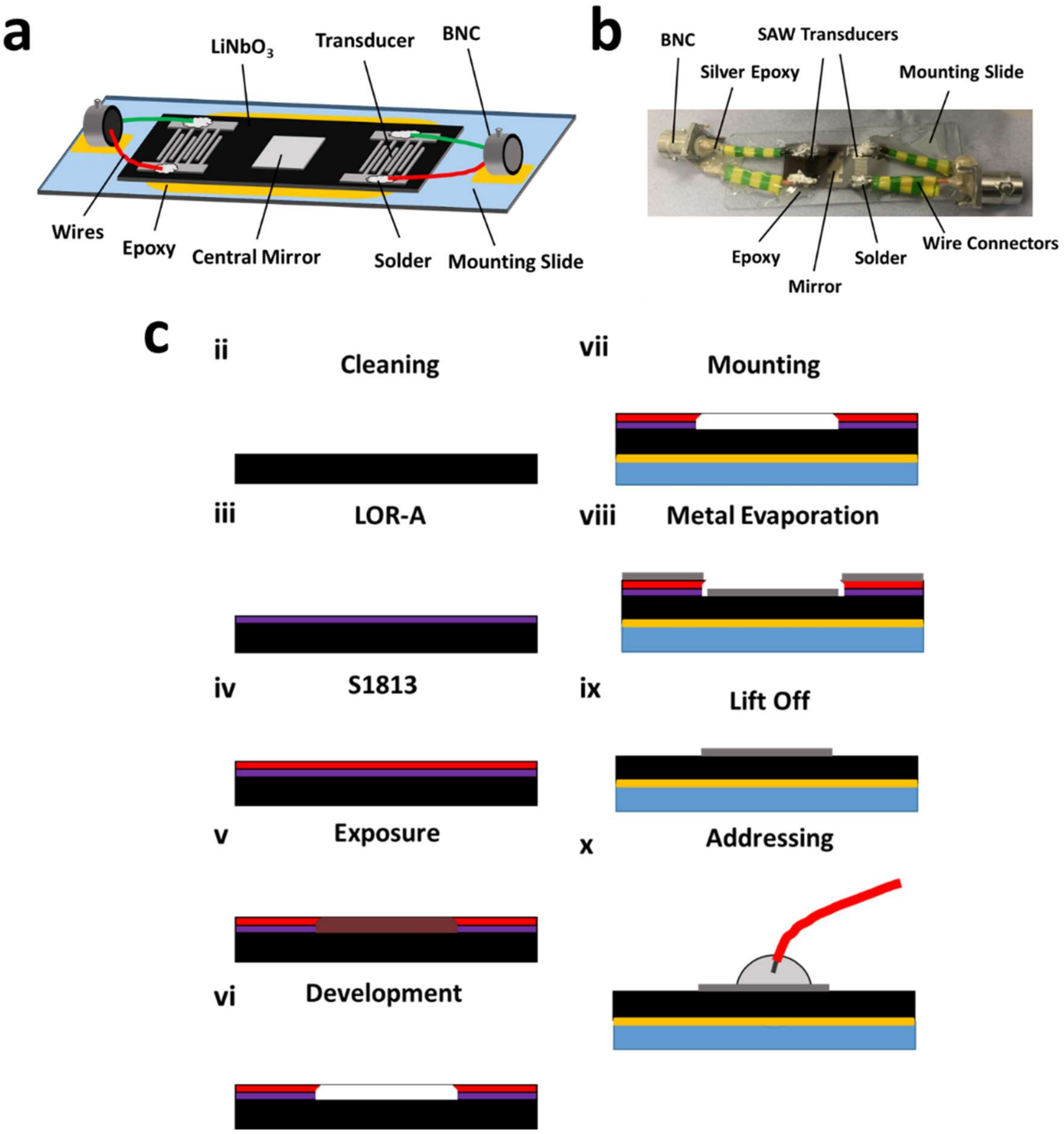

Figure 8.15. A schematic (a) and photo (b) of the fabricated SAW devices. (c) Illustrates the fabrication steps.

8.3.2 SAW Device Characterisation

Using the techniques outlined in 8.3.1 two main types of SAW devices were created: Uniformly spaced ten electrode pair devices of w= 30, 50 and 100µm (U30, U50 and U100, respectively) and devices with twelve pairs of chirped electrodes with w=40, 50…140,150 µm (C40:150). The smallest electrode width (w_{min}) was limited by the maximum producible frequency (f_{max}) of the function generators available. This was 40MHz (TGA12100 function generator, Aim TTi), which when combined with equation (8-8), gives,

$$w_{min} = \frac{\lambda_{min}}{4} = \frac{v_{sub}}{4f_{max}} \approx 25\mu m \tag{8-21}$$

where λ_{min} is the wavelength of the smallest achievable SAW.

The SAW devices were first electronically addressed to measure the resonance frequencies, as shown in Figure 8.16a. The voltage from the function generator (V_{FG}) was set and measured using the oscilloscope (V_{app}). This was applied to the first set of IDTs, creating a SAW, this wave was measured electronically as the second set of IDTs (V_{rec}). The SAW transmission efficiency (κ) was measured as f was varied where,

$$\kappa = \frac{V_{\mathrm{rec}}}{V_{\mathrm{app}}}. \tag{8-22}$$

Measurements of $V_{app}/\ V_{FG}$ and κ as functions of frequency for several devices are shown in Figure 8.16b and Figure 8.16c respectively. Theoretical values of f_{res} (calculated using equation (8-8)) and a v_s of 3980ms^{-1}) are marked in the Figures. In Figure 8.16c, the data is fitted with Lorentzian fits,

$$\kappa = \frac{2A}{\pi} \times \frac{\sigma}{4(f - f_{res})^2 + \sigma^2}, \tag{8-23}$$

where for the fittings shown A=0.08,0.11 f_{res}=9.85, 19.58 MHz and σ=0.4 and 1.2MHz for the w= 100μm and 50μm device respectively. Figure 8.16d shows results for C40:150. A predicted form of the chirped device is included of form,

$$\kappa = \sum_{n=12} \frac{2A_n}{\pi} \times \frac{\sigma_n}{4(f - f_{res,n})^2 + \sigma_n^2}, \tag{8-24}$$

where the subscript ‘n’ denotes the nth of the 12 finger pairs. The parameters were taken to be,

$$A_n = \frac{\bar{A}}{10}, \tag{8-25}$$

$$\sigma_n = \bar{\sigma} \tag{8-26}$$

and

$$f_{res,n} = \frac{v_s}{4w_n}, \tag{8-27}$$

where $\bar{\sigma}$ and $\bar{A}$ are the average of the values from w=50μm and 100μm. Despite the simplicity of the proposed response reasonable agreement can be found. Notably, there is a significant deviation a frequencies below around 9MHz. This may be due to the thickness of the LiNbO3 substrate (500μm) becoming similar to the penetration depth of the SAW wave, which can cause significant scattering of the wave increasing attenuation.

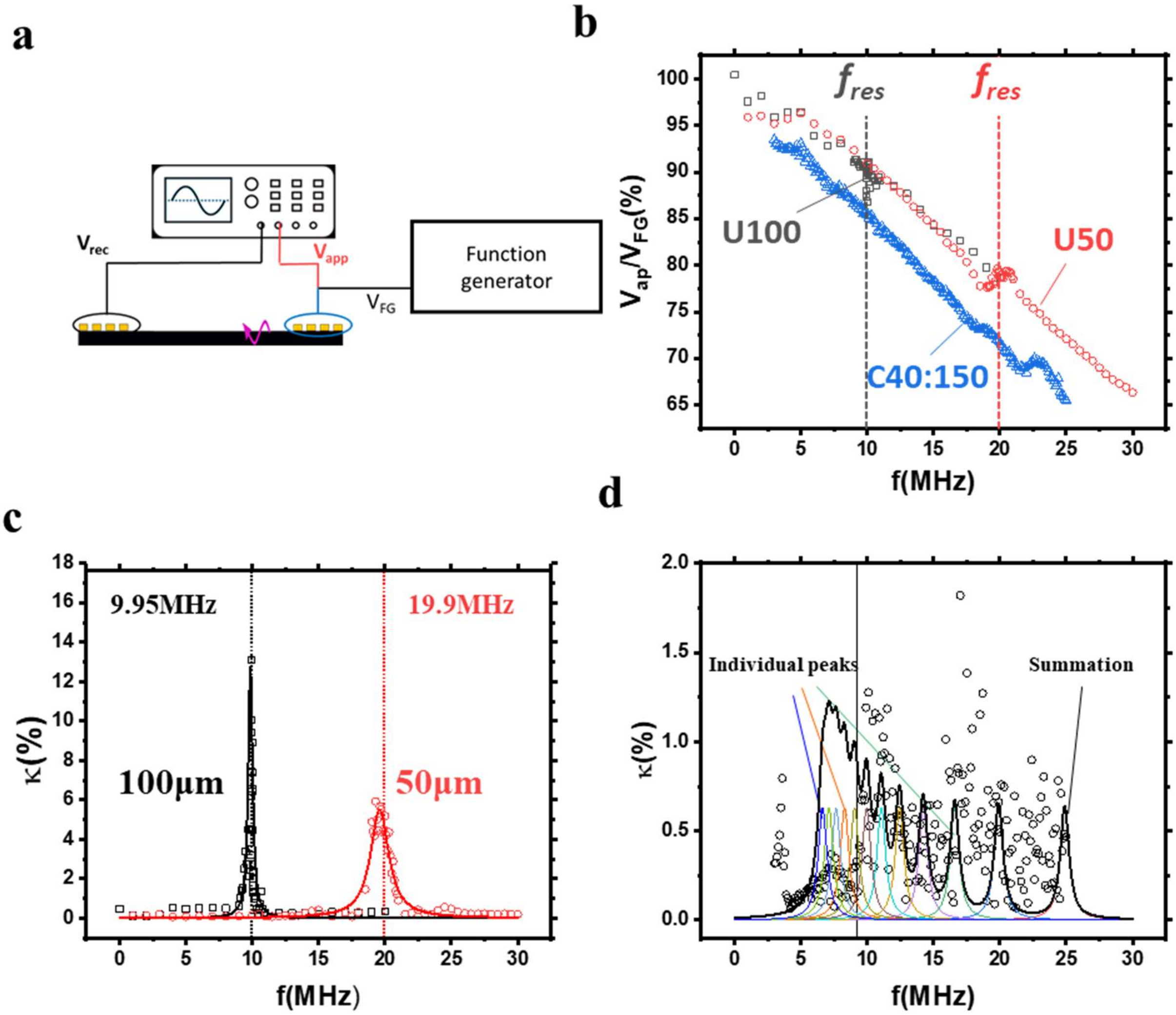

Figure 8.16 (a) The addressing scheme for the SAW device with V_{FG}, V_{app} and V_{rec} all labelled. (b) The reduction in output of the function generator as frequency is increased. (c) Measured κ as a function of frequency in U50 (red) and U100 (black). The dotted lines indicate the theoretical plots found using the v_s in the wafer and using equation (8-8). (d) Results from C40:150 (circular points), along with the model labelled 'summation' made up of the individual peaks from each finger pair.

8.3.3 Interactions of SAW and NLCs

Several device configurations of 'droplet' and 'capillary' types were used to examine the effects of the SAW devices on NLCs. These will be introduced and discussed in sections 8.4.1 and 8.4.2 respectively. Each device was viewed using reflection POM allowing effects on the NLC to be observed. The NLCs varied, where E7, MLC2081 and MBBA were all used. All experiments were undertaken at ambient temperatures (T=22±4°C).

8.4 Results and Discussion

8.4.1 SAW Interactions with NLC droplets.

8.4.1.a *Effect of Increasing SAW Intensity*

The first configuration was a SAW device driven in contact with an NLC droplet (see Figure 8.17a). The droplets were placed on the mirrored section of the device and observed using POM as f and V_{FG} was varied. Figure 8.17b, shows a plot comparing κ as frequency was varied in a U50 device with and without a droplet of E7. A significant reduction in κ value is observed due to the addition of the droplet, indicating a significant amount of energy is being removed from the SAW and being passed into the droplet. At resonance, V_{rec} and κ are shown in Figure 8.17c-d. Here, distinct regions in parameters V_{rec} and κ are observed. To quantify the energy loss due to the droplet, Figure 8.17e plots ΔV_{rec} as a function of V_{FG}, where,

$$\Delta V_{rec} = V_{rec}(no\ droplet) - V_{rec}(droplet). \tag{8-28}$$

These plots were combined POM images taken simultaneously (Figure 8.17f) and observations of the NLC textures noted. Within each voltage region:

- **I.** **Wide Domain Formation.** Here the wide domains form, which are without threshold. Loss of energy into the droplet causes V_{rec} to be less than that without the droplet.
- **II.** **Disclination Formation**. Within the flow many disclination lines appeared which would become trapped in the acoustic streaming vortices. Simultaneously, V_{rec} would become plateaued as V_{FG} increased, indicating nearly all additional electrical energy being pumped in was being converted to kinetic energy in the droplet.
- **III.** **Translation/Damage**. Here the entire droplet was changed in some way by the acoustic field either being moved or the surface being punctured. Generally, this increased ΔV_{rec} and was irreversible (reducing the voltage would not cause droplet to recover previous behaviour).

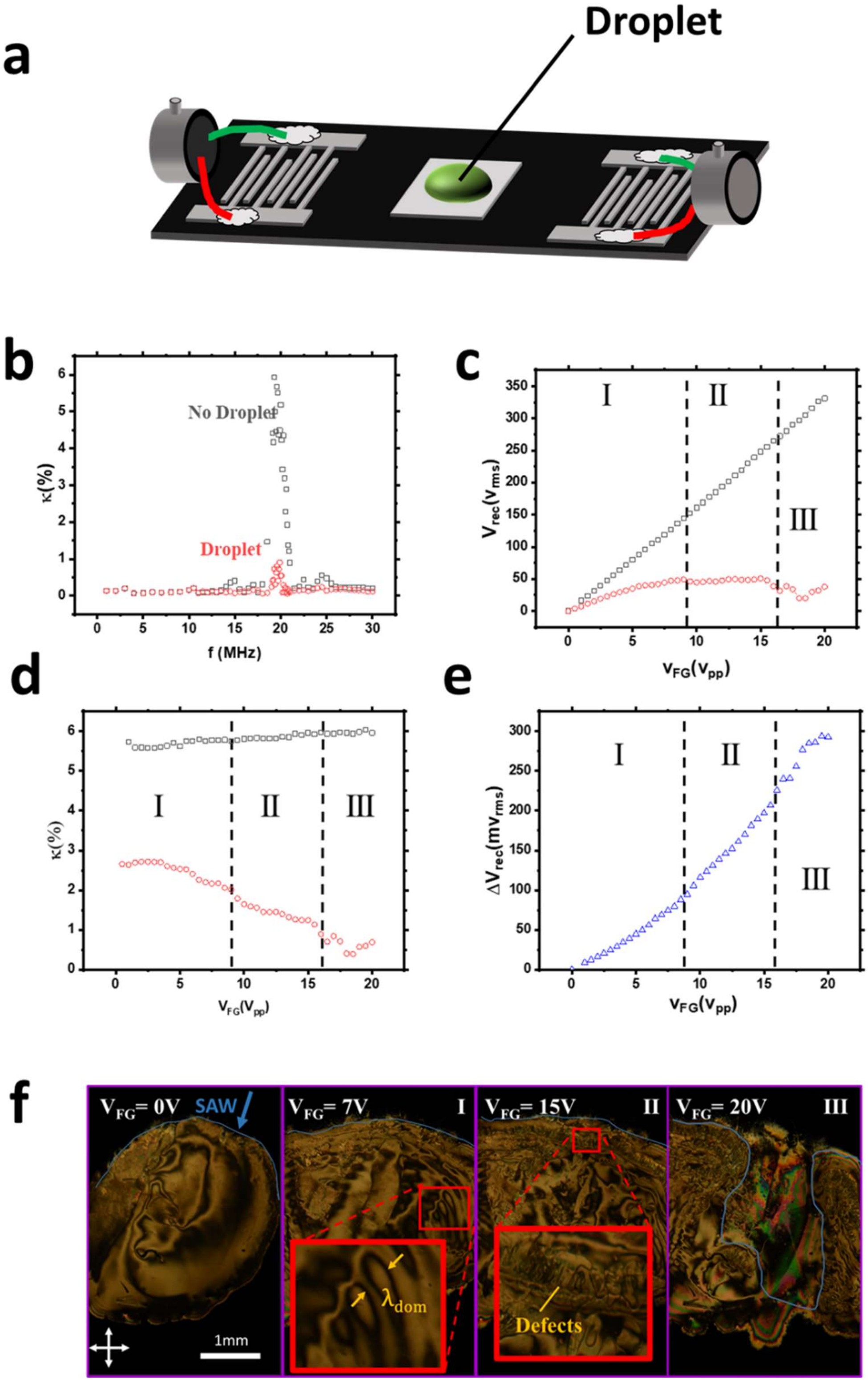

Figure 8.17. Characterisation of a uniform 50μm IDT device with a droplet of E7. (a-d) Differences in SAW transmission with and without the NLC droplet. (a) κ against frequency (V_{FG}=20V_{pp}) (b) V_{rec} vs V_{FG} is at resonance, (f=19.32MHz). (c) κ against V_{FG} at resonance (d) Δv_{rec} vs V_{FG}. (e) Images of the droplet at several V_{FG} taken using reflection POM. Voltages are given in the top left of each image and all were taken under crossed polarisers in reflection mode. The direction of SAW and the scale bar shown in the first image are the same for each image. Red boxes indicate regions where zoomed in images are included.

8.4.1.b *Measurement of Domain Sizes*

To examine the efficacy of equation (8-11) at describing the size of the periodic domains in droplet devices all uniform devices had periodicity measured. Examples of measurements of a single period are shown in Figure 8.18a. Figure 8.18b shows obtained values are compared to theoretical values using equation (8-11) and the value v_s for E7 of 1720 ± 70ms^{-1} (obtained for ambient temperatures in Chapter 7). Errors in the values λ_{dom} ($\Delta\lambda_{dom}$) were taken to be ±10μm due to limited number of periods possible to measure and model error taken from uncertainty in value v_s. Comparing theory to experimental data excellent agreement can be seen.

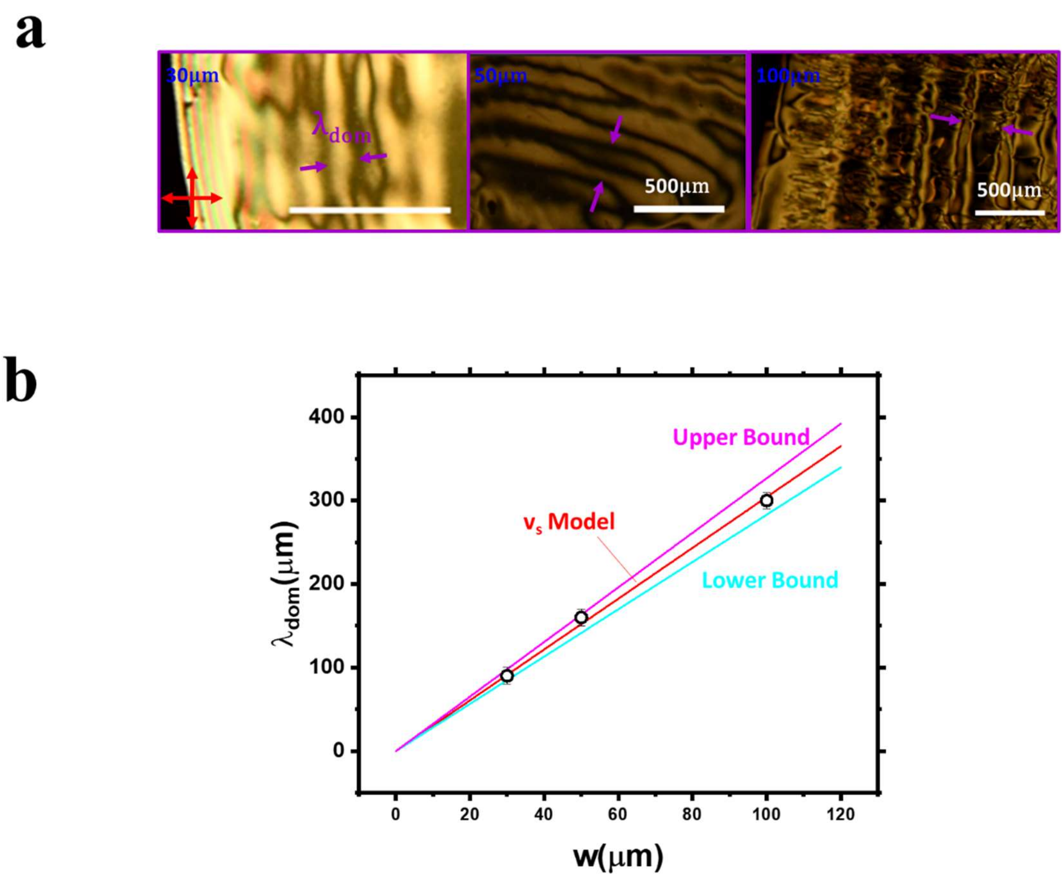

Figure 8.18(a) Photographs of domains formed in U30, U50 and U100 devices taken in reflection mode with crossed polarisers. Purple arrows show the measurement of a single λ_{dom} where several such were used to obtain values λ_{dom}. (b) Obtained values λ_{dom} compared to the model given by equation (8-11).

The experiments were repeated in sample C40:150, to attempt to create hydrodynamic gratings of variable pitch. κ as a function of frequency is shown in Figure 8.19a. The value dropped significantly when the droplet of E7 was added, similarly to the uniform devices. Less interaction was visible compared to that seen in the uniform electrode devices, this is likely has the same cause as the significantly lower κ value in general (taken to be due to less pairs of IDT of each size). The highest attainable voltage ($20V_{pp}$) was applied to maximize interaction and the frequency varied. At many frequencies, several periodic domains formed and their values λ_{dom} were recorded. Because less visible periodic domains were visible, the value $\Delta\lambda_{dom}$ was taken to be,

$$\Delta\lambda_{dom} = \frac{\lambda_{dom}}{2N}. \tag{8-29}$$

Results of λ_{dom} are shown in Figure 8.19b, together with the theoretical values obtained from v_s measurements and equation (8-11). The agreement between experiment and theory is significantly worse than those seen in the uniform electrode devices (Figure 8.18b). This may have several reasons: firstly the error in points is greater due to fewer domains being visible making measurement more challenging. It is also likely the SAW being produced is of poorer quality, as several finger pairs may each be being partially driven, confusing material response significantly. Despite not obeying (8-11), the behaviour with λ_{sub} appears to be reasonably linear where λ_{sub} is below a value of around 300µm after which λ_{dom} does not appear to grow significantly. This may again be caused by the fact the wavelength approaches the value d_{sub}(marked in Figure 8.18b) causing scattering effects and significant attenuation of wavelengths above this value.

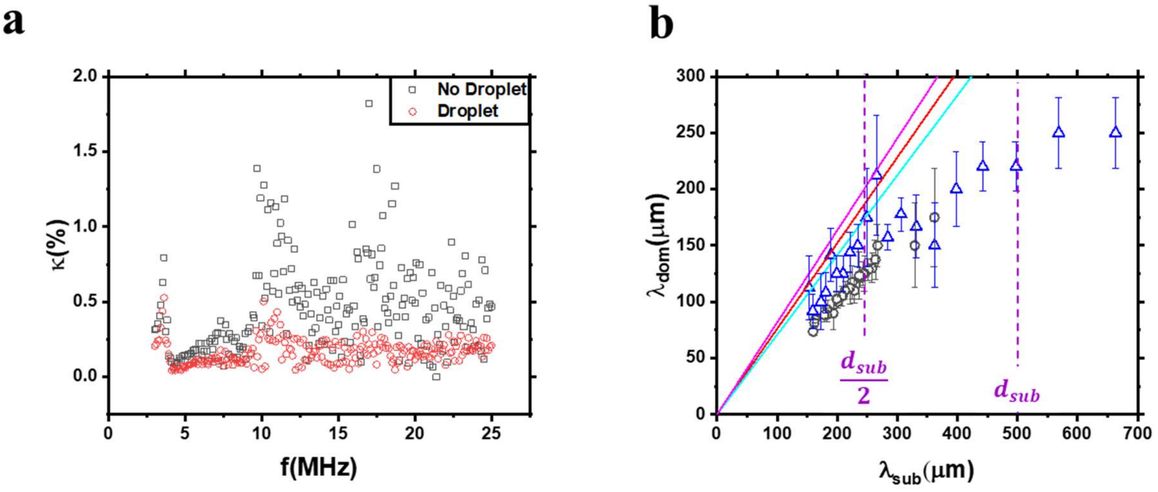

Figure 8.19. Results from the chirped electrode devices driven by droplets. (a) The device κ measurement with and without the droplet. (b) λ_{dom} against λ_{sub} where two data sets are shown (set 1 black circles, set 2 blue triangles). The data in (a) was taken simultaneously with measurements from data set 2.Lines show the expected range in λ_{dom} from the value v_s (similarly to Figure 8.18b).

8.4.2 SAW Interaction with Capillaries of Nematic Liquid Crystal

8.4.2.a *Capillary Devices*

The interaction of NLCs with SAWs in capillaries was also investigated. An example of a device is pictured in Figure 8.20, where a glass top plate has been added with Mylar spacers to form a capillary of thickness d. Both the glass plate and the substrate were coated with a layer of polyimide of homeotropic alignment (SE1211). These devices were filled with a layer of NLC (E7 or MLC2081), using a spatula and standard capillary filling methods.

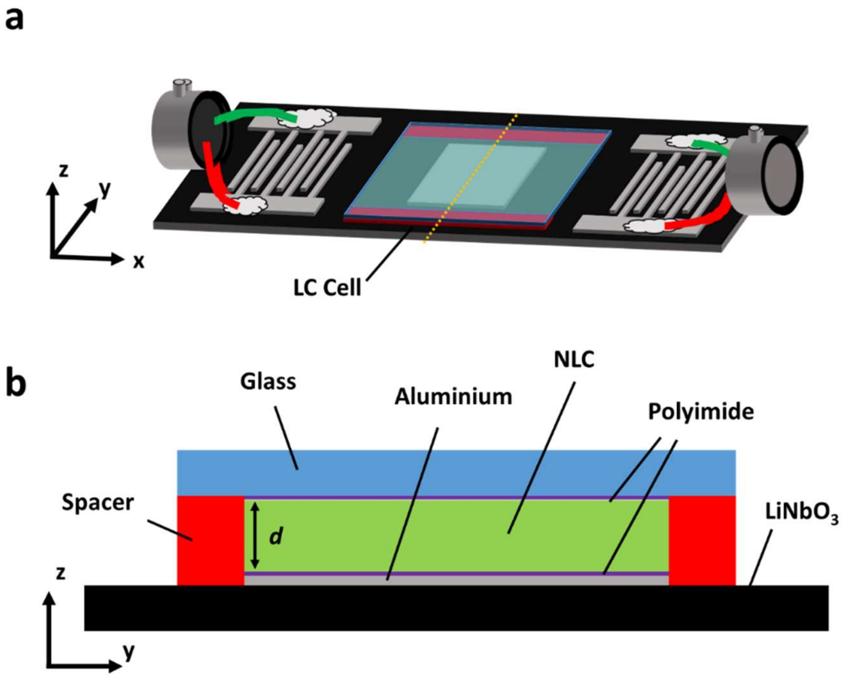

Figure 8.20 SAW liquid crystal capillary device schematics. (a) A schematic of the device. (b) A cross section through the centre of the device (marked as dotted yellow line in (a)).

In these devices, periodic domains similar to those observed in the droplets formed when the SAW was applied. Generally, the domains were less visible than in the droplet case. This is likely caused by thinner layers of NLC, which would increase anchoring energies and reduce optical path difference.

8.4.2.b *Effect of Increasing SAW Intensity*

An example of the domains in an E7 device (d=70μm, U50) as the voltage was increased at resonance is shown in Figure 8.21. These domains showed no defined threshold, reduced in amplitude with distance from the edge and deteriorated in uniformity at high acoustic intensities. The values λ_{dom} in this U50 device was 150±10μm, where (8-11) predicts 152±2 μm indicating agreement with theory. However (8-11) lacks any dependence of λ_{dom} on d despite such being reported by Miyano and Shen[24,25] (see Figure 8.13a). Similar results were obtained for U100 devices filled with MLC 2081.

Here, λ_{dom} values of 220±40µm and 230±30µm were obtained in devices of 23µm and 120µm respectively.

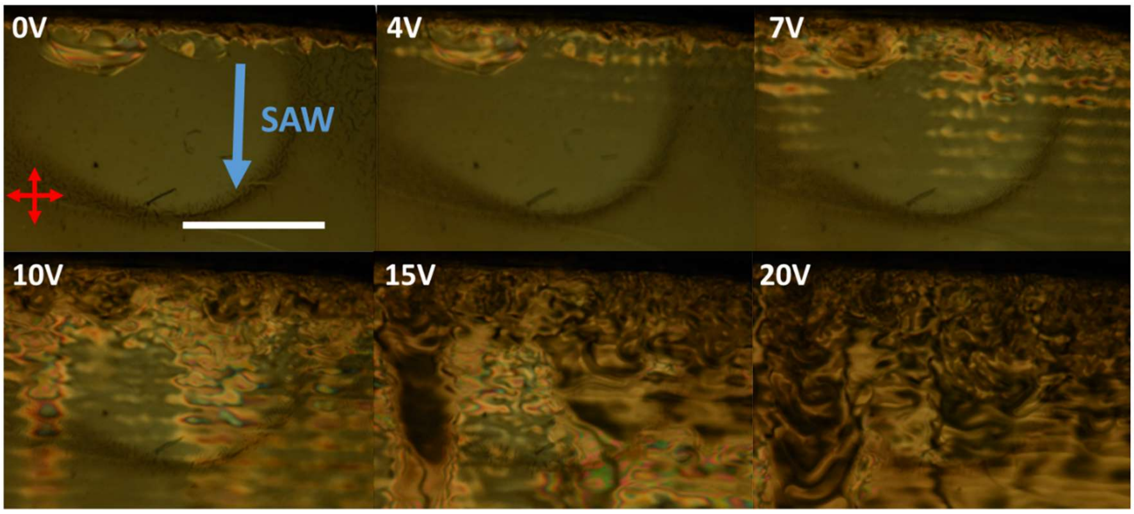

Figure 8.21 Photographs taken with POM of SAW-NLC textures at a variety of applied voltages. The SAW direction, crossed polarizers and scale bar (=1mm) shown in the first image is the same for all images.

8.4.2.c *Variable Pitch Behaviour in Chirped Device*

To demonstrate how SAW devices could operate as variable pitch optical gratings, a capillary device was fabricated of type C40:150 and d=70µm. The frequency was varied at the highest attainable voltage, and the values λ_{dom} measured. The domains formed were more sparsely located throughout the device, where it was typical that only one or two domains could be measured at one time (see Figure 8.22a). This is likely due to the lower acoustic intensity. The dependence of λ_{dom} with applied frequency f is shown in Figure 8.22b, where a clear trend of reducing λ_{dom} as f is increased can be seen. These are compared to results, which would be predicted from equation (8-11), where there is reasonable agreement.

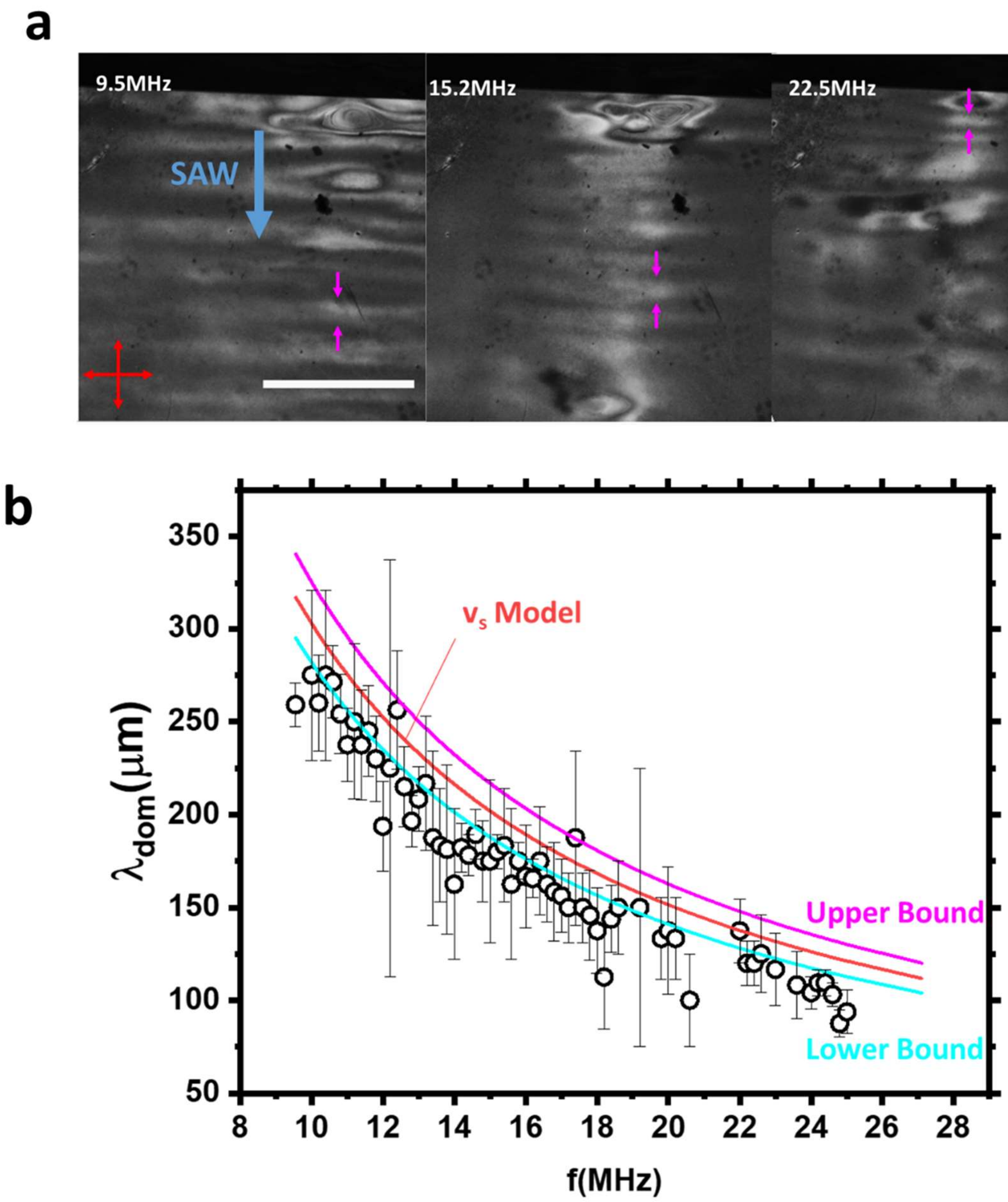

Figure 8.22. Grating created using chirped SAW device. (a) Photographs of the domains at various frequencies. Due to faintness of domains in some cases contrast has been increased and the colour set to greyscale. (b) The measurement of λ_{dom} in the capillary device as frequency was varied. This is compared to equation (8-11) where upper and lower bounds represent the error in the measurement v_s in E7.

8.5 Conclusions

This chapter provides an examination of the interactions between both bulk and surface acoustic waves and NLCs. In this, preliminary results investigating the interactions of BAWs and NLCs were presented. Here, two kinds of periodic structure of period λ_{dom} were observed. Firstly, wide domains appeared in samples of homeotropic alignment when longitudinal fields were applied. Here [388,395],

$$\lambda_{dom} \approx \frac{\lambda_A}{4}.$$

The second kind of domains were shorter in period and observed either when Piezo disks were driven in their radial mode, or when driven by longitudinal waves, but close to an interface. The period of these short domains obey,

$$\lambda_{dom} \approx d,$$

and are thought to be caused by a significant shear component in the acoustic field[408].

Interactions between the formation of the wide domains and the Fréedericksz transition were also investigated. Here, it was concluded the effect of the acoustic field was complex due to dual actions of inducing flow within the device (locally lowering the threshold voltage) and coupling to the director (seeking to orient $\boldsymbol{n}$ perpendicular to acoustic transmission).

Following this, experiments investigating SAW induced transitions in NLCs were discussed. Methods to fabricate and analyse SAW transducers using the facilities available during the project was given. The SAW devices were placed into contact with NLCs either in droplet or sandwich device configurations. As intensity was increased, domains were first observed, then defects were seen to form within the material. The domains, which formed within the material, were located at the edge closest to the source of the SAW. These appeared to decay in amplitude further into the material, which was taken to be due to attenuation. The period of domains in devices of uniform spacing were seen to obey a relation taken from literature that[189],

$$\lambda_{dom} = \frac{\lambda_A}{\left(\frac{v_{sub}}{v_{LC}} - 1\right)}$$

Chirped electrode devices which could create SAW waves of varying λ_A by varying frequency were also fabricated. These were used create devices capable of continuously varying the value λ_{dom} through frequency modulation. The range of values λ_{dom} observed were 100µm to 450µm, which are likely further reducible with access to more refined SAW fabrication techniques and equipment to address them. The potential of these SAW induced hydrodynamic gratings will be discussed in further detail in the following chapter.

Chapter 9 Conclusions of Project and Future Research Directions

This chapter reviews the work presented in the thesis, summarises the key findings with conclusions and discusses the possible future directions. Firstly, Section 9.1 reviews the results on creating Diffractive Optical Elements (DOEs) with hydrodynamic phenomena using both ionic flow (EHDI) and ultrasonic fields (AHDI). In this section, the experimental results from Chapters 5 to 8 are combined with the theoretical results from Chapter 4 to assess the demonstrated and theoretical limits of such devices as DOE. Section 9.2 provides a summary of other key conclusions made within the project where in addition to hydrodynamic DOEs, other observations and dependencies will be discussed. Section 9.3 presents future avenues of research including ideas to improve hydrodynamic DOE performance through possible modifications to devices and improve the fundamental understanding of the materials involved.

9.1 Assessment of Hydrodynamic Gratings as Diffractive Optical Elements

9.1.1 Calamitic EHDI

In creating variable pitch DOEs, key desirable properties are, small grating sizes (Λ_{gr}), wide continuous range ($\Delta\Lambda_{gr}$), high maximum optical phase difference (ϕ_{max}) and a blazed shape. In examining EHDI in standard calamitic Nematic Liquid Crystals (NLC), Λ_{gr} was found to reliably exist within a range dictated by device spacing (d),

$$\frac{d}{2} < \Lambda_{gr} < d. \tag{9-1}$$

Or in terms of optical wavevector (q_{opt}),

$$\frac{2\pi}{d} < q_{opt} < \frac{4\pi}{d}. \tag{9-2}$$

To examine the limit of such devices, the director tilt out of plane (ψ) is assumed to be,

$$\psi(x) = \psi_{max}\cos(q_{opt}x)\sin\left(\frac{\pi z}{d}\right). \tag{9-3}$$

Leading to approximate expression for optical phase difference (ϕ)[274],

$$\phi(x) = \phi_{max}\cos(q_{opt}x). \tag{9-4}$$

Assuming Raman-Nath (RN) diffraction[173], this sinusoidal phase grating has a maximum diffraction efficiency of the first order ($\eta_{m=1}$) of 34%, which occurs when ϕ_{max}=3.70±0.05. From diffraction experiments presented in Chapter 5 the low and high frequency values of $\eta_{m=1}$ for the phase grating ($\eta_{m=2}$ in the chapter) are plotted as a function of Λ_{gr} in Figure 9.1 (black sqaures). Here, the solution to a sinusoidal RN grating has been placed through the points, where results indicate maximum efficiency ($\eta_{m=1}$=34%) will occur when $d \approx 45\mu m$. This is problematic due to a fundamental issue with EHDI gratings, that smaller Λ_{gr} leads to smaller efficiencies due to roll shrinkage. When the device becomes thicker it will become less efficient as it has higher ϕ_{max} than its optimum value.

To put results in context of current technology, results for a Reflective Liquid Crystal on Silicon (R-LCoS) Electronically Addressed Spatial Light Modulator (EASLM) creating a blazed structure are included in Figure 9.1 (taken from reference [28]). Although the R-LCoS device also suffers from losses at small Λ_{gr}, due to its ability to induce blazed structures the efficiencies are far higher. The R-LCoS also has the significant advantage of a single device being able to vary across all Λ_{gr} values (provided Λ_{gr}> pixel size*)*, while results from calamitic EHDI indicate they can only vary by a factor of 2.

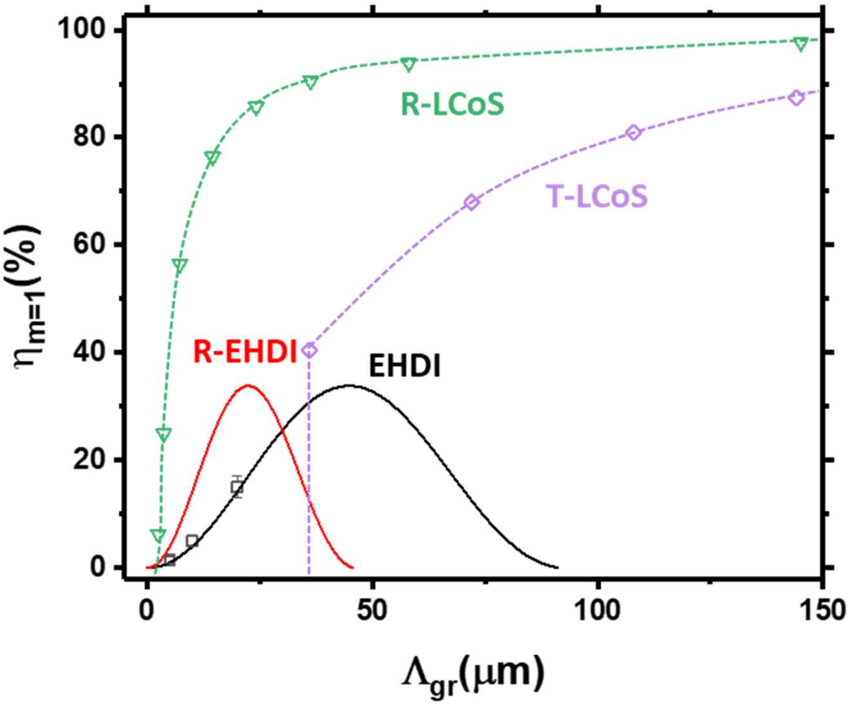

Figure 9.1. Comparison of calamitic EHDI diffractive performance compared to reflective and transmissive LCoS devices. A reflective EHDI (R-EHDI) is also included where Λ_{gr} is halved due to passing through the material twice. Data from R-LCoS taken from reference [136]*. Data for T-LCoS are taken from minimum pixel sizes given in reference* [446] *combined with results from section 4.4.2.*

The comparison of EHDI to R-LCoS is not quite suitable as EASLMs utilize a silicon backplane to achieve small pixel sizes [136]. This means the light passes through the device twice, doubling the ϕ

values achieved. To account for this, a predicted plot of reflective EHDI (R-EHDI) is included in Figure 9.1 (this performance could be achieved experimentally by including a mirror on the device backing). As can be seen this achieves the higher efficiencies at smaller Λ_{gr} values, however is still outperformed by R-LCoS.

Transmissive LCOS (T-LCoS) devices also exist and have far larger pixel sizes. For comparison, commercial reflective and transmissive devices by Holoeye have 3.74 and 36 µm pixels respectively[446,447]. No data of the performance of the transmissive device acting as a beam steering DOE could be found in literature. Assuming that it acts to create an approximately digitized phase ramp with a minimum feature width *(w)* of 36µm, the results from section 4.4.2 indicate performance shown in Figure 9.1. From this, we predict that calamitic EHDI DOEs outperforms T-LCoS when small Λ_{gr} are required.

9.1.2 Dimeric EHDI

Chapter 6 demonstrated the utilization of materials of novel elastic constants to tune the period Λ_{gr} of an EHDI pattern. Here, the limits given in equation (9-1) were expanded to approximately,

$$0.3d < \Lambda_{gr} < 1.3d. \qquad (9\text{-}5)$$

These limits were not reached at the same temperature, so focussing on the temperature where the smallest Λ_{gr} were observed, it was found to obey the limits,

$$0.3d < \Lambda_{gr} < 0.8d. \qquad (9\text{-}6)$$

Assuming this reduction in pitch size does not affect ϕ_{max} in a device of the same spacing, a theoretical plot of $\eta_{m=1}$ in a device filled with the dimeric material is compared to the calamitic mixture in Figure 9.2, where the dimeric mixture has higher efficiency for the same Λ_{gr}; however, this is speculative and needs confirmation with experiment. It is likely that smaller Λ_{gr} and higher efficiencies are achievable through further optimization of material viscoelastic and electronic properties. This would require a more systematic study to establish the important viscoelastic and dielectric parameters to tune. It is likely that such methods would only improve the performance incrementally, considering the relatively modest difference between equations (9-1) and (9-6) despite a large changes in k_{33}. The lack of asymmetry remains major limitation, in applying EHDI to DOE as it greatly limits maximum efficiency.

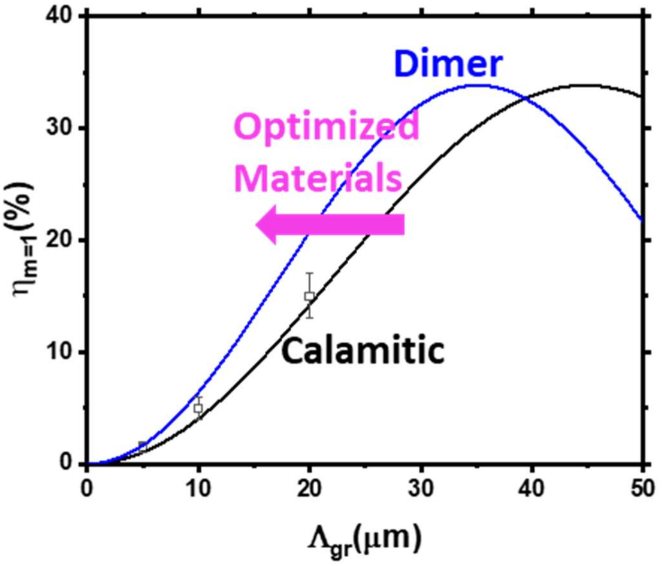

Figure 9.2. Efficiency of gratings attainable by dimeric and calamitic mixtures. The dimer mixtures performance migrates to smaller Λ_{gr}. It may be through further understanding of the process and optimization of material this behaviour can be further improved (pink arrow).

9.1.3 SAW Domains

In Chapter 8, hydrodynamic gratings within NLCs induced by SAW devices are considered. These appeared to tilt the director varying the outgoing phase profile of reflected light. The grating period (Λ_{gr}) was demonstrated to be determined by the acoustic wavelength (λ_A) and the relative speeds of sound in the substrate (v_{sub}) and the NLC (v_{LC})[189],

$$\Lambda_{gr} = \frac{\lambda_A}{\left(\frac{v_{sub}}{v_{LC}} - 1\right)}. \tag{9-7}$$

Experimental results indicate that this relation holds in the region 100 μm<Λ_{gr}<450 μm, which are supported by previous results from Miyano and Inoue et al. [24,25,435]. This work did not establish a minimum value Λ_{gr}. With standard lithographic techniques, sub μm feature size SAW devices can be achieved [448]. However, it is unlikely that if, for example, λ_A was shrunk to 100 nm ($f_A \approx 10$ GHz) that equation (9-7) would hold to create a usable diffraction grating with a variable sub-micron pitch. This is due to issues arising from: *(i)* increased attenuation of the wave, *(ii)* relaxation of the interaction between material and SAW, *(iii)* increased required power and *(iv)* low phase contrast caused by small tilt and thin devices. It may be these issues can be overcome through judicious design of both the LC materials (tuning appropriate viscoelastic constants as in Chapter 6 [114]) and acoustic devices (for example using larger number of SAW electrodes, or curving them to focus waves, increasing power[449]).Future directions on this work will be presented in section 9.3.2.

9.1.4 Longitudinal BAW Domains

The prominent kind of BAW domains observed in this work were induced by longitudinal driving and were found to approximately obey[388,395],

$$\Lambda_{gr} \approx \frac{\lambda_A}{4}. \tag{9-8}$$

For all devices examined in this work, this gives a value Λ_{gr} too large to be promising for diffractive gratings. To shrink Λ_{gr} to a useful scale (≈10 μm) would require exceptionally thin disks of PZT ($\lambda_A \approx d_{PZT}$ for resonance driving). These results are not promising for hydrodynamic DOEs, however, potential methods of *(i)* improving longitudinal BAW performance for DOEs with the more promising shear waves or *(ii)* their use in lenses are discussed in sections 9.3.4 and 9.3.5, respectively.

9.2 Conclusions

This thesis has presented results and analysis from a variety of experiments relevant to creating DOEs using hydrodynamic phenomena within NLCs. Numerical calculations of diffraction patterns of theoretical gratings using Python were presented (Chapter 4). These methods were used to examine several relevant phase structures to NLC DOEs. In doing so, an examination of the effect of several kinds of imperfections within blazed structures were presented, specifically digitization and smoothing. Experimental results on the first method of forming DOEs using hydrodynamics in NLCs, in this case utilizing ionic flow, were presented (Chapter 5). For the most promising 'Normal Roll' EHDI mode, equations were ascertained which satisfactorily described the behaviour of the onset voltage (V_C) and wavevector (q_{opt}) as frequency *(f)* was varied with fourth power relations. A simple model of circular motion was used to explain this fourth power dependency. In the experiments, the effect of varying device spacing *(d)*, sample conductivity *(σ)*, Temperature *(T)* and elastic constants *(k_{ii})* were investigated. The value q_{opt} was found to strongly depend upon d, meaning wide-angle gratings were attainable in thinner devices; however, these had lower phase contrast leading to lower diffraction efficiencies. q_{opt} and diffraction efficiency were seen to have little dependency on sample conductivity, provided it was sufficient to allow the sample to display the NR mode of EHDI. The conductivity was seen to determine the frequency limits of EHDI, where samples with more ions could maintain EHDI phenomena to higher frequencies. Varying T changed many of the systems viscoelastic and electronic parameters simultaneously, which lead to complex behaviour of q_{opt} and V_C. Temperature dependency of elastic constants and thermal dissipative effects was determined to likely play a role within this behaviour. Finally, the effect of elastic constants on the value q_{opt} was investigated, where a correlation between q_{opt} and both $\frac{1}{k_{33}}$ and $\frac{k_{11}}{k_{33}}$ was seen (Chapter 6). This was argued to occur due to rolls changing their shape to being more ovular, due to a lessening in free energy increase associated with bend deformation. An analysis of the electronic and elastic properties of a mixture composed of MLC 2081 and dimer CB7CB was described. This material had non-standard properties including, very low k_{33} and $\Delta\varepsilon$, which switches sign as a function of T. The origin of these odd behaviours was taken to be the non-standard properties of dimer CB7CB. Where the material has increased number of bent conformers as temperature decreases, decreasing $\Delta\varepsilon$ and k_{33}.

NLC hydrodynamics were further investigated using acoustic fields. The speed of sound (v_s) in the NLC mixture E7 was measured using a Pitcher and Catch (P&C) method that was developed during this project (Chapter 7). In this chapter, relevant background physics, the setup built to conduct measurements, and validation of technique are all given. v_s was measured in E7 as a function of T, where a reasonable value in the context of other similar studies was obtained. The results closest to room temperature were taken to be most accurate, where a v_s of 1720±70ms^{-1} was measured. Further, hydrodynamics of NLCs induced by high power acoustic fields were studied, where the aim was to form periodic structures (Chapter 8). Firstly, an examination was made of longitudinal BAW devices. Two types of domain were identified in these devices, of wide and short period. It was concluded the long period domains were caused by the longitudinal field, while the short were caused by secondary shear waves. The longitudinal BAW locally reduced the Fréedericksz transition threshold. The inducement of flow within the material was understood to be the main cause this effect. Methods and results from investigating SAW interactions with NLCs was presented in Chapter 8. Hydrodynamic domains were seen within the NLC; however, they decayed as they penetrated deeper into the sandwich device, which was attributed to attenuation. Results indicate, the relative speed of sound in the substrate (v_{sub}) and the LC (v_{LC}), as well as the period of the acoustic wave (λ_A) determine the domains size. A novel chirped electrode design was utilized which allowed the period to be continuously varied from around 275 to 100µm as driving acoustic frequency (f_A) increased. With more refined SAW fabrication techniques these grating periods are likely further reducible.

Section 9.1 of the current chapter brought together the important elements of previous chapters to give an assessment of the operational capabilities of DOEs based on NLC hydrodynamics. Lack of asymmetry of the optical patterns formed is the main limitation for efficient gratings; however, the devices have certain advantages over current transmissive technologies. Section 9.3 given below will expand upon the conclusions made here, suggesting further research directions, which could be pursued to either improve hydrodynamic DOEs or better understand observed phenomena key to their operation.

9.3 Future Research Directions

9.3.1 Stacking EHDI Hydrodynamic Gratings

The main issue with utilizing both kinds of hydrodynamic gratings is the lack of asymmetry within the grating structure. This limits the efficiency to an absolute maximum of 50%. An idea to improve such is to utilize the mathematical principle that we can construct a sawtooth structure (f_{blazed}) by adding an infinite sum of sinusoidal waves of varying amplitude and wave vector,

$$f_{blazed} = \sum_{k=1}^{\infty} A_k \sin(q_k x), \tag{9-9}$$

where,

$$A_k = \frac{A_1}{k}, \tag{9-10}$$

$$q_k = kq_1, \tag{9-11}$$

k is the harmonic number, A_1 and q_1 are the amplitude and wavevector of the first harmonic.

From the results presented in this thesis, calamitic EHDI sandwich devices display gratings in the range,

$$q_0 < q_{opt} < 2q_0, \tag{9-12}$$

where,

$$q_0 = \frac{2\pi}{d}. \tag{9-13}$$

Consider k EHDI devices stacked as shown in Figure 9.3a. Here, the k^{th} device has a spacing d_k where,

$$d_k = \frac{d_1}{k}. \tag{9-14}$$

This means for low frequency driving, the wavevector of the k^{th} device *($q_{opt,k}$)* is,

$$q_{opt,k} = kq_{opt,1}. \tag{9-15}$$

Assuming the value of director tilt within EHDI is independent of *d,* the maximum optical phase difference of each k^{th} layer ($\phi_{max,\,k}$) may be written,

$$\phi_{max,k} = \frac{\phi_{max,1}}{k}. \tag{9-16}$$

This gives a phase profile of each k^{th} layer *(ϕ_k,* see Figure 9.3b) as,

$$\phi_k(x) = \phi_{max,k}\sin(q_{opt,k}x) = \frac{\phi_{max,1}}{k}\sin(kq_{opt,1}x). \tag{9-17}$$

For the device shown in Figure 9.3a, these assumptions give a total the outgoing optical phase difference (ϕ_{sum}) as,

$$\phi_{sum}(x) = \sum_{k=1}^{k=k}\phi_k = \sum_{k=1}^{k=k}\phi_{max,k}\sin(q_{opt,k}x) = \sum_{k=1}^{k=k}\frac{\phi_{max,1}}{k}\sin(kq_{opt,1}x). \tag{9-18}$$

Comparing this to equation (9-9), (9-18) approaches a blazed grating as k tends to infinity. This is illustrated in Figure 9.3c, which plots the development of the shape ϕ_{sum} as k increases.

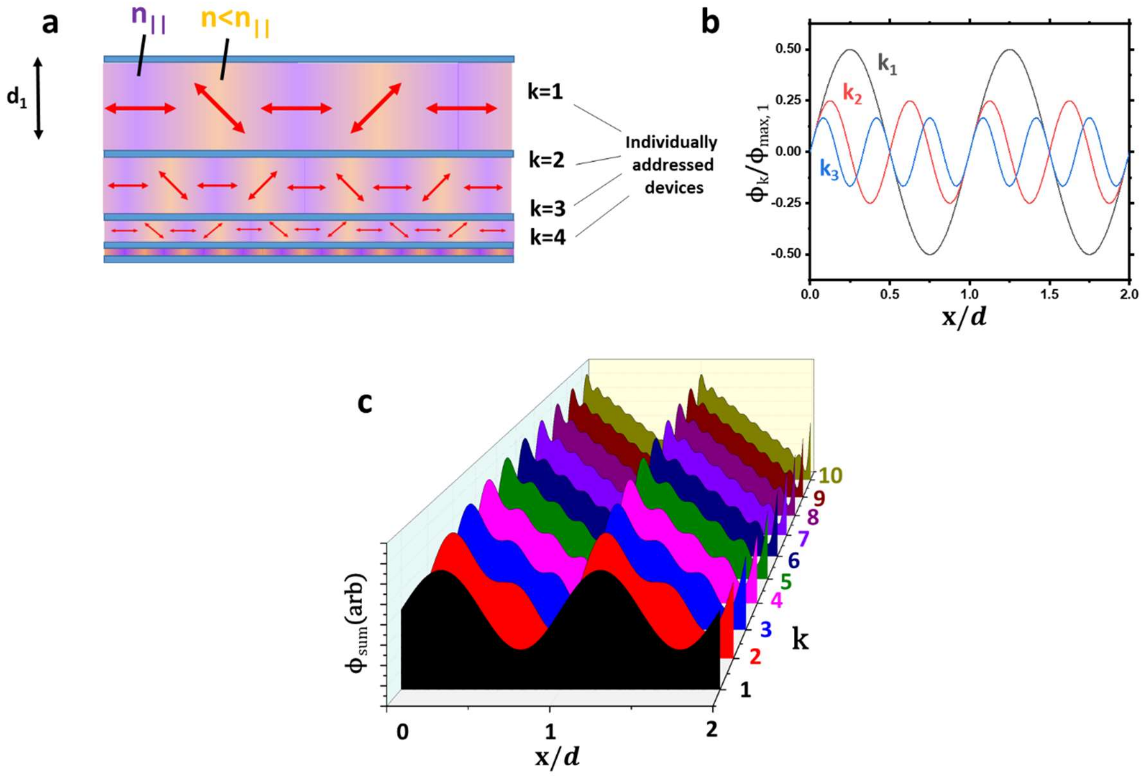

Figure 9.3. Stacked EHDI device operating principle. (a) k devices stacked which are individually addressed to create diffractive gratings. (b) The first three harmonics where amplitude and period decrease with k. (c) A waterfall plot showing the effect on ϕ of moving through k gratings. As k tends to ∞ the device should approach a perfect blazed grating.

We now seek to assess this device's function as a DOE. Firstly, potential efficiency of the device was calculated using equation (9-18) and the diffraction programme presented in Chapter 4. A key assumption of this is that the device is thin, acting as a Raman-Nath grating. Figure 9.4a plots the calculated diffraction efficiencies of the $m = 0$ and $+1$ orders (η_m) of gratings with several k as functions of ϕ_{max}. The maximum efficiency (η_{opt}) and the ϕ_{max} at which they occur (ϕ_{opt}) are seen to increase with k (Figure 9.4b-c)

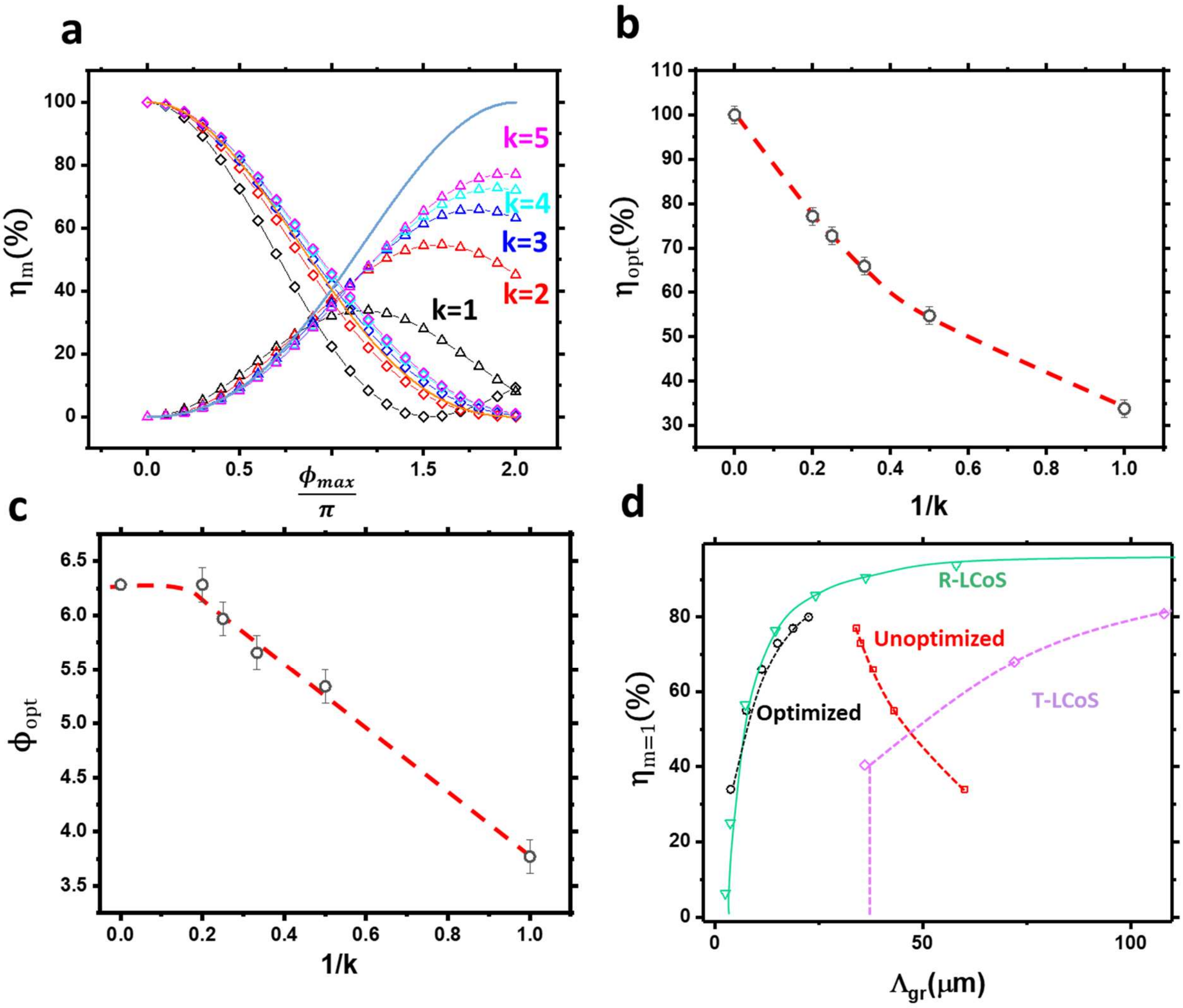

Figure 9.4. Figures assessing potential function of the stacked device. (a) Diffraction analysis of the efficiency of the m=1 (diamonds) and m=2 (triangles). This also includes a plot of a perfect blazed grating (orange and blue lines). (b) The highest obtainable efficiencies (η_{opt}) as a function of 1/k. (c) value ϕ_{max} at which η_{opt} occurs (ϕ_{opt}) as a function of 1/k. (d) Results from predicted optimized and un-optimized stacked device function compared to the R-LCoS and T-LCoS. Dashed lines in graphs are guides for the eye.

From results presented on calamitic EHDI, each device should be able to reduce its value Λ_{gr} by a factor of two as frequency is increased. As this occurs, the ϕ_{max} will also reduce to around half its original value. This means if a device were designed such that under low frequency driving ($\Lambda_{gr}=d_1$) $\phi_{max}=\phi_{opt}$, when Λ_{gr} is decreased to $\frac{d_1}{2}$, ϕ_{max} would also decrease to $\frac{\phi_{opt}}{2}$. From results in Figure 9.4a, this reduction in ϕ_{max} would lead to a large drop in efficiency (for example for k=5, η_1 would reduce from 77% to 35%). To reduce these losses it would be beneficial to design the device such that $\phi_{max}=\phi_{opt}$ when $\Lambda_{gr}\approx 0.75d_1$. Here, as the device would always operate within 25% of ϕ_{opt} the efficiency would be higher (for example for k=5, η_1 would always be between 77% and 65%).

Firstly, we investigate the performance of an optimized device, where through better tuning of the material parameters or including several devices of each spacing, any ϕ_{max} is assumed to be attainable when $\Lambda_{gr}\approx 0.75d_1$. This means the device's function is only limited by the minimum feature size d_k (taken to be $5\mu m$). This leads to the relationship,

$$\Lambda_{gr} \approx 0.75d_1 = 0.75\big(k(5\mu m)\big), \tag{9-19}$$

From this the values η_{opt} as a function of Λ_{gr} can be obtained, where larger k are possible for larger Λ_{gr}, which increases η_{opt}. Results for this optimized performance are compared to R-LCoS and T-LCoS in Figure 9.4d. The device is predicted to perform very similarly to the R-LCoS, while working in transmission and being able to continually vary Λ_{gr} by a factor of two.

We now consider the device function without such optimization processes. For maximum efficiency the device should be driven at $\phi_{max}=\phi_{opt}$, where ϕ_{opt} varies with k (Table 9-1). Using the results from section 9.1.1 a ϕ_{max} value of 3.7 was predicted to occur in 45µm spaced device undergoing EHDI. If the total thickness of the LC layers in the stacked device (d_{LC}) is written,

$$d_{LC} = \sum_k d_k = \sum_k \frac{d_1}{k}, \tag{9-20}$$

then for $\phi_{max}=\phi_{opt}$ to be induced and $\Lambda_{gr}=0.75d_1$, d_{LC} should obey,

$$d_{LC}(k) = \frac{1}{0.75}\left(\frac{\phi_{opt}(k)}{3.7} \times 45\mu m\right). \tag{9-21}$$

This leads to thick layers of LC, which in turn limit potential for small Λ_{gr}, which are summarised in Table 9-1. Higher k devices have more layers contributing to ϕ_{max}, meaning d_1 can be thinner. This leads to increasing η_{opt} with decreasing Λ_{gr}. The results from the optimized single stack are included in Figure 9.4d. This behaviour would not last to small Λ_{gr}, as eventually the minimum d_k limit discussed previously would become important.

Overall, particularly in comparing the results from the optimized and un-optimized cases the performance of the device requires further practical and theoretical investigation, including more detailed optical analysis (such as ray tracing[122,276,450]) and further optimization of the materials (for high tilt and high birefringence). If performance approaching that shown for the optimized device in in Figure 9.4d could be achieved, its impact on applications which require transmissive beam steering (e.g. Smart windows[451,452]) could be dramatic.

Table 9-1. Parameters required for driving the un-optimized stacked devices. The maximum efficiency (η_{opt}), phase at which it occurs (ϕ_{opt}), the total thickness of all LC layers (d_{LC}) the thickness of the first LC layer (d_1) the thickness of the last LC layer (d_k) and the period of the grating (Λ_{gr}) when driven at $\Lambda_{gr}=0.75d_1$.

k	$\eta_{opt}(\%)$	ϕ_{opt}	**d_{LC}(μm)**	**d_1(μm)**	**Min d_k(μm)**	**Λ_{gr} (μm)**
1	34	3.7	80	80	80	60
2	55	5.3	86	57	29	43
3	66	5.6	91	50	17	38
4	73	6.0	97	47	12	35
5	77	6.28	102	45	9	34

9.3.2 Superposition of SAW Modes

The general idea of superimposing gratings discussed in section 9.3.1 can also be applied to SAW devices. Consider the device shown in Figure 9.5a. Here, two separately addressed chirped SAW transducers are driven to produce waves of different acoustic wavelengths (dictated by the applied frequency). If the tilt of the director was found to follow this pattern, the same structure ϕ_{sum} as given in equation (9-18) for $k=2$ would be formed in the device. The advantage of this device compared to the stacked EHDI devices is that only a single LC layer is required, while more SAW components could be added for the device to get closer to a blazed structure (Figure 9.5b). This would give the same values η_{opt} given in Figure 9.4a. Additionally the SAW transducers can be aligned such they impose waves from orthogonal orientations, which would allow bi-axial steering. The drawback is the device would likely have to operate in reflection mode as although SAW waves can be coupled in using glass, the shapes of the acoustic field would likely be lost. The practical limits would also be dependent on ability to reduce the attenuation processes seen in this project.

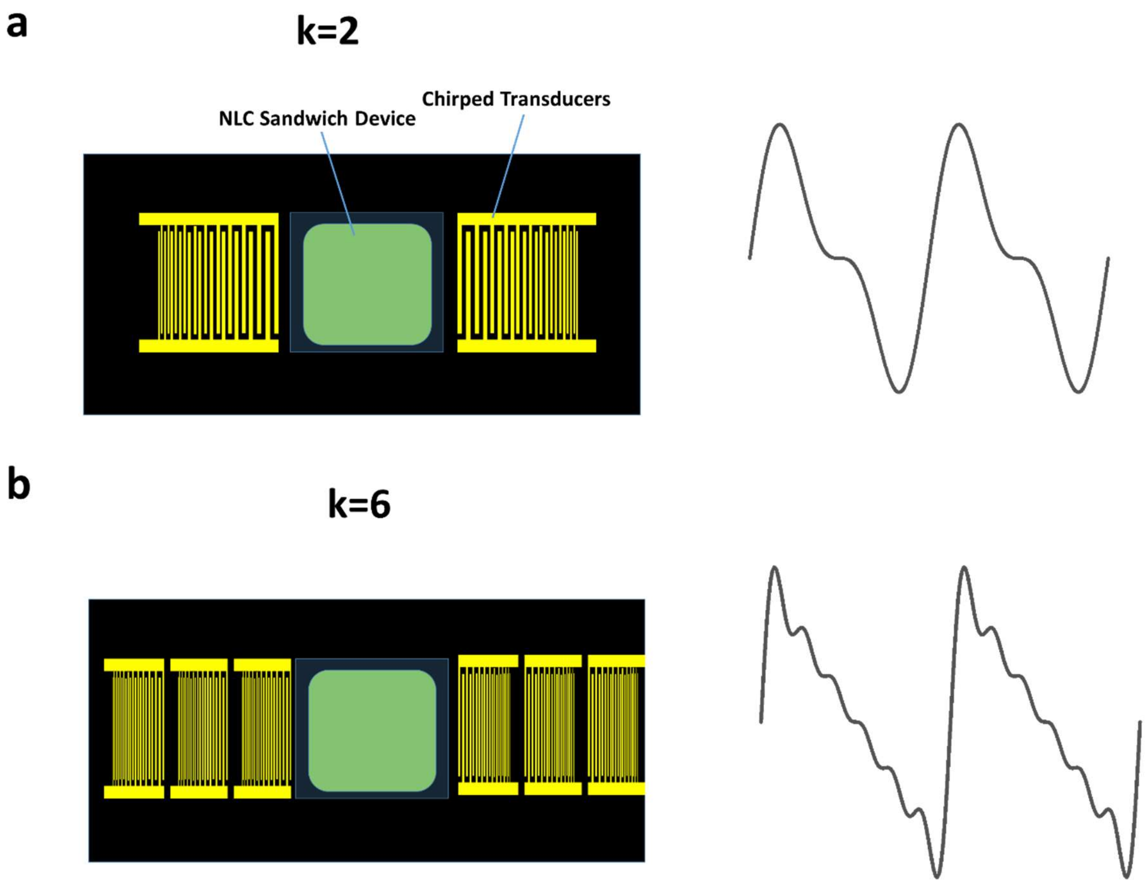

Figure 9.5. Superposition of SAW modes devices using k transducers. (a) The device with k=2 and (b) k=6. The right hand side shows the optical pattern becoming more similar to a blazed grating as k increases, indicating more efficient steering.

9.3.3The Chevron Mode-Normal Mode Transition in EHDI

As discussed in section 9.1.1 and 9.1.2, the displayed wavevectors of EHDI patterns (q_{opt}) exist within limits. In calamitic materials as q_{opt} increases with frequency, when it approaches a value of $\frac{4\pi}{d}$ the texture changes from the NR mode to the Chevron Pattern (CP, see Figure 9.6a). The CP pattern strongly resembles two ropes twined around one another such as those shown in Figure 9.6b, and have been extensively studied by Huh et al.[336,453]. Here, we hypothesize that the formation of the CP mode is caused by the fact that two rolls have sufficiently small period overlay on top of one another. In 1972, Penz and Ford found overlaying of rolls to be a valid solution to the electrohydrodynamic equations when working in 2D (Figure 9.6c)[282]. The twisting nature of the CP pattern is clearly more complex than the simple overlaying of rolls shown in Figure 9.6c. This likely arises from Penz and Ford's work only considering 2- dimensions, where naturally this 3-dimmensional effect would not be seen. The fact the rolls twist around one another rather than overlaying uniformly is likely linked to calamitic NLC materials usually having relatively low twist elastic constants (k_{22}). Full understanding of the formation of this mode requires significantly more work and is beyond the scope of this project.

One promising research direction for investigating the effect would be creating negative mixtures with varying k_{22}, and observe effects on the CP pattern. This could be achieved by doping calamitic mixtures with small amount of bent core materials shown to have this effect [454]. Similarly, to the work presented in Chapter 6, the behaviours of the pattern as a function of different k_{ii} could be investigated to find dependencies.

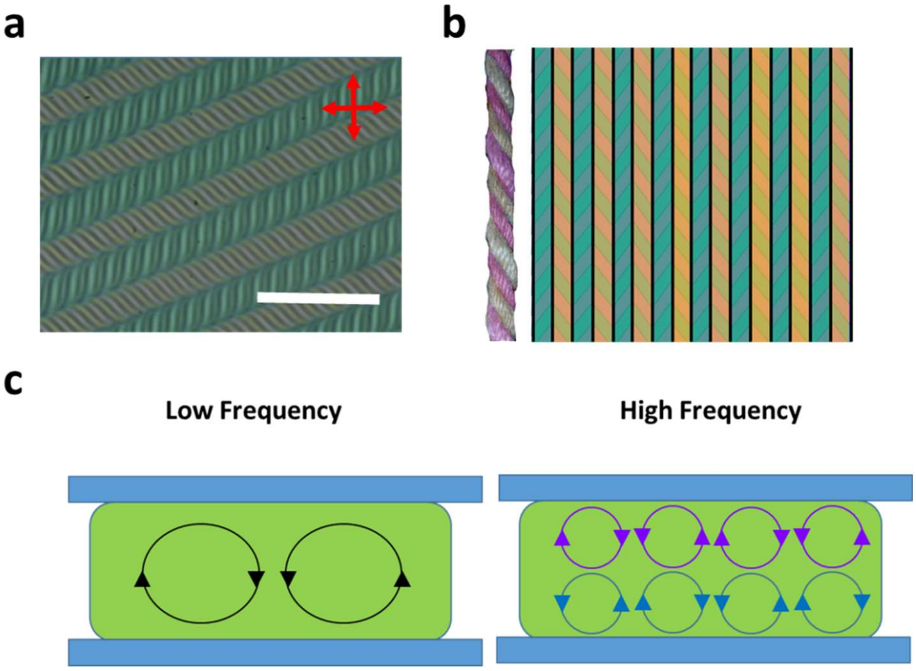

Figure 9.6 (a) Photo of the chevron pattern, scale bar is 100µm. (b) Comparing the chevron pattern to that of a twisted rope. (c) Hydrodynamic rolls forming on top of one another when driven to high frequencies (based on image from reference [282]*).*

9.3.4 BAW Guiding Structures

The most promising structures for DOEs seen under BAW driving were the short pitch domains. Our results in addition to those reported by Mullin et al. [408] indicate that these are likely caused by the longitudinal acoustic field transferring to shear at interfaces. The pitch of these short domains appeared to be mainly dictated by device spacing, however if the effects are similar to those seen in EHDI it is likely that a frequency dependency also exists. Only limited work was completed in this project to investigate this; however, a relatively simple expansion of the work would be to examine the effect of piezoelectric disk radial mode resonance frequency on domain size. If a frequency dependence was observed, such devices could show similar promise to those based on EHDI.

Another possible direction is to utilize some physical waveguiding structures within the device to efficiently transfer the longitudinal signal into shear waves. A schematic of such is shown in Figure

9.7a, where small prisms have been incorporated into the device to reorient acoustic field to become more shear. Here, the reorientation of the acoustic waves is determined by the relative speeds of sound in the wave guide *(v_{wg})* and the LC *(v_{LC})*. Figure 9.7b shows a calculation of the angle of deflection of the wave *($\Delta\theta$)* using Snell's Law. Here,

$$\frac{v_{LC}}{v_{wg}} = \frac{sin(\theta_{LC})}{sin(\theta_{wg})}, \tag{9-22}$$

giving,

$$\Delta\theta = \theta_{wg} - \theta_{LC} = \theta_{wg} - \sin^{-1}\left(\sin(\theta_{wg})\frac{v_{LC}}{v_{wg}}\right). \tag{9-23}$$

$\Delta\theta$ for several values $\frac{v_{LC}}{v_{wg}}$ are plotted as functions of θ_{wg} in Figure 9.7c. This indicates the values $\Delta\theta$ are fairly small unless $\frac{v_{LC}}{v_{wg}}$ is very small or θ_{wg} is large.

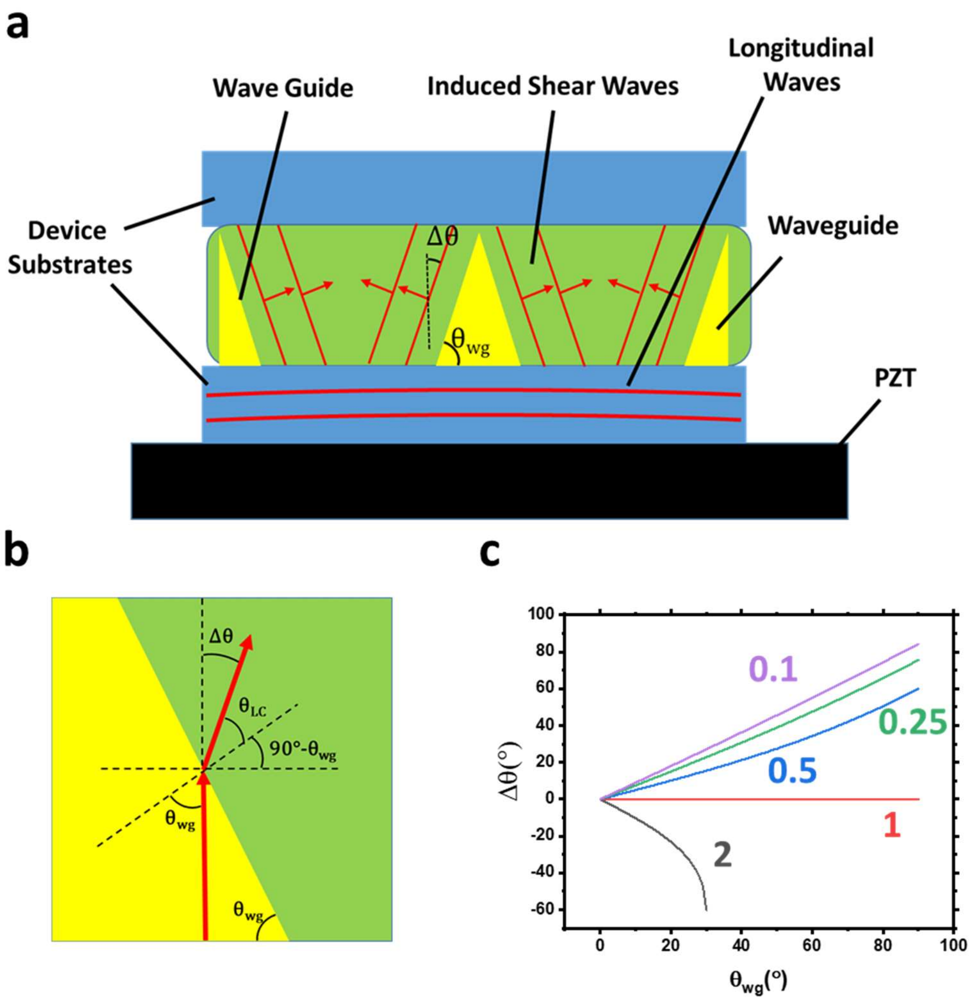

Figure 9.7.Operation of a wave guided BAW device. (a) Schematic of a longitudinal BAW device, where a solid wave guiding structure is incorporated to reorient waves to have larger horizontal components. (b) Calculations of reorientation ($\Delta\theta$) of wave direction using Snell's law. (c) Plots of $\Delta\theta$ for various values v_{LC}/v_{WG}.

9.3.5 BAW Lenses

A possible application of the results for BAW NLC devices are lenses, where several studies of ultrasonic NLC lenses have recently published[399,455,456]. A major issue in the creation LC adaptive lenses is the fact that when pixelated electrodes are used to address the lenses, the LC does not smoothly reorient, but does so sharply at points due to the proximity to electrodes[144]. This is illustrated in Figure 9.8a, and is causes particular issues if wide apertures are desired. Much work has been undertaken to reduce this effect with a wide range of techniques such as additional ‘floating’ electrodes [147,148], dielectric relief structures [149–151] and resistive electrodes [152–156] or a combination of these being used[108,157,158]. From results shown in Section 8.1.3, if the effect of director coupling was used in combination of electric field a superior lensing structure would be likely to form, where close to the centre of the device as the acoustic field is more intense, more reorientation would occur (Figure 9.8b). A limit of this is that the device would be reflection only, however results from Shimizu et al. [399] have shown efficient coupling from a BAW into an LC device via glass.

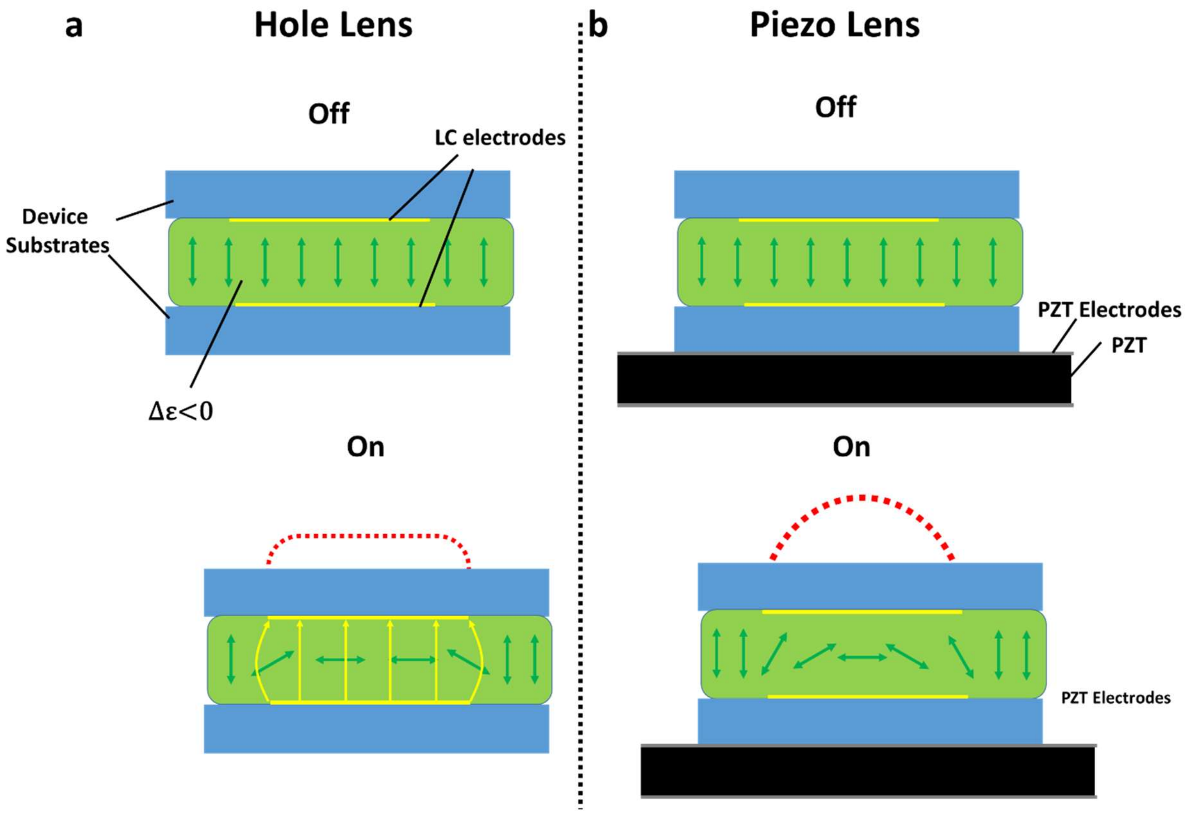

Figure 9.8. BAW aided lenses. (a) A typical hole patterned lens, such as that given in reference [144]. *The lensing structure of this device is the red dotted line, where the desirable smooth curve is not seen, due to sharp reorientation close to the electrode edges. (b) The BAW aided device. The addition of BAW and electric field leads to the LC closest to the centre of the device reorienting most and spreading more smoothly to electrode edges. This would allow a more curved lensing structure, and allow wider aperture devices.*

9.3.6 Broadband Acoustic Spectroscopy of Liquid Crystals

The experiments examining the speed of sound in NLCs were brief within this project as the objective was simply to ascertain a value of the speed of sound in E7. These could be expanded upon using the equipment assembled and techniques developed in this project. Most simply, it would be highly interesting to undertake attenuation measurements on materials, ideally at several frequencies to confirm the picture of acoustic relaxation phenomena in LCs.

Another highly interesting set of experiments could be undertaken using broadband (chirped) SAW devices. If a sample of LC material were to be placed on a device capable of varying frequency from for example 10MHz-10GHz and the losses into the material measured, it is likely measurements of the relaxation of various elastic processes could be obtained. Such techniques have previously been used for probing the dynamics of polymeric[457] and biological materials [458,459], however no studies using such techniques on nematic liquid crystals were found in a search of the literature.

9.3.7 Summary

In section 9.3 some possible directions for continuation of the project have been presented. They are fairly broad in scope which reflects the content of the project which has contained elements of liquid crystal science, dielectrics, acoustics, hydrodynamics and engineering. These ideas may prove useful to future researchers in this field.

References

1. Schadt, M.; Helfrich, W. Voltage-dependent optical activity of a twisted nematic liquid crystal. *Appl. Phys. Lett.* **1971**, *18*, 127–128, doi:10.1063/1.1653593.

2. Heilmeier, G.H.; Zanoni, L.A.; Barton, L.A. Dynamic scattering in nematic liquid crystals. *Appl. Phys. Lett.* **1968**, *13*, 46–47, doi:10.1063/1.1652453.

3. Kowel, ST, Kornreich, PG, Cleverly, D. Adaptive liquid crystal lens 1982.

4. Efron, U.; Grinberg, J.; Braatz, P.O.; Little, M.J.; Reif, P.G.; Schwartz, R.N. The silicon liquid-crystal light valve. *J. Appl. Phys.* **1985**, *57*, 1356–1368, doi:10.1063/1.334487.

5. Love, G.D. Adaptive Optics and Lenses. In *Handbook of Liquid Crystals*; Wiley-VCH Verlag GmbH & Co. KGaA: Weinheim, Germany, 2014; pp. 1–27.

6. Jones, J.C. The fiftieth anniversary of the liquid crystal display. *Liq. Cryst. Today* **2018**, *27*, 44–70, doi:10.1080/1358314X.2018.1529129.

7. Hilsum, C. Flat-panel electronic displays: A triumph of physics, chemistry and engineering. *Philos. Trans. R. Soc. A Math. Phys. Eng. Sci.* 2010, *368*, 1027–1082.

8. Jones, J.C. Rising in the east: 'The Liquid Crystal Display Story' , edited by N. Koide. *Liq. Cryst. Today* **2015**, *24*, 118–122, doi:10.1080/1358314X.2015.1050842.

9. Lavrentovich, O.D. Liquid crystals, photonic crystals, metamaterials, and transformation optics. *Proc. Natl. Acad. Sci.* **2011**, *108*, 5143–5144, doi:10.1073/pnas.1102130108.

10. Mistry, D.; Connell, S.D.; Mickthwaite, S.L.; Morgan, P.B.; Clamp, J.H.; Gleeson, H.F. Coincident molecular auxeticity and negative order parameter in a liquid crystal elastomer. *Nat. Commun.* **2018**, *9*, 1–9, doi:10.1038/s41467-018-07587-y.

11. Bunning, T.J.; Natarajan, L. V.; Tondiglia, V.P.; Sutherland, R.L. Holographic polymer-dispersed liquid crystals (H-PDLCs). *Annu. Rev. Mater. Sci.* **2000**, *30*, 83–115, doi:10.1146/annurev.matsci.30.1.83.

12. Dozov, I. On the spontaneous symmetry breaking in the mesophases of achiral banana-shaped molecules. *Europhys. Lett.* **2001**, *56*, 247–253, doi:10.1209/epl/i2001-00513-x.

13. Shen, Y.; Dierking, I. Perspectives in Liquid-Crystal-Aided Nanotechnology and Nanoscience. *Appl. Sci.* **2019**, *9*, 2512, doi:10.3390/app9122512.

14. Woltman, S.J.; Jay, G.D.; Crawford, G.P. Liquid-crystal materials find a new order in

biomedical applications. *Nat. Mater.* **2007**, *6*, 929–938, doi:10.1038/nmat2010.

15. Guo, C.; Wang, J.; Cao, F.; Lee, R.J.; Zhai, G. Lyotropic liquid crystal systems in drug delivery. *Drug Discov. Today* **2010**, *15*, 1032–1040, doi:10.1016/J.DRUDIS.2010.09.006.

16. Robinson, C. The Cholesteric Phase in Polypeptide Solutions and Biological Structures. *Mol. Cryst.* **1966**, *1*, 467–494, doi:10.1080/15421406608083287.

17. Hirst, L.S.; Charras, G. Liquid crystals in living tissue. *Nat. 2017 5447649* **2017**, *544*, 164–165, doi:10.1038/544164a.

18. Kralj, M.; Kralj, M.; Kralj, S. Topological Defects in Nematic Liquid Crystals: Laboratory of Fundamental Physics. *Phys. status solidi* **2021**, 2000752, doi:10.1002/pssa.202000752.

19. Lavrentovich, O.D. Topological defects in dispersed words and worlds around liquid crystals, or liquid crystal drops. *Liq. Cryst.* **1998**, *24*, 117–126, doi:10.1080/026782998207640.

20. Williams, R. Domains in Liquid Crystals. *J. Chem. Phys.* **1963**, *39*, 384–388, doi:10.1063/1.1734257.

21. Kashnow, R.A.; Bigelow, J.E. Diffraction from a Liquid Crystal Phase Grating. *Appl. Opt.* **1973**, *12*, 2302, doi:10.1364/AO.12.002302.

22. Carr, E.F. Influence of Electric Fields on the Molecular Alignment in the Liquid Crystal p - (Anisalamino)-phenyl Acetate. *Mol. Cryst.* **1969**, *7*, 253–268, doi:10.1080/15421406908084876.

23. Helfrich, W. Conduction-Induced Alignment of Nematic Liquid Crystals: Basic Model and Stability Considerations. *J. Chem. Phys.* **1969**, *51*, 4092–4105, doi:10.1063/1.1672632.

24. Miyano, K.; Shen, Y.R. Domain pattern excited by surface acoustic waves in a nematic film. *Appl. Phys. Lett.* **1976**, *28*, 473–475, doi:10.1063/1.88847.

25. Miyano, K.; Shen, Y.R. Excitation of stripe domain patterns by propagating acoustic waves in an oriented nematic film. *Phys. Rev. A* **1977**, *15*, 2471–2485, doi:10.1103/PhysRevA.15.2471.

26. Kapustina, O.A.; Statnikov, Y.G. *Effect of ultrasonic surface waves on liquid crystals*; 1973; Vol. 37, p. 117;.

27. Kapustina, O.A. Acoustooptical Phenomena in Liquid Crystals. *Mol. Cryst. Liq. Cryst.* **1984**, *112*, 1–164, doi:10.1080/00268948408076296.

28. McManamon, P.F.; Bos, P.J.; Escuti, M.J.; Heikenfeld, J.; Serati, S.; Xie, H.; Watson, E.A. A Review of Phased Array Steering for Narrow-Band Electrooptical Systems. In Proceedings of the Proceedings of the IEEE; 2009; Vol. 97, pp. 1078–1096.

29. He, Z.; Gou, F.; Chen, R.; Yin, K.; Zhan, T.; Wu, S.-T. Liquid Crystal Beam Steering Devices: Principles, Recent Advances, and Future Developments. *Crystals* **2019**, *9*, 292, doi:10.3390/cryst9060292.

30. Vertogen, G.; de Jeu, W.H. Introduction. In *Thermotropic Liquid Crystals, Fundamentals*; Springer, Berlin, Heidelberg, 1988; pp. 3–19.

31. de Gennes, P.G. Prost, J. Liquid Crystals: Main Types and Properties. In *The Physics of Liquid Crystals*; Oxford University Press, 1993; pp. 1–40.

32. Fréedericksz, V.; Zolina, V. Forces causing the orientation of an anisotropic liquid. *Trans. Faraday Soc.* **1933**, *29*, 919–930, doi:10.1039/TF9332900919.

33. McManamon, P.F.; Ataei, A. Progress and opportunities in the development of nonmechanical beam steering for electro-optical systems. *Opt. Eng.* **2019**, *58*, 1, doi:10.1117/1.oe.58.12.120901.

34. Williams, R. Liquid crystals in an electric field. *Nature* **1963**, *199*, 273–274, doi:10.1038/199273a0.

35. Lin, H.-C.; Chen, M.-S.; Lin, Y.-H. A Review of Electrically Tunable Focusing Liquid Crystal Lenses. *Trans. Electr. Electron. Mater.* **2011**, *12*, 234–240, doi:10.4313/TEEM.2011.12.6.234.

36. Komolkin, A. V.; Laaksonen, A.; Maliniak, A. Molecular dynamics simulation of a nematic liquid crystal. *J. Chem. Phys.* **1994**, *101*, 4103–4116, doi:10.1063/1.467460.

37. Picken, S.J.; Van Gunsteren, W.F.; Duijnen, P.T. Van; De Jeu, W.H. A molecular dynamics study of the nematic phase of 4-n-pentyl-4′-cyanobiphenyl. *Liq. Cryst.* **1989**, *6*, 357–371, doi:10.1080/02678298908029087.

38. Gray, G.W.; Harrison, K.J.; Nash, J.A. New family of nematic liquid crystals for displays. *Electron. Lett.* **1973**, *9*, 130, doi:10.1049/el:19730096.

39. Chien, S.C.; Chen, H.H.; Chen, H.C.; Yang, Y.L.; Hsu, H.F.; Shih, T.L.; Lee, J.J. Stable, low-temperature discotic nematic superstructures by incorporating a laterally substituted sidearm in hexakis(phenylethynyl)benzene discogens. *Adv. Funct. Mater.* **2007**, *17*, 1896–1902, doi:10.1002/adfm.200601019.

40. Luckhurst, G.R.; Yeates, R.N. Orientational order of a spin probe dissolved in nematic liquid crystals. An electron resonance investigation. *J. Chem. Soc. Faraday Trans. 2* **1976**, *72*, 996, doi:10.1039/f29767200996.

41. Blinov, L.M. Phase Transitions. In *Structure and Properties of Liquid Crystals*; Springer Netherlands: Dordrecht, 2011; pp. 111–148.

42. Haller, I. Thermodynamic and static properties of liquid crystals. *Prog. Solid State Chem.* **1975**, *10*, 103–118, doi:10.1016/0079-6786(75)90008-4.

43. Frank, F.C. On the theory of liquid crystals. *Discuss. Faraday Soc.* **1958**, *25*, 19, doi:10.1039/df9582500019.

44. Oseen, C.W. The theory of liquid crystals. *Trans. Faraday Soc.* **1933**, *29*, 883, doi:10.1039/tf9332900883.

45. Cui, M.; Kelly, J.R. Temperature Dependence of Visco-Elastic Properties of 5CB. *Mol. Cryst. Liq. Cryst. Sci. Technol. Sect. A Mol. Cryst. Liq. Cryst.* **1999**, *331*, 49–57, doi:10.1080/10587259908047499.

46. Babakhanova, G.; Parsouzi, Z.; Paladugu, S.; Wang, H.; Nastishin, Y.A.; Shiyanovskii, S. V; Sprunt, S.; Lavrentovich, O.D. Elastic and viscous properties of the nematic dimer CB7CB. *Phys. Rev. E* **2017**, *96*, 062704, doi:10.1103/PhysRevE.96.062704.

47. Balachandran, R.; Panov, V.P.; Vij, J.K.; Kocot, A.; Tamba, M.G.; Kohlmeier, A.; Mehl, G.H. Elastic properties of bimesogenic liquid crystals. *Liq. Cryst.* **2013**, *40*, 681–688, doi:10.1080/02678292.2013.765973.

48. Sathyanarayana, P.; Mathew, M.; Li, Q.; Sastry, V.S.S.S.; Kundu, B.; Le, K. V; Takezoe, H.; Dhara, S. Splay bend elasticity of a bent-core nematic liquid crystal. *Phys. Rev. E* **2010**, *81*, 010702, doi:10.1103/PhysRevE.81.010702.

49. Jákli, A. Liquid crystals of the twenty-first century – nematic phase of bent-core molecules. *Liq. Cryst. Rev.* **2013**, *1*, 65–82, doi:10.1080/21680396.2013.803701.

50. Kaur, S. Elastic properties of bent-core nematic liquid crystals: the role of the bend angle. *Liq. Cryst.* **2016**, *43*, 2277–2284, doi:10.1080/02678292.2016.1232442.

51. Kundu, B.; Pratibha, R.; Madhusudana, N. V Anomalous Temperature Dependence of Elastic Constants in the Nematic Phase of Binary Mixtures Made of Rodlike and Bent-Core Molecules. *Phys. Rev. Lett.* **2007**, *99*, 247802, doi:10.1103/PhysRevLett.99.247802.

52. Adlem, K.; Copič, M.ˇ; Luckhurst, G.R.; Mertelj, A.; Parri, O.; Richardson, R.M.; Snow, B.D.; Timimi, B.A.; Tuffin, R.P.; Wilkes, D. Chemically induced twist-bend nematic liquid crystals, liquid crystal dimers, and negative elastic constants. *Phys. Rev. E* **2013**, *88*, 22503, doi:10.1103/PhysRevE.88.022503.

53. Cestari, M.; Diez-Berart, S.; Dunmur, D.A.; Ferrarini, A.; De La Fuente, M.R.; Jackson, D.J.B.; Lopez, D.O.; Luckhurst, G.R.; Perez-Jubindo, M.A.; Richardson, R.M.; et al. Phase behavior and properties of the liquid-crystal dimer 1 ,7-bis(4-cyanobiphenyl-4-yl) heptane: A twist-bend

nematic liquid crystal. *Phys. Rev. E* **2011**, *84*, 31704, doi:10.1103/PhysRevE.84.031704.

54. Kim, Y.B.; Olin, H.; Park, S.Y.; Choi, J.W.; Komitov, L.; Matuszczyk, M.; Lagerwall, S.T. Rubbed polyimide films studied by scanning force microscopy. *Appl. Phys. Lett.* **1995**, *66*, 2218–2219, doi:10.1063/1.113172.

55. Kobayashi, S.; Kuroda, K.; Matsuo, M.; Nishikawa, M. Alignment Films for Liquid Crystal Devices. In *The Liquid Crystal Display Story*; Springer Japan: Tokyo, 2014; pp. 59–80 ISBN 9784431548591.

56. Ito, T.; Nakanishi, K.; Nishikawa, M.; Yokoyama, Y.; Takeuchi, Y. Regularity and narrowness of the intervals of the microgrooves on the rubbed polymer surfaces for liquid crystal alignment. *Polym. J.* **1995**, *27*, 240–246, doi:10.1295/polymj.27.240.

57. Toney, M.F.; Russell, T.P.; Logan, J.A.; Kikuchi, H.; Sands, J.M.; Kumar, S.K. Near-surface alignment of polymers in rubbed films. *Nature* **1995**, *374*, 709–711, doi:10.1038/374709a0.

58. Uchida, T.; Ohgawara, M.; Wada, M. Liquid crystal orientation on the surface of obliquely-evaporated silicon monoxide with homeotropic surface treatment. *Jpn. J. Appl. Phys.* **1980**, *19*, 2127–2136, doi:10.1143/JJAP.19.2127.

59. Jones, J.C.; Bryan-Brown, G.P.; Wood, E.L.; Graham, A.; Brett, P.; Hughes, J.R. Novel bistable liquid crystal displays based on grating alignment. In Proceedings of the Liquid Crystal Materials, Devices, and Flat Panel Displays; SPIE, 2000; Vol. 3955, p. 84.

60. Berreman, D.W. Solid surface shape and the alignment of an adjacent nematic liquid crystal. *Phys. Rev. Lett.* **1972**, *28*, 1683–1686, doi:10.1103/PhysRevLett.28.1683.

61. Creagh, L.T.; Kmetz, A.R. Mechanism of Surface Alignment in Nematic Liquid Crystals. *Mol. Cryst. Liq. Cryst.* **1973**, *24*, 59–68, doi:10.1080/15421407308083389.

62. S, B.J.; Jerome, B. Surface effects and anchoring in liquid crystals. *Reports Prog. Phys.* **1991**, *54*, 391–451, doi:10.1088/0034-4885/54/3/002.

63. Bryan-Brown, G.; Wood, E.; Sage, I. Weak surface anchoring of liquid crystals. *Lett. to Nat.* **1999**.

64. Yaroshchuk, O.; Reznikov, Y. *Photoalignment of liquid crystals: Basics and current trends*; The Royal Society of Chemistry, 2012; Vol. 22, pp. 286–300;.

65. Tseng, M.-C.; Fan, F.; Lee, C.-Y.; Murauski, A.; Chigrinov, V.; Kwok, H.-S. Tunable lens by spatially varying liquid crystal pretilt angles. *J. Appl. Phys.* **2011**, *109*, 083109, doi:10.1063/1.3567937.

66. Yaroshchuk, O.; Kyrychenko, V.; Tao, D.; Chigrinov, V.; Kwok, H.S.; Hasebe, H.; Takatsu, H. Stabilization of liquid crystal photoaligning layers by reactive mesogens. **2009**, doi:10.1063/1.3168526.

67. Jackson, P.O.; O’Neill, M.; Duffy, L.W.; Hindmarsh, P.; Kelly, S.M.; Owen, G.J. An investigation of the role of cross-linking and photodegradation of side-chain coumarin polymers in the photoalignment of liquid crystals. *Chem. Mater.* **2001**, *13*, 694–703, doi:10.1021/cm0011413.

68. Obi, M.; Morino, S.; Ichimura, K. Factors affecting photoalignment of liquid crystals induced by polymethacrylates with coumarin side chains. *Chem. Mater.* **1999**, *11*, 656–664, doi:10.1021/cm980533v.

69. Chigrinov, V.; Sun, J.; Wang, X. Photoaligning and photopatterning: New LC technology. *Crystals* 2020, *10*.

70. Chigrinov, V. Photoaligning and Photopatterning — A New Challenge in Liquid Crystal Photonics. *Crystals* **2013**, *3*, 149–162, doi:10.3390/cryst3010149.

71. Sze-Yan Yeung, F.; Xie, F.-C.; Tsz-Kai Wan, J.; Kay Lee, F.; C Tsui, O.K.; Sheng, P.; Kwok, H.-S. Liquid crystal pretilt angle control using nanotextured surfaces. *J. Appl. Phys. Appl. Phys. Lett. Appl. Phys. Lett.* **2006**, *99*, 124506–51910, doi:10.1063/1.2206067.

72. Yeung, F.S.; Ho, J.Y.; Li, Y.W.; Xie, F.C.; Tsui, O.K.; Sheng, P.; Kwok, H.S. Variable liquid crystal pretilt angles by nanostructured surfaces. *Appl. Phys. Lett.* **2006**, *88*, 1–3, doi:10.1063/1.2171491.

73. Nissan Chemicals *Polyimide Data Sheet: Alignment Coatings for LCDs-SUNEVER Series -1*;

74. Blinov, L.M.; Kabayenkov, A.Y.; Sonin, A.A. Experimental studies of the anchoring energy of nematic liquid crystals. *Liq. Cryst.* **1989**, *5*, 645–661, doi:10.1080/02678298908045415.

75. Rapini, A.; Papoular, M. Distorsion d’une lamelle nématique sous champ magnétique conditions d’ancrage aux parois. *Le J. Phys. Colloq.* **1969**, *30*, C4-54-C4-56, doi:10.1051/jphyscol:1969413.

76. Miri, T. Viscosity and Oscillatory Rheology. In *Practical Food Rheology: An Interpretive Approach*; John Wiley & Sons, Ltd, 2010; pp. 7–28 ISBN 9781405199780.

77. Orr, R.; Pethrick, R.A. Viscosity coefficients of nematic liquid crystals: I. Oscillating plate viscometer measurements and rotational viscosity measurements: K15 †. *Liq. Cryst.* **2011**, *38*, 1169–1181, doi:10.1080/02678292.2011.602121.

78. Ericksen, J.L. Continuum Theory of Liquid Crystals of Nematic Type. *Mol. Cryst.* **1969**, *7*, 153–

164, doi:10.1080/15421406908084869.

79. Leslie, F.M. Theory of Flow Phenomena in Liquid Crystals. In; Elsevier, 1979; Vol. 4, pp. 1–81.

80. Leslie, F.M. Continuum theory for nematic liquid crystals. *Contin. Mech. Thermodyn.* **1992**, *4*, 167–175, doi:10.1007/BF01130288.

81. Osipov, M.A.; Terentjev, E.M. Rotational Diffusion and Rheological Properties of Liquid Crystals. *Zeitschrift fur Naturforsch. - Sect. A J. Phys. Sci.* **1989**, *44*, 785–792, doi:10.1515/zna-1989-0903.

82. Parodi, O. Stress tensor for a nematic liquid crystal. *J. Phys.* **1970**, *31*, 581–584, doi:10.1051/jphys:01970003107058100.

83. W. Stewart, I. Continuum Theory for Liquid Crystals. In *Handbook of Liquid Crystals*; Wiley-VCH Verlag GmbH & Co. KGaA: Weinheim, Germany, 2014; pp. 1–36.

84. Kneppe, H.; Schneider, F. Determination of the rotational viscosity coefficient γ1 of nematic liquid crystals. *J. Phys. E.* **1983**, *16*, 512–515, doi:10.1088/0022-3735/16/6/015.

85. Schönhals, A.; Kremer, F. Broadband Dielectric Measurement Techniques (10-6 Hz to 1012 Hz). In *Broadband Dielectric Spectroscopy*; Springer Berlin Heidelberg: Berlin, Heidelberg, 2003; pp. 35–57.

86. Schönhals, A.; Kremer, F. Theory of Dielectric Relaxation. In *Broadband Dielectric Spectroscopy*; Springer Berlin Heidelberg: Berlin, Heidelberg, 2003; pp. 1–33.

87. Cole, K.S.; Cole, R.H. Dispersion and Absorption in Dielectrics I. Alternating Current Characteristics. *J. Chem. Phys* **1941**, *9*, 341, doi:10.1063/1.1750906.

88. Havriliak, S.; Negami, S. A complex plane representation of dielectric and mechanical relaxation processes in some polymers. *Polymer (Guildf).* **1967**, *8*, 161–210, doi:10.1016/0032-3861(67)90021-3.

89. Baker-Jarvis, J.; Kim, S. The Interaction of Radio-Frequency Fields with Dielectric Materials at Macroscopic to Mesoscopic Scales. *J. Res. Natl. Inst. Stand. Technol.* **2012**, *117*, 1, doi:10.6028/jres.117.001.

90. Feynman, R. The Origin of the Refractive Index. In *The Feynman Lectures on Physics.*; California Institute of Technology.

91. Schönhals, A.; Kremer, F. Analysis of Dielectric Spectra. In *Broadband Dielectric Spectroscopy*; Springer Berlin Heidelberg: Berlin, Heidelberg, 2003; pp. 59–98.

92. Naemura, S.; Sawada, A. Ion Generation in Liquid Crystals under Electric Field. *Mol. Cryst. Liq. Cryst. Sci. Technol. Sect. A. Mol. Cryst. Liq. Cryst.* **2000**, *346*, 155–168, doi:10.1080/10587250008023875.

93. Gosse, B.; Gosse, J.P. Degradation of liquid crystal devices under d.c. excitation and their electrochemistry. *J. Appl. Electrochem.* **1976**, *6*, 515–519, doi:10.1007/BF00614539.

94. Perlmutter, S.H.; Doroski, D.; Moddel, G. Degradation of liquid crystal device performance due to selective adsorption of ions. *Appl. Phys. Lett.* **1996**, *69*, 1182–1184, doi:10.1063/1.117404.

95. Jones, J. Dielectric Behaviour of Liquis Crystals Lecture 10. PHYS5016M Soft Matter Physics: Liquid Crystals. University of Leeds. 2016.

96. Maier, W.; Meier, G. Eine einfache Theorie der dielektrischen Eigenschaften homogen orientierter kristallinflüssiger Phasen des nematischen Typs. *Zeitschrift fur Naturforsch. - Sect. A J. Phys. Sci.* **1961**, *16*, 262–267, doi:10.1515/zna-1961-0309.

97. Vuks, M. Determination of the Optical Anisotropy of Aromatic Molecules from the Double Refraction of Crystals. *Opt. Spectrosc.* **1966**.

98. de Gennes, P.G. Prost, J. Dynamical Properties of Nematics. In *The Physics of Liquid Crystals*; Oxford University Press, 1993; pp. 198–262.

99. Jones, J.C. Liquid Crystal Displays. In *The Handbook of Optoelectronics*; CRC Press, 2017; pp. 137–224 ISBN 9781315156996.

100. Welford, K.R.; Sambles, J.R. Analysis of Electric Field Induced Deformations in a Nematic Liquid Crystal for any Applied Field. *Mol. Cryst. Liq. Cryst.* **1987**, *147*, 25–42, doi:10.1080/00268948708084622.

101. Clark, M.G.; Raynes, E.P.; Smith, R.A.; Tough, R.J.A. Measurement of the permittivity of nematic liquid crystals in magnetic and electric fields using extrapolation procedures. *J. Phys. D. Appl. Phys.* **1980**, *13*, 2151–2164, doi:10.1088/0022-3727/13/11/025.

102. Heilmeier, G.H.; Zanoni, L.A.; Barton, L.A. Dynamic scattering: A new electrooptic effect in certain classes of nematic liquid crystals. *Proc. IEEE* **1968**, *56*, 1162–1171, doi:10.1109/PROC.1968.6513.

103. Beeckman, J. Liquid-crystal photonic applications. *Opt. Eng.* **2011**, *50*, 081202, doi:10.1117/1.3565046.

104. Jull, E.I.L.; Gleeson, H.F. All-optical responsive azo-doped liquid crystal laser protection filter. *Opt. Express* **2018**, *26*, 34179, doi:10.1364/OE.26.034179.

105. Sato, S. Applications of Liquid Crystals to Variable-Focusing Lenses. *Opt. Rev.* **1999**, *6*, 471–485, doi:10.1007/s10043-999-0471-z.

106. Algorri, J.F.; Zografopoulos, D.C.; Urruchi, V.; Sánchez-Pena, J.M. Recent Advances in Adaptive Liquid Crystal Lenses. *Crystals* **2019**, *9*, 272, doi:10.3390/cryst9050272.

107. Bailey, J.; Morgan, P.; Gleeson, H.; Jones, J. Switchable Liquid Crystal Contact Lenses for the Correction of Presbyopia. *Crystals* **2018**, *8*, 29, doi:10.3390/cryst8010029.

108. Jamali, A.; Bryant, D.; Zhang, Y.; Grunnet-Jepsen, A.; Bhowmik, A.; Bos, P.J. Design of a large aperture tunable refractive Fresnel liquid crystal lens. *Appl. Opt.* **2018**, *57*, B10, doi:10.1364/AO.57.000B10.

109. Kim, J.; Oh, C.; Serati, S.; Escuti, M.J. Wide-angle, nonmechanical beam steering with high throughput utilizing polarization gratings. *Appl. Opt.* **2011**, *50*, 2636, doi:10.1364/AO.50.002636.

110. Love, G.D.; Major, J. V.; Purvis, A. Liquid-crystal prisms for tip-tilt adaptive optics. *Opt. Lett.* **1994**, *19*, 1170, doi:10.1364/ol.19.001170.

111. Matic, R.M. Blazed phase liquid crystal beam steering. In Proceedings of the Laser Beam Propagation and Control; Weichel, H., DeSandre, L.F., Eds.; International Society for Optics and Photonics: Los Angeles, 1994; Vol. 2120, pp. 194–205.

112. Wang, X.; Wilson, D.; Muller, R.; Maker, P.; Psaltis, D. Liquid-crystal blazed-grating beam deflector. *Appl. Opt.* **2000**, *39*, 6545, doi:10.1364/AO.39.006545.

113. Lindquist, R.G.; Leslie, T.M.; Kulick, J.H.; Nordin, G.P.; Jarem, J.M.; Kowel, S.T.; Friends, M. High-resolution liquid-crystal phase grating formed by fringing fields from interdigitated electrodes. *Opt. Lett.* **1994**, *19*, 670, doi:10.1364/OL.19.000670.

114. Morris, R.; Jones, J.C.; Nagaraj, M. Variable pitch hydrodynamic electro-optic gratings utilising bent liquid crystal dimers. *Soft Matter* **2020**, *16*, 10439–10453, doi:10.1039/d0sm01425g.

115. Morris, R.; Jones, C.; Nagaraj, M. Liquid Crystal Devices for Beam Steering Applications. *Micromachines* **2021**, *12*, 247, doi:10.3390/mi12030247.

116. Bailey, J.; Kaur, S.; Morgan, P.B.; Gleeson, H.F.; Clamp, J.H.; Jones, J.C. Design considerations for liquid crystal contact lenses. *J. Phys. D. Appl. Phys.* **2017**, *50*, 485401, doi:10.1088/1361-6463/aa9358.

117. Titus, C.M.; Bos, P.J.; Lavrentovich, O.D. Efficient accurate liquid crystal digital light deflector. In Proceedings of the Diffractive and Holographic Technologies, Systems, and Spatial Light Modulators VI; Cindrich, I., Lee, S.H., Sutherland, R.L., Eds.; 1999; pp. 244–253.

118. Susumu Sato, L.; Sugiyama, A.; Sato, R.; Sato, S.; Susumu Sato, L.; Sugiyama, A.; Sato, R.; Sato, S. Liquid-crystal lens-cells with variable focal length. *Jpn. J. Appl. Phys.* **1979**, *18*, 1679–1684, doi:10.1143/JJAP.18.1679.

119. Sinzinger, S.; Jahns, J. Refractive microoptics. In *Microoptics*; Wiley, 2003; pp. 93–131.

120. Saleh, B.E.A.; Teich, M.C. Ray Optics. In *Fundamentals of Photonics*; John Wiley & Sons, Inc.: New York, USA, 1991; Vol. 5, pp. 1–40 ISBN 0471839655.

121. Moore, D.T. Gradient-index optics: a review. *Appl. Opt.* **1980**, *19*, 1035, doi:10.1364/ao.19.001035.

122. Beliakov, G.; Chan, D.Y.C. Analysis of inhomogeneous optical systems by the use of ray tracing I Planar systems. *Appl. Opt.* **1997**, *36*, 5303, doi:10.1364/AO.36.005303.

123. Teichman, J.A. Measurement of gradient index materials by beam deflection, displacement, or mode conversion. *Opt. Eng.* **2013**, *52*, 112112, doi:10.1117/1.oe.52.11.112112.

124. Nishimoto, Y. Variable-focal-length lens using an electrooptic effect. US Patent No: 4,466,703. 1982.

125. Kowel, S.T.; Cleverly, D.S.; Kornreich, P.G. Focusing by electrical modulation of refraction in a liquid crystal cell. *Appl. Opt.* **1984**, *23*, 278, doi:10.1364/AO.23.000278.

126. Beeckman, J.; Yang, T.-H.; Nys, I.; George, J.P.; Lin, T.-H.; Neyts, K. Multi-electrode tunable liquid crystal lenses with one lithography step. *Opt. Lett.* **2018**, *43*, 271, doi:10.1364/ol.43.000271.

127. Valley, P.; Mathine, D.L.; Dodge, M.R.; Schwiegerling, J.; Peyman, G.; Peyghambarian, N. Tunable-focus flat liquid-crystal diffractive lens. *Opt. Lett.* **2010**, *35*, 336, doi:10.1364/ol.35.000336.

128. McKnight, D.J.; Johnson, K.M.; Serati, R.A. 256 × 256 liquid-crystal-on-silicon spatial light modulator. *Appl. Opt.* **1994**, *33*, 2775, doi:10.1364/AO.33.002775.

129. Johnson, K.M.; McKnight, D.J.; Underwood, I. Smart Spatial Light Modulators Using Liquid Crystals on Silicon. *IEEE J. Quantum Electron.* **1993**, *29*, 699–714, doi:10.1109/3.199323.

130. Wang, X. Performance evaluation of a liquid-crystal-on-silicon spatial light modulator. *Opt. Eng.* **2004**, *43*, 2769, doi:10.1117/1.1794706.

131. Wang, X.; Wang, B.; Pouch, J.; Miranda, F.; Fisch, M.; Anderson, J.E.; Sergan, V.; Bos, P.J. Liquid crystal on silicon(LCOS) wavefront corrector and beam steerer. *Proc. SPIE* **2003**, *5162*, 139–146, doi:10.1117/12.511504.

132. Inoue, T.; Tanaka, H.; Fukuchi, N.; Takumi, M.; Matsumoto, N.; Hara, T.; Yoshida, N.; Igasaki, Y.; Kobayashi, Y. LCOS spatial light modulator controlled by 12-bit signals for optical phase-only modulation. In Proceedings of the Emerging Liquid Crystal Technologies II; Chien, L.-C., Ed.; SPIE, 2007; Vol. 6487, p. 64870Y.

133. Chen, H.-M.; Yang, J.-P.; Yen, H.-T.; Hsu, Z.-N.; Huang, Y.; Wu, S.-T. Pursuing High Quality Phase-Only Liquid Crystal on Silicon (LCoS) Devices. *Appl. Sci.* **2018**, *8*, 2323, doi:10.3390/app8112323.

134. Efron, U. *Spatial light modulator technology : materials, devices, and applications*; Marcel Dekker, 1995; ISBN 9780824791087.

135. Cotter, L.K.; Drabik, T.J.; Dillon, R.J.; Handschy, M.A. Ferroelectric-liquid-crystal/silicon-integrated-circuit spatial light modulator. *Opt. Lett.* **1990**, *15*, 291, doi:10.1364/OL.15.000291.

136. Zhang, Z.; You, Z.; Chu, D. Fundamentals of phase-only liquid crystal on silicon (LCOS) devices. *Light Sci. Appl.* **2014**, *3*, e213–e213, doi:10.1038/lsa.2014.94.

137. Huang, Y.; Liao, E.; Chen, R.; Wu, S.-T. Liquid-Crystal-on-Silicon for Augmented Reality Displays. *Appl. Sci.* **2018**, *8*, 2366, doi:10.3390/app8122366.

138. de Boer, D.K.G.; Hiddink, M.G.H.; Sluijter, M.; Willemsen, O.H.; de Zwart, S.T. Switchable lenticular based 2D/3D displays. In Proceedings of the Stereoscopic Displays and Virtual Reality Systems XIV; Woods, A.J., Dodgson, N.A., Merritt, J.O., Bolas, M.T., McDowall, I.E., Eds.; SPIE, 2007; Vol. 6490, p. 64900R.

139. Yang, J.-P.; Chen, H.-M.P.; Huang, Y.; Wu, S.-T.; Hsu, C.; Ting, L.; Hsu, R. Sub-KHz 4000-PPI LCoS Phase Modulator for Holographic Displays. *SID Symp. Dig. Tech. Pap.* **2018**, *49*, 772–775, doi:10.1002/sdtp.12359.

140. Andersen, M.H.; Rommel, S.D.; Davis, S.R. Liquid crystal waveguide for dynamically controlling polarized light. US Patent No:US 8,989,523 B2 2015.

141. Anderson, M.; Davis, S.; Rommel, S. Tunable laser having liquid crystal waveguide 2005.

142. Davis, S.R.; Farca, G.; Rommel, S.D.; Martin, A.W.; Anderson, M.H. Analog, non-mechanical beam-steerer with 80 degree field of regard. In Proceedings of the Acquisition, Tracking, Pointing, and Laser Systems Technologies XXII; Chodos, S.L., Thompson, W.E., Eds.; SPIE, 2008; Vol. 6971, p. 69710G.

143. Davis, S.R.; Farca, G.; Rommel, S.D.; Johnson, S.; Anderson, M.H. Liquid crystal waveguides: new devices enabled by >1000 waves of optical phase control.; Chien, L.-C., Ed.; 2010; p. 76180E.

144. Nose, T.; Masuda, S.; Sato, S. A Liquid Crystal Microlens with Hole-Patterned Electrodes on Both Substrates. *Jpn. J. Appl. Phys.* **1992**, *31*, 1643–1646, doi:10.1143/JJAP.31.1643.

145. Ye, M.; Hayasaka, S.; Sato, S. Liquid Crystal Lens Array with Hexagonal-Hole- Patterned Electrodes Liquid Crystal Lens Array with Hexagonal-Hole-Patterned Electrodes. *Japanese J. Appl. Phys. Mao Ye al Jpn. J. Appl. Phys* **2004**, *43*, doi:10.1143/JJAP.43.6108.

146. Tuantranont, A.; Bright, V.M.; Zhang, J.; Zhang, W.; Neff, J.A.; Lee, Y.C. Optical beam steering using MEMS-controllable microlens array. *Sensors Actuators A Phys.* **2001**, *91*, 363–372, doi:10.1016/S0924-4247(01)00609-4.

147. Li, L.; Bryant, D.; Van Heugten, T.; Bos, P.J. Near-diffraction-limited and low-haze electro-optical tunable liquid crystal lens with floating electrodes. **2013**, doi:10.1364/OE.21.008371.

148. Hsu, C.; Jhang, J.; Huang, C.-Y. Large aperture liquid crystal lens with an imbedded floating ring electrode. *Opt. Express* **2016**, *24*, 16722, doi:10.1364/OE.24.016722.

149. Sova, O.; Reshetnyak, V.; Galstian, T.; Asatryan, K. Electrically variable liquid crystal lens based on the dielectric dividing principle. *J. Opt. Soc. Am. A* **2015**, *32*, 803, doi:10.1364/JOSAA.32.000803.

150. Asatryan, K.; Presnyakov, V.; Tork, A.; Zohrabyan, A.; Bagramyan, A.; Galstian, T. Optical lens with electrically variable focus using an optically hidden dielectric structure. *Opt. Express* **2010**, *18*, 13981, doi:10.1364/OE.18.013981.

151. Lin, H.-C.; Lin, Y.-H. An electrically tunable-focusing liquid crystal lens with a low voltage and simple electrodes. *Opt. Express* **2012**, *20*, 2045, doi:10.1364/oe.20.002045.

152. Hassanfiroozi, A.; Huang, Y.-P.; Javidi, B.; Shieh, H.-P.D. Dual layer electrode liquid crystal lens for 2D/3D tunable endoscopy imaging system. *Opt. Express* **2016**, *24*, 8527, doi:10.1364/OE.24.008527.

153. Chang, Y.-C.; Jen, T.-H.; Ting, C.-H.; Huang, Y.-P. High-resistance liquid-crystal lens array for rotatable 2D/3D autostereoscopic display. **2014**, doi:10.1364/OE.22.002714.

154. Naumov, A.F.; Loktev, M.Y.; Guralnik, I.R.; Vdovin, G. Liquid-crystal adaptive lenses with modal control. *Opt. Lett.* **1998**, *23*, 992, doi:10.1364/OL.23.000992.

155. Li, L.; Bryant, D.; Bos, P.J. Liquid crystal lens with concentric electrodes and inter-electrode resistors. *Liq. Cryst. Rev.* **2014**, *2*, 130–154, doi:10.1080/21680396.2014.974697.

156. Li, L.; Bryant, D.; Van Heugten, T.; Bos, P.J. Physical limitations and fundamental factors affecting performance of liquid crystal tunable lenses with concentric electrode rings. *Appl. Opt.* **2013**, *52*, 1978–1986, doi:10.1364/AO.52.001978.

157. Jamali, A.; Bryant, D.; Bhowmick, A.K.; Bos, P.J. Large area liquid crystal lenses for correction of presbyopia. **2020**, doi:10.1364/OE.408770.

158. Li, R.; Chu, F.; Tian, L.-L.; Gu, X.-Q.; Zhou, X.-Y.; Wang, Q.-H. Liquid crystal lenticular lens array with extended aperture by using gradient refractive index compensation. *Liq. Cryst.* **2020**, *00*, 1–7, doi:10.1080/02678292.2020.1783707.

159. Thie, M.W.; Lukins, J.T.; Gregory, D.A. Optically addressed SLM-based holographic display. In Proceedings of the Visual Information Processing IV; Huck, F.O., Juday, R.D., Eds.; SPIE, 1995; Vol. 2488, pp. 408–416.

160. Lin, S.-H.; Huang, B.-Y.; Li, C.-Y.; Yu, K.-Y.; Chen, J.-L.; Kuo, C.-T. Electrically and optically tunable Fresnel lens in a liquid crystal cell with a rewritable photoconductive layer. *Opt. Mater. Express* **2016**, *6*, 2229, doi:10.1364/OME.6.002229.

161. Schaal, F.; Rutloh, M.; Weidenfeld, S.; Stumpe, J.; Michler, P.; Pruss, C.; Osten, W.; Seki, T.; Hosoki, A.; Aoki, K. Optically addressed modulator for tunable spatial polarization control. *Opt. Imaging Metrol.* **2012**, *2*, 12328–12338, doi:10.1364/OE.26.028119.

162. Lee, Y.-J.; Gwag, J.S.; Kim, Y.-K.; Jo, S.I.; Kang, S.-G.; Park, Y.R.; Kim, J.-H. Control of liquid crystal pretilt angle by anchoring competition of the stacked alignment layers. *Appl. Phys. Lett.* **2009**, *94*, 041113, doi:10.1063/1.3068003.

163. Jeong, H.C.; Park, H.G.; Lee, J.H.; Jang, S.B.; Oh, B.Y.; Seo, D.S. Ion beam-induced topographical and chemical modification on the poly(styrene-co-allyl alcohol) and its effect on the molecular interaction between the modified surface and liquid crystals. *Mater. Chem. Phys.* **2016**, *182*, 94–100, doi:10.1016/j.matchemphys.2016.07.009.

164. Gorkunov, M. V; Kasyanova, I. V; Artemov, V. V; Mamonova, A. V; Palto, S.P. Precise local control of liquid crystal pretilt on polymer layers by focused ion beam nanopatterning. *Beilstein J. Nanotechnol* **2019**, *10*, 1691–1697, doi:10.3762/bjnano.10.164.

165. Bezruchenko, V.S.; Muravsky, A.A.; Murauski, A.A.; Stankevich, A.I.; Mahilny, U. V. Tunable Liquid Crystal Lens Based on Pretilt Angle Gradient Alignment. *Mol. Cryst. Liq. Cryst.* **2016**, *626*, 222–228, doi:10.1080/15421406.2015.1106890.

166. Smith, N.; Gass, P.; Tillin, M.; Raptis, C.; Burbridge, D. Micropatterned Alignment of Liquid Crystals. *Sharp Tech. J.* **2005**, *9*, 5–10.

167. Wang, X.-Q.; Srivastava, A.K.; Chigrinov, V.G.; Kwok, H.-S. Switchable Fresnel lens based on micropatterned alignment. **2013**, doi:10.1364/OL.38.001775.

168. Patel, J.S.; Rastani, K. Electrically controlled polarization-independent liquid-crystal Fresnel

lens arrays. *Opt. Lett.* **1991**, *16*, 532, doi:10.1364/OL.16.000532.

169. Chigrinov, V.G.; Kozenkov, V.M.; Kwok, H.-S. Photoalignment of LCs. In *Photoalignment of Liquid Crystalline Materials*; John Wiley & Sons, Ltd, 2008; pp. 69–100.

170. Suhara, T.; Kobayashi, K.; Nishihara, H.; Koyama, J. Graded-index Fresnel lenses for integrated optics. *Appl. Opt.* **1982**, *21*, 1966, doi:10.1364/ao.21.001966.

171. Encyclopædia Britannica Fresnel Lens. *Encycl. Br.*

172. Michigan Lighthouse Conservancy: Fresnel Lenses Available online: http://www.michiganlights.com/fresnel.htm (accessed on Oct 27, 2020).

173. Gaylord, T.K.; Moharam, M.G. Thin and thick gratings: terminology clarification. *Appl. Opt.* **1981**, *20*, 3271, doi:10.1364/ao.20.003271.

174. Goodman, J.W. Foundations of Scalar Diffraction Theory. In *Introduction to Fourier Optics*; Roberts and Company, 2005; pp. 31–62 ISBN 0974707724.

175. Goodman, J.W. Fresnel and Fraunhofer Diffraction. In *Introduction to Fourier Optics*; Roberts & Company, 2005; pp. 63–96 ISBN 0974707724.

176. Shang, X.; Tan, J.Y.; Willekens, O.; De Smet, J.; Joshi, P.; Cuypers, D.; Islamaj, E.; Beeckman, J.; Kristiaan, N.; Vervaeke, M.; et al. Electrically Controllable Liquid Crystal Component for Efficient Light Steering. *IEEE Photonics J.* **2015**, *7*, doi:10.1109/JPHOT.2015.2402592.

177. Wilkinson, T. Holography and Information Storage. In *Handbook of Liquid Crystals*; Wiley-VCH Verlag GmbH & Co. KGaA: Weinheim, Germany, 2014; pp. 1–41.

178. Márquez, A.; Martínez-Guardiola, F.J.; Francés, J.; Neipp, C.; Ramírez, M.G.; Calzado, E.M.; Morales-Vidal, M.; Gallego, S.; Beléndez, A.; Pascual, I. Analytical modeling of blazed gratings on two-dimensional pixelated liquid crystal on silicon devices. *Opt. Eng.* **2020**, *59*, 1, doi:10.1117/1.OE.59.4.041208.

179. Tseng, M.C.; Lee, C.Y.; Li, Y.W.; Kwok, H.S. P-124: Study of stacked alignment layers on a single substrate with spatial liquid crystal pretilt angles and its applications. In Proceedings of the 48th Annual SID Symposium, Seminar, and Exhibition 2010, Display Week 2010; 2010; Vol. 3, pp. 1731–1734.

180. Xiang, X.; Kim, J.; Komanduri, R.; Escuti, M.J. Nanoscale liquid crystal polymer Bragg polarization gratings. *Opt. Express* **2017**, *25*, 19298, doi:10.1364/OE.25.019298.

181. Pancharatnam, S. Achromatic combinations of birefringent plates. *Proc. Indian Acad. Sci. - Sect. A* **1955**, *41*, 137–144, doi:10.1007/BF03047098.

182. Lee, Y.-H.; Tan, G.; Zhan, T.; Weng, Y.; Liu, G.; Gou, F.; Peng, F.; Tabiryan, N. V; Gauza, S.; Wu, S.-T. Recent progress in Pancharatnam-Berry phase optical elements and the applications for virtual/augmented realities. **2017**, doi:10.1515/odps-2017-0010.

183. Cakmakci, O.; Rolland, J. Head-worn displays: A review. *IEEE/OSA J. Disp. Technol.* **2006**, *2*, 199–216, doi:10.1109/JDT.2006.879846.

184. Steinvall, O.; Soderman, U.; Ahlberg, S.; Sandberg, M.; Letalick, D.; Jungert, E. Airborne laser radar: Systems and methods for reconnaissance and terrain modelling. *Laser Radar Technol. Appl. Iv* **1999**, *3707*, 12–26, doi:10.1117/12.351338.

185. NASA *Industrial Productivity*. 2011, pp. 154–155.

186. Srivastava, A.K.; Ma, Y.; Chigrinov, V.G.; Kong, H.; Hoi, ;; Kwok, S. Field Sequential Color Ferroelectric Liquid Crystal Display Cell. US Patent No: 9,366,934 B2 2016.

187. Kramer, L.; Pesch, W. Convection Instabilities in Nematic Liquid Crystals. *Annu. Rev. Fluid Mech.* **1995**, *27*, 515–539, doi:10.1146/annurev.fl.27.010195.002503.

188. Buka, A.; Éber, N.; Pesch, W.; Kramer, L.; Eber, N.; Pesch, W. Convective Patterns in Liquid Crystals Driven by an Electric Field. *Electron. Cryst. Commun.* **2005**, 55–82, doi:10.1007/1-4020-4355-4_02.

189. Kapustina, O.A. Ultrasound-initiated structural transformations in liquid crystals (A review). *Acoust. Phys.* **2008**, *54*, 180–196, doi:10.1134/S106377100802005X.

190. Wyatt, P.J.M. Thesis: Grating Aligned Ferroelectric Liquid Crystal Devices, University of Leeds, 2019.

191. Vig, J.R. UV/ozone cleaning of surfaces. In Proceedings of the Proceedings - The Electrochemical Society; 1990.

192. Madou, M.J. Fundamentals of Microfabrication: The Science of Miniaturization. *Fundam. Microfabr. Sci. Miniaturization* **2002**, 49, doi:10.1038/nmat2518.

193. Barron, A.R.; Chiang, P.-T.; Gullapalli, S.; Hamilton, C.E.; Holden, J.; Kelty, C.; Kirganskaya, I.; Luttge, A.; Saha, A.; Smith, C.; et al. Wafer Formation and Processing. In *Chemistry of Electronic Materials*; 2011; pp. 115–162 ISBN 0006-8993 (Print)r0006-8993 (Linking).

194. Helbert, J. Resist Technology-Design, Processing and Applications. In *Handbook of VLSI Microlithography: Principles, Technology and Applications*; Glendinning, W., Helbert, J., Eds.; 1991; pp. 41–141.

195. Hacker, N. Photoresists and their development. In *Processes in Photoreactive Polymers*; 1995;

pp. 368–405.

196. Sakawaki, S.; Asaka, J. Spin coating process. *Met. Finish.* **2003**, *101*, 85, doi:10.1016/S0026-0576(03)80089-2.

197. Meyerhofer, D. Characteristics of resist films produced by spinning. *J. Appl. Phys.* **1978**, *49*, 3993–3997, doi:10.1063/1.325357.

198. Zöcher, H. Optical anisotropy of selectively absorbing substances; mechanical production of anisotropy. *Naturwissenschaften* **1925**.

199. Yang, F.; Zoriniants, G.; Ruan, L.; Sambles, J.R. Optical anisotropy and liquid-crystal alignment properties of rubbed polyimide layers. *Liq. Cryst.* **2007**, *34*, 1433–1441, doi:10.1080/02678290701732970.

200. Hallam, B.T.; Sambles, J.R. Liquid Crystals Groove depth dependence of the anchoring strength of a zero order grating-aligned liquid crystal Groove depth dependence of the anchoring strength of a zero order grating-aligned liquid crystal. *Liq. Cryst.* **2000**, *27*, doi:10.1080/02678290050122051.

201. Lee, E.S.; Saito, Y.; Miyashita, T.; Uchida, T. Orientation of Polymer Molecules in rubbed Alignment Layer. *Jpn. J. Appl. Phys.* **1993**, *32*, L1822–L1825, doi:10.1143/JJAP.32.L1822.

202. Jones, R.C. A New Calculus for the Treatment of Optical SystemsI Description and Discussion of the Calculus. *J. Opt. Soc. Am.* **1941**, *31*, 488, doi:10.1364/josa.31.000488.

203. Vaughan, M.P. Polarisation. In *Optics*; University College Cork, 2014; pp. 131–154.

204. Jones, J.C.; Wahle, M.; Bailey, J.; Moorhouse, T.; Snow, B.; Sargent, J. Polarisation independent liquid crystal lenses and contact lenses using embossed reactive mesogens. *J. Soc. Inf. Disp.* **2020**, *28*, 211–223, doi:10.1002/jsid.874.

205. Macdonald, J.R.; Johnson, W.B. Fundamentals of Impedance Spectroscopy. In *Impedance Spectroscopy: Theory, Experiment, and Applications, Second Edition*; John Wiley & Sons, Inc., 2005; pp. 1–26 ISBN 0471647497.

206. Brimicombe, P. Functions for fitting permittivity data from planar cells. In *Software Documentation for Matlab Programs*; University of Manchester, 2010; pp. 42–47.

207. Bogi, A.; Faetti, S. Elastic, dielectric and optical constants of 4′-pentyl-4-cyanobiphenyl. *Liq. Cryst.* **2001**, doi:10.1080/02678290010021589.

208. Brochard, F.; Leger, L.; Meyer, R.B. Freedericksz transition of a homeotropic nematic liquid crystal in rotating magnetic fields. *Le J. Phys. Colloq.* **1975**, *36*, doi:10.1051/jphyscol:1975139.

209. Hecht Ch8: Polarization. In *Optics*; Pearson, 2016 ISBN 9781292096933.

210. Sinzinger, S.; Jahns, J.J. *Microoptics*; Wiley-VCH: Weinheim, FRG, 2003; ISBN 9783527603404.

211. Love, G. *Handbook of Liquid Crystals: Volume 8: Chapter 12 Adaptive Optics and Lenses*; Goodby, JW, Collings, PJ, Kato, T, Yschierske, C, Gleeson, HF, Raynes, P., Ed.; Wiley, 2015; Vol. 24; ISBN 9783527620555.

212. Chen, H.; Weng, Y.; Xu, D.; Tabiryan, N. V; Wu, S.-T. Beam steering for virtual/augmented reality displays with a cycloidal diffractive waveplate. *Opt. Express* **2016**, *24*, 7287, doi:10.1364/OE.24.007287.

213. Chang, C.; Bang, K.; Wetzstein, G.; Lee, B.; Gao, L. Toward the next-generation VR/AR optics: a review of holographic near-eye displays from a human-centric perspective. *Optica* **2020**, *7*, 1563, doi:10.1364/optica.406004.

214. Ke, Y.; Chen, J.; Lin, G.; Wang, S.; Zhou, Y.; Yin, J.; Lee, P.S.; Long, Y. Smart Windows: Electro-, Thermo-, Mechano-, Photochromics, and Beyond. *Adv. Energy Mater.* 2019, *9*, 1902066.

215. Niv, A.; Biener, G.; Kleiner, V.; Hasman, E. Formation of complex wavefronts by use of quasiperiodic subwavelength structures. In Proceedings of the Micromachining Technology for Micro-Optics and Nano-Optics II; Johnson, E.G., Nordin, G.P., Eds.; 2004; Vol. 5347, p. 126.

216. NumPy community 3.11 Discrete Fourier Transform. In *NumPy Reference 1.11.0. Available at: https://docs.scipy.org/doc/numpy-1.11.0/numpy-ref-1.11.0.pdf*; 2016; pp. 640–644.

217. Harris, C.R.; Millman, K.J.; van der Walt, S.J.; Gommers, R.; Virtanen, P.; Cournapeau, D.; Wieser, E.; Taylor, J.; Berg, S.; Smith, N.J.; et al. Array programming with NumPy. *Nature* **2020**, *585*, 357–362, doi:10.1038/s41586-020-2649-2.

218. Meshalkin, A.Y.; Podlipnov, V. V; Ustinov, A. V; Achimova, E.A. Analysis of diffraction efficiency of phase gratings in dependence of duty cycle and depth. In Proceedings of the Journal of Physics: Conference Series; IOP Publishing, 2019; Vol. 1368, p. 22047.

219. Harvey, J.E.; Pfisterer, R.N. Understanding diffraction grating behavior: including conical diffraction and Rayleigh anomalies from transmission gratings. *Opt. Eng.* **2019**, *58*, 1, doi:10.1117/1.OE.58.8.087105.

220. Loewen, E.G.; Nevière, M.; Maystre, D. Grating efficiency theory as it applies to blazed and holographic gratings. *Appl. Opt.* **1977**, *16*, 2711, doi:10.1364/ao.16.002711.

221. Steiner, R.; Pesch, A.; Erdmann, L.H.; Burkhardt, M.; Gatto, A.; Wipf, R.; Diehl, T.; Vink,

H.J.P.; van den Bosch, B.G. Fabrication of low straylight holographic gratings for space applications. In Proceedings of the Imaging Spectrometry XVIII; SPIE, 2013; Vol. 8870, p. 88700H.

222. Glaser, T. High-end spectroscopic diffraction gratings: Design and manufacturing. *Adv. Opt. Technol.* **2015**, *4*, 25–46, doi:10.1515/aot-2014-0063.

223. Li, G.; Mathine, D.L.; Valley, P.; Äyräs, P.; Haddock, J.N.; Giridhar, M.S.; Williby, G.; Schwiegerling, J.; Meredith, G.R.; Kippelen, B.; et al. Switchable electro-optic diffractive lens with high efficiency for ophthalmic applications. *Proc. Natl. Acad. Sci. U. S. A.* **2006**, *103*, 6100–6104, doi:10.1073/pnas.0600850103.

224. Apter, B.; Efron, U.; Bahat-Treidel, E. On the fringing-field effect in liquid-crystal beam-steering devices. *Appl. Opt.* **2004**, *43*, 11, doi:10.1364/AO.43.000011.

225. Kim, Y.; Won, K.; An, J.; Hong, J.-Y.; Kim, Y.; Choi, C.-S.; Song, H.; Song, B.; Suk Kim, H.; Bae, K.-D.; et al. Large-area liquid crystal beam deflector with wide steering angle. *Appl. Opt.* **2020**, *59*, 7462, doi:10.1364/ao.398863.

226. Honma, M.; Nose, T.; Yanase, S.; Yamaguchi, R.; Sato, S. Liquid-Crystal Blazed Gratings with Spatially Distributed Pretilt Angle. *Jpn. J. Appl. Phys.* **2010**, *49*, 061701, doi:10.1143/JJAP.49.061701.

227. Jones, J.C. Defects, flexoelectricity and RF communications: the ZBD story. *Liq. Cryst.* **2017**, doi:10.1080/02678292.2017.1365383.

228. Jones, S.A.; Bailey, J.; Walker, D.R.E.; Bryan-Brown, G.P.; Jones, J.C. Method for Tuneable Homeotropic Anchoring at Microstructures in Liquid Crystal Devices. *Langmuir* **2018**, *34*, 10865–10873, doi:10.1021/acs.langmuir.8b01951.

229. Spencer, T.J.; Care, C.M.; Amos, R.M.; Jones, J.C. Zenithal bistable device: Comparison of modeling and experiment. *Phys. Rev. E - Stat. Nonlinear, Soft Matter Phys.* **2010**, *82*, doi:10.1103/PhysRevE.82.021702.

230. Zografopoulos, D.C.; Kriezis, E.E. Switchable beam steering with zenithal bistable liquid-crystal blazed gratings. *Opt. Lett.* **2014**, *39*, 5842, doi:10.1364/OL.39.005842.

231. Jones, J.C. The Zenithal Bistable Display: From concept to consumer. *J. Soc. Inf. Disp.* **2008**, *16*, 143, doi:10.1889/1.2835021.

232. Morris, R.; Jones, J.C.; Nagaraj, M. Continuously variable diffraction gratings using electroconvection in liquid crystals for beam steering applications. *J. Appl. Phys.* **2019**, *126*, 224505, doi:10.1063/1.5128205.

233. Melcher, J.R.; Taylor, G.I. Electrohydrodynamics: A Review of the Role of Interfacial Shear Stresses. *Annu. Rev. Fluid Mech.* **1969**, *1*, 111–146, doi:10.1146/annurev.fl.01.010169.000551.

234. Vlahovska, P.M. Electrohydrodynamics of Drops and Vesicles. *Annu. Rev. Fluid Mech.* **2019**, *51*, 305–330, doi:10.1146/annurev-fluid-122316-050120.

235. Davidson, S.M.; Wessling, M.; Mani, A. On the Dynamical Regimes of Pattern-Accelerated Electroconvection OPEN. *Nat. Publ. Gr.* **2016**, doi:10.1038/srep22505.

236. Yang, J.; Lu, F.; Kostiuk, L.W.; Kwok, D.Y. Electrokinetic microchannel battery by means of electrokinetic and microfluidic phenomena. *J. Micromechanics Microengineering* **2003**, *13*, 963–970, doi:10.1088/0960-1317/13/6/320.

237. Kikuchi, H. Introduction. In *Electrohydrodynamics in Dusty and Dirty Plasmas*; Astrophysics and Space Science Library; Springer Netherlands: Dordrecht, 2001; Vol. 258 ISBN 978-90-481-5656-6.

238. Schneider, J.M. Electrohydrodynamic Stability of Space-Charge-Limited Currents in Dielectric Liquids. I. Theoretical Study. *Phys. Fluids* **1970**, *13*, 1948, doi:10.1063/1.1693190.

239. Watson, P.K. Electrohydrodynamic Stability of Space-Charge-Limited Currents in Dielectric Liquids. II. Experimental Study. *Phys. Fluids* **1970**, *13*, 1955, doi:10.1063/1.1693191.

240. Kramer, L.; Pesch, W. Electrohydrodynamic Instabilities in Nematic Liquid Crystals. In *Pattern Formation in Liquid Crystals*; Springer, New York, NY, 1996; Vol. 27, pp. 221–255 ISBN 9781461276807.

241. Kartha, T.R.; Mallik, B.S. Ionic conductance and viscous drag in water-in-salt electrolytes for lithium and sodium ion batteries and supercapacitors. *Mater. Today Commun.* **2020**, *25*, 101588, doi:10.1016/j.mtcomm.2020.101588.

242. Guan, Y.; Novosselov, I. Two relaxation time lattice Boltzmann method coupled to fast Fourier transform Poisson solver: Application to electroconvective flow. *J. Comput. Phys.* **2019**, *397*, 108830, doi:10.1016/j.jcp.2019.07.029.

243. Cross, M.C.; Hohenberg, P.C. Pattern formation outside of equilibrium. *Rev. Mod. Phys.* **1993**, *65*, 851–1112, doi:10.1103/RevModPhys.65.851.

244. Lacroix, J.C.; Atten, P.; Hopfinger, E.J. Electro-convection in a dielectric liquid layer subjected to unipolar injection. *J. Fluid Mech.* **1975**, *69*, 539–563, doi:10.1017/S0022112075001553.

245. Luo, K.; Wu, J.; Yi, H.L.; Tan, H.P. Three-dimensional finite amplitude electroconvection in dielectric liquids. *Phys. Fluids* **2018**, *30*, doi:10.1063/1.5010421.

246. Dierking, I.; Flatley, A.; Greenhalgh, D. Voronoi patterns in liquid crystal textures. *J. Mol. Liq.* **2021**, *335*, 116553, doi:10.1016/j.molliq.2021.116553.

247. Dubois-Violette, E.; de Gennes, P.G.; Parodi, O. Hydrodynamic instabilities of nematic liquid crystals under A. C. electric fields. *J. Phys.* **1971**, *32*, 305–317, doi:10.1051/jphys:01971003204030500.

248. Guyon, E.; Pieranski, P. Convective instabilities in nematic liquid crystals. *Physica* **1974**, *73*, 184–194, doi:10.1016/0031-8914(74)90234-1.

249. Madhusudana, N. V Electroconvective instabilities in nematic liquid crystals. *Phase Transitions A Multinatl. J.* **1994**, *50*, 177–191, doi:10.1080/01411599408200373.

250. Blinov, L.M. Domain Instabilities in liquid crystals. *Le J. Phys. Colloq.* **1979**, *40*, C3-247-C3-258, doi:10.1051/jphyscol:1979348.

251. Buka, A.; Eber, N.; Pesch, W. Convective Patterns in Liquid Crystal Driven by Electric Field: An overview of the onset behaviour. *Electron. Cryst. Commun.* **2005**, 1–27.

252. Tavener, S.J.; Mullin, T.; Blake, G.I.; Cliffe, K.A. Numerical bifurcation study of electrohydrodynamic convection in nematic liquid crystals. *Phys. Rev. E - Stat. Nonlinear, Soft Matter Phys.* **2001**, *63*, 1–12, doi:10.1103/PhysRevE.63.011708.

253. Zimmermann, W. Pattern Formation in Electro-hydrodynamic Convection. *MRS Bull.* **1991**, *16*, 46–56, doi:10.1557/S0883769400057900.

254. Kai, S.; Zimmermann, W. Pattern Dynamics in the Electrohydrodynamics of Nematic Liquid Crystals. *Prog. Theor. Phys. Suppl.* **1989**, *99*, 458–492, doi:10.1143/PTPS.99.458.

255. Buka, A. Pattern Formation in Liquid Crystals. *Phys. Scr.* **1989**, *1989*, 114–117, doi:10.1088/0031-8949/1989/T25/019.

256. Smith, I.W.; Galerne, Y.; Lagerwall, S.T.; Dubois-Violette, E.; Durand, G. Dynamics of Electrohydrodynamic Instabilities in Nematic Liquid Crystals. *Le J. Phys. Colloq.* **1975**, *36*, C1-237-C1-259, doi:10.1051/jphyscol:1975142.

257. Larinova, L.; Kapustin, A.P. No Titl. *Kristallografya* **1964**, *9*.

258. Buka; Dressel, B.; Otowski, W.; Camara, K.; Toth-Katona, T.; Kramer, L.; Lindau, J.; Pelzl, G.; Pesch, W.; Buka, A.´; et al. Electroconvection in nematic liquid crystals with positive dielectric and negative conductivity anisotropy. *Phys. Rev. E - Stat. Physics, Plasmas, Fluids, Relat. Interdiscip. Top.* **2002**, *66*, 8, doi:10.1103/PhysRevE.66.051713.

259. Buka, A.; Dressel, B.; Kramer, L.; Pesch, W. Direct transition to electroconvection in a

homeotropic nematic liquid crystal. In Proceedings of the Chaos; 2004; Vol. 14, pp. 793–802.

260. Scheuring, M.; Kramer, L.; Peinke, J. Formation of chevrons in the dielectric regime of electroconvection in nematic liquid crystals. *Phys. Rev. E* **1998**, *58*, 2018–2026, doi:10.1103/PhysRevE.58.2018.

261. Schneider, U.; De La, M.; Juarez, T.; Zimmermann, W.; Rehberg, I. *Phase shift of dielectric rolls in electroconvection*; 1992; Vol. 46;.

262. Thom, W.; Zimmermann, W.; Kramer, L. The influence of the flexoelectric effect on the electrohydrodynamic instability in nematics. *Liq. Cryst.* **1989**, *4*, 309–316, doi:10.1080/02678298908029184.

263. Ribotta, R.; Joets, A.; Lei, L. Oblique roll instability in an electroconvective anisotropic fluid. *Phys. Rev. Lett.* **1986**, *56*, 1595–1597, doi:10.1103/PhysRevLett.56.1595.

264. Kochowska, E.; Éber, N.; Buka, Á.; Otowski, W. Square patterns and their dynamics in electroconvection. In Proceedings of the Molecular Crystals and Liquid Crystals; Taylor and Francis Inc., 2005; Vol. 435, pp. 243/[903]-253/[913].

265. Huh, J.-H.; Osoguchi, H. Formation of grid patterns in an ac-driven electroconvection system. *Phys. Rev. E* **2020**, *101*, 62701, doi:10.1103/PhysRevE.101.062701.

266. Heilmeier, G.H.; Zanoni, L.A. Guest-Host Interaction in Nematic Liquid Crystals- a new electro-optic effect. *Appl. Phys. Lett.* **1968**, *13*, 91–92, doi:10.1063/1.1652529.

267. Bohren, C.F.; Huffman, D.R. Absorption and Scattering by a Sphere. In *Absorption and Scattering of Light by Small Particles*; Wiley-VCH Verlag GmbH, 2007; pp. 82–129.

268. Bohren, C.F.; Huffman, D.R. Particles Small Compared with the Wavelength. In *Absorption and Scattering of Light by Small Particles*; Wiley-VCH Verlag GmbH, 2007; pp. 130–157.

269. Huh, J.H.; Kuribayashi, A.; Kai, S. Noise-controlled pattern formation and threshold shift for electroconvection in the conduction and dielectric regimes. *Phys. Rev. E - Stat. Nonlinear, Soft Matter Phys.* **2009**, *80*, 066304, doi:10.1103/PhysRevE.80.066304.

270. Huh, J.H.; Hidaka, Y.; Yusuf, Y.; Éber, N.; Tóth-Katona, T.; Buka, Á.; Kai, S. Prewavy pattern: A director-modulation structure in nematic liquid crystals. *Mol. Cryst. Liq. Cryst. Sci. Technol. Sect. A Mol. Cryst. Liq. Cryst.* **2001**, *364*, 111–122, doi:10.1080/10587250108024981.

271. Shasti, M.; Gleeson, J.T.; Luchette, P.; Kosa, T.; Munoz, A.F.; Taheri, B. Enhancement in electro-optic properties of dynamic scattering systems through addition of dichroic dyes. *AIP Adv.* **2018**, *8*, doi:10.1063/1.5036947.

272. Sims, M.T. Dyes as guests in ordered systems: current understanding and future directions. *Liq. Cryst.* **2016**, doi:10.1080/02678292.2016.1189613.

273. Zhan, Y.; Lu, H.; Jin, M.; Zhou, G. Electrohydrodynamic instabilities for smart window applications. *Liq. Cryst.* **2019**, 1–7, doi:10.1080/02678292.2019.1692929.

274. John, T.; Behn, U.; Stannarius, R. Laser diffraction by periodic dynamic patterns in anisotropic fluids. *Eur. Phys. J. B* **2003**, *35*, 267–278, doi:10.1140/epjb/e2003-00277-1.

275. John, T.; Heuer, J.; Stannarius, R. Influence of excitation wave forms and frequencies on the fundamental time symmetry of the system dynamics, studied in nematic electroconvection. *Phys. Rev. E - Stat. Nonlinear, Soft Matter Phys.* **2005**, *71*, doi:10.1103/PhysRevE.71.056307.

276. Bohley, C.; Heuer, J.; Stannarius, R. Optical properties of electrohydrodynamic convection patterns: rigorous and approximate methods. *J. Opt. Soc. Am. A* **2005**, *22*, 2818, doi:10.1364/JOSAA.22.002818.

277. Orsay Liquid Crystal Group Hydrodynamic instabilities in nematic liquids under ac electric fields. *Phys. Rev. Lett.* **1970**, *25*, 1642–1643, doi:10.1103/PhysRevLett.25.1642.

278. Madhusudana, N. V.; Raghunathan, V.A. Influence of flexoelectricity on electrohydrodynamic instabilities in nematics. *Liq. Cryst.* **1989**, *5*, 1789–1812, doi:10.1080/02678298908045689.

279. Kramer, L.; Bodenschatz, E.; Pesch, W.; Thom, W.; Zimmermann, W. Invited Lecture. New results on the electrohydrodynamic instability in nematics. *Liq. Cryst.* **1989**, *5*, 699–715, doi:10.1080/02678298908045420.

280. Tóth-Katona, T.; Éber, N.; Buka, Á. Flexoelectricity in Electroconvection. *Mol. Cryst. Liq. Cryst.* **2009**, *511*, 11/[1481]-24/[1494], doi:10.1080/15421400903048461.

281. Krekhov, A.; Pesch, W.; Éber, N.; Tóth-Katona, T.; Buka, Á. Nonstandard electroconvection and flexoelectricity in nematic liquid crystals. *Phys. Rev. E* **2008**, *77*, 021705, doi:10.1103/PhysRevE.77.021705.

282. Penz, P.A.; Ford, G.W. Electromagnetic Hydrodynamics of Liquid Crystals. *Phys. Rev. A* **1972**, *6*, 414–425, doi:10.1103/PhysRevA.6.414.

283. Zhang, B.; Kitzerow, H. Pattern Formation in a Nematic Liquid Crystal Mixture with Negative Anisotropy of the Electric Conductivity—A Long-Known System with “Inverse” Light Scattering Revisited. *J. Phys. Chem. B* **2016**, *120*, 6865–6871, doi:10.1021/acs.jpcb.6b05080.

284. Allen, Bloom; Daniel Louis, R. Method for increasing the conductivity of electrically resistive organic materials 1975.

285. Lappa, M. A mathematical and numerical framework for the analysis of compressible thermal convection in gases at very high temperatures. *J. Comput. Phys.* **2016**, *313*, 687–712, doi:10.1016/j.jcp.2016.02.062.

286. Mandle, R.J.; Stevens, M.P.; Goodby, J.W. Developments in liquid-crystalline dimers and oligomers. *Liq. Cryst.* **2017**, *44*, 2046–2059, doi:10.1080/02678292.2017.1343500.

287. Imrie, C.T.; Henderson, P.A. Liquid crystal dimers and higher oligomers: Between monomers and polymers. *Chem. Soc. Rev.* **2007**, *36*, 2096–2124, doi:10.1039/b714102e.

288. Henderson, P.A.; Imrie, C.T. Methylene-linked liquid crystal dimers and the twist-bend nematic phase. *Liq. Cryst.* **2011**, *38*, 1407–1414, doi:10.1080/02678292.2011.624368.

289. Borshch, V.; Kim, Y.-K.; Xiang, J.; Gao, M.; Jákli, A.; Panov, V.P.; Vij, J.K.; Imrie, C.T.; Tamba, M.G.; Mehl, G.H.; et al. Nematic twist-bend phase with nanoscale modulation of molecular orientation. *Nat. Commun.* **2013**, *4*, 2635, doi:10.1038/ncomms3635.

290. Cestari, M.; Frezza, E.; Ferrarini, A.; Luckhurst, G.R. Crucial role of molecular curvature for the bend elastic and flexoelectric properties of liquid crystals: Mesogenic dimers as a case study. *J. Mater. Chem.* **2011**, *21*, 12303–12308, doi:10.1039/c1jm12233a.

291. Paterson, D.A.; Abberley, J.P.; Harrison, W.T.; Storey, J.M.; Imrie, C.T. Cyanobiphenyl-based liquid crystal dimers and the twist-bend nematic phase. *Liq. Cryst.* **2017**, *44*, 1–20, doi:10.1080/02678292.2016.1274293.

292. Zhang, Z.; Panov, V.P.; Nagaraj, M.; Mandle, R.J.; Goodby, J.W.; Luckhurst, G.R.; Jones, J.C.; Gleeson, H.F. Raman scattering studies of order parameters in liquid crystalline dimers exhibiting the nematic and twist-bend nematic phases. *J. Mater. Chem. C* **2015**, *3*, 10007–10016, doi:10.1039/C5TC02174J.

293. Panov, V.P.; Nagaraj, M.; Vij, J.K.; Panarin, Y.P.; Kohlmeier, A.; Tamba, M.G.; Lewis, R.A.; Mehl, G.H. Spontaneous Periodic Deformations in Nonchiral Planar-Aligned Bimesogens with a Nematic-Nematic Transition and a Negative Elastic Constant. *Phys. Rev. Lett.* **2010**, *105*, 167801, doi:10.1103/PhysRevLett.105.167801.

294. Ungar, G.; Percec, V.; Zuber, M. Influence of molecular structure on the nematic-nematic transition in polyethers based on 1-(4-hydroxyphenyl)-2-(2-R-4-hydroxyphenyl)ethane where R=CH3 and Cl, and flexible spacers with an odd number of methylene units. *Polym. Bull.* **1994**, *32*, 325–330, doi:10.1007/BF00308544.

295. Sebastián, N.; Robles-Hernández, B.; Diez-Berart, S.; Salud, J.; Luckhurst, G.R.; Dunmur, D.A.; López, D.O.; de la Fuente, M.R. Distinctive dielectric properties of nematic liquid crystal

dimers. *Liq. Cryst.* **2017**, doi:10.1080/02678292.2016.1218963.

296. Atkinson, K.L.; Morris, S.M.; Castles, F.; Qasim, M.M.; Gardiner, D.J.; Coles, H.J. Flexoelectric and elastic coefficients of odd and even homologous bimesogens. *Phys. Rev. E* **2012**, *85*, 012701, doi:10.1103/PhysRevE.85.012701.

297. Babakhanova, G. Elastic Effects in Flexible Dimeric and Elastomer Nematics, Kent State Univerisity, 2019.

298. Kaur, S.; Addis, J.; Greco, C.; Ferrarini, A.; Görtz, V.; Goodby, J.W.; Gleeson, H.F. Understanding the distinctive elastic constants in an oxadiazole bent-core nematic liquid crystal. *Phys. Rev. E - Stat. Nonlinear, Soft Matter Phys.* **2012**, *86*, 41703, doi:10.1103/PhysRevE.86.041703.

299. Xiang, Y.; Goodby, J.W.; Görtz, V.; Gleeson, H.F. Revealing the uniaxial to biaxial nematic liquid crystal phase transition via distinctive electroconvection. *Appl. Phys. Lett.* **2009**, *94*, 193507, doi:10.1063/1.3138867.

300. Shen, D.; Pegenau, A.; Diele, S.; Wirth, I.; Tschierske, C. Molecular Design of Nonchiral Bent-Core Liquid Crystals with Antiferroelectric Properties. *J. Am. Chem. Soc.* **2000**, *122*, 1593–1601, doi:10.1021/ja993572w.

301. Majumdar, M.; Salamon, P.; Jákli, A.; Gleeson, J.T.; Sprunt, S. Elastic constants and orientational viscosities of a bent-core nematic liquid crystal. *Phys. Rev. E* **2011**, *83*, 031701, doi:10.1103/PhysRevE.83.031701.

302. Dantlgraber, G.; Eremin, A.; Diele, S.; Hauser, A.; Kresse, H.; Pelzl, G.; Tschierske, C. Chirality and Macroscopic Polar Order in a Ferroelectric Smectic Liquid-Crystalline Phase Formed by Achiral Polyphilic Bent-Core Molecules. *Angew. Chemie Int. Ed.* **2002**, *41*, 2408, doi:10.1002/1521-3773(20020703)41:13<2408::AID-ANIE2408>3.0.CO;2-M.

303. Meyer, C.; Luckhurst, G.R.; Dozov, I. Flexoelectrically Driven Electroclinic Effect in the Twist-Bend Nematic Phase of Achiral Molecules with Bent Shapes. *Phys. Rev. Lett.* **2013**, *111*, 067801, doi:10.1103/PhysRevLett.111.067801.

304. Etxebarria, J.; Blanca Ros, M. Bent-core liquid crystals in the route to functional materials. *J. Mater. Chem.* **2008**, *18*, 2919, doi:10.1039/b803507e.

305. Kaur, S.; Liu, H.; Addis, J.; Greco, C.; Ferrarini, A.; Görtz, V.; Goodby, J.W.; Gleeson, H.F. The influence of structure on the elastic, optical and dielectric properties of nematic phases formed from bent-core molecules. *J. Mater. Chem. C* **2013**, *1*, 6667–6676, doi:10.1039/c3tc31545b.

306. Bradshaw, M.J.; Raynes, E.P.; Bunning, J.D.; Faber, T.E. The Frank constants of some nematic liquid crystals. *J. Phys.* **1985**, *46*, doi:10.1051/jphys:019850046090151300ï.

307. Tuchband, M.R.; Shuai, M.; Graber, K.A.; Chen, D.; Radzihovsky, L.; Klittnick, A.; Foley, L.; Scarbrough, A.; Porada, J.H.; Moran, M.; et al. The twist-bend nematic phase of bent mesogenic dimer CB7CB and its mixtures. In Proceedings of the APS March Meeting 2016; 2015.

308. Cvetinov, M.; Obadović, D.; Stojanović, M.; Lazar, D.; Vajda, A.; Éber, N.; Fodor-Csorba, K.; Ristić, I. Mesophase behaviour of binary mixtures of bent-core and calamitic compounds. *Liq. Cryst.* **2013**, *40*, 1512–1519, doi:10.1080/02678292.2013.822938.

309. Trbojevic, N.; Read, D.J.; Nagaraj, M. Dielectric properties of liquid crystalline dimer mixtures exhibiting the nematic and twist-bend nematic phases. *Phys. Rev. E* **2017**, *96*, 52703, doi:10.1103/PhysRevE.96.052703.

310. Srigengan, S.; Nagaraj, M.; Ferrarini, A.; Mandle, R.; Cowling, S.J.; Osipov, M.A.; Pająk, G.; Goodby, J.W.; Gleeson, H.F. Anomalously low twist and bend elastic constants in an oxadiazole-based bent-core nematic liquid crystal and its mixtures; contributions of spontaneous chirality and polarity. *J. Mater. Chem. C* **2018**, *6*, 980–988, doi:10.1039/C7TC04664B.

311. Buka, Á.; Éber, N.; Fodor-Csorba, K.; Jákli, A.; Salamon, P. Physical properties of a bent-core nematic liquid crystal and its mixtures with calamitic molecules. *Phase Transitions* **2012**, *85*, 872–887, doi:10.1080/01411594.2012.689834.

312. Parthasarathi, S.; Rao, D.S.S.; Palakurthy, N.B.; Yelamaggad, C. V; Krishna Prasad, S. Binary System Exhibiting the Nematic to Twist-Bend Nematic Transition: Behavior of Permittivity and Elastic Constants. *J. Phys. Chem. B* **2016**, *120*, 5056–5062, doi:10.1021/acs.jpcb.6b03048.

313. Tanaka, S.; Takezoe, H.; Éber, N.; Fodor-Csorba, K.; Vajda, A.; Buka, Á. Electroconvection in nematic mixtures of bent-core and calamitic molecules. *Phys. Rev. E* **2009**, *80*, 021702, doi:10.1103/PhysRevE.80.021702.

314. Chakraborty, S.; Chakraborty, A.; Das, M.K.; Weissflog, W. Effect of the hockey-shaped mesogen as an additive on the critical behaviour at the smectic A to nematic phase transition. *J. Mol. Liq.* **2016**, *219*, 608–613, doi:10.1016/j.molliq.2016.04.002.

315. Chakraborty, S.; Chakraborty, A.; Das, M.K.; Weissflog, W. Dielectric investigation on some binary mixtures of hockey-stick-shaped liquid crystal and octyloxy-cyanobiphenyl. *Phase Transitions* **2019**, *92*, 806–815, doi:10.1080/01411594.2019.1642476.

316. Salamon, P.; Éber, N.; Buka, Á.; Gleeson, J.T.; Sprunt, S.; Jákli, A. Dielectric properties of mixtures of a bent-core and a calamitic liquid crystal. *Phys. Rev. E* **2010**, *81*, 031711,

doi:10.1103/PhysRevE.81.031711.

317. Meyer, C.; Luckhurst, G.R.; Dozov, I. The temperature dependence of the heliconical tilt angle in the twist-bend nematic phase of the odd dimer CB7CB. *J. Mater. Chem. C* **2015**, *3*, 318–328, doi:10.1039/C4TC01927J.

318. Dunmur, D.A.; Luckhurst, G.R.; De La Fuente, M.R.; Diez, S.; Peréz Jubindo, M.A. Dielectric relaxation in liquid crystalline dimers. *J. Chem. Phys.* **2001**, *115*, 8681–8691, doi:10.1063/1.1409365.

319. Sugisawa, S.Y.; Tabe, Y. Induced smectic phases of stoichiometric liquid crystal mixtures. *Soft Matter* **2016**, *12*, 3103–3109, doi:10.1039/c6sm00038j.

320. Gleeson, H.F.; Liu, H.; Kaur, S.; Srigengan, S.; Görtz, V.; Mandle, R.; Lydon, J.E. Self-assembling, macroscopically oriented, polymer filaments; a doubly nematic organogel. *Soft Matter* **2018**, *14*, 9159–9167, doi:10.1039/C8SM01638K.

321. Trbojevic, N. Templating Novel Thermotropic Liquid Crystal Phases, The University of Leeds, 2020.

322. Wiant, D.; Gleeson, J.T.; Éber, N.; Fodor-Csorba, K.; Jákli, A.; Tóth-Katona, T. Nonstandard electroconvection in a bent-core nematic liquid crystal. *Phys. Rev. E* **2005**, *72*, 041712, doi:10.1103/PhysRevE.72.041712.

323. Kaur, S.; Belaissaoui, A.; Goodby, J.W.; Görtz, V.; Gleeson, H.F. Nonstandard electroconvection in a bent-core oxadiazole material. *Phys. Rev. E - Stat. Nonlinear, Soft Matter Phys.* **2011**, *83*, 41704, doi:10.1103/PhysRevE.83.041704.

324. Tadapatri, P.; Krishnamurthy, K.S. Competing Instability Modes in an Electrically Driven Bent-Core Nematic Liquid Crystal. *J. Phys. Chem. B* **2012**, *116*, 782–793, doi:10.1021/jp210383p.

325. Petrov, M.; Keskinova, E.; Katranchev, B.; Naradikian, H. Electroconvection in dimeric nematic liquid crystals with short-range smectic C order: dynamical characteristics. *Liq. Cryst.* **2011**, *38*, 41–52, doi:10.1080/02678292.2010.524944.

326. Petrov, M.; Katranchev, B.; Keskinova, E.; Naradikian, H. The electroconvection in dimeric nematic liquid crystals. In Proceedings of the Journal of Optoelectronics and Advanced Materials; 2007; Vol. 9, pp. 438–441.

327. Gleeson, H.F.; Kaur, S.; Görtz, V.; Belaissaoui, A.; Cowling, S.; Goodby, J.W. The Nematic Phases of Bent-Core Liquid Crystals. *ChemPhysChem* **2014**, *15*, 1251–1260, doi:10.1002/cphc.201400014.

328. Varanytsia, A.; Chien, L.-C. Giant Flexoelectro-optic Effect with Liquid Crystal Dimer CB7CB.

Sci. Rep. **2017**, *7*, 41333, doi:10.1038/srep41333.

329. Éber, N.; Xiang, Y.; Buka, Á. Bent core nematics as optical gratings. *J. Mol. Liq.* **2018**, *267*, 436–444, doi:10.1016/j.molliq.2017.09.025.

330. Balachandran, R.; Panov, V.P.; Panarin, Y.P.; Vij, J.K.; Tamba, M.G.; Mehl, G.H.; Song, J.K. Flexoelectric behavior of bimesogenic liquid crystals in the nematic phase – observation of a new self-assembly pattern at the twist-bend nematic and the nematic interface. *J. Mater. Chem. C* **2014**, *2*, 10217–10217, doi:10.1039/C4TC90153C.

331. Tadapatri, P.; Krishnamurthy, K.S.; Weissflog, W. Multiple electroconvection scenarios in a bent-core nematic liquid crystal. *Phys. Rev. E* **2010**, *82*, 031706, doi:10.1103/PhysRevE.82.031706.

332. Kochowska, E.; Németh, S.; Pelzl, G.; Buka, Á. Electroconvection with and without the Carr-Helfrich effect in a series of nematic liquid crystals. *Phys. Rev. E* **2004**, *70*, 011711, doi:10.1103/PhysRevE.70.011711.

333. Katranchev, B.; Petrov, M. Prewavy electrohydrodynamic instability in dimeric nematic liquid crystals with short range smectic “c” order. *Comptes Rendus L’Academie Bulg. des Sci.* **2009**, *62*, 329–334.

334. Krishnamurthy, K.S.; Palakurthy, N.B.; Yelamaggad, C. V Confined Electroconvective and Flexoelectric Instabilities Deep in the Freedericksz State of Nematic CB7CB. *J. Phys. Chem. B* **2017**, *121*, 5447–5454, doi:10.1021/acs.jpcb.7b03072.

335. Haller, I. Elastic constants of the nematic liquid crystalline phase of p-methoxybenzylidene-p-n-butylaniline (MBBA). *J. Chem. Phys.* **1972**, *57*, 1400–1405, doi:10.1063/1.1678416.

336. Huh, J.H.; Hidaka, Y.; Rossberg, A.G.; Kai, S. Pattern formation of chevrons in the conduction regime in homeotropically aligned liquid crystals. *Phys. Rev. E - Stat. Physics, Plasmas, Fluids, Relat. Interdiscip. Top.* **2000**, *61*, 2769–2776, doi:10.1103/PhysRevE.61.2769.

337. Pezeril, T. [INVITED] Laser generation and detection of ultrafast shear acoustic waves in solids and liquids. *Opt. Laser Technol.* **2016**, *83*, 177–188, doi:10.1016/j.optlastec.2016.03.019.

338. Povey, M.J.W. (Malcolm J.W.. Water. In *Ultrasonic Techniques for Fluids Characterization*; 1997; pp. 11–44.

339. Uchino, K. The Development of Piezoelectric Materials and the New Perspective. In *Advanced Piezoelectric Materials: Science and Technology*; Woodhead Publishing Limited, 2010; pp. 1–89 ISBN 978-1-84569-534-7.

340. King, T.G.; Preston, M.E.; Murphy, B.J.M.; Cannell, D.S. Piezoelectric ceramic actuators: A

review of machinery applications. *Precis. Eng.* **1990**, *12*, 131–136, doi:10.1016/0141-6359(90)90084-C.

341. Pukada, E. History and recent progress in piezoelectric polymers. *IEEE Trans. Ultrason. Ferroelectr. Freq. Control* **2000**, *47*, 1277–1290, doi:10.1109/58.883516.

342. Ueberschlag, P. PVDF piezoelectric polymer. *Sens. Rev.* 2001, *21*, 118–125.

343. Fukada, E.; Yasuda, I. On the Piezoelectric Effect of Bone. *J. Phys. Soc. Japan* **1957**, *12*, 1158–1162, doi:10.1143/JPSJ.12.1158.

344. Setter, N. ABC of Piezoelectricity and Piezoelectric Materials. In *Piezoelectric Materials in Devices: Extended Reviews on Current and Emering Piezoelectric Materials, Technology, and Applications*; Piezoelectric materials for the end user; N. Setter, 2002; pp. 1–27 ISBN 2970034603.

345. Ball, P. Stealing a lead on lead. *Nat. Mater.* **2010**, *9*, 98–98, doi:10.1038/nmat2618.

346. Erhart, J.; Půlpán, P.; Pustka, M. Piezoelectric Ceramic Materials. In *Piezoelectric Ceramic Resonators*; Bergmann, C., Ed.; Topics in Mining, Metallurgy and Materials Engineering; Springer International Publishing: Cham, 2017; pp. 11–26 ISBN 978-3-319-42480-4.

347. Pasechnik, S. V.; Chigrinov, V.G.; Shmeliova, D. V. Ultrasound in Liquid Crystals. In *Liquid Crystals*; Wiley, 2009; pp. 111–177.

348. Dávila, M.J.; Gedanitz, H.; Span, R. Speed of sound in saturated aliphatic alcohols (propan-2-ol, butan-2-ol, and 2-methylpropan-1-ol) and alkanediols (ethane-1,2-diol, propane-1,2- and -1,3-diol) at temperature between 253.15 K and 353.15 K and pressures up to 30 MPa. *J. Chem. Thermodyn.* **2016**, *101*, 199–206, doi:10.1016/j.jct.2016.06.001.

349. Scholz, C.W.; Span, R. Speeds of Sound in Methanol at Temperatures from 233.33 to 353.21 K at Pressures up to 20 MPa. *Int. J. Thermophys.* **2021**, *42*, 65, doi:10.1007/s10765-021-02811-2.

350. Del Grosso, V.A.; Mader, C.W. Speed of Sound in Pure Water. *J. Acoust. Soc. Am.* **1972**, *52*, 1442–1446, doi:10.1121/1.1913258.

351. Povey, M.J.W.; Hindle, S.A.; Kennedy, J.D.; Stec, Z.; Taylor, R.G. The molecular basis for sound velocity in n-alkanes, 1-alcohols and dimethylsiloxanes. *Phys. Chem. Chem. Phys.* **2003**, *5*, 73–78, doi:10.1039/b206425a.

352. Garrett, S.L. Attenuation of Sound. In *Understanding Acoustics*; Springer, 2020; pp. 673–698.

353. Shields, F.D. Thermal Relaxation in Fluorine. *J. Acoust. Soc. Am.* **1962**, *34*, 271–274, doi:10.1121/1.1928109.

354. Isakovich, M.A.; Chaban, I.A. Propagation of Sound in Strongly Viscous Liquids. *Sov. J. Exp. Theor. Phys.* **1966**, *23*, 893.

355. Garrett, S.L. Elasticity of Solids. In *Understanding Acoustics*; Springer, 2020; pp. 179–233.

356. Hecksher, T.; Olsen, N.B.; Dyre, J.C. *Model for the alpha and beta shear-mechanical properties of supercooled liquids and its comparison to squalane data*; 2017;

357. Rayleigh, Lord XXXIV. On the transmission of light through an atmosphere containing small particles in suspension, and on the origin of the blue of the sky. *London, Edinburgh, Dublin Philos. Mag. J. Sci.* **1899**, *47*, 375–384, doi:10.1080/14786449908621276.

358. Mie, G. Beiträge zur Optik trüber Medien, speziell kolloidaler Metallösungen. *Ann. Phys.* **1908**, *330*, 377–445, doi:10.1002/andp.19083300302.

359. Povey, M.J.W. Scattering of Sound. In *Ultrasonic Techniques for Fluids Characterization*; Elsevier, 1997; pp. 91–140 ISBN 13:978-0-12-563730-5.

360. Dukhin, A.S.; Goetz, P.J. Acoustic Spectroscopy for Concentrated Polydisperse Colloids with High Density Contrast. *Langmuir* **1996**, *12*, 4987–4997, doi:10.1021/la951085y.

361. McClements, D.J.; Povey, M.J.W. Scattering of ultrasound by emulsions. *J. Phys. D. Appl. Phys.* **1989**, *22*, 38–47, doi:10.1088/0022-3727/22/1/006.

362. Epstein, P.S.; Carhart, R.R. The Absorption of Sound in Suspensions and Emulsions. I. Water Fog in Air. *J. Acoust. Soc. Am.* **1953**, *25*, 553–565, doi:10.1121/1.1907107.

363. Allegra, J.R.; Hawley, S.A. Attenuation of Sound in Suspensions and Emulsions: Theory and Experiments. *J. Acoust. Soc. Am.* **1972**, *51*, 1545–1564, doi:10.1121/1.1912999.

364. Mougin, P.; Wilkinson, D.; Roberts, K.J.; Tweedie, R. Characterization of particle size and its distribution during the crystallization of organic fine chemical products as measured in situ using ultrasonic attenuation spectroscopy. *J. Acoust. Soc. Am.* **2001**, *109*, 274–282, doi:10.1121/1.1331113.

365. Kieffer, S.W. Sound speed in liquid-gas mixtures: Water-air and water-steam. *J. Geophys. Res.* **1977**, *82*, 2895–2904, doi:10.1029/JB082i020p02895.

366. Krokhin, A.A.; Arriaga, J.; Gumen, L.N. Speed of sound in periodic elastic composites. *Phys. Rev. Lett.* **2003**, *91*, doi:10.1103/PhysRevLett.91.264302.

367. Eden, D.; Garland, C.W.; Williamson, R.C. Ultrasonic investigation of the nematic-isotropic phase transition in MBBA. *J. Chem. Phys.* **1973**, *58*, 1861–1868, doi:10.1063/1.1679444.

368. Nagai, S.; Martinoty, P.; Candau, S. Ultrasonic investigation of nematic liquid crystals in the

isotropic and nematic phases. *J. Phys.* **1976**, *37*, 769–780, doi:10.1051/jphys:01976003706076900.

369. Mullen, M.E.; Lüthi, B.; Stephen, M.J. Sound velocity in a nematic liquid crystal. *Phys. Rev. Lett.* **1972**, *28*, 799–801, doi:10.1103/PhysRevLett.28.799.

370. Edmonds, P.D.; Orr, D.A. Ultrasonic Absorption and Dispersion at Phase Transitions in Liquid Crystalline Compounds. *Mol. Cryst.* **1966**, *2*, 135–166, doi:10.1080/15421406608083066.

371. Natale, G.G. The contribution of ultrasonic measurements to the study of liquid crystals. I. Nematics. *J. Acoust. Soc. Am.* **1978**, *63*, 1265–1278, doi:10.1121/1.381878.

372. Grammes, C.; Krüger, J.K.; Bohn, K.P.; Baller, J.; Fischer, C.; Schorr, C.; Rogez, D.; Alnot, P. Universal relaxation behavior of classical liquid crystals at hypersonic frequencies. *Phys. Rev. E* **1995**, *51*, 430–440, doi:10.1103/PhysRevE.51.430.

373. Sátiro, C.; Vitoriano, C. Director fluctuations in nematic liquid crystals induced by an ultrasonic wave. *Phys. Rev. E* **2012**, *86*, 011701, doi:10.1103/PhysRevE.86.011701.

374. Ko, J.-H.; Hwae Hwang, Y.; Kim, J.-H. Sound propagation in 5CB liquid crystals homogeneously confined in a planar cell. *J. Inf. Disp.* **2009**, *10*, 72–75, doi:10.1080/15980316.2009.9652084.

375. Bradberry, G.W.; Clarke, C.F. Temperature dependence and asymmetry of the hypersound velocity in cyanobiphenyl liquid crystals. *Phys. Lett. A* **1983**, *95*, 305–308, doi:10.1016/0375-9601(83)90026-9.

376. Bacri, J.C. Effets d'un champ magnétique sur l'atténuation et la vitesse des ondes ultrasonores dans un cristal liquide nématique. *J. Phys.* **1974**, *35*, 601–607, doi:10.1051/jphys:01974003507-8060100.

377. Vaughan, J.M. Brillouin scattering in the nematic and isotropic phases of a liquid crystal. *Phys. Lett. A* **1976**, *58*, 325–328, doi:10.1016/0375-9601(76)90254-1.

378. Liao, Y.; Clark, N.A.; Pershan, P.S. Brillouin scattering from smectic liquid crystals. *Phys. Rev. Lett.* **1973**, *30*, 639–641, doi:10.1103/PhysRevLett.30.639.

379. Mattsson, J.; Forrest, J.A.; Börjesson, L. Quantifying glass transition behavior in ultrathin free-standing polymer films. *Phys. Rev. E* **2000**, *62*, 5187–5200, doi:10.1103/PhysRevE.62.5187.

380. Lubbers, J.; Graaff, R. A simple and accurate formula for the sound velocity in water. *Ultrasound Med. Biol.* **1998**, *24*, 1065–1068, doi:10.1016/S0301-5629(98)00091-X.

381. Elouali, M.; Beyens, C.; Elouali, F.Z.; Yaroshchuk, O.; Abbar, B.; Maschke, U. Dispersions of

Diamond Nanoparticles in Nematic Liquid Crystal/Polymer Materials. *Mol. Cryst. Liq. Cryst.* **2011**, *545*, 77/[1301]-84/[1308], doi:10.1080/15421406.2011.571977.

382. Cooper, J. *Compositional Analysis of Merck E7 Liquid Crystal Intermediates Using UltraPerformance Convergence Chromatography (UPC 2) with PDA Detection*; Waters Corperation, Manchester, 2013;

383. Venkatacharyulu, P.; Gupta, A.V.N.; Rao, J. V.; Prasad, K.S.R.; Prasad, N.V.L.N. Phase transition studies in 50CB and 80CB. *Cryst. Res. Technol.* **1989**, *24*, 835–844, doi:10.1002/crat.2170240822.

384. Humphries, R.L.; Luckhurst, G.R. A statistical theory of liquid crystalline mixtures. Components of different size. *Chem. Phys. Lett.* **1973**, *23*, 567–570, doi:10.1016/0009-2614(73)89030-X.

385. Park, J.W.; Bak, C.S.; Labes, M.M. Effects of Molecular Complexing on the Properties of Binary Nematic Liquid Crystal Mixtures. *J. Am. Chem. Soc.* 1975, *97*, 4398–4400.

386. Brás, A.R.; Dionísio, M.; Huth, H.; Schick, C.; Schönhals, A. Origin of glassy dynamics in a liquid crystal studied by broadband dielectric and specific heat spectroscopy. *Phys. Rev. E - Stat. Nonlinear, Soft Matter Phys.* **2007**, *75*, 061708, doi:10.1103/PhysRevE.75.061708.

387. Kundu, S.K.; Okudaira, S.; Kosuge, M.; Shinyashiki, N.; Yagihara, S. Broadband dielectric spectroscopy of a nematic liquid crystal in benzene. *J. Chem. Phys.* **2008**, *129*, 164509, doi:10.1063/1.2993255.

388. Kapustina, O.A. Ultrasonic Properties. In *Handbook of Liquid Crystals*; Demus, D., Goodby, J., Gray, G., Spiess, H., Eds.; Wiley-VCH Verlag, 1998; pp. 549–568.

389. Chandrasekhar, S. Propagation of elastic waves in liquid crystals. *Proc. R. Soc. London. Ser. A. Math. Phys. Sci.* **1964**, *281*, 92–98, doi:10.1098/rspa.1964.0170.

390. Selinger, J. V.; Spector, M.S.; Greanya, V.A.; Weslowski, B.T.; Shenoy, D.K.; Shashidhar, R. Acoustic realignment of nematic liquid crystals. *Phys. Rev. E* **2002**, *66*, 051708, doi:10.1103/PhysRevE.66.051708.

391. Sátiro, C.; Vitoriano, C. Director-density coupling theory of the acousto-optic effect in nematic liquid crystals. *Phys. Rev. E - Stat. Nonlinear, Soft Matter Phys.* **2011**, *84*, doi:10.1103/PhysRevE.84.041702.

392. Helfrich, W. Orienting Action of Sound on Nematic Liquid Crystals. *Phys. Rev. Lett.* **1972**, *29*, 1583–1586, doi:10.1103/PhysRevLett.29.1583.

393. Nagaï, S.; Peters, A.; Candau, S. Acousto-optical effects in a nematic liquid crystal. *Rev. Phys.*

Appliquée **1977**, *12*, 21–30, doi:10.1051/rphysap:0197700120102100.

394. Laidlaw, W.G. Response of a Nematic Liquid Crystal to an Acoustic Field. *Mol. Cryst. Liq. Cryst.* **1980**, *59*, 13–26, doi:10.1080/00268948008073495.

395. Sripaipan, C.; Hayes, C.F.; Fang, G.T. Ultrasonically-induced optical effect in a nematic liquid crystal. *Phys. Rev. A* **1977**, *15*, 1297–1303, doi:10.1103/PhysRevA.15.1297.

396. Malanoski, A.P.; Greanya, V.A.; Weslowski, B.T.; Spector, M.S.; Selinger, J. V.; Shashidhar, R. Theory of the acoustic realignment of nematic liquid crystals. *Phys. Rev. E* **2004**, *69*, 021705, doi:10.1103/PhysRevE.69.021705.

397. Greanya, V.A.; Spector, M.S.; Selinger, J. V.; Weslowski, B.T.; Shashidhar, R. Acousto-optic response of nematic liquid crystals. *J. Appl. Phys.* **2003**, *94*, 7571, doi:10.1063/1.1628381.

398. Mailer, H.; Likins, K.L.; Taylor, T.R.; Fergason, J.L. Effect of ultrasound on a nematic liquid crystal. *Appl. Phys. Lett.* **1971**, *18*, 105–107, doi:10.1063/1.1653581.

399. Shimizu, Y.; Koyama, D.; Taniguchi, S.; Emoto, A.; Nakamura, K.; Matsukawa, M. Periodic pattern of liquid crystal molecular orientation induced by ultrasound vibrations. *Appl. Phys. Lett.* **2017**, *111*, 231101, doi:10.1063/1.5010213.

400. Dion, J.L.; Jacob, A.D. A new hypothesis on ultrasonic interaction with nematic liquid crystal. *Appl. Phys. Lett.* **1977**, *31*, 490–493, doi:10.1063/1.89753.

401. Hayes, C.F. Evidence for Acoustic Streaming in the Nematic Acousto-Optic Effect. *Mol. Cryst. Liq. Cryst.* **1980**, *59*, 317–328, doi:10.1080/00268948008071431.

402. Kapustina, O.A.; Romanova, O. V. High-frequency acoustic domains in liquid crystals. *Crystallogr. Reports* **2001**, *46*, 103–110, doi:10.1134/1.1343136.

403. Kapustina, O.A. Dual nature of the orientational effect of ultrasound on liquid crystals. *Crystallogr. Reports* **2017**, *62*, 745–752, doi:10.1134/S1063774517050091.

404. Kozhevnikov, E.N. Deformation of a homeotropic nematic liquid crystal layer at oblique incidence of an ultrasonic wave. *Acoust. Phys.* **2005**, *51*, 688–694, doi:10.1134/1.2130900.

405. Scudieri, F.; Bertolotti, M.; Melone, S.; Albertini, G. Acoustohydrodynamic instability in nematic liquid crystals. *J. Appl. Phys.* **1976**, *47*, 3781–3783, doi:10.1063/1.323261.

406. Candau, S.; Ferre, A.; Peters, A.; Waton, G.; Pieranski, P. Acoustical Streaming in a Film of Nematic Liquid Crystal. *Mol. Cryst. Liq. Cryst.* **1980**, *61*, 7–30, doi:10.1080/00268948008081981.

407. Kozhevnikov, E.N. Acoustic streaming in a nematic liquid crystal layer under binary action of

sound waves and viscous waves. *Acoust. Phys.* **2010**, *56*, 24–32, doi:10.1134/S1063771010010045.

408. Mullin, T.; Peacock, T. Hydro dynamic instabilities in nematic liquid crystals under oscillatory shear. *Proc. R. Soc. A Math. Phys. Eng. Sci.* **1999**, *455*, 2635–2653, doi:10.1098/rspa.1999.0420.

409. Pollet, B.; Despesse, G.; Costa, F. A New Non-Isolated Low-Power Inductorless Piezoelectric DC-DC Converter. *IEEE Trans. Power Electron.* **2019**, *34*, 11002–11013, doi:10.1109/TPEL.2019.2900526.

410. Anikeev, D.I.; Bocharov, Y. V.; Vuzhva, A.D. Reduction of threshold of acousto-optic effect in a nematic crystal subject to combined actions. *Liq. Cryst.* **1989**, *6*, 593–596, doi:10.1080/02678298908034178.

411. Dierking, I.; Marshall, O.; Wright, J.; Bulleid, N. Annihilation dynamics of umbilical defects in nematic liquid crystals under applied electric fields. *Phys. Rev. E* **2005**, *71*, 061709, doi:10.1103/PhysRevE.71.061709.

412. Biryukov, S. V.; Gulyaev, Y. V.; Krylov, V. V.; Plessky, V.P. Basic Types of Surface Acoustic Waves in Solids. In; 1995; pp. 1–17.

413. Fu, Y.Q.; Luo, J.K.; Nguyen, N.T.; Walton, A.J.; Flewitt, A.J.; Zu, X..; Li, Y.; McHale, G.; Matthews, A.; Iborra, E.; et al. Advances in piezoelectric thin films for acoustic biosensors, acoustofluidics and lab-on-chip applications. *Prog. Mater. Sci.* **2017**, *89*, 31–91, doi:10.1016/j.pmatsci.2017.04.006.

414. Jen, S.; Bobkowski, R. Black lithium niobate SAW device fabrication and performance evaluation. In Proceedings of the 2000 IEEE Ultrasonics Symposium. Proceedings. An International Symposium (Cat. No.00CH37121); IEEE, 2000; Vol. 1, pp. 269–273.

415. Potter, G.; Tokranova, N.; Rastegar, A.; Castracane, J. Design, fabrication, and testing of surface acoustic wave devices for semiconductor cleaning applications. *Microelectron. Eng.* **2016**, *162*, 100–104, doi:10.1016/j.mee.2016.04.006.

416. Roditi International - Photonic Materials Lithium Niobate Available online: http://www.roditi.com/SingleCrystal/LiNbO3/LiNbO3.html (accessed on Feb 5, 2021).

417. Fall, D.; Duquennoy, M.; Ouaftouh, M.; Smagin, N.; Piwakowski, B.; Jenot, F. Generation of broadband surface acoustic waves using a dual temporal-spatial chirp method. *Cit. J. Acoust. Soc. Am.* **2017**, *142*, 108, doi:10.1121/1.4994676.

418. Ding, X.; Lin, S.-C.S.; Kiraly, B.; Yue, H.; Li, S.; Chiang, I.-K.; Shi, J.; Benkovic, S.J.; Huang, T.J. On-chip manipulation of single microparticles, cells, and organisms using surface acoustic

waves., doi:10.1073/pnas.1209288109/-/DCSupplemental.

419. Wixforth, A.; Strobl, C.; Gauer, C.; Toegl, A.; Scriba, J.; Guttenberg, Z. V. Acoustic manipulation of small droplets. *Anal. Bioanal. Chem.* **2004**, *379*, 982–991, doi:10.1007/s00216-004-2693-z.

420. Wiklund, M.; Green, R.; Ohlin, M. Acoustofluidics 14: Applications of acoustic streaming in microfluidic devices. *Lab Chip* 2012, *12*, 2438–2451.

421. Ding, X.; Li, P.; Lin, S.C.S.; Stratton, Z.S.; Nama, N.; Guo, F.; Slotcavage, D.; Mao, X.; Shi, J.; Costanzo, F.; et al. Surface acoustic wave microfluidics. *Lab Chip* 2013.

422. Alghane, M.; Chen, B.X.; Fu, Y.Q.; Li, Y.; Luo, J.K.; Walton, A.J. Experimental and numerical investigation of acoustic streaming excited by using a surface acoustic wave device on a 128° YX-LiNbO 3 substrate. *J. Micromechanics Microengineering* **2011**, *21*, 015005, doi:10.1088/0960-1317/21/1/015005.

423. Du, X.Y.; Fu, Y.Q.; Luo, J.K.; Flewitt, A.J.; Milne, W.I. Microfluidic pumps employing surface acoustic waves generated in ZnO thin films. *J. Appl. Phys* **2009**, *105*, 24508, doi:10.1063/1.3068326.

424. Frommelt, T.; Gogel, D.; Kostur, M.; Talkner, P.; Hanggi, P.; Wixforth, A. Flow patterns and transport in Rayleigh surface acoustic wave streaming: combined finite element method and raytracing numerics versus experiments. *IEEE Trans. Ultrason. Ferroelectr. Freq. Control* **2008**, *55*, 2298–2305, doi:10.1109/TUFFC.928.

425. Dung Luong, T.; Trung Nguyen, N. Surface Acoustic Wave Driven Microfluidics – A Review. *Micro Nanosyst.* **2010**, *2*, 217–225, doi:10.2174/1876402911002030217.

426. Rayleigh, Lord On the Circulation of Air observed in Kundt's Tubes, and on some Allied Acoustical Problems. *Philos. Trans. R. Soc. London* **1884**, *175*, 1–21.

427. Alghane, M.; Fu, Y.Q.; Chen, B.X.; Li, Y.; Desmulliez, M.P.Y.; Walton, A.J. Streaming phenomena in microdroplets induced by Rayleigh surface acoustic wave. *J. Appl. Phys.* **2011**, *109*, 114901, doi:10.1063/1.3586040.

428. Qi, A.; Friend, J.; Yeo, L. A miniaturized surface acoustic wave atomizer with a disposable pump-free liquid supply system for continuous atomization. In Proceedings of the NEMS 2011 - 6th IEEE International Conference on Nano/Micro Engineered and Molecular Systems; 2011; pp. 289–292.

429. Nam-Trung Nguyen; White, R.M. Acoustic streaming in micromachined flexural plate wave devices: numerical simulation and experimental verification. *IEEE Trans. Ultrason.*

Ferroelectr. Freq. Control **2000**, *47*, 1463–1471, doi:10.1109/58.883536.

430. Park, J.; Destgeer, G.; Kim, H.; Cho, Y.; Sung, H.J. In-droplet microparticle washing and enrichment using surface acoustic wave-driven acoustic radiation force. *Lab Chip* **2018**, *18*, 2936–2945, doi:10.1039/C8LC00733K.

431. Guo, F.; Mao, Z.; Chen, Y.; Xie, Z.; Lata, J.P.; Li, P.; Ren, L.; Liu, J.; Yang, J.; Dao, M.; et al. Three-dimensional manipulation of single cells using surface acoustic waves. *Proc. Natl. Acad. Sci.* **2016**, *113*, 1522–1527, doi:10.1073/pnas.1524813113.

432. Zhou, Y. Comparison of numerical models for bulk and surface acoustic wave-induced acoustophoresis in a microchannel. *Eur. Phys. J. Plus* **2020**, *135*, 696, doi:10.1140/epjp/s13360-020-00697-x.

433. Sato, S.; Ueda, H. Effects of Surface Acoustic Waves on Molecular Orientation in Nematic Liquid Crystals. *Jpn. J. Appl. Phys.* **1981**, *20*, L511–L514, doi:10.1143/JJAP.20.L511.

434. Toda, K.; Inoue, M.; Moritake, H.; Yoshino, K. Analysis of acoustic streaming in nematic liquid-crystal cell. *Japanese J. Appl. Physics, Part 1 Regul. Pap. Short Notes Rev. Pap.* **2005**, *44*, 316–323, doi:10.1143/JJAP.44.316.

435. Inoue, M.; Moritake, H.; Toda, K. Periodic Property of Domain in Nematic Liquid Crystal Induced by Elastic Wave. *Jpn. J. Appl. Phys.* **2000**, *39*, 3125–3129, doi:10.1143/JJAP.39.3125.

436. Yoshino, K.; Inoue, M.; Moritake, H.; Toda, K. Study of orientation of liquid crystal molecules at interface by shear horizontal wave. In Proceedings of the IEEE International Conference on Conduction and Breakdown in Dielectric Liquids, ICDL; 2002; pp. 386–389.

437. Liu, Y.J.; Ding, X.; Lin, S.C.S.; Shi, J.; Chiang, I.K.; Huang, T.J. Surface acoustic wave driven light shutters using polymer-dispersed liquid crystals. *Adv. Mater.* **2011**, *23*, 1656–1659, doi:10.1002/adma.201003708.

438. Bury, P.; Veveričík, M.; Kúdelčík, J.; Kopčanský, P.; Timko, M.; Závišová, V. Structural Changes in Liquid Crystals Doped with Rod-Like Magnetic Particles Studied by Surface Acoustic Waves. **2017**, *131*, doi:10.12693/APhysPolA.131.913.

439. Bury, P.; Kúdelčík, J.; Hardoň, Š.; Veveričik, M.; Kopčanský, P.; Timko, M.; Závišová, V. Effect of spherical magnetic particles on liquid crystals behavior studied by surface acoustic waves. *J. Magn. Magn. Mater.* **2017**, *423*, 57–60, doi:10.1016/j.jmmm.2016.09.023.

440. Bury, P.; Veveričík, M.; Černobila, F.; Kopčanský, P.; Timko, M.; Závišová, V. Study of structural changes in nematic liquid crystals doped with magnetic nanoparticles using surface acoustic waves. *Crystals* **2020**, *10*, 1–14, doi:10.3390/cryst10111023.

441. Edwards, R.S.; Ward, J.; Zhou, L.Q.; Trushkevych, O. The interaction of polymer dispersed liquid crystal sensors with ultrasound. *Appl. Phys. Lett.* **2020**, *116*, 044104, doi:10.1063/1.5139598.

442. Harada, Y.; Koyama, D.; Fukui, M.; Emoto, A.; Nakamura, K.; Matsukawa, M. Molecular Orientation in a Variable-Focus Liquid Crystal Lens Induced by Ultrasound Vibration. *Sci. Rep.* **2020**, *10*, doi:10.1038/s41598-020-62481-2.

443. Ozaki, R.; Aoki, M.; Yoshino, K.; Toda, K.; Moritake, H. Effective viscosity for nematic-liquid-crystal viscosity measurement using a shear horizontal wave. *Phys. Rev. E - Stat. Nonlinear, Soft Matter Phys.* **2010**, *81*, doi:10.1103/PhysRevE.81.061703.

444. Moritake, H.; Ozaki, R.; Yoshino, K. Effects of ultrasonic wave propagating in liquid crystals on substrate. In Proceedings of the 2008 IEEE International Conference on Dielectric Liquids; IEEE, 2008; pp. 1–4.

445. Shipley Company MF 319 Data Sheet 1997.

446. HOLOEYE Photonics AG LC 2012 Spatial Light Modulator (transmissive) – HOLOEYE Photonics AG Available online: https://holoeye.com/lc-2012-spatial-light-modulator/ (accessed on Jul 24, 2021).

447. HOLOEYE Photonics AG GAEA-2 10 Megapixel Phase Only LCOS-SLM Available online: https://holoeye.com/gaea-4k-phase-only-spatial-light-modulator/ (accessed on Mar 11, 2019).

448. Achenbach, S.; Klymyshyn, D.; Mappes, T.; Kachayev, A.; Subramanian, V.; Wells, G.; Mohr, J. Submicron-scale surface acoustic wave resonators fabricated by high aspect ratio X-ray lithography and aluminum lift-off. *Microsyst. Technol.* **2008**, *14*, 1715–1719, doi:10.1007/s00542-007-0498-7.

449. Fang, S.R.; Zhang, S.Y.; Lu, Z.F. SAW focusing by circular-arc interdigital transducers on YZ-LiNbO. *IEEE Trans. Ultrason. Ferroelectr. Freq. Control* **1989**, *36*, 178–184, doi:10.1109/58.19148.

450. Beliakov, G.; Chan, D.Y.C. Analysis of inhomogeneous optical systems by the use of ray tracing II Three-dimensional systems with symmetry. *Appl. Opt.* **1998**, *37*, 5106, doi:10.1364/AO.37.005106.

451. Shang, X.; Meeus, L.; Cuypers, D.; De Smet, H. Fast switching cholesteric liquid crystal optical beam deflector with polarization independence. *Sci. Rep.* **2017**, *7*, 6492, doi:10.1038/s41598-017-06944-z.

452. Hillmer, H.H.; Iskhandar, M.S.Q.; Hasan, M.K.; Akhundzada, S.; Al-Qargholi, B.; Tatzel, A.

MOEMS micromirror arrays in smart windows for daylight steering. *J. Opt. Microsystems* **2021**, *1*, 014502, doi:10.1117/1.JOM.1.1.014502.

453. Huh, J.H.; Hidaka, Y.; Kai, S. New classification of chevrons in electroconvection in homeotropically-aligned nematics. *Mol. Cryst. Liq. Cryst. Sci. Technol. Sect. A Mol. Cryst. Liq. Cryst.* **2001**, *366*, 833–840, doi:10.1080/10587250108024024.

454. Srigengan, S.; Liu, H.; Osipov, M.A.; Mandle, R.; Cowling, S.J.; Gleeson, H.F. Anomalies in the twist elastic behaviour of mixtures of calamitic and bent-core liquid crystals. *Liq. Cryst.* **2020**, *47*, 895–907, doi:10.1080/02678292.2019.1687767.

455. Shimizu, Y.; Koyama, D.; Fukui, M.; Emoto, A.; Nakamura, K.; Matsukawa, M. Ultrasound liquid crystal lens. *Appl. Phys. Lett.* **2018**, *112*, 161104, doi:10.1063/1.5027131.

456. Onaka, J.; Iwase, T.; Fukui, M.; Koyama, D.; Matsukawa, M. Ultrasound liquid crystal lens with enlarged aperture using traveling waves. *Opt. Lett.* **2021**, *46*, 1169, doi:10.1364/OL.414295.

457. Wohltjen, H.; Dessy, R. Surface acoustic wave probes for chemical analysis. III. Thermomechanical polymer analyzer. *Anal. Chem.* **2002**, *51*, 1470–1475, doi:10.1021/AC50045A026.

458. Fourati, N.; Lazerges, M.; Vedrine, C.; Fougnion, J.-M.; Zerrouki, C.; Rousseau, L.; Lepeut, P.; Bonnet, J.J.; Pernelle, C. Surface Acoustic Waves Sensor for DNA-Biosensor Development. *Sens. Lett.* **2009**, *7*, 847–850, doi:10.1166/sl.2009.1160.

459. Gao, Y.; Fajrial, A.K.; Yang, T.; Ding, X. Emerging on-chip surface acoustic wave technology for small biomaterials manipulation and characterization. *Biomater. Sci.* **2021**, *9*, 1574–1582, doi:10.1039/D0BM01269F.